Accretion regimes and variability in young stars: imprints on UV photometry

Laura Venuti

UNIVERSITÀ DEGLI STUDI DI PALERMO

UNIVERSITÉ GRENOBLE ALPES

THÈSE

Pour obtenir le grade de

DOCTEUR DE L'UNIVERSITÉ GRENOBLE ALPES

préparée dans le cadre d'une cotutelle entre l'*Université Grenoble Alpes* et l'*Università degli Studi di Palermo*

Spécialité : **Astrophysique et Milieux Dilués**

Arrêté ministériel : le 6 janvier 2005 - 7 août 2006

Présentée par

Laura VENUTI

Thèse dirigée par **Jérôme BOUVIER**
codirigée par **Giovanni PERES**

préparée au sein de l'**Institut de Planétologie et d'Astrophysique de Grenoble** et de l'**INAF – Osservatorio Astronomico di Palermo "G. S. Vaiana"**

dans l'**Ecole Doctorale de Physique**

Accretion regimes and variability in young stars: imprints on UV photometry

Thèse soutenue publiquement le **23 Octobre 2015**,
devant le jury composé de :

M. Juan Manuel ALCALA'
Astronome, INAF-OAC, Rapporteur
Mme Matilde FERNANDEZ
Chercheuse, IAA-CSIC, Rapporteur
M. Jonathan FERREIRA
Professeur, IPAG/UJF, Examinateur, Président
M. Fabio REALE
Professeur, UNIPA/INAF-OAPa, Examinateur
M. Jérôme BOUVIER
DR1, IPAG, Directeur de thèse
M. Giovanni PERES
Professeur, UNIPA/INAF-OAPa, co-Directeur de thèse

UNIVERSITÀ DEGLI STUDI DI PALERMO

UNIVERSITÉ GRENOBLE ALPES

THÈSE

Pour obtenir le grade de

DOCTEUR DE L'UNIVERSITÉ GRENOBLE ALPES

préparée dans le cadre d'une cotutelle entre l'*Université Grenoble Alpes* et l'*Università degli Studi di Palermo*

Spécialité : **Astrophysique et Milieux Dilués**

Arrêté ministériel : le 6 janvier 2005 - 7 août 2006

Présentée par

Laura VENUTI

Thèse dirigée par **Jérôme BOUVIER**
codirigée par **Giovanni PERES**

préparée au sein de l'**Institut de Planétologie et d'Astrophysique de Grenoble** et de l'**INAF – Osservatorio Astronomico di Palermo ''G. S. Vaiana''**

dans l'**Ecole Doctorale de Physique**

Accretion regimes and variability in young stars: imprints on UV photometry

Thèse soutenue publiquement le **23 Octobre 2015**,
devant le jury composé de :

M. Juan Manuel ALCALA'
Astronome, INAF-OAC, Rapporteur
Mme Matilde FERNANDEZ
Chercheuse, IAA-CSIC, Rapporteur
M. Jonathan FERREIRA
Professeur, IPAG/UJF, Examinateur, Président
M. Fabio REALE
Professeur, UNIPA/INAF-OAPa, Examinateur
M. Jérôme BOUVIER
DR1, IPAG, Directeur de thèse
M. Giovanni PERES
Professeur, UNIPA/INAF-OAPa, co-Directeur de thèse

Acknowledgements

« E quindi uscimmo a riveder le stelle » (D. Alighieri, *Divina Commedia*, *Inferno XXXIV*)

Let's start from the end. Because the end is just as the beginning. A little girl gazing in wonderment at the infinity of the night sky. Just like that, a glimpse between two piles of bricks; and it never looks the same, and it always feels like the first time. And even when the stars become points on a diagram, after a whole day spent chasing them on the screen of a computer, you go out in the night and instinctively look up, and the sky is always there, ready to catch you in the enchantment of its poetry.

Shortly before starting my PhD, I heard someone saying that the three most important ingredients for an astronomer are fascination with observing the stars, doubts, and encounters. The first element is what brought me to approach the world of Astronomy; the third is what brough me here, writing these words; discovering the second and embracing it as a most important part of scientific growth is what led me to completing these three years of research and being eager to do more. For all of this, and much more, I would like to express my gratitude to Jérôme. Thanks for always trusting me, even when I did not; thanks for letting me being wrong and figuring that out by myself; thanks for always being willing to listen, and for your thorough responses; thanks for the long hours of discussions and exchanges; thanks for your cordiality, affability, and good humor. I would also like to thank Giovanni, whom I first met as a Bachelor student, at a time when "astronomy" was little more than a word for me. Thanks for introducing me to Astrophysics, for fostering my interest in the study of the stars and for encouraging me to pursue it; thanks for your mentoring and your valuable advice. Thanks to both of you for allowing me to do a joint PhD between Grenoble and Palermo, and thus benefit from assiduous interaction with diverse expertise and viewpoints during my work.

I should mention here the CSI 2264 Collaboration, within which the study related in this thesis has been developed. I would like to thank in particular Silvia Alencar, Ann Marie Cody, Kevin Covey, Ettore Flaccomio, Lynne Hillenbrand, Jonathan Irwin, Giusi Micela, Luisa Rebull, John Stauffer, for numerous discussions and exchanges of information and ideas. Thanks to the ODYSSey team at IPAG and to the YSOs experts in Palermo, for encouraging me to present regularly the advances in my thesis work and for their attentive comments and suggestions. I also thank Juan-Manuel Alcalà and Matilde Fernandez for accepting to review my thesis manuscript, and Jonathan Ferreira and Fabio Reale for integrating my defense committee in the quality of examiners.

Essential to the good functioning of life at the lab are the administration and IT groups. I would like to thank them for helping me with solving the various little technical or bureaucratic problems that unavoidably arose during my stay. A special mention goes to Richard: he may not remember it, but he was the first who showed me around upon my arrival at IPAG and made me feel at home.

During these three years, spent in good part abroad, I had the opportunity to travel a little bit. I discovered France, of which I had limited knowledge before starting my PhD, and set foot in Switzerland, Germany, and even the US. However, the most amazing trips that I will remember from my time in Grenoble are those simple, everyday discussions around lunch or coffee break with students, postdocs and researchers from all over the world. Adriano, Alana, Ana, Colin, Dipan, Francesco, Francisco, Helio, Jaqueline, Javier, Julia, Kike, Melinda, Nathalia, Nicole, Raquel, Sudeep, Susmita, Thiago, Victor: thanks for all you have taught me in these intercultural exchanges. I have crossed paths with some of you only for a short while, with others for a longer interval; but each of you has left something to me. I now know a bit more of geography, I learnt some Portuguese and even some Bengali; but especially, it feels like I had

never really perceived the vastness of the world before. I hope that the bonds that we have developed will endure in the years to come.

Special thanks to my office-mates of "bureau 013", Susmita, Victor, and Sudeep (even if for a short time). Thanks for sharing the everyday madness (I will never forget the "jump out of teenage"), the joys and frustrations of life at the lab. And speaking of Susmita, I cannot omit mentioning Ritam: getting close to him, watching him as he grew up, started to walk and to speak was the most unexpected and incredible experience associated with my PhD period. Thanks to both Susmita and Ritam for their help in "releasing the pressure" during the toughest phases of thesis-writing, and to them and Nirupam for "the best end of thesis-writing ever".

I should not forget here the "friends of a lifetime"; in particular, thanks to Anna for being there without fail since the times of high school. We have changed in so many ways since the day we first met, and we hardly get to see each other more than a few times per year, but nothing of that really matters, and time after time we find each other just as we used to do before. Also thanks to Giuseppe, with whom I shared the undergraduate university studies; as we embarked on analogous tracks, we have always been a constant reference and support to each other.

Last but not least, my thought goes to my family, without whom many things would have been much harder. Thanks to my parents for their unconditional support, and to my sisters for keeping my feet on the groud; thanks for your affection and esteem. And I owe a special acknowledgement to my aunt for the numerous exchanges on the Grenoble-Milano line during my PhD.

The last paragraph is for my grandparents, who will never read these lines. I was still little when Nonna Mariuccia passed away, and not much more grown-up when Nonno Peppino followed her; their memories are stored in the drawers of my childhood. Nonna Sara accompanied me for a longer while, till I first set foot in Grenoble. She was the one who taught me how to read, before I started to go to school. She knew before me that I would eventually go on a PhD, but she was not there to see it happen; I wish I were able to make that phone call to tell her "You were right". Nonno Ciccio was there till almost the end, till the first words of this manuscript were written. I will always remember our discussions around dinner about telescopes and observing sites, and his surprised expression when I once told him that I would stay at the Observatory until late for work: "What can you possibly observe? It's so cloudy!"

Contents

List of Tables

List of Figures

Chapter 1

Introduction

Contents

1.1 On the origin of the T Tauri case

1.1.1 A new class of young, variable stars

« I know the stars / are wild as dust / and wait for no man's discipline / but as they wheel / from sky to sky they rake / our lives with pins of light » (L. Cohen, "Another Night with Telescope")

Some years ago, as a young student at the first approach with accretion disks in young stars, I came across those lines which open the classic review on T Tauri stars written by Claude Bertout in 1989. These words provide a perfect synthesis of the complex, bewildering, often unpredictable nature of these objects, on one side, and of the strong fascination for these precursors of our own Sun on the other, which has motivated significant observational and modeling effort over the last 60 years.

A wild, unpredictable nature, that defies any pre-existing classification scheme, is indeed at the very base of the T Tauri star (TTS) definition. The archetype of the class, *T Tauri*, was

first introduced as a remarkable case among variable stars[1] by A. H. Joy in 1942, and "rapid and entirely irregular light-changes" were noted as a distinctive trait. A first attempt at categorizing similar objects followed in Joy (1945). The author grouped "eleven irregular variable stars [...] sufficiently different from other known classes of variables to warrant the recognition of a new type of variable stars whose prototype is T Tauri". Criteria for membership in this new class included: i) rapid irregular light variations of about 3 mag; ii) spectral type F5-G5, with emission lines resembling those of the solar chromosphere; iii) low luminosity; iv) association with dark or bright nebulosity. Objects belonging to this class were observed to display "irregular and unpredictable" light curves, that "vary greatly from year to year and from star to star".

Early tentative interpretations of the peculiar properties of T Tauri stars, notably of their spatial connection with nebular material, assumed they are main-sequence (MS) field dwarfs accidentally passing through diffuse nebulae and interacting with them. Ambartsumian (1947, 1949) was the first to sense that these objects are, in fact, extremely young, newborn stars, still contracting toward the MS. In his pioneering work on stellar associations, he noticed that TTS tend to occur in groups, rather than isolated, forming what he called "T-associations"; moreover, he observed that T-associations are often found in connection with "O-associations", similar groups of objects containing very early-type (O or B) stars. Based on this observational evidence, and on the short lifetimes of massive OB stars (which implies these must be of recent formation), he postulated the young evolutionary status of the (lower-mass) T Tauri stars; this, in turn, provided the grouds for the idea that, in our Galaxy, "the birth of stellar associations and formation of stars within the latter from some other form of matter goes on continuously almost before our eyes" (Ambartsumian 1949), rather than having occurred in a single process several billion years ago[2].

Almost a decade elapsed before Ambartsumian's theory on the youth of TTS spread and met with wide recognition across the astronomic community (see, e.g., Herbig 1957). In the meantime, the original sample of 11 stars, upon which Joy had founded his definition of TTS, had been enlarged by a factor of 10, which enabled Herbig (1962) to promote new spectroscopic criteria for membership in the class: i) hydrogen lines and H and K lines of Ca II observed in emission; ii) presence of the fluorescent Fe I emission lines λ4063 and λ4132; iii) possible presence of forbidden [S II] and [O I] lines (though not always observed); iv) strong Li I λ6707 absorption. This latter property is especially indicative of the pre-main sequence (PMS) status of TTS, since this element is depleted rapidly in early stellar evolution. As noted by the author, objects that satisfy these criteria are also found to be associated with dark or bright nebulosities and to display light variations, hence making two of Joy's original criteria redundant. By that time, the interpretation of T Tauri stars as newly formed stars was supported by solid observational evidence, and represented the only hypothesis that could provide a convincing explanation of the peculiar spatial properties of TTS populations (association with nebulosities and with O- and B-type stars), of the wide absorption lines found in their spectra and of their typical location above the main sequence (i.e., at higher luminosities) on a Hertzsprung-Russell (HR) diagram. Further arguments for their youth, such as their kinematic association with the dark clouds (e.g. Herbig 1977b), would appear later.

The census of TTS in nearby star-forming regions increased rapidly over the following years

[1] Serendipitous discovery of T Tauri dates back to October 1852 and is owed to J. R. Hind, who correctly supposed its variable nature to justify its absence from the most recent sky maps available (Herbig 1953).

[2] As reported in Blaauw (1958): « The importance of the associations for the study of star formation and stellar evolution was for the first time properly evaluated by Ambartsumian (1949). He stressed the fact that we are dealing with unstable groups of stars which cannot have existed in their present form during an interval of more than a few tens of millions of years, or one percent of the age of the galaxy. The inference was that the stars constituting the associations have been formed only recently. It is now generally assumed that star formation has taken place in the Galaxy from its earliest stage up to the present, and is still going on. »

(Herbig & Kameswara Rao 1972, already list over 300 spectroscopically identified sources in Orion); most sources in the class were found to be low-mass, late K- or early M-type stars (Cohen & Kuhi 1979).

1.1.2 The T Tauri phenomenon across the spectrum

T Tauri stars were first detected and categorized based on observational data in the *optical*; however, it soon became evident that distinctive features of these objects appear over a much broader wavelength domain.

At the time of Herbig's (1962) review, it was already known that these sources typically display a flux excess in the blue and, particularly, the *ultraviolet* regions of their spectra with respect to their photospheric colors (e.g., Haro & Herbig 1955; Walker 1956). Observations also showed a tendency for ultraviolet excess to accompany intense line emission. Interpretation of this feature would have to await Walker's (1972) insightful analysis of ultraviolet-excess stars in the Orion Nebula Cluster and in NGC 2264. He suggested that the blue continuum and emission-line spectrum exhibited by these objects are produced in zones, at the stellar surface, impacted by infalling material from the circumstellar environment. Interestingly, the author considered two possible scenarios for the material infall onto the star: one where it is spherically symmetric, and a second where it is confined to a region of moderate vertical extent around the star. This represented the first study to prepare the ground for the association of the UV excess in T Tauri stars with accretion of material from a circumstellar disk.

Mendoza V. (1966) reported multicolor photometric investigation of 26 TTS, on wavelengths ranging from the ultraviolet (U-band, 0.36 μm) to the near-infrared (M-band, 5 μm). His study confirmed the presence of a characteristic ultraviolet excess for the majority of his targets. To the surprise of the author, data also showed a significant *infrared* excess for all the stars in the sample, with values up to several magnitudes above the intrinsic, spectral type-dependent, colors. The hypothesis contemplated to explain this feature invoked a composite system with a small stellar core and a large surrounding envelope; emission from the first component would dominate the short-wavelength photometry, while long-wavelength photometry would take significant contribution from thermal re-radiation from the envelope (Mendoza V. 1968). This observational picture matched the global predictions of first hydrodynamical models of collapsing protostellar clouds and PMS evolution (e.g. Larson 1969): namely that, at a given moment in its early evolution, the "young stellar object" (YSO; Strom 1972) would consist of a central core surrounded by a circumstellar envelope of gas and dust, gradually accreted by the core. A few years later, Cohen (1973) explored the photometric properties of T Tauri stars in the mid-infrared (2–20 μm) and drew similar conclusions: thermal emission from circumstellar dust was designated as the possible source of the long-wavelength brightness detected for most of the objects in the study (about 30 from various star-forming regions). In the following years, the interpretation of dust, rather than gas, as being responsible for the near- and mid-infrared excess emission observed for T Tauri stars met with growing evidence (e.g. Rydgren & Vrba 1981), and was ultimately supported by similar investigation of YSO spectra in the far-infrared (up to 100 μm; Rucinski 1985). Gaseous emission models could not reproduce the behavior (i.e., the λ-dependence) of the infrared emitted spectrum (*spectral energy distribution*, or *SED*) of these objects, as reconstructed from observations; hence, solid grains were retained as the most likely responsible for TTS infrared emission from $\sim$2 μm to 2 mm (Hartmann 1998). This conclusion also provided compelling evidence for a non-isotropic distribution of dust particles around the star. If the amount of dust required to produce the observed infrared excess were distributed in a spherical shell around the central protostar, this would determine a huge visual extinction A_V (Beckwith et al. 1990), a factor of $10^2 - 10^3$ higher than the values actually observed, which would practically conceal the central source in the optical. The clear inconsistency between

these theoretical inferences and the observations indicated that dust must instead be distributed highly non-uniformly, in a flattened region around the star, so that there is no significant concentration of dusty material along the line of sight to the object in most geometrical configurations. This circumstellar material is contained within a few hundred AU of the central star (Terebey et al. 1993), as indicated by interferometric maps of millimetric continuum emission (e.g. Keene & Masson 1990, see also Fig. 1.1b); these features are all consistent with a picture of disk-like distribution of material around the star.

1.1.3 T Tauri phase in the paradigm of low-mass early stellar evolution

The exploration of the *X-ray* domain started in the late '70s with the launch of the Einstein Observatory. Ku & Chanan (1979) were the first to suggest that T Tauri stars might be responsible for the X-ray emission detected in the Orion Nebula. These first indications on TTS being X-ray emitters were developed and confirmed in the studies of Walter & Kuhi (1981, 1984). Authors reported investigation of 23 known pre-main sequence objects in different fields, and detection of X-ray emission in about one third of cases. They also noticed that most detections occurred for stars with relatively low Hα equivalent width (EW) in their sample. X-ray emission was interpreted to arise in a small region close to the photosphere (corona).

The characterization of activity in the X-rays marked a most important step in the study of T Tauri stars. These works revealed the ubiquitous presence of a large population of PMS stars, clearly identified as such based on their spatial association with dark clouds, the strong Lithium absorption and the location above the MS track on the HR diagram, which displayed a strong X-ray emission but did not fit in the picture of a *"classical" T Tauri stars (CTTS)*, i.e., they did not show IR excess nor strong line emission (Walter 1986). These observations, indicative of the absence of circumstellar material around these objects, led to the definition of a new, complementary class of PMS objects, that Walter defined "naked" T Tauri stars. A spectroscopic definition for these stars (Hα EW < 10 Å) was proposed in the catalog of Herbig & Bell (1988), who introduced the notation of *"weak-line T Tauri stars" (WTTS)*. WTTS and CTTS were suggested to represent "two components of a single population of low-mass PMS stars", with no sharp transition but a "continuum of spectral properties" connecting the most extreme cases in the two groups (Walter et al. 1988).

The discovery of WTTS was instrumental in achieving a deeper understanding of the T Tauri nature. WTTS were interpreted as CTTS' subsequent evolutionary step toward the Main Sequence[3]. The T Tauri phenomenon soon appeared as "one aspect of stellar formation that can no longer be treated independently of other aspects" (Bertout 1989); the "T Tauri" phase in star formation was defined as stage where the infalling envelope is cleared and the previously embedded protostar+disk system becomes optically visible (Shu & Adams 1987). This is the last step of the star formation process, which gives birth to a young solar-type star.

1.2 Disks around young stars

1.2.1 Star formation in a nutshell

The idea of a rotating flattened distribution of material around young stars has a long history. At the end of the XVIII century, the German philosopher Immanuel Kant (1755) and the French

[3]This subject is still a matter of controversy. Although CTTS eventually stop accreting from their disks, and then turn into WTTS, a significant overlap in ages between the WTTS and CTTS populations is usually detected (e.g., Kenyon & Hartmann 1995), which implies that the age parameter is not sufficient indication to the evolutionary state of a young star.

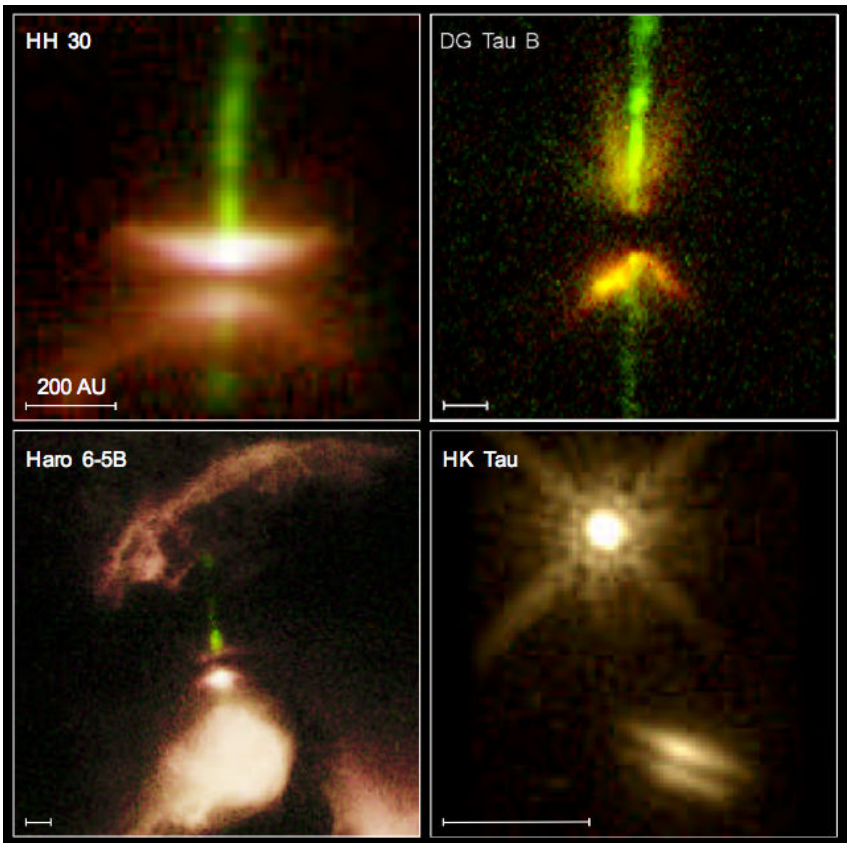

(a) Images of disks in young stellar objects, obtained with the Wide Field and Planetary Camera 2 (WFPC2) onboard the *Hubble Space Telescope* (HST): the circumstellar disks and prominent gaseous jets associated with the Herbig-Haro object HH 30 (upper left panel) and the T Tauri star DG Tau B (upper right panel), where the central source is hidden from direct view and revealed by its light reflected off the surface of the disk; the edge-on disk, collimated jets and a cloud complex of dust and gas surrounding the object Haro 6-5B (lower left panel); the binary star HK Tau (lower right panel), where one of the components is surrounded by a disk seen edge-on. (Credit: Chris Burrows (STScI), John Krist (STScI), Karl Stapelfeldt (JPL) and colleagues, the WFPC2 Science Team and NASA)

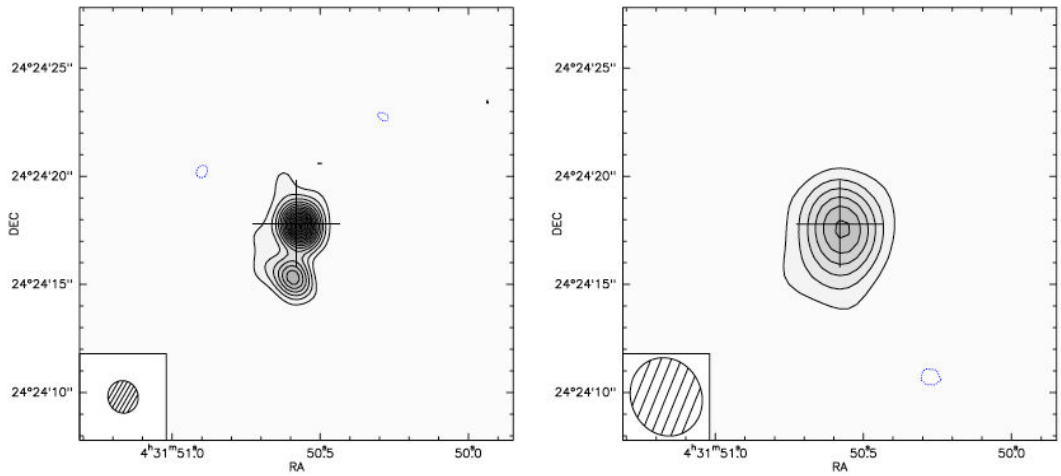

(b) Emission contour maps of HK Tau at 1.4 mm (left) and 2.7 mm (right). From Duchêne et al. (2003).

Figure 1.1: Observational evidence of the presence of disks around young stars, (a) from direct imaging with the *Hubble Space Telescope*, and (b) from millimetric observations of gas and dust emission in the circumstellar environment.

scholar Pierre-Simon Laplace (1798) independently observed that the orbits of the celestial bodies which compose the Solar System were nearly coplanar[4,5]. They concluded that this peculiarity had origin in the process itself that gave birth to the Solar System, and supposed that, at the beginning, the matter which would eventually produce the Sun, the planets and the minor bodies was distributed in a low-density rotating nebula, which extended beyond the actual size of the solar system, that would progressively collapse under the effect of gravity and flatten along its spin axis due to the centrifugal force, determining a disk-like distribution of material around the center of gravitational collapse (the Sun-to-be), on the equatorial plane of this latter (the *nebular hypothesis* for the origin of the Solar System; Wolf 1884b,a). This rotating disk, in the Kant-Laplace model, was considered to be the birth site of planets orbiting around the central star.

This idea contains in embryo the main traits of the currently accepted picture of star formation. While nearly two centuries elapsed before final evidence for disks around pre-Main Sequence (PMS) stars was gained from direct imaging (Fig. 1.1a), circumstellar disks are now considered a ubiquitous product of the earliest stages of star formation, with a major impact on early stellar evolution.

Stars are born in dense cores inside molecular clouds (Stahler & Palla 2005; Lada 2005). Dense cores are the densest regions of the interstellar medium, and are found at the smallest scales in the hierarchical structure of dark cloud complexes in the Galaxy. They have diameters of the order of ~ 0.1 pc, masses of the order of 10 $M_\odot$, $A_V > 10$, temperatures of around 10 K and densities of $\sim 10^4$ particles/cm^3. Zeeman effect measurements in dark cloud regions indicate magnetic fields of the order $\sim$30 μG (Goodman et al. 1989).

At the beginning, dense cores are held in equilibrium by the force balance between thermal and magnetic pressure of the gas, on one side (outward push that would tend to disperse the concentration of particles), and self-gravity, on the other side (inward push that would drive the core to collapse on itself). This balance can be disrupted by the action of external radiation onto the molecular cloud, or by other triggering events (e.g., the interaction of the cloud with supernova shock waves or spiral density waves), which determine an enhancement in the external pressure. If the cloud is sufficiently massive[6], it may become unstable under the effect of these processes, and gravitational collapse may be ignited.

If conditions for collapse are met, the cloud begins to contract; gravitational potential energy is released and transformed into thermal energy of the gas and then into radiation. The infall starts at large radii, where pressure support is less important. Because of the low initial density, at this stage the cloud is optically thin; hence the internal energy gained from the process can be effectively radiated away and the collapse is isothermal. Local increase in density implies

[4] « If [...] we consider that six planets with ten satellites describe orbits around the Sun as their centre and all of them move towards one side, namely that side to which the Sun itself turns, which rules over all their orbits through the force of its attraction, that the orbits do not deviate far from a common plane, namely that of the extended solar equator, [...] then we are moved to believe that one cause, whatever it may be, has had a pervasive influence in the entire space of the system, and that the unity in the direction and position of the planetary orbits is a consequence of the agreement they all must have had with the material cause by which they were set in motion. » (I. Kant, *Universal Natural History and Theory of the Heavens*, Part II, Chapter I)

[5] « [...] Des phénomènes aussi extraordinaires ne sont point dus à des causes irrégulières. En soumettant au calcul leur probabilité, on trouve qu'il y a plus de deux cent mille milliards à parier contre un qu'ils ne sont point l'effet du hasard, ce qui forme une probabilité bien supérieure à celle de la plupart des événements historiques dont nous ne doutons point. Nous devons donc croire, au moins avec la même confiance, qu'une cause primitive a dirigé les mouvements planétaires. » (P.-S. Laplace, *Exposition du système du monde*, Livre V, Chapitre VI)

[6] An indicator of the minimum scales which can collapse gravitationally is provided by *Jeans mass*, defined as $M_J = \left(\frac{\pi c_s^2}{G}\right)^{3/2} \rho_o^{-1/2}$, where c_s and ρ_o are sound speed and density in an isothermal, initially uniform gas (Hartmann 2009).

that individual fragments of the parental cloud may become gravitationally unstable on their own (see expression for the Jeans mass M_J[6]) and continue their dynamical collapse as separate condensation nuclei. This dynamical cloud fragmentation is enhanced by the centrifugal force exerted on individual cloud fragments as a result of the increase in angular velocity due to angular momentum conservation during cloud contraction; such fragments may be ejected from the cloud and continue the collapsing process on their own. A single cloud may give birth to hundreds of stars, as suggested by the fact that young stars are typically found in star clusters or associations, rather than isolated; this scenario is illustrated in numerical simulations (e.g., Bate et al. 2003). Even at the scales of dense cores, at least two stars are usually formed out of the material which compose a single core (Stahler & Palla 2005).

Inside each fragment, the collapse is non-homologous: the inner region collapses on shorter timescales than the outer region. As a result, the density increases rapidly in the core center, which then becomes opaque to its own radiation and starts heating up under the effect of further external compression. This determines an increase in pressure in the innermost regions, which counteracts and delecerates the inward drift of material from the surrounding envelope of material. As the outer gas layer of the inner core radiates freely in the infrared, internal pressure is released and core contraction is re-enhanced. The inner region of the initial cloud fragment has given birth to a protostar surrounded by an infalling envelope. The process of gravitational collapse of dense cores and subsequent formation of protostars takes place on timescales of roughly 10^5 years, or free-fall time (Garcia et al. 2011).

Since the collapse phase occurs on a dynamical timescale, the angular momentum the cloud core possesses at the beginning of the rapid collapse cannot be transferred efficiently to the external medium; due to the large size of the initial cloud core, even small initial rotational velocities will be significantly amplified during the gravitational collapse due to angular momentum conservation, thus preventing infalling material from accreting directly, i.e. radially, onto the protostellar core. This determines the formation of a rotationally supported circumstellar disk (Hartmann 2009).

Overall properties can be derived by assuming a fixed central mass equal to M. If material with specific angular momentum h falls on a circular orbit around the central mass while maintaining its angular momentum, then the radius R of the circular orbit is given by

$$R = \frac{h^2}{GM} \tag{1.1}$$

If we assume spherical symmetry for the gravitational collapse process, all the material which arrives at the centre at a given instant of time comes from the same initial radius r_0 within the cloud; if the protostellar cloud core is initially in uniform rotation with angular velocity Ω, the specific angular momentum at r_0 varies with the angle θ from the rotation axis as

$$h = \Omega r_0^2 \sin\theta.$$

Thus, infalling material from different directions will have different angular momenta and arrive at the equatorial plane at differing radii. Material near the rotation axis will fall in close to the central star, while material coming from regions at $\theta \sim \pi/2$ will fall in to a maximum centrifugal radius given by

$$r_c = r_0^4 \frac{\Omega^2}{GM} \tag{1.2}$$

In the assumptions of a spherically symmetric initial cloud and of axisymmetric rotation, the process has complete symmetry above and below the equatorial plane $\theta = \pi/2$. Thus, the momentum fluxes of the infalling material on either side of the disk plane perpendicular to the disk have the same magnitude and opposite directions, resulting in a shock layer at the equator,

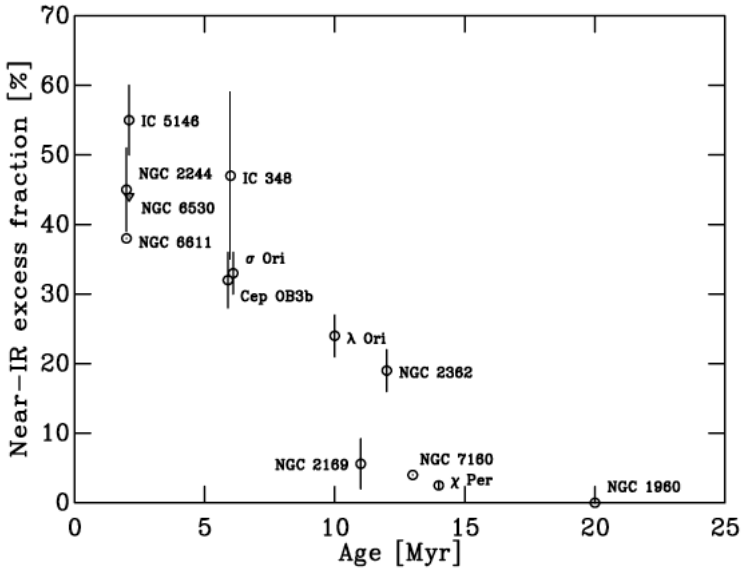

Figure 1.2: Fraction of stars with near-IR excess disk emission as a function of the average age cluster. Almost all objects are surrounded by a circumstellar disk at an age of ∼1 Myr; this fraction drops to about 50% after a few Myr and by an age of 5-10%, most of the young stellar objects have cleared their disks. From Bell et al. (2013).

which dissipates the kinetic energy of motion perpendicular to the equatorial plane. This leads to an accumulation of matter in a thin structure in the equatorial plane, i.e. to the formation of a rotating disk, whose diameter can vary between a few hundred and a few thousand AU (Hartmann 2009).

At the end of the collapse phase in the star formation process, a system composed of a central protostar surrounded by a disk is thus born. The system then enters the phase of *disk accretion*. This has a longer duration than the previous phase, typically extending over a few Myr, as deduced from the analysis of the disk frequency rate as a function of age in young clusters and star-forming regions (Fig. 1.2). At the beginning of the accretion phase, the mass of the protostar is about 5×10^{-2} $M_\odot$ (Stahler & Palla 2005) and the central temperature of the core is not sufficient to ignite nuclear reactions. Most of the mass of the star is built during the earliest stages of the accretion phase, prior to the T Tauri evolutionary phase, when the protostar is still embedded in its envelope (Calvet & D'Alessio 2011).

In the following sections, I will focus on the structure of circumstellar disks around young stars and on the physics which governs disk accretion. To complete the overview on the star formation process and its interconnection with the formation of planetary systems, I shall summarize here in a few lines the ultimate fate of disks around protostars.

Dust disks within ∼20 AU distance to the central star tend to "clear" (i.e., to become undetectable in infrared excess studies) on timescales of a few Myr (Hartmann 2009). Dusty component tends to settle into the disk midplane due to the drag forces resulting from interaction with the gas (Lada 2005). In this process the micron-sized dust grains collide and can merge together forming increasingly massive solid particles. Iteration of this process and merging with condensates produced in cooling processes in the disks lead to the formation of kilometer-sized planetesimals, which may produce terrestrial planets by accretion with other planetesimals or accrete gaseous atmospheres and thus constitute the cores of giant planets (Lada 2005). Gas removal is thought to be caused by photoevaporation by the extreme ultraviolet radiation of the

central star (Hartmann 2009).

As the protostellar core begins the accretion phase, its luminosity is dominated by accretion. Once a protostar reaches a mass of about 0.2 - 0.3 $M_\odot$, the central temperature reaches 10^6 K and nuclear reactions of deuterium burning are ignited, thus providing the protostar with another source of luminosity. Accretion can continue until the central temperature of the protostar reaches 10^7 K and hydrogen fusion is ignited (Lada 2005). The ignition of hydrogen burning marks the beginning of the Main Sequence phase of stellar lifetime. The stage of accretion and final condensation by which a protostar finally evolves in a Main Sequence star lasts on average several tens of Myr, but this length of time can strongly vary depending on the stellar mass (from tens of thousands of years for a $\sim$15 $M_\odot$ star to hundreds of Myr for a $\sim$0.1 $M_\odot$ star).

1.2.2 Structure and physics of circumstellar disks

Magnetic fields

Recent measurements of the Zeeman broadening of photospheric absorption lines (e.g., Johns-Krull 2007) have shown that mean magnetic fields of a few kG are typically found at the surface of CTTS. The origin of such strong large-scale magnetic fields is likely attributable to dynamo processes (Donati & Landstreet 2009). Spectropolarimetric studies of magnetic field topology at the surface of CTTS have illustrated that, while some TTS host simple large-scale, dipolar field structure, other exhibit complex, multipolar magnetic fields (Gregory et al. 2012). Large-scale stellar field lines permeate the stellar surface; these may have a complex geometry (Donati & Landstreet 2009), although the dipolar component, which falls off more slowly with distance than higher-order components, appears to be dominating in the star-disk coupling (Gregory et al. 2012; see Sect. 1.3.1). The magnetic field may have a strength of $\sim$1 G in the inner regions of the disk; values of a few mG are instead measured at typical distances of $\sim 10^3$ AU from the central object (Donati & Landstreet 2009).

Magnetic fields in CTTS have a most important role in the dynamics of disk accretion, as illustrated in the following sections.

Angular momentum transport inside the disk

In order for disk accretion to occur, a net inward flow of material must take place in the disk. This is possible if angular momentum is extracted from the inner region of the disk and transferred to a small fraction of disk particles at large radial distances.

In a first approximation, we can describe the disk as a series of concentric rings in Keplerian rotation around the central object of mass M, with angular velocity depending on the distance R to the protostar as $\Omega_K(R) = \left(GM/R^3\right)^{1/2}$. The expression for Ω_K indicates that an inner ring rotates faster than its neighboring outer ring. Hence, friction between two neighboring rings in the disk will tend to spin up the external ring and spin down the internal ring, i.e., to transfer angular momentum outward. Since the gravitational potential constrains the orbital motion in the Keplerian description, the decelerated material from the inner ring will be carried inwards, while material from the outer ring will move to larger radii. Since energy is lost in the process due to frictional dissipation, the net gravitational potential energy of the system must decrease, which is achieved with a net inward motion of disk mass (as illustrated in Lynden-Bell & Pringle 1974).

A classic mechanism considered for the coupling and mixing of adjacent rings in a gaseous disk is *turbulent viscosity* (e.g., Frank et al. 2002). In this picture, single particles in the disk are subject to chaotic motion with typical scale λ (corresponding to the mean free path) and random velocity $\tilde{v}$, and can diffuse from one ring to another, thus yielding angular momentum exchange

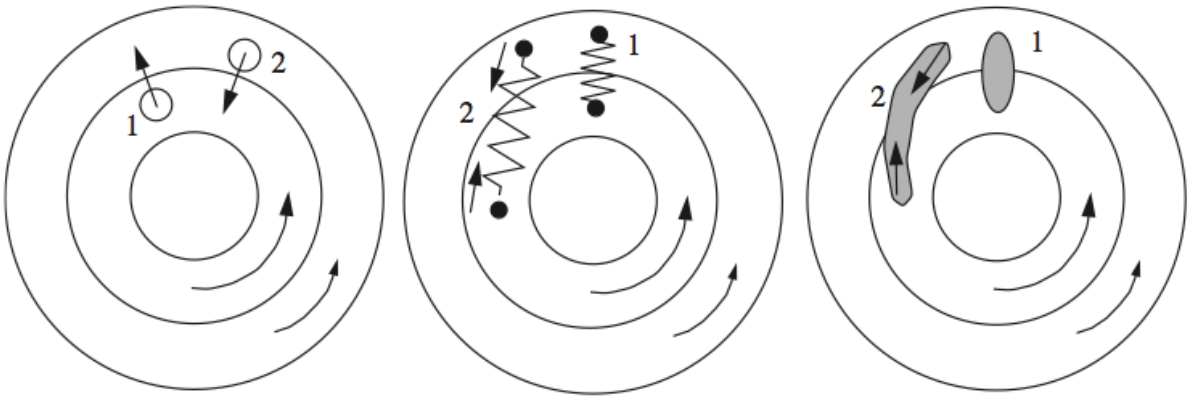

Figure 1.3: Schematic view of different possible mechanisms for angular momentum transfer in a shearing disk. The left panel illustrates particle diffusion between the inner and the outer disk ring, combined with viscous friction and differential rotation of the two rings. The middle panel illustrates the situation where the two differentially rotating disk rings are connected by magnetic field lines. The right panel illustrates the dynamical evolution of gravitational instability, with a radial excess of material being sheared out by the differential rotation between the two rings. In all pictures, 1 indicates the starting configuration, and 2 its dynamical evolution. From Hartmann (2009).

(left panel of Fig. 1.3). The product of λ by $\tilde{\mathrm{v}}$ defines the kinematic viscosity ν associated with the shearing motion between two rings of the disk: $\nu = \lambda\,\tilde{\mathrm{v}}$. In the assumption of a geometrically thin accretion disk, composed of particles which essentially move on circular orbit in a single plane, the time evolution of the ring is governed by the equations of mass conservation and of angular momentum conservation in a viscous fluid, and by the differential torque exterted at its inner and outer boundaries due to the differential rotation in the disk. In the case of a constant viscosity ν, Lynden-Bell & Pringle (1974) showed that, starting with an initial density distribution representing a ring at radius R_1, the surface density of the disk as a function of radial distance and time is described by

$$\Sigma(x, t_d) = \frac{x^{-1/4} t_d^{-1}}{2\pi R_1^2} \exp\left[\frac{-(1+x^2)}{2t_d}\right] I_{1/4}\left(\frac{x}{t_d}\right) , \tag{1.3}$$

where $x = R/R_1$, $t_d = 6\nu t/R_1^2$ and $\mathrm{I}_{1/4}$ is the modified Bessell function of fractional order. This solution is illustrated in Fig. 1.4; the net effect of the viscosity is to spread the ring of material, ultimately concentrating mass at smaller radii, while small amounts of matter are pushed to large distances to conserve angular momentum (Hartmann 2009). The quantity R_1^2/ν which appears in the definition of the time coordinate corresponds to the average time for a particle in the ring to diffuse a distance R_1 in a random walk.

In a steady disk, where the inward mass flux is constant in time, the expression for the surface density distribution given by the conservation of the angular momentum flux is (Hartmann 2009)

$$\Sigma = \frac{\dot{M}}{3\pi\nu}\left[1 - \left(\frac{R_\star}{R}\right)^{1/2}\right] , \tag{1.4}$$

where $R_\star$ is the stellar radius and it is assumed that the shear goes to zero close to the stellar surface.

The viscosity ν is often described using the parametric α prescription introduced by Shakura & Sunyaev (1973), originally in the context of disks around black holes. In this prescription, $\nu = \alpha c_s H$, where c_s is the sound speed in the medium, H is the scale height and α is a parameter

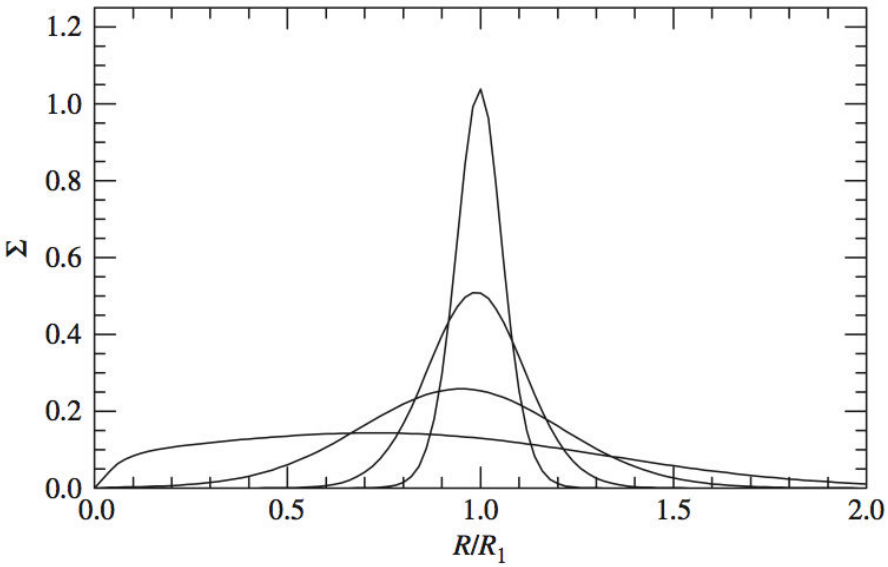

Figure 1.4: Diffusion of a ring of material, initially at radial distance R_1 from the center, in a viscous disk with constant viscosity ν. Each curve shows the surface distribution of material at a different time: at instant $t = 0$, all the mass is concentrated at R=R_1; as time progresses, the density at R_1 decreases and more and more mass is distributed to smaller radii. A tail of matter moves out to larger radii in order to conserve angular momentum. From Hartmann (2009).

that describes the efficiency of the angular momentum transport mechanism. In the assumption that, for turbulence in the disk, the scale λ of the eddies is less than the disk scale height H and the turbulent velocity $\tilde{v}$ is less than the sound speed c_s, $\alpha \leq 1$ (Pringle 1981). In this description, Eq. 1.4 becomes

$$\Sigma = \frac{\dot{M}}{3\pi\alpha c_s H}\left[1 - \left(\frac{R_\star}{R}\right)^{1/2}\right]. \tag{1.5}$$

It can be noted from Eq. 1.5 that $\dot{M} \propto \nu\Sigma \propto \alpha c_s H\Sigma$; hence, higher viscosity in the disk leads to larger mass accretion rate for a given surface density.

Numerical simulations of pure hydrodynamic mixing by turbulent convection between adjacent rings in the disk have shown that the mechanism is not effective in transporting angular momentum outwards; in fact, the resulting transport is small and on average directed inward (e.g., Stone & Balbus 1996). This can be understood by looking at the schematic picture in Fig. 1.3: particles in the inner ring have lower angular momentum than particles in the outer ring, as a result of the Keplerian velocity distribution; hence, diffusion of particles from the inner to the outer ring has the effect of moving lower angular momentum outward. Similarly, particles which diffuse from the outer to the inner ring bring higher angular momentum inward. Additional mechanisms are then needed to enhance the viscosity of the disk and carry angular momentum outward.

Magnetorotational instability (MRI) is one possible mechanism to produce an α-type viscosity. This is schematically illustrated in the middle panel of Fig. 1.3. Assume two neighboring disk rings are initially connected by a magnetic field line in the radial direction. The differential rotation between the two rings will have the effect of stretching the field line; the restoring force of the "spring" will tend to spin up the outer ring and spin down the inner ring. This will determine an inward movement of the decelerated material in the inner ring, which fall in deeper to

the potential well and increases its angular velocity further; conversely, the accelerated material in the outer ring will be pushed outward and slow down. This enhances the stretching of the magnetic field line, resulting in longer and longer loops of magnetic fields. The development of this instability is contingent upon the presence of ionized gas in the disk, whose particles can effectively couple with the magnetic field. It is believed that the energetic (X-ray) irradiation from the central young object may act as an efficient mechanism for producing non-thermal ionization of disks. This ionizing source is likely effective only on the external layers of the circumstellar disk; the innermost regions, close to the midplane of the disk, are not penetrated by stellar flux. Assuming that angular momentum transport in disks is driven by magnetic fields, these internal regions will then be inactive in this respect (the "dead zones" described in Gammie 1996).

Another mechanism that may contribute to the picture of angular momentum transport in disks is *gravitational instability* (illustrated in the right panel of Fig. 1.3). This may take place when the disk is massive enough relative to the central object (e.g., in the earliest stages of disk evolution). In this condition, it might be self-gravitating. Assume a radially extended concentration of mass is present in the disk. Differential rotation between adjacent disk rings will cause it to be elongated in a trailing spiral arm. If the gravitational instability is strong enough to keep the mass concentration bound together in spite of the shearing, the inner part of the spiral arm will pull on the outer part of the spiral arm, tending to accelerate the outer region. This causes a net flow of angular momentum outward. When a small region in a self-gravitating disk is compressed, its self-gravity is increased, but the process also determines an increase in its spin velocity, which produces a centrifugal force to oppose gravity. The balance of these two effects leads to the instability criterion. Numerical simulations indicate that gravitational instabilities can generate turbulence which appears as unsteady, spiral wave density structures. This type of exchange mechanism is effective on larger scales in the disk compared to viscous friction, which has a local effect.

Temperature gradient and vertical structure

The viscous friction between two differentially rotating rings of disk determines a local rate of mechanical energy dissipation, which is assumed to be radiated away from the system. The energy loss per unit area is given by (Hartmann 2009)

$$\dot{E}(R) = \frac{1}{2}\,\nu\,\Sigma\left(\frac{R d\Omega}{dR}\right)^2. \tag{1.6}$$

In the case of a steady accretion disk (Eq. 1.4), this becomes

$$\dot{E}(R) = \frac{3GM\dot{M}}{8\pi R^3}\left[1-\left(\frac{R_\star}{R}\right)^{1/2}\right]. \tag{1.7}$$

In the assumption that the disk surface radiates as a black-body, the effected temperature of the disk can be computed as

$$T_d^4 = \frac{3GM\dot{M}}{8\pi R^3\sigma}\left[1-\left(\frac{R_\star}{R}\right)^{1/2}\right]. \tag{1.8}$$

This solution goes to zero at the inner edge of the disk as a result of the boundary conditions assumed on the angular momentum. At larger radii, the temperature is higher in the inner regions of the disk and decreases outwards.

This analysis does not include the thermal emission component arising from disk irradiation from the central star, which in T Tauri stars can be the dominant mechanism heating the disk.

Adding this contribution notably result in a larger amount of flux at longer wavelengths, with a corresponding flatter dependence of λF_λ on λ than that derived for a standard viscous accretion disk, as can be observed in Fig. 1.5. Typical disk temperatures range from order ∼1000 K in the inner regions (e.g., Muzerolle et al. 2003a) to order ∼10 K in the outer regions (e.g., Dutrey et al. 2007). Disks are not vertically isothermal, but the temperature decreases from the surface to the midplane, as a result of the heating from stellar irradiation which impacts primarily the upper layers of the disk.

Indications on the scale height of the disk can be derived by assuming that the disk is in hydrostatic equilibrium in the vertical (z) direction (that is, no flow is present perpendicular to the disk surface). The force balance in the z direction then implies that the vertical component of gravity exerted over a particle at the disk surface from the central mass M must be balanced by the vertical supporting pressure gradient:

$$\frac{dP}{dz} = -\frac{GM\rho}{(R^2+z^2)}\frac{z}{\sqrt{R^2+z^2}} \tag{1.9}$$

For a geometrically thin disk, $R >> z$ and Eq. 1.9 can be approximated as $dP/dz = -GM\rho z/R^3$; in addition, adopting an ideal gas law $P = \rho c_s^2$ and assuming that c_s is constant in z, Eq. 1.9 for the density structure becomes

$$\rho = \rho_0 \exp\left(-\frac{z^2}{2H^2}\right),\ H = \sqrt{\frac{R^3 c_s^2}{GM_\star}} = R\,\frac{c_s}{\Omega_K R} \equiv R\,\frac{c_s}{v_\phi}\,, \tag{1.10}$$

where v_ϕ is the Keplerian tangential velocity. Eq. 1.10 shows that i) the scale height H increases with R, i.e. the disk is not flat, and ii) the H/R ratio increases with R, which means that the disk is "flared" (Kenyon & Hartmann 1987), i.e., the disk isodensity contours tend to curve away from the disk midplane.

This last point is very important for the total disk emission, because a flared disk will effectively capture and re-radiate a larger fraction of the stellar flux than a flat disk (this fraction depends on the cosinus of the angle between the impinging beam of radiation and the local normal to the disk surface). This translates to larger excess fluxes at longer wavelengths relative to what is expected for a purely viscous disk or a flat irradiated disk (Fig. 1.5), which matches observations.

1.3 Disk accretion in T Tauri stars

Earlier models of the evolution of steady viscous disks around young stars (e.g. Lynden-Bell & Pringle 1974; Bertout et al. 1988) assumed that the disks reach down to the stellar photosphere. The interaction between the accretion disk and the central star would thus occur in a narrow equatorial boundary layer. From Eq. 1.7, integrated over the disk and assuming that the initial radial distance of the accreting material is much larger than the stellar radius $R_\star$, we obtain that half of the accretion luminosity $L_{acc} = GM_\star \dot{M}/R_\star$ is radiated from the disk surface, as a result of the viscous friction between disk rings that determines the inward flow of material down to the stellar surface. In this picture, when the material reaches the boundary layer, it spins at an angular velocity corresponding to the Keplerian $\Omega_K(R_\star)$. This is significantly faster than the spin velocity of the star itself. Hence, the accreting material has to lose its excess kinetic energy at the interface between the star and the disk. This energy dissipation produces the second half of the accretion luminosity. The excess emission associated with the accretion process then arises from a hot equatorial belt at the stellar photosphere whose extent is comparable to the disk scale height at the stellar equator.

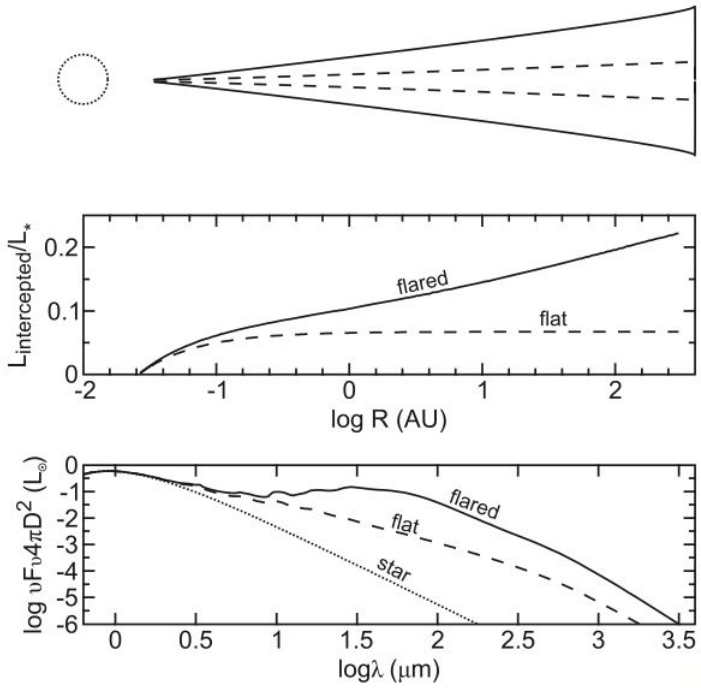

Figure 1.5: Comparison of the disk geometry (upper panel), fraction of stellar flux intercepted (middle panel) and emitted spectral energy distribution (lower panel) for a flared disk as opposed to a flat disk. From Garcia et al. (2011).

The boundary layer description is able to explain in general terms the hot continuum emission observed at short wavelengths for CTTS; however, the model is incapable of accounting for the observed emission line profiles, which are typically asymmetric, with large velocity shifts, and may display redshifted absorption in the line wings (e.g., Edwards et al. 1994), indicative of high-velocity material infall onto the star. Moreover, in this scenario, since the infalling material carries significantly more angular momentum than an element on the central star surface, angular momentum transfer associated with the equatorial accretion of material from the disk should determine a spinning up of the star to angular velocities close to the break-up velocity, if disk accretion lasts long enough (e.g., Hartmann & Stauffer 1989). In contrast, typical rotation periods measured for CTTS (e.g., Hartmann & Stauffer 1989; Bouvier et al. 1993) are up to an order of magnitude smaller than the break-up velocity. Further observational evidence in contrast with the boundary layer paradigm for disk accretion in T Tauri stars arose from the measurement of typical ranges of near-infrared excesses associated with CTTS (Meyer et al. 1997), which were too small compared to the values expected from disk models extending down to the stellar surface, but could be interpreted assuming a moderate inner disk hole (inner disk edge located at about 1–6 $R_\star$ from the stellar surface).

1.3.1 Magnetospheric accretion

The currently accepted model for mass transfer from the disk to the star is *magnetospheric accretion* (e.g., review by Bouvier et al. 2007b).

The scenario of a magnetically controlled matter flow from a circumstellar disk onto the central object was originally developed by Ghosh & Lamb (1979) to describe disk accretion in neutron star systems. This formalism was first applied to the case of young stars by Camenzind (1990) and Königl (1991), assuming an axisymmetric dipolar stellar magnetic field on the large

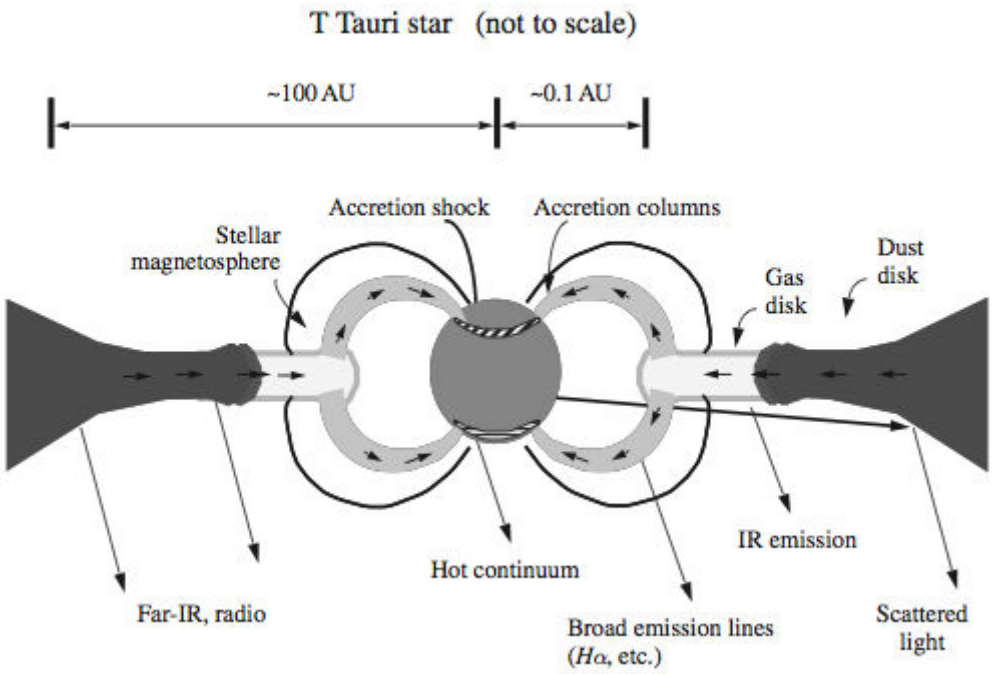

Figure 1.6: Schematic picture of accretion in T Tauri stars in a steady, axisymmetric regime. The magnetic field disrupts the circumstellar disk at a distance of a few stellar radii from the star surface. Material infall from the inner disk to the central star is then channeled by the magnetic field lines and the impact of the accreting column at the stellar surface occurs at near free-fall velocities on the regions close to the magnetic poles. Accelerated material along the accretion funnel produces the broad emission lines typical of CTTS spectra, while the localized shock at the stellar surface is responsible for the hot excess continuum. From Hartmann (2009).

scale.

A schematic picture of the model is shown in Fig. 1.6. The theoretical premise for the magnetospheric accretion model lies on the following consideration. In the presence of a sufficiently strong stellar magnetic field, at a certain distance from the central source the ram pressure of the accreting material P_{ram} will be balanced by the magnetic pressure P_B:

$$P_{ram} \equiv \frac{1}{2}\,\rho v^2 = \frac{B^2}{4\pi} \equiv P_B\,, \tag{1.11}$$

In the case of spherical accretion, Eq. 1.11 becomes

$$B^2 = \dot{M}\frac{v_{in}}{r^2}\,, \tag{1.12}$$

where v_{in} is the infall velocity.

When this pressure balance occurs, the accreting material, if sufficiently ionized, cannot fall in freely; its motion will start to be governed by the magnetic field. By introducing assumptions on the structure of the magnetic field and on the infall velocity, it is possible to compute the radial distance from the star where the accretion flux is disrupted by the magnetic field (i.e., the *truncation radius* r_T). In the case of a dipolar field, the strength of the field at a distance r from the central source is $B = B_\star(R_\star/r)^3$; if we assume further that the infall velocity at radius r is the free-fall velocity from infinity, we obtain (Bouvier et al. 2007b; Hartmann 2009)

$$\frac{r_T}{R_\star} = \frac{B_\star^{4/7} R_\star^{5/7}}{\dot{M}^{2/7}(2GM_\star)^{1/7}} = 7.1 \left(\frac{B}{1\,kG}\right)^{4/7} \left(\frac{\dot{M}}{10^8\,M_\odot/yr}\right)^{-2/7} \left(\frac{M_\star}{0.5\,M_\odot}\right)^{-1/7} \left(\frac{R_\star}{2\,R_\odot}\right)^{5/7}, \tag{1.13}$$

where B is the surface magnetic field, $\dot{M}$ is the mass accretion rate, and $M_\odot$ and $R_\odot$ are the stellar mass and radius, respectively.

In the case of disk accretion, the expression in Eq. 1.13 provides an upper estimate for r_T; in fact, disk densities are typically large, due to the fact that the azimuthal velocity in the disks are comparable to the free-fall velocities whereas the radial drift is very small; this translates to disk ram pressures which are larger than free-fall ram pressures, and hence the radius where the magnetic pressure offsets the ram pressure is pushed closer to the star. This leads to modifications in the numerical factor of Eq. 1.13, while the parametric dependence remains unchanged. Typical values of r_T are of order $\sim 5\ R_\star$.

The truncation radius corresponds to the radial distance between the central star and the inner edge of the disk, where this is disrupted by the magnetic field. A magnetospheric cavity then extends between the star surface and the inner disk, as the interface through which the interaction between the young star and its disk takes place. Since the magnetosphere is anchored to the star, it rotates at the same angular velocity as the latter. Another important radial distance in the context of the star-disk interaction is the co-rotation radius r_C, defined as the radius at which the angular velocity of the star and the Keplerian velocity of the disk are the same. In the picture of magnetospheric accretion, it is assumed that the truncation radius r_T lies between the stellar radius $R_\star$ and the co-rotation radius r_C: if r_T were larger than r_C, the star would rotate faster than the disk ring at the inner edge; hence, the coupling between the disk and the star would transfer angular momentum from the star to the disk, which would experience a centrifugal force that would tend to push the gas outward. Conversely, if $r_T < r_C$, the field lines connecting the star and the disk will transfer angular momentum from the disk to the star, thus allowing accretion to occur.

At radius r_T, disk matter is then lifted from the diskplane and flows along the magnetic field lines, forming accretion columns. The funnel flow is subsonic close to the disk, but it is accelerated along the field line and reaches the star surface at near free-fall velocities (e.g., Romanova et al. 2002). The impact produces an accretion shock close to the magnetic poles; in the case of the stable, axisymmetric dipolar picture in Fig. 1.6, the impact between the accretion columns and the accretion columns occurs in two narrow rings, symmetric with respect to the disk plane, located at high latitudes on the stellar surface.

In the assumption that the hot continuum emission of CTTS is produced by the accreting gas as it shocks at the stellar surface, the corresponding luminosity, i.e., the accretion luminosity, can be expressed as

$$L_{hot} \equiv L_{acc} = \frac{GM\dot{M}}{R_\star}\left(1 - \frac{R_\star}{r_T}\right). \tag{1.14}$$

Observational supporting evidence for magnetospheric accretion

The magnetospheric accretion paradigm is strongly supported by its predictive capability of many observational features associated with CTTS.

The accretion shock at the stellar surface produces the prominent hot continuum emission observed at short wavelengths; this additional flux component has the effect of reducing the apparent depth of stellar absorption lines ("veiling"). Thermal emission from the disk is responsible for the infrared part of the SED of these systems.

Emission lines are produced in the accretion columns. The center of the lines originates in the region where disk matter is lifted from the disk; this region is characterized by low velocities but large emitting volumes. Accelerated material along the accretion funnel, above the diskplane, is instead responsible for the large velocity shifts observed in the line wings. Redshifted absorption components ("inverse P Cygni profiles"; e.g., Walker 1972) occur when high-velocity material, infalling from a distance of a few stellar radii in the accretion funnel, intercepts and absorbs the background emission from the accretion shock.

Characteristic features associated with CTTS are powerful, highly collimated jets (e.g., Ferreira 1997). These often display discrete knots of emission, and can extend for distances of $10^3 - 10^4$ AU from the central source. An associated feature detected around young stars occurs as molecular outflows. These consist of shells of ambient gas swept up by the jet bow shock, plus a surrounding slower, wider-angle component. Most of the kinetic energy is quickly dissipated as the high-velocity material shocks with the ambient molecular medium. These episodes of mass ejection appear to be deeply connected with the disk accretion process, and find their collocation in the picture of magnetospheric accretion. Jets are likely produced as a result of magnetocentrifugal acceleration from the circumstellar disk. Material is initially launched from the rotating disk along open, hourglass-shaped magnetic field lines (e.g., Banerjee & Pudritz 2006). At sufficiently large cylindrical radii, the magnetic field is too weak to enforce co-rotation with the star. Thus, the gas coupled with the magnetic field line tends to expand away from the rotation axis of the system, and its angular velocity consequently decreases by angular momentum conservation. This process determines the magnetic field line to wind up in an opening spiral in the azimuthal direction, around the rotation axis (Hartmann 2009). Hence, a toroidal field is developed, which collimates the flow along the rotation axis, perpendicularly to the diskplane. Jets are produced in a small opening angle ($\lesssim 30°$) close to the central source; material channeled along open field lines threading the disk at larger radial distances and wider angles produces slower disk winds (Frank et al. 2014). Signatures of material outflow are detected in the emission lines in CTTS spectra as blueshifted absorption components; jets may also be associated with emission in forbidden lines.

A more realistic picture of magnetospheric accretion

The depiction of the magnetospheric accretion process in Fig. 1.6, although conveying the basic physical principles, is an oversimplification of the actual dynamics of disk accretion in CTTS. The assumption of axisymmetry, for instance, is not met in the reality: magnetic map reconstruction for several CTTS from Zeeman-Doppler imaging (see Gregory et al. 2012) has shown that misalignments of a few $\times 10°$ between the stellar magnetic axis and rotation axis are common.

Fig. 1.7 illustrates the magnetospheric accretion pattern expected, from 3D simulations (Romanova et al. 2004), in the case of a dipolar magnetic field slightly inclined with respect to the rotation axis of the system. In this configuration, the disk is still disrupted at the truncation radius r_T, but the morphology of the magnetospheric accretion flow is more complex. For small misalignment angles Θ between the rotation axis and the magnetic axis ($\Theta \lesssim 30°$), matter typically accretes in two streams. These are located at opposite latitudes, as the accretion columns tend to form at the regions where the magnetic poles are closest to the disk plane. These two "curtains" of accretion determine the formation of a bow-shaped accretion shock close to the magnetic poles. In the inclined dipole configuration, the inner disk regions tend to be warped at the base of the two accretion columns (e.g., Bouvier et al. 1999), as a result of the dynamical disk-magnetosphere interaction, which determines a thickening of the inner regions of the disk with accumulation of material close to the magnetosphere; this geometrically translates to the formation of two trailing spiral arms in the case of accretion occurring in two separate streams for an inclined dipole (Bouvier et al. 2007b).

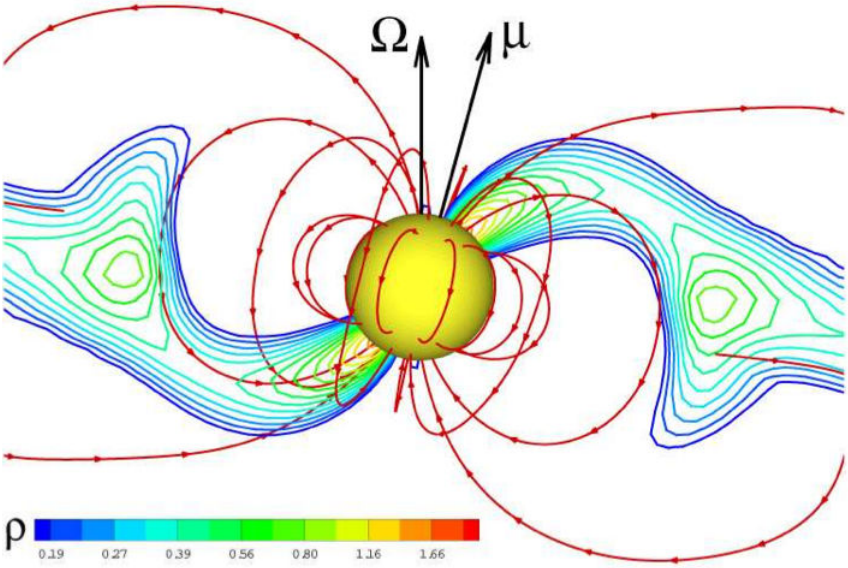

Figure 1.7: A slice of the funnel stream obtained in 3D simulations for an inclined dipole ($\Theta = 15°$). The contour lines show density levels, from the minimum (blue) to the maximum (red). From Romanova et al. (2004).

In case of large misalignments between the magnetic field axis and the rotation axis of the star, the picture of accretion is more complicated. The system tends to develop several accretion streams, which impact the stellar photosphere in a bar-like region which crosses the surface of the star near the magnetic poles.

If the interaction between the disk and the stellar magnetosphere occurs in a region close to the co-rotation radius r_C, but not only at r_C, the two components will be rotating differentially with respect to each other. This determines a progressive distortion (inflation) of the magnetic field lines in the course of a few rotational cycles, which impacts the magnetically-channeled accretion flow. At the state of maximum field line inflation, accretion may even be halted. Eventually, magnetic field lines reconnect and the initial field configuration is restored; accretion activity is also resumed.

Stable or unstable accretion regime?

The scenario of magnetospheric accretion explored previously assumes that the process, governed by a large-scale dipolar field (be it aligned or tilted with respect to the rotation axis of the system), is intrinsically stable. However, this condition may not be verified in several cases. Indeed, numerical simulations based on magnetohydrodynamical models have predicted that disk accretion in CTTS may occur through instability-dominated regimes as well.

A comparative illustration of magnetospheric accretion in a stable vs. unstable regime is shown in Fig. 1.8. This displays the results of simulations presented in Kurosawa & Romanova (2013).

The left panel of the Figure provides another illustration of the stable accretion regime with inclined dipole discussed in the previous section. Funnel-flow accretion occurs in an ordered fashion, with two separate accretion streams directed along the magnetic equator following the shortest magnetospheric paths from the disk to the stellar surface. Material in the streams is deposited onto the stellar surface at high latitudes, close to the magnetic poles.

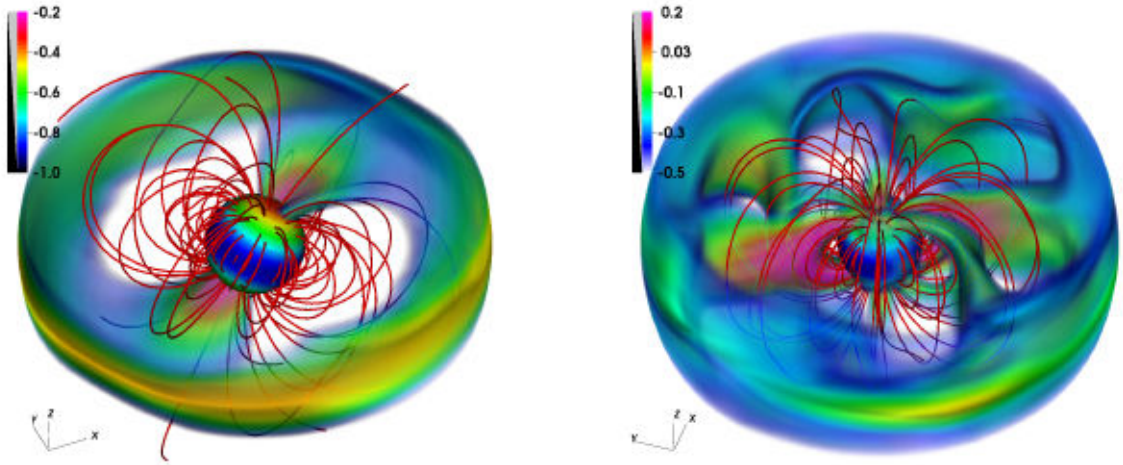

Figure 1.8: Examples of the magnetospheric accretions in a stable (left panel) and an unstable (right panel) regimes. The background colours show the volume rendering of the density (in logarithmic scales and in arbitrary units). The sample magnetic field lines are shown as red lines. From Kurosawa & Romanova (2013).

The right panel of the Figure illustrates the possible geometry of the matter flow formed in an instability-driven accretion regime. One type of instability that may develop in CTTS disks is the Rayleigh-Taylor instability at the interface between the accretion disk and the magnetosphere (Kulkarni & Romanova 2008), due to the lower-density magnetospheric plasma pushing against the higher-density disk matter. This engenders the formation of disk matter structures in the form of tongues of gas, which penetrate the magnetosphere in between the field lines. These tongues of gas maintain their equatorial drifts until they are intercepted by the more intense magnetic field close to the stellar surface; magnetospheric control of the accretion stream is then reinstated and smaller-scale accretion columns are formed, which hit the stellar surface at random locations. This process translates to a stochastic and rapidly varying distribution of accretion shocks onto the star.

The stable and unstable accretion regimes are not mutually exclusive. In intermediate accretion regimes, funnels and tongues can coexist (Kulkarni & Romanova 2008). In these cases, accretion will occur mainly through two accretion funnels, but random accretion funnels can also appear in the magnetosphere; this is reflected in the light curves of the system as a periodic compoent with the superposition of a stochastic component of variability.

It is also interesting to note that, even in the case of stable magnetospheric funnel-flow accretion, sudden transitions to different regimes or geometries may occur. A paradigmatic case in this respect is AA Tau, an accreting YSO seen almost edge-on, which hosts a predominantly dipolar magnetic field slightly tilted relative to the rotation axis. Light variations for this objects were monitored assiduously for over twenty years (Bouvier et al. 1999, 2003, 2007a), and the system consistently exhibited the same average photometry, light curve shape and periodicity, before changing drastically on much shorter timescales ($\lesssim$ year; Bouvier et al. 2013).

1.3.2 Disk–locking?

As mentioned earlier, one of the questions linked with disk accretion and early stellar evolution is how to reconcile the theoretical expectation that young stars should be spun up by mass and angular momentum transfer from the disk, and hence rotate at velocities close to break-up speed as they contract toward the Zero-Age Main Sequence (ZAMS), with the observational evidence

that typical rotation rates for T Tauri stars are much slower, typically amounting to a merely a fraction of the break-up velocity.

Königl (1991) proposed the so-called *disk-locking* mechanism solution to the angular momentum problem. After Ghosh & Lamb (1979), he discussed that a magnetic field of the order of kilogauss, whose field lines thread the disk around the co-rotation radius r_C, could act as an effective brake to prevent the star from spinning up. In this scenario, the braking torque transmitted by the field lines coupled with the disk at larger distances than r_C (where the disk rotates more slowly than the star) would balance the spin-up torque exerted by disk material inside r_C. Inside the truncation radius r_T, the magnetic stress is large enough to remove the excess angular momentum carried by the disk matter flow.

A somewhat different description is proposed in Shu et al. (1994). In the assumption that r_T is smaller than r_C, they define two different magnetospheric regions: one between r_T and r_C, and the second external to r_C. In the $r_T < r < r_C$ region, funnel flow develops and eventually climbs onto the magnetic field lines and is channeled to the star surface; although disk material in this region rotates faster than the star, the interaction between the magnetosphere and the disk may actually determine an angular momentum transfer to the disk, as a result of the ability of the strong magnetic field to enforce near-corotation with the star in this disk region. In the $r > r_C$ region, excess angular momentum is transferred to the disk; part of this is removed by viscous torques, while the remaining fraction may be carried away by magnetocentrifugally-driven winds.

One consequence of this model that identifies the main braking source for young stars in the magnetosphere-disk coupling is that, once the disk accretion phase is over, the star can spin up freely toward the ZAMS. Hence, from an observational point of view, if the model is valid, we would expect to measure rotation periods for disk-free WTTS which are statistically smaller than those measured for CTTS. Several studies in the last decades have explored this accretion-rotation connection (see, e.g., discussions in Cauley et al. 2012 and Bouvier et al. 2014), with somewhat controversial results.

Rebull et al. (2004) investigated period distributions for several young clusters, and concluded that a significant fraction of PMS stars evolve at nearly constant angular velocity in the first ∼3–5 Myr. This time scale is well consistent with disk lifetime estimates inferred from analyses of the frequency of near-IR excess sources as a function of age. Hence, this conclusion would support the idea that an effective braking mechanism operates in young stars during the disk accretion phase. Empirical evidence for significantly different (though overlapping) rotation rate distributions between the CTTS (disk-bearing) and WTTS (disk-free) populations, with the latter rotating faster on average than the former, has been derived for NGC 6530 (2 Myr; Henderson & Stassun 2012), the Orion Nebula Cluster (ONC, 2 Myr; Herbst et al. 2002; Cieza & Baliber 2007), NGC 2264 (3 Myr; Lamm et al. 2005; Affer et al. 2013), Cep OB3b (6 Myr; Littlefair et al. 2010). Typical values of rotation periods are of a few (∼1-5) days for WTTS and several (∼4-10) days for CTTS. Fallscheer & Herbst (2006) investigated the connection between U-V excess and rotation periods for a sample of stars in NGC 2264 and reported evidence in favor of the disk-locking paradigm (statistical association of slow rotation periods with higher U-V excesses).

On the other hand, no connection between rotation rate and the presence of a disk is detected in the study of Cody & Hillenbrand (2010) on the σ Orionis cluster (6 Myr). Furthermore, contradictory results were obtained for the same ONC and NGC 2264 clusters by Stassun et al. (1999) and Rebull (2001) and by Makidon et al. (2004), respectively, which may indicate that different properties in the starting samples investigated (e.g., different mass ranges probed) may lead to contrasting conclusions. A theoretical complication in the disk-locking picture arises from the fact that, while (multipolar) magnetic fields at the TTS surface have intensities of a few kG, observations indicate that the strength of the dipolar component which threads the disk

may be down to a factor of 10 smaller (Gregory et al. 2012), possibly not strong enough to act as an efficient braking source in the disk-locking model described earlier. The issue of rotation braking during the disk phase has been recently re-evaluated by Matt & Pudritz (2005b,a), who suggested that accretion-powered stellar winds may provide alone the necessary spin-down torque to counterbalance the spin-up torque of the accretion flow. Magnetospheric ejections of material (Zanni & Ferreira 2013) may also act as an efficient mechanism to extract angular momentum from the systems.

1.4 The manifold variability of T Tauri stars

Photometric investigations of the physics of T Tauri systems take advantage of two complementary types of diagnostics: characterizing the colors of the stars (i.e., probing the wavelength domain) and exploring stellar variability (i.e., probing the time domain). Colors are a tracer of the slope of the SED in different regions of the spectrum, and hence provide insight into the dominant components of the emission and, therefore, into the physical mechanisms at the base of the observed photometric properties. Monitoring photometric variability enables studies of the dynamics of evolution and of the relevant timescales for the physical processes of interest to the dominant features of the systems.

As discussed in Sect. 1.1, prominent variability is a defining mark of T Tauri stars. Photometric variations are observed on a wide range of wavelengths (X-rays, optical, infrared) and on all timescales investigated so far (from $\lesssim$ hours to days, months and years). Besides, young stars display strong spectroscopic variability, and variations of the polarization in TTS, indicative of the distribution of circumstellar dust, are documented as well (e.g., review by Appenzeller & Mundt 1989).

In the following, I will focus on the different flavors of photometric variability exhibited by young stars in the optical and at short wavelengths. This probes the properties of the stellar photosphere and the star-disk close environment. Sect. 1.4.1 explores the types of light variations observed on timescales from days to weeks; in Sect. 1.4.2, I will present the nature of variability on much shorter (hours) and longer (years) timescales.

1.4.1 Variability on mid-term (days to weeks) timescales

In 1994, Herbst et al. presented a comprehensive catalog of $UBVRI$ light curves for 80 young stars. This gathered photometric data obtained on various telescopes and surveys over a time span of several years, with tens of epochs (light curve points) for each source. The comparative analysis of this sample enabled the authors to identify four main types of photometric behaviors (see Fig, 1.9), corresponding to distinct physical processes that would dominate the observed variability pattern for different groups.

Type I variability, responsible for the well-behaved, periodic light curves observed for WTTS, consists in a simple rotational modulation effect produced by a non-homogeneous distribution of dark cool spots at the stellar surface, whose nature is linked to the underlying magnetic activity of the stars. Starspots are assumed to develop at the foot points of magnetic loops, where convective motions are inhibited by the strong magnetic fields; hence, the surface distribution of cold spots may provide indications on the geometry and complexity of the stellar magnetic field. Photometric amplitudes detected for Type I-variables are moderate, ranging from $\lesssim 0.1$ to ~ 0.5 mag in the optical, and decline from bluer to redder wavelengths; this occurs because the contrast between the cool spot distribution and the photosphere diminishes toward longer wavelengths (see Fig. 4.11 in Chapter 4 of this thesis). The overall light curve pattern remains stable over tens to hundreds of rotational cycles (i.e., over months to years), which suggests that

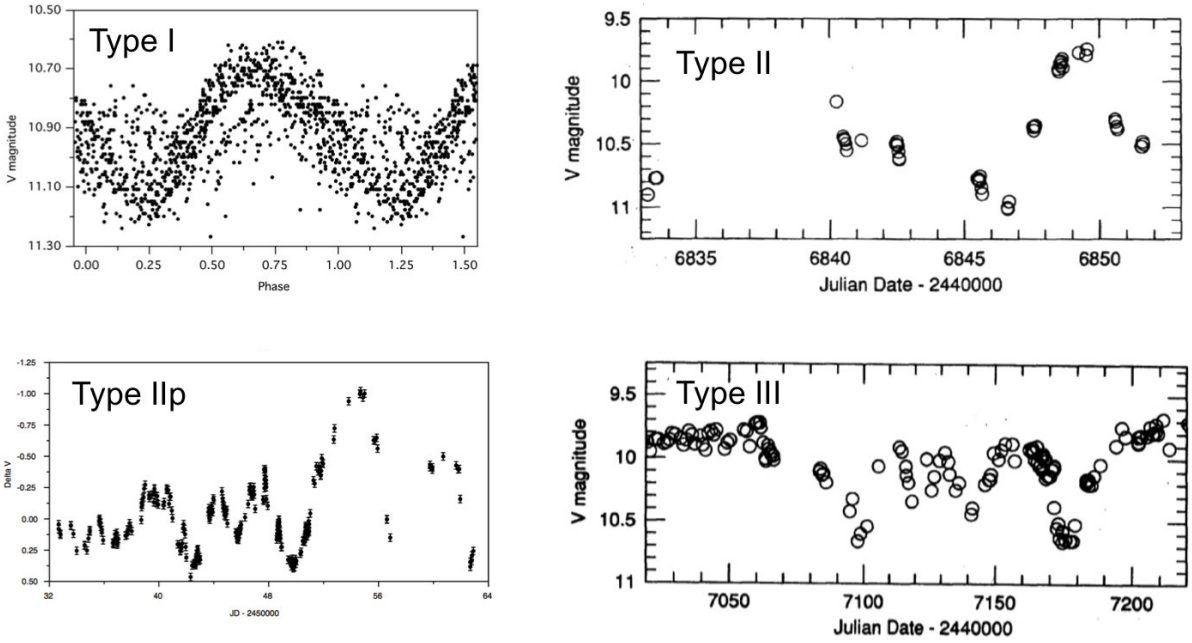

Figure 1.9: Examples of V-band light curves for each of the four variable types identified among T Tauri stars by Herbst et al. (1994): V410 Tau (upper left, phased light curve) for Type I (cold spot-modulated) variability (figure adapted from Ménard & Bertout 1999); RW Aur (upper right) for Type II (aperiodic) variability (figure adapted from Herbst et al. 1994); DF Tau (lower left) for Type IIp (hot-spot modulated) variability (figure adapted from Ménard & Bertout 1999); RY Tau (lower right) for Type III (circumstellar extinction) variability (figure adapted from Herbst et al. 1994).

such spots are long-lived, although the exact shape of the light curve "unit" (one period) may vary from one cycle to the other, reflecting corresponding changes in the spot distribution and properties.

The optical variability of WTTS can be entirely accounted for by cold spot modulation (additional sources of variability associated with chromospheric activity, i.e. flares, may also be present at shorter wavelengths on the shorter term). Cold spots are also expected at the surface of accreting CTTS, which are similarly magnetically active; however, cold spot modulation represents only a single, underlying component of variability in these cases, on top of which more prominent flux variations of different origin shape the light curve pattern. The interplay between various sources of variability for CTTS is at the base of the huge diversity in light curve morphology detected across the group, with large (up to a few mag) photometric amplitudes and often irregular profiles, where semi-periodic components coexist with rapid, stochastic flux variations and fading events.

Type II variability, specific to CTTS, originates then in a changing mixture of cool magnetic spots and hot accretion spots (formed where the accretion columns impact the surface of the star). In some cases, a definite periodicity, associated with spot modulation, is detected in CTTS light curves, at least at some epochs; these cases are classified as *Type IIp variability* in Herbst et al.'s 1994 scheme. Type IIp objects differ from Type I objects in the variability amplitudes, which tend to be larger in the first group than in the second group; this is especially true at UV wavelengths, dominated by the emission from the hot spots. As for the Type I variability group, amplitudes observed in Type II variability decrease for increasing wavelength; however, the transition is steeper in the second group than in the first. Type I and Type IIp variability are also distinguished by the fact that the periodic behavior typical of Type IIp objects is often less stable and more rapidly evolving that the smooth patterns reconstructed for objects in the

first group. This occurrence, and the fact that irregular variation patterns are more common than definite periodicities among CTTS, suggests that accretion spots evolve on much shorter lifetimes compared to magnetic spots.

A different origin is associated with *Type III variability*. This is observed only among disk sources. Objects in this category show light curves with typical brightness level close to the maximum luminosity state, interspersed by dips of up to a few magnitudes with little color dependence in the amplitude. An increase in the degree of polarization may accompany the epochs of fading. Herbst et al. (1994) interpreted this type of variables to be dominated by variable circumstellar extinction. Although many of the objects identified as members of this group were more massive Herbig Ae/Be stars in Herbst et al.'s sample, a number of earlier-type T Tauri stars were found to exhibit similar behavior. Remarkable progress in understanding this type of photometric behavior was marked by the detailed large-epoch investigation of the object AA Tau (Bouvier et al. 1999, 2003, 2007a), which has become the prototype of the class of T Tauri variables with recurring flux dips in their light curves. In AA Tau, the system is seen at high inclinations (almost edge-on), which provides the observer with privileged access to structures in the inner disk. The episodes of obscuration are thought to arise from a warped inner disk (see discussion in Sect. 1.3.1) which corotates with the star and periodically occults part of the photosphere. Later studies (Alencar et al. 2010) have shown that AA Tau does not represent an isolated case, but that a relatively large (about 20%) fraction of CTTS cluster members may share similar properties. While a part of these objects display a definite and stable periodicity, as in the case of AA Tau, for a similar number of objects the episodes of obscuration occur aperiodically.

1.4.2 Variability on shorter and longer timescales

While variability on day timescales is a ubiquitous feature of T Tauri stars, detection of strong variability on short ($\lesssim$hours) timescales, in excess of what expected based on the mid-term trend, is less frequent (e.g., Gahm et al. 1995). One source of variability on short timescales, detected primarily at short wavelengths (UV, X-rays), is magnetic flares. These comprise a phase of sudden brightness increase that protracts over a few hours at most, followed by a phase of somewhat slower, though still rapid, brightness decay. Flares derive from energy release above magnetized surface regions. Flares are more easily detected in WTTS, where no other source of variability than magnetic activity is present, although they appear in CTTS as well (e.g., Worden et al. 1981).

An interesting phenomenon that has been documented on long timescales (decades) is the so-called "FU Orionis outbursts" (Herbig 1977a). FU Orionis stars are thought to be CTTS which experience a strong luminosity outburst. The increase in brightness occurs on timescales of several hundred days; this phase is followed by long-term luminosity decline. A possible interpretation of this phenomenon is the onset of disk instabilities, which lead to non-steady accretion and increases of the accretion rate by several orders of magnitude (Ménard & Bertout 1999).

1.4.3 The space-borne revolution in YSO variability studies

The mid-2000s marked an important turnpoint in the exploration of YSO variability, with the launches of the *Spitzer Space Telescope* (2003) and of the *COnvection, ROtation and planetary transits (CoRoT)* space mission (2007). Until that moment, the understanding on the nature of variability for young stars was built on a number of ground-based multiwavelength monitoring campaigns performed at the end of the XX century. These, as discussed in Sect. 1.4.1, have enabled thorough characterization of the global features pertaining to different variable groups,

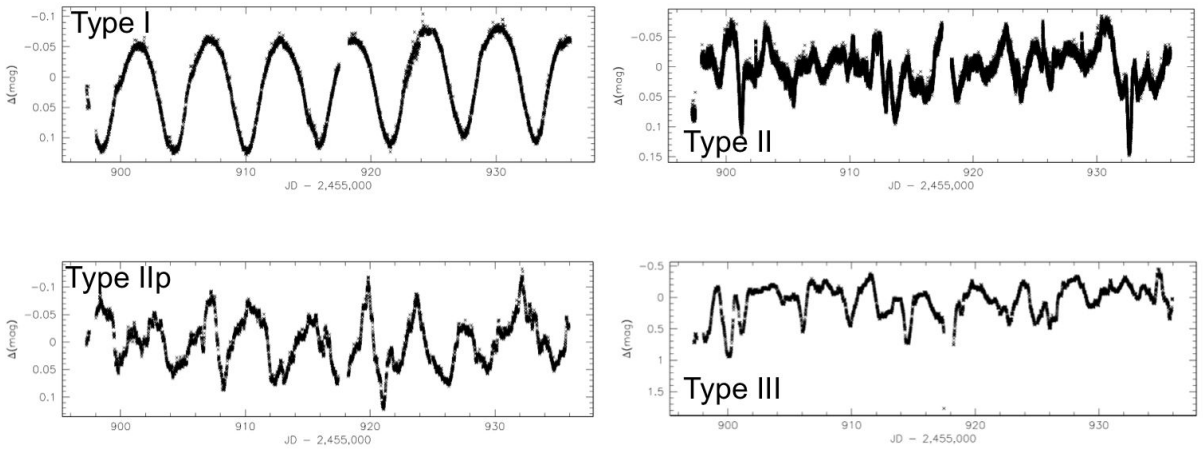

Figure 1.10: Examples of prototypes of Herbst et al.'s (1994 variability types among young stars monitored with the satellite *CoRoT* (∼R-band) in NGC 2264. Comparison of this Figure with Fig. 1.9 illustrates the improved capability of space-based surveys for exploration of YSO variability.

and identification of the broad physical scenarios related to each of them. However, a detailed description of the variability exhibited by individual sources from ground-based observations is hampered by several factors. The time domain accessible from the groud is intrinsically limited on the short timescales (< day) due to the day/night alternation, which renders it difficult to detect or parse characteristic timescales of variability of the order of hours; moreover, obtaining extended well-sampled coverage on periods of more than a few weeks is quite challenging because of telescope time allocation and contingency of good weather conditions. This results in time gaps at different baselines in the light curves of objects monitored from the groud (as can be seen on Fig. 1.9). In addition, variable atmospheric seeing limits the photometric accuracy that can be obtained from the ground (typically of the order of ∼0.01 mag in the optical and ∼0.1 mag at short wavelengths). These limitations are especially relevant in the analysis of Type II and Type III variability (Fig. 1.9): ground-based photometry may allow identification of generic aperiodic flux variations, but cannot resolve their detailed structure.

Fig. 1.10 illustrates examples of the different variable types defined in Herbst et al. (1994), selected among members of the NGC 2264 cluster observed with the *CoRoT* satellite. With photometric accuracy down to ∼0.001 mag and cadence down to a few minutes, space-based light curves offer nearly continuous monitoring of stellar variability on baselines that can extend to several weeks or months. This enables us to accurately retrace the small-scale details of the variability features exhibited by young stars, hence filling the gaps of ground-based observations. A detailed characterization of the variability pattern, of the characteristic timescales of single variability features and of their time evolution is critical to achieve a comprehensive picture of these systems and of the underlying physics (notably, for CTTS, the dynamics of star-disk interaction, the mechanisms governing the accretion process, and the structure and geometry of star-disk systems).

In March 2008, *CoRoT* was employed to monitor the optical variability of several hundred young stars in the NGC 2264 clusters on a baseline of 23 days. This survey provided first regular, well-cadenced variability monitoring, covering several rotational cycles, for a large sample of young stars; it provided significant new insight into the dynamics of the accretion process in young stars, as related in the work by Alencar et al. (2010). Similarly to what done in Herbst et al. (1994), the authors separated CTTS into three groups according to light curve morphology: periodic sinusoidal-like light curves, dominated by modulation from long-lived surface spots; periodic light curves which appear "flat-topped" (i.e., which exhibit a flat maximum interrupted

by minima that vary in width and depth from cycle to cycle); aperiodic light curves. The second group gathered objects which were AA Tau-like in nature. Their analysis illustrated that the AA Tau-like behavior is fairly common among CTTS (observed in about 20% of the objects investigated); as in the AA Tau case, these light variations are assumed to be driven by obscuring material located in the inner disk, near the co-rotation radius. Changes in shape and width of light curve dips then reflect the dynamics of star-disk interaction. Non-steady accretion was instead suggested to explain the irregular morphology of light variations observed for objects in the third variability class.

It should be noted that associating color information with the analysis of time-dependence in variability studies is critical to distinguish between different physical scenarios. Multiwavelength photometry on the optical and UV wavelength range may help discriminate on the nature of projected surface spots, as discussed in Sect. 1.4.1 after the analysis of Herbst et al. (1994) (see also Vrba et al. 1993 and analysis in Chapter 4 of this thesis). On the other hand, exploring the infrared wavelength domain is of interest to probe the structure of the inner disk region of YSOs (see, e.g., the ongoing *Spitzer* program YSOVAR, Rebull et al. 2014). Coordinated investigations of YSO variability at different wavelengths, covering different timescales with adequate sampling rate and encompassing large samples of young stars, are, thus, of great importance to achieve a comprehensive description of the physics of these objects. This motivation has led to the *Coordinated Synoptic Investigation of NGC 2264* (CSI 2264) program (Cody et al. 2014), performed three years ago. This program is the most extensive and thorough investigation of YSO variability ever attempted; a number of ground-based and space-borne observatories were coordinated to address multi-color variability of hundreds of young stars in the NGC 2264 cluster, on timescales ranging from minutes to over a month. The program is discussed in detail in Chapter 2 of this manuscript; it represents the framework for the thesis work presented here.

1.5 Open issues in disk accretion from an observational perspective

Over the last decades, several effort has been devoted to measuring mass accretion rates for large samples of CTTS, with the aim at characterizing their dependence on several stellar parameters (like mass and age) and thus helping define a plausible theoretical scenario of how disk accretion occurs.

Observations show typical mass accretion rates of $\sim 10^{-8}$ $M_\odot$/yr at an age of a few Myr. An important question regarding mass accretion in TTS is whether $\dot{M}_{acc}$ statistically depends on $M_\star$, and what is the functional form of this relationship. This is of primary interest to test the predictions of different possible models for mass and angular momentum transport in disks. For instance, the model of layered MRI-driven accretion proposed in Gammie (1996)[7], modified as in Hartmann et al. (2006) to take into account disk irradiation by the star, would yield a dependence of the type $\dot{M}_{acc} \propto M_\star^\alpha$, with $\alpha \sim 1$.

First observational analyses of the $\dot{M}_{acc}$–$M_\star$ dependence (e.g., Muzerolle et al. 2003b) have reported $\dot{M}_{acc} \propto M_\star^2$. This is significantly steeper than the relationship in the layered MRI accretion model. Alexander & Armitage (2006) suggested that the observed relationship may be the result of varying disk initial conditions with stellar mass, followed by viscous disk evolution.

[7]This model assumes that the angular momentum transport in circumstellar disks in driven by magnetic fields and can take place only in the regions of the disk that are sufficiently ionized, that is, in the innermost regions and in a surface layer of roughly constant surface density, on both sides of the disk midplane, which is directly impacted by the external ionizing radiation. The accretion flow in this model is hence confined to these active layers of the disk, while the central layer of the disk, close to the midplane, is decoupled from the field due to the low ionization level in its interior.

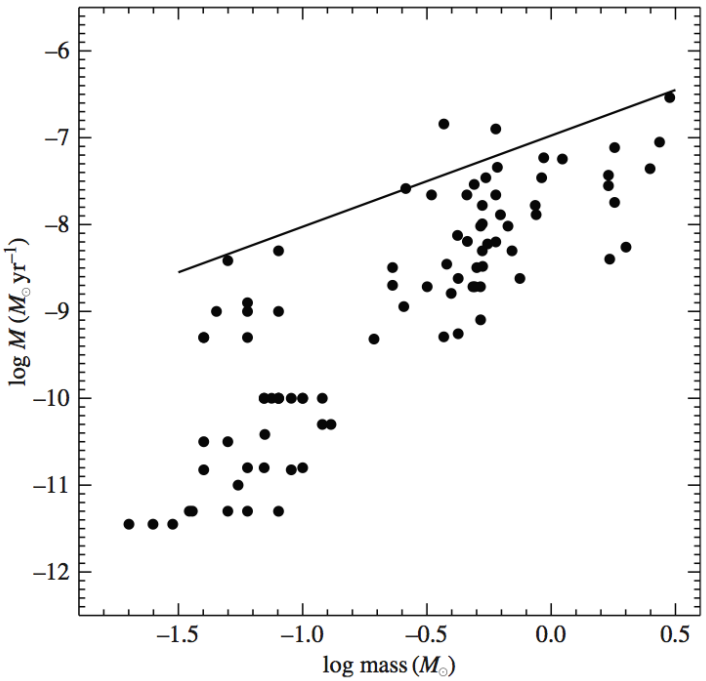

Figure 1.11: Mass accretion rates for young stars as a function of stellar mass. The straight line indicates the relation $\dot{M}_{acc} = 0.1\, M_\star/10^6\, yr$, above which sustained accretion for a typical age of 1 Myr would imply an initial disk mass likely to be gravitationally unstable. From Hartmann et al. (2006).

An earlier evolutionary scenario proposed by Padoan et al. (2005) to explain the observed mass dependence assumed that the star-disk system does not evolve in isolation, but interacts with the parent molecular cloud. In this picture, the observed mass accretion rates onto the stars are determined essentially by a mechanism of Bondi-Hoyle accretion onto the star-disk system travelling through the ambient gas. This scenario, however, does not seem to provide a satisfactory physical description, because it neglects angular momentum transport in the disk, which appears to be a critical aspect in the dynamical evolution of the system.

Recently, somewhat shallower exponents for the relationship between $\dot{M}_{acc}$ and $M_\star$ have been derived as well (for instance, Rigliaco et al. 2011 found $\dot{M}_{acc} \propto M_\star^{1.6}$ in the σ Ori cluster). As noted by Hartmann et al. (2006) (see Fig. 1.11), a large scatter in $\dot{M}_{acc}$ values at a given $M_\star$ among populations of similar age are detected. While a global $\dot{M}_{acc} \propto M_\star^\alpha$ relationship which describes the average behavior observed for the bulk of the data can be inferred, this does not represent a universal prescription. Indeed, the relationship appears to become weaker from the lower to the upper envelope of the $\dot{M}_{acc}$–$M_\star$ distribution in Fig. 1.11, which suggests that differing mechanisms could be dominant in different accretion and mass regimes (indeed, different disk masses and evolutionary timescales may be associated with different stellar masses, and recent studies, e.g. Gregory et al. 2012, have shown that different magnetic topologies at the stellar surface tend to correspond to different spectral types). A connected issue in studies of the $\dot{M}_{acc}$–$M_\star$ dependence is evaluating the impact of observational selection effects, such as the limited knowledge at the lowest accretion regimes, due to the fact that low continuum excesses are more difficult to detect above the stellar emission, especially for more luminous (i.e., higher-mass) stars.

More questions arise about the nature of the large spread in $\dot{M}_{acc}$ values at any given $M_\star$, that is typically observed from surveys of accretion properties for large populations of stars. Is this an intrinsic feature of the picture of variability one may derive across the populations of

young clusters, or does it simply reflect uncertainties in the $\dot{M}_{acc}$ measurements and/or stellar variability? If it is real, what is its physical content? Which elements may play a role in the detection of a range in accretion regimes for stars of similar properties? Does the spread in $\dot{M}_{acc}$ reflect a diverse nature of the mechanisms that govern disk accretion in individual sources? Moreover, several studies (e.g., Sicilia-Aguilar et al. 2010) have shown that $\dot{M}_{acc}$ tends to decrease with age as $\dot{M}_{acc} \propto t^{-\eta}$, $\eta \sim 1.5$ (Hartmann et al. 1998); may then the point scatter on the $\dot{M}_{acc}$–$M_\star$ plane be a tracer of differential evolution among the populations investigated?

Variability studies may also provide important contributions to understanding the actual mechanisms that govern the dynamics of accretion. For instance, what are the characteristic timescales for CTTS (as opposed to WTTS) and what is the relative weight of different variability components (e.g., rapid spot evolution vs. rotational modulation) for accreting objects? What can these observations reveal about the nature and stability of the accretion process?

1.5.1 Aim and outline of this thesis

The thesis work presented here proposes to investigate the points discussed above, targeting the PMS population of the young open cluster NGC 2264.

The analysis was anchored to simultaneous optical and UV monitoring of stellar variability on timescales varying from a hours (minimum cadence) to weeks (duration of the monitoring survey). These were performed as part of the CSI 2264 program mentioned earlier (Sect. 1.4.3). The survey and dataset, as well as the region explored in this study, are introduced in Chapter 2. As highlighted in Sect. 1.3.1, UV observations reveal the characteristic hot continuum emission arising from the accretion shock, and hence provide a direct diagnostics of ongoing accretion activity. Investigations of accretion from photometric diagnostics have the added virtue of being readily applicable to large samples of objects, thanks to the availability of large field-of-view telescopes, which enable, for instance, extensive mapping of the UV colors of whole star-forming regions to build statistical population studies from homogeneous datasets.

The first part of the work was devoted to characterizing the UV colors of young stars as an accretion diagnostics. From the UV excess measurements, I derived an instantaneous map of accretion properties across the cluster and examined their variability on hour-to-day timescales. I could thus estimate the impact of stellar variability on the $\dot{M}_{acc}$ vs. $M_\star$ picture of the cluster, and investigate the properties of the latter with reference to the diverse nature of CTTS in NGC 2264.

As a second step, I explored the detailed variability pattern for individual cluster members, and combined magnitude and color variations to discriminate the nature of their main variability features. I then examined the strength of variability exhibited by cluster members on different baselines, to determine the dominant timescales of variability for TTS and the implications for the nature of the accretion process.

Finally, I investigated light curve periodicity across the full sample of members. In the assumption that the detected modulation corresponds to the rotational period of the stars, I examined the period distribution inferred for the cluster and separated the contribution from disk-bearing and disk-free objects, in order to explore any dependence of the typical spin rate on the presence of disk accretion.

Chapter 2

The *Coordinated Synoptic Investigation of NGC 2264*

Contents

In December 2011, the improved capability of space-based surveys in time domain exploration and the benefits of a multi-wavelength approach to YSOs variability were combined in the unprecedented *Coordinated Synoptic Investigation of NGC 2264* project (P.I. = J. Stauffer, at Spitzer Science Center, & G. Micela, at INAF-OAPa; see Cody et al. 2014). This campaign (hereafter *CSI 2264*) consisted of a unique cooperative effort including 15 ground and space-based telescope, aimed at providing first simultaneous monitoring of flux behavior, from the IR to the X-rays, on timescales ranging from hours to weeks, for several hundred disk-bearing (CTTS) and disk-free (WTTS) young stars.

The campaign targeted the star-forming region NGC 2264, a well populated, young open cluster, whose high scientific interest combines with the peculiarity of being the only young region that could be observed simultaneously with all major space telescopes (*Spitzer* in the infrared, *CoRoT* in the optical, *Chandra* in the X-rays) according to their orbital constraints. The observing program started on Dec. 1, 2011, and extended over nearly 3 months; the photometric variability of several thousand objects in the NGC 2264 field was monitored in the infrared, in the optical, in the UV and in the X-rays, and optical spectra were obtained at several epochs for about a hundred interesting targets to monitor the evolution of the Hα line profile.

Sect. 2.1 provides a brief description of the NGC 2264 region, while the CSI 2264 observing campaign is described in detail in Sect. 2.2.

2.1 The young open cluster NGC 2264

The star cluster that would later be designated as *NGC 2264* (Dreyer 1888) was discovered by William Herschel on 18^{th} January 1784, around the bright star S Monocerotis or 15 Monocerotis (Herschel 1786). New observations, performed two years later, led to the identification of a

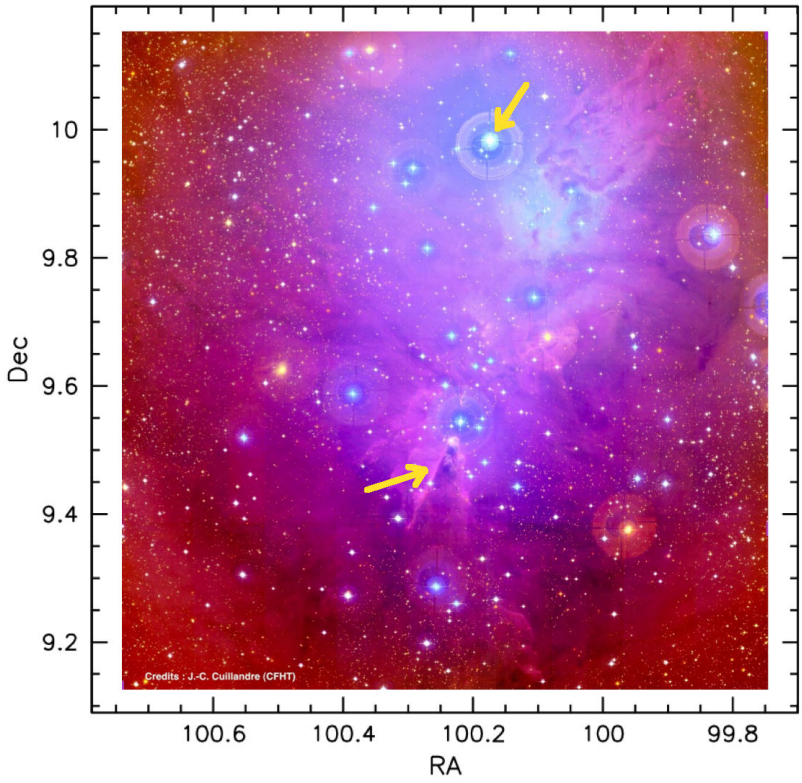

Figure 2.1: CFHT/MegaCam $u\,g\,r$ color image of NGC 2264 (credit: J.-C. Cuillandre). The imaged regions has a physical size of about 13.5 parsecs. The yellow arrows in the upper and lower half of the image indicate the positions of S Mon and of the Cone Nebula, respectively.

nebulous complex, associated with the star cluster, located slighty to the south of 15 Mon (Herschel 1789). Both components are globally referred to as the NGC 2264 region.

First indications on the presence of variable stars in NGC 2264 resulted from the work of Wolf (1924). In 1954, Herbig uncovered a population of 84 Hα-emission stars toward the cluster, distributed nearly centrally on the associated dark nebula; he further noticed that most of the known variables in the cluster did display emission lines. These results allowed him to conclude that "the great majority of the emission-Hα stars associated with NGC 2264 are T Tauri stars". The youth of NGC 2264 was confirmed in the three-color photometric and spectroscopic study by Walker (1956). The author noted that, while the position of early-type (O7 to A0) cluster stars on a color-magnitude diagram followed closely the normal main sequence track, later-type objects were systematically displaced above the main sequence, by an amount of 1.5 to 2 mag in the V-band. He then concluded that the lower-mass component of the cluster population consisted of extremely young stars, "still in the process of contracting from the prestellar medium". By comparing the HR diagram of the cluster to the theoretical predictions of Henyey et al. (1955), Walker inferred an age estimate of 3×10^6 yr for the cluster and its stellar population.

Since these first seminal works, and thanks to its remarkably favorable properties, NGC 2264 has been a benchmark for star formation studies (as attested by the ample literature existing to date on the subject; a recent review can be found in Dahm 2008).

The cluster is located at a distance of about 760 pc (Sung et al. 1997; Gillen et al. 2014) in the local spiral arm of our Galaxy, and is seen in projection against a large molecular cloud complex, spanning over two degrees north and west of the cluster center, that serves as a screen against contamination from background stars. In addition, foreground extinction is quite low

($A_V \lesssim 0.4$; Sung et al. 1997; Rebull et al. 2002) and fairly uniform across the region, although the A_V for individual members can be somewhat higher due to local extinction effects or more embedded location within the molecular cloud. S Mon, an O7 V multiple star located in the northern half of the cluster (Fig. 2.1), is the brightest stellar member of NGC 2264; the OB population of the cluster comprise about twenty additional objects (e.g. Morgan et al. 1965). In the southern part of NGC 2264, a prominent feature is the Cone Nebula, a pillar of cold molecular gas and dust, illuminated by early-type stars in the region.

NGC 2264 has a hierarchical structure (e.g. Mathieu 1986; Lada et al. 1993) and several cloud cores can be identified across the molecular cloud complex. Optical and infrared sources are predominantly distributed in two separate areas within the region, one close to S Mon and the other located to the north of the Cone Nebula; several studies have shown evidence for further subclustering (e.g. Piche 1993; Lada & Lada 2003). The current population of the cluster may be the result of several, sequential episodes of star formation (e.g. Adams et al. 1983), and active star formation is still ongoing within the region, as attested by the presence of Herbig-Haro objects (e.g. Reipurth et al. 2004), molecular outflows (e.g. Margulis et al. 1988) and embedded sources (e.g. Wolf-Chase et al. 2003; Young et al. 2006). One prominent site of star formation activity is located several arcminutes north of the tip of the Cone Nebula, and another one can be found at about one third of the distance from the Cone Nebula to S Mon. The average age of NGC 2264 is thought to be of about 3 Myr[1] (Walker 1956; Mendoza V. & Gomez 1980; Sung et al. 2004; Mayne & Naylor 2008), although with an apparent age dispersion of several Myr across the cluster (Park et al. 2000; Rebull et al. 2002; Dahm & Simon 2005).

NGC 2264 possesses an extremely rich, well-characterized population of young stars, amounting to ∼1500 confident members and a few thousand candidates to the latest census (Cody et al. 2014). The bulk of members are distributed within a one square degree region of sky, well accessible with large-camera telescopes. Investigations were performed in the near- (Lada et al. 1993; Rebull et al. 2002; Young et al. 2006) and mid-infrared (Young et al. 2006; Teixeira et al. 2006; Sung et al. 2009; Teixeira et al. 2012), in the optical (Walker 1956; Rebull et al. 2002; Lamm et al. 2004; Dahm & Simon 2005; Sung et al. 2008), in the X-rays (Ramírez et al. 2004; Rebull et al. 2006; Flaccomio et al. 2006, 2010); membership was probed by means of photometric, spectroscopic, or kinematic (Fűrész et al. 2006) criteria. The large population of the cluster spans a variety of evolutionary stages, from embedded, Class 0/I protostars, to Class II, disk-bearing sources (CTTS), to Class III objects (WTTS) which have already dissipated their circumstellar disks and contract toward the ZAMS; the disk fraction among cluster members is estimated to be around 40% (e.g. Rebull et al. 2002).

2.2 The CSI 2264 project

2.2.1 Overview of the observing campaign

The observing program was built around 30-day-long continuous, simultaneous monitoring in the optical and in the IR with the *CoRoT* (Baglin et al. 2009) and *Spitzer* (Werner et al. 2004) space telescopes, respectively.

[1]The age of young stellar clusters is typically inferred from isochrone fitting with PMS models on a color-magnitude diagram. As noted by, e.g., Park et al. (2000) and Rebull et al. (2002), different sets of models can yield nominal age estimates that differ by up to a few Myr. Naylor (2009) recently proposed a new method, based on fitting the color-magnitude diagrams of stars between the Zero-Age Main Sequence and terminal-age MS in young clusters. Comparison between these new, MS age estimates and those based on PMS model-fitting shows that the former can be larger than the latter by a factor of 2. This technique was extended in Bell et al. (2013) to derive a new age scale for young clusters; on this new scale, NGC 2264 would have an age of 2–7 Myr (T. Naylor, private communication).

Coordinated Synoptic Investigation of NGC 2264: observations

Telescope	Instrument	Dates	Band(s)	Time Sampling
Spitzer	IRAC/mapping	Dec. 3, 2011–Jan. 1, 2012	3.6 μm, 4.5 μm	101 min
Spitzer	IRAC/staring	Dec. 3; Dec. 5–6; Dec. 7–8; Dec. 8–9, 2011	3.6 μm, 4.5 μm	15 s
CoRoT	E2 CCD	Dec. 1, 2011– Jan 3, 2012	3000-10000Å	32 s (high cadence), 512 s
MOST	Science CCD	Dec. 5, 2011–Jan. 14, 2012	3500–7500Å	24.1, 51.2 s[1]
Chandra	ACIS-I	Dec. 3, 2011–Dec. 9, 2011	0.5–8 keV	$\sim$3.2 s[2]
VLT	Flames, UVES	Dec. 4, 2011–Feb. 29, 2012	4800–6800Å	20–22 epochs
CFHT	MegaCam	Feb. 14, 2012–Feb. 28. 2012	u,r	30 epochs
PAIRITEL	2MASS camera	Dec. 5, 2011–Jan. 3, 2012	J,H,K	1–12 epochs
USNO 40-inch telescope	CCD	Nov. 22, 2011–Mar. 9, 2012	I	912–1026 epochs
Super-LOTIS	CCD	Nov. 11, 2011–Mar. 1, 2012	I	495–522 epochs
NMSU 1m telescope	CCD	Oct. 12, 2011–Mar. 4, 2012	I	47–54 epochs
Lowell 31-inch telescope	CCD	Oct. 12, 2011–Jan. 14, 2012	I	44 epochs
OAN 1.5m telescope	CCD	Jan. 10, 2012–Feb. 15, 2012	V, I	23–28 epochs
KPNO 2.1m telescope	FLAMINGOS	Dec. 16, 2011–Jan. 3, 2012	J,H,K_S	40–52 epochs
FLWO 60-inch telescope	KeplerCam	Nov. 30, 2011–Jan. 26, 2012	U	35–60 epochs
ESO 2.2m telescope	WFI	Dec. 24, 2012–Dec. 29, 2011	U, V, I	25–45 epochs
CAHA 3.5m telescope	Omega 2000	Dec. 5, 2011–Feb. 18, 2012	J,H,K	35 epochs
CAHA 3.5m telescope	LAICA	Jan. 25-26, 2012	u, r	20 epochs

Figure 2.2: Observing runs associated with the CSI 2264 campaign. From Cody et al. (2014)

CoRoT monitored the cluster nearly continuously from December 1, 2011 to January 9, 2012, with a small interruption of about one day around December 22, 2011 due to telescope pointing problems. The large field of view available on the instrument (over one square degree) was quite adequate to fit NGC 2264 in its entire spatial extent. Observations were carried out with two CCDs on the focal plane of the telescope. A large bandpass, extending from $\sim$3 700 to 10 000 Å and peaking around the V+R filters, is adopted at the camera; the instrument provides "white light" data by flux integration over the whole bandwidth. Data collected from one of the two CCDs, originally dedicated to exoplanetary science in the *CoRoT* mission, are additionally passed through a low-resolution dispersion prism to produce three-color photometry in "red", "green" and "blue"; however, this color information, available for a part of the targets in our campaign, was sparse and subject to systematics, hence only white flux data were retained for our purposes. Light curves of most objects are sampled at a cadence of 512 s, which translates into over 6 300 observing epochs spread over 38 days; a high–cadence mode with time sampling of 32 s was used for a small subset of objects. Data are retrieved from the satellite only for a predetermined list of targets, that here comprised about 500 confirmed cluster members and over 1 500 candidates, along with over 2 000 field stars. Fully processed light curves, obtained from aperture photometry, were delivered by the *CoRoT* pipeline (Samadi et al. 2007), which performs background subtraction and corrections for gain and zero offset, jitter, and electromagnetic interference. Isolated outliers are also automatically flagged in the reduction procedure and were discarded for analysis purposes. A significant fraction of light curves was affected by two prominent discontinuities, due to detector temperature jumps, that appeared at the same epochs for all cases, indicatively around the 18th and the 28th day of observation. These were corrected by computing a weighted flux difference at the two sides of each jump. The second discontinuity was preceded by an aberrant data point, which was rejected uniformly across the sample.

Spitzer observations were performed with the two operational channels of the *InfraRed Array Camera* (IRAC; Fazio et al. 2004) instrument at 3.6 μm and 4.5 μm, and extended from December 3, 2011 to January 1, 2012. A region of about 0.8°$\times$ 0.8° toward NGC 2264 was targeted, split in a series of contiguous fields of 5.2' $\times$ 5.2' (FOV of a single IRAC channel). During the first week of observations, the cluster was monitored in "staring mode" for about four days; in this time lapse, the telescope was pointed uninterruptedly to a single field located to the north of the Cone Nebula tip, and repeated frames were taken at this position for 19 to 26 hour-long blocks without interruptions, with an integration time of 4.4 s for each exposure. FOVs for the two IRAC channels are separated on the sky by about 7', hence observations in staring mode

were performed for two disjoint set of objects at the two wavelengths. For the remaining part of the campaign, *Spitzer* observations were performed in "mapping mode". Each field in the whole NGC 2264 region observed was visited about 12 times a day, with a total integration time of about 40 s per point on the sky. During every sixth round of mapping, a high dynamic range mode was applied, with integration time of 1.6 s, in order to recover the brighter population component, saturated in the longer exposure. Basic calibrated data images were released by the Spitzer Science Center pipeline, and were processed following the routine described in Gutermuth et al. (2009) to generate the light curves. When both 40 s and 1.6 s exposure data were available for a given frame, the former was selected if the count level did not exceed two thirds of the detection threshold; otherwise, the measurement from the latter was retained. Two-color light curves were obtained for about 10 000 point sources in the observed region; high cadence light curves were additionally obtained for 290 sources at 3.6 μm and 259 sources at 4.5 μm.

Additional optical monitoring from space was acquired with the *Microvariability and Oscillation of STars* (MOST) telescope, that provided light curves in a broad-band filter (3500–7500 Å) for about 70 NGC 2264 objects over the time window from December 5, 2011 to January 13, 2012. The space fleet enlisted for the campaign was completed with the *Chandra* X-ray Observatory, which monitored the X-ray (0.1–10 keV) variability of cluster members on hour timescales (about 10 epochs per day) on December 3, 5, 7, and 11, 2011, for a total exposure time of 300 ks.

A dozen of ground-based telescopes were employed in coordination with the space observatories to provide broader wavelength coverage and contemporaneous spectroscopic information on YSO variability. A full list is reported in Fig. 2.2.

Among these, the *Fibre Large Array Multi Element Spectrograph* (FLAMES) of the Very Large Telescope (VLT) was used to obtain spectra in the region of Hα and Li 6707Å. The FLAMES field of view has a diameter of 25'; two pointings were carried out to observe the central part of the cluster. The instrument can perform observations with two spectrographs: GIRAFFE, that can target up to 130 objects at a time with intermediate resolution (R $\simeq$ 17 000) and UVES, that offers high resolution (R $\simeq$ 40 000) but can target only up to 8 objects at a time. The first mode was used to perform the bulk of the observations for the CSI 2264 campaign; 20 to 22 epochs of spectra were obtained between December 4, 2011 and February 29, 2012, among which 6 simultaneous with *CoRoT* monitoring. UVES high-resolution spectra were obtained for some of the brightest sources in the field.

The wide-field imager MegaCam (Boulade et al. 2003), mounted at the *Canada-France-Hawaii Telescope* (CFHT), was designated to perform UV (u-band) monitoring of NGC 2264, simultaneous with optical (r-band) monitoring, with the specific goal to detect and monitor the UV excess displayed by accreting cluster members. The analysis and interpretation of these CFHT observations set up the core of the thesis work reported here; therefore, a detailed description of the MegaCam dataset and of its reduction is presented below.

2.2.2 CFHT dataset

MegaPrime and MegaCam at CFHT

MegaCam, operational since 2003, is a wide-field camera hosted in the dedicated prime focus environment MegaPrime on the Canada-France-Hawaii 3.6 meter telescope (a facility of the Mauna Kea Observatory). The camera is a mosaic of 36 CCDs (a square of 4 rows of 9 CCDs) and covers a field of view of 0.96 $\times$ 0.94 square degrees. Each CCD has a size of 2048$\times$4612 pixels; the size of a pixel is 13.5 μm, for a pixel scale of 0.185 arcsec/pixel. A small gap of about 13 arcsec (70 pixels) separates each CCD from the adjacent ones; in addition, two large gaps (about 80 arcsecs, or 425 pixels) separate the first from the second and the third from the fourth CCD row (see left panel of Fig. 2.3). Each CCD is read out by two amplifiers, for a total readout

	u	g	r	i
Central λ (Å)	3740	4870	6250	7700
$\lambda_{\rm min}$ (Å) at 50%	3370	4140	5640	6980
$\lambda_{\rm max}$ (Å) at 50%	4110	5590	6850	8430
Bandwidth (Å)	740	1450	1210	1450
Mean transmission (%)	69.7	84.6	81.4	89.4

Table 2.1: Central wavelength, bandwidth and transmission for MegaPrime filters used for this work. Adapted from http://www.cfht.hawaii.edu/Instruments/Imaging/Megacam/specsinformation.html

time of 35 s. The mosaic is installed in a cryostat where CCDs are cooled down to -120 °C, to minimize thermal noise. A wide-field corrector is installed in front of the camera, as well as an image-stabilizing unit, a glass plate placed in the optical beam in front of the camera that can be tilted to produce a displacement of the image proportional to the angle of tilt and hence perform small corrections of the image position on the focal plane of MegaCam.

MegaPrime is equipped with a filter jukebox that can hold up to 8 filters. Four broad-band filters were used for obtaining the observations relevant to the present work: u^*, g', r', and i' (hereafter labeled u, g, r, i for brevity of notation)[2]. Those, together with the z'-band filter (not adopted here), were designed to match closely the Sloan Digital Sky Survey (SDSS) photometric system (Fukugita et al. 1996), whose wide bandpasses ensure high efficiency for faint object detection and cover the entire accessible optical window. The CFHT u-band filter differs somewhat from its SDSS counterpart (bluer response); this reflects a specific choice of design, aimed at taking advantage of the lesser amount of UV extinction that affects the Mauna Kea site compared to the site (Apache Point Observatory, New Mexico) where the 2.5 meter telescope used for the SDSS survey is located. The bandpasses of the filters are illustrated in Fig. 2.3 (right panel), and information on central wavelengths and bandwidths are reported in Table 2.1.

MegaCam observing runs on NGC 2264

Starting on February 14, 2012, and for a period of two weeks, we monitored the u-band and r-band variability of objects in the NGC 2264 field with MegaCam, in the context of the CSI 2264 campaign. The target was observed during 11 nights distributed along the 14-day-long run; among these, 7 nights were photometric. A single $u + r$ observing block, consisting of five dithered exposures in u and five dithered exposures in r, obtained consecutively, was performed repeatedly on each observing night during the run, at a cadence varying from 20 min to 1.5 h. Individual exposures performed were of 3 s in the r-band and of 60 s in the u-band, for a total integration time of 15 s in r and 300 s in u in each observing sequence. The 5-step dithering pattern adopted allowed us to compensate for the presence of bad pixels and small gaps on the CCD mosaic, although large gaps are still present on the final assembled images of the region. On February 28, 2012, we also obtained a deep mapping of the region in the i-band. As for u- and r-band observations, a 5-step dithering pattern was used; the observing sequence was performed in two different exposure modes, a first with integration time of 180 s for single exposure, aimed at detecting all sources in the FOV, and a second with short exposures of 5 s, to recover the bright sources saturated in the long exposure mode.

[2] As of semester 2015A, these filters are getting replaced by a new set of broad-band filters. These new filters have a larger footprint than the previous set; the central wavelengths and passbands for the redder filters are almost unvaried, while the g and u filters peak at slightly bluer wavelengths than the corresponding old filters. A comparison of the transmission curves for old and new sets of filters is shown in the right panel of Fig. 2.3.

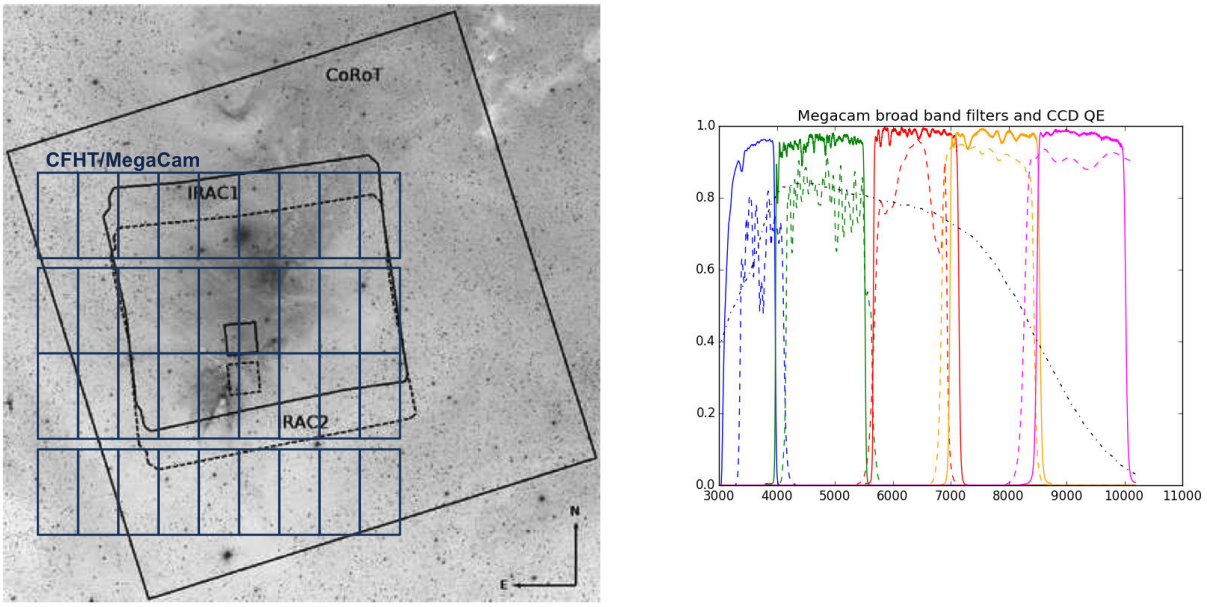

Figure 2.3: The left panel shows the field of view for CFHT/MegaCam observations, compared to the regions covered with *CoRoT* and the two *Spitzer*/IRAC channels, during the CSI 2264 campaign. The background image of the NGC 2264 region was retrieved from the Digitized Sky Survey. The largest square region corresponds to the *CoRoT* FOV (1.3°× 1.3°). The smaller square regions inside the FOVs for IRAC observations represent the areas surveyed in staring mode with IRAC1 (3.6 μm; solid line) and with IRAC2 (4.5 μm; dashed line), respectively. The region mapped with MegaCam is marked in blue; the structure of the CCD mosaic, with the two large gaps separating the first row of CCDs from the second and the third from the fourth, can be observed. The figure is adapted from Cody et al. (2014). The right panel shows the mean trasmission curves for the set of broad-band filters adopted at MegaCam (from http://www.cfht.hawaii.edu/Instruments/Imaging/Megacam/specsinformation.html; wavelengths on the x-axis are in Å; transmittivity on the y-axis is normalized to 1). The u-band filter is displayed in blue, g is in green, r is in red, i is in yellow, and z is in magenta. Dashed lines indicate the old set of filters, adopted at the camera until semester 2014B (and the filters of interest for the present study), while solid lines indicate the new set of broad-band filters introduced from semester 2015A to replace the previous set. The black dot-dashed curve indicated the CCD quantum efficiency.

The NGC 2264 MegaCam survey held in February 2012 was preceded by a preliminary feasibility study, performed with the same instrument in December 2010. That consisted of a deep $u\,g\,r$ mapping of the region. In the r-band, observations were obtained as a sequence of five, 10 s-long, dithered exposures; in u and g, the same 5-step dithering pattern was repeated in two different exposure modes, short (10 s) and long (60 s), in order to obtain a good signal/noise (S/N) for the whole sample of objects without saturating the brightest sources. All images were obtained over a continuous temporal sequence within the night.

A summary log of the observing runs on NGC 2264 performed with CFHT/MegaCam in December 2010 and February 2012 is reported in Table 2.2.

For this study, we combined and used both surveys described above, in order to get a full, 4-band map of the region and a detailed picture of variability at UV and optical wavelengths on timescales ranging from a few hours to a couple of weeks (which typically correspond to 2-3 rotational cycles for young stars in NGC 2264; e.g., Affer et al. 2013).

Date	*Flag$_{phot}$*[a]	*Filter*	*Exposure time (s)*	*n° obs. seq.*[b]	*Survey*
Dec. 12, 2010	1	u	60	1	mapping
		u	10		
		g	60		
		g	10		
		r	10		
Feb. 15, 2012	1	u	60	3	monitoring
		r	3		
Feb. 16, 2012	1	u	60	3	monitoring
		r	3		
Feb. 17, 2012	0	u	60	4	monitoring
		r	3		
Feb. 18, 2012	0	u	60	7	monitoring
		r	3		
Feb. 19, 2012	0	u	60	3	monitoring
		r	3		
Feb. 21, 2012	1	u	60	3	monitoring
		r	3		
Feb. 24, 2012	1	u	60	3	monitoring
		r	3		
Feb. 26, 2012	2	u	60	4	monitoring
		r	3		
Feb. 27, 2012	2	u	60	4	monitoring
		r	3		
Feb. 28, 2012	2	u	60	3	monitoring
		r	3		
		i	180	1	mapping
		i	5		
Feb. 29, 2012	0	u	60	1	monitoring
		r	3		

Table 2.2: Log of CFHT/MegaCam mapping and monitoring surveys of NGC 2264. [(a)]Flag on observing conditions: 1 = night was photometric; 2 = parts of the night were photometric; 0 = night was non-photometric. [(b)]Number of observing sequences performed during the night (i.e., number of times the same observing block was repeated during the night).

Data reduction and photometric calibration

Before being distributed, images were pre-processed at CFHT through the Elixir pipeline (Magnier & Cuillandre 2004); this procedure is aimed at correcting for instrumental signatures across the CCD mosaic (bad pixel clusters or columns, dark current, bias, non-uniformity in the response), as well as at providing a first astrometric and photometric (zero-point) calibration.

Individual, dithered fields obtained along a given observing sequence during the mapping survey were then co-added in a single master frame for each filter and exposure time. This mosaic stacking is performed by using the astrometric solution to match same sources on different frames, and then computing the mean or median count rate detected for each point across the set of five images. These average count rates are then used to build the final frame. This allows us to discard spurious signal detections (e.g., cosmic rays) from the final images and to correct for the small gaps that separate each CCD from the neighboring ones on the detector grid (since each exposure is slightly shifted with respect to the other four, a given point may be projected onto the gap during a given exposure, but a signal detection can be retrieved for it on other exposures). At this step, two maps of the region were produced in each of the u, g and i filters (one with long integration time and the other with short integration time), while a single map with short integration time was produced for the r-band. This part of the image processing was carried out at the Terapix center at the Institut d'Astrophysique de Paris, who provided us with the final co-added frames.

We then processed each assembled master frame with the SExtractor (Bertin & Arnouts 1996) and PSFEx (Bertin 2011) tools to detect point souces in the field and extract the relevant photometry. This analysis was performed in three steps. At first, we run a preliminary aperture photometry routine with a detection threshold of $10\,\sigma$ above the local background, in order to extract only brighter sources. This selection of objects was then used as input to run a pre-PSF fitting routine, aimed at testing the optimal parameters for the PSF function to be used for analyzing the images. Eventually, a new PSF-fitting routine was run, this time setting the detection threshold at $3\,\sigma$, to build the final, deep catalog of the region at those wavelengths.

Individual catalogs obtained from each master frame (two in each of the u, g and i filters, in two different exposure modes, plus one in the r-band) were cleaned of saturated objects (extraction flag ≥ 4), spurious detections (mag = 99), galaxies (typically faint and with pixel radius larger than the bulk of point sources), objects in the pre-saturation non-linearity zone (count level close to saturation threshold and flux radius[3] larger than average). I then combined long and short exposure catalogs in a given filter, where present, to obtain a unique photometric catalog for each spectral band and avoid duplicates. Objects common to the long and short exposures were used to evaluate the photometric accuracy, to measure and correct for small magnitude offsets between the results of the two exposures modes and to estimate the λ-dependent and exposure-dependent saturation start. When assembling the final single-band catalogs, objects were retrieved from the long exposures where possible, as those provide the most favorable signal-to-noise ratios; sources that appeared saturated or close to saturation in the long exposures were recovered from the short-exposure catalog, when available; sources brighter than the short-exposure saturation threshold were discarded.

To obtain a complete, 4-color catalog of the region, I cross-correlated single-band catalogs using the Tool for OPerations on Catalogs And Tables (TOPCAT; Taylor 2005). To match each source in a given table to its counterpart at the other wavelengths, I adopted a sky radius of 1 arcsec in u, g, r (which were obtained one after the other in the same night); this matching radius was enlarged to 2 arcsecs to incorporate the i-band measurements, obtained at a different epoch and in poorer observing conditions (lower angular resolution; J. Irwin, private commu-

[3]Radius that contains 50% of the total flux of the object.

(mag)	u	g	r	i
mag range	15-23.5	14-21.5	13.5-20.5	13-19.5
Saturation start	<12.5	<13	<13.5	12.5
Detection limit	23.5	21.5	20.5	19.5
Completeness	21.5	19.5	18.5	17.5

Table 2.3: Magnitude range, detection limits and completeness in the CFHT $u\,g\,r\,i$ survey of NGC 2264.

nication). Only best (i.e. closest) symmetric matches were retained. The final CFHT catalog of the NGC 2264 field comprises about 9 000 sources with a complete u, g, r, i photometric set; these cover a range of 7 magnitudes and the sample is estimated to be complete over a range of 5-6 magnitudes (Table 2.3).

To evaluate the possible impact of misidentifications between different filters, I performed the cross-correlation a second time and selected all matches found, for a given source, within the radius adopted. Only about 2.9% of sources in the field of view were found to have multiple matches; among these, in over 75% of the cases the difference in separation between the best matched pair and the next best match is larger than 0.5 arcsec, which roughly corresponds to the flux radius. In addition, barely 20% of these objects with multiple counterparts within the matching radius are projected onto the cluster area, whereas most of them are located onto the external regions of the field of view. For the statistical purposes of this study, the impact of potential misidentifications in the catalog cross-correlation procedure is considered to be negligible.

A similar approach was pursued to reduce the u and r-band data obtained during the monitoring survey of NGC 2264, but in this case each exposure was processed individually to contribute one observing epoch to the reconstructed light curves, and hence enable characterization of the variability pattern from short to mid-term timescales. The master frame built from the i-band, which provides the deepest chart of the region and where the nebulosity component was the least conspicuous, was used as a reference for the photometry extraction; for each source, an aperture was placed down on each u and r image at the position predicted from the i-band source detection and the amount of flux within this aperture has been extracted to build the light curve. Light curves were produced by Jonathan Irwin at the Harvard-Smithsonian Center for Astrophysics.

Instrumental photometry was calibrated to the SDSS photometric system. In the calibration procedure, I allowed for both a zero-point offset and a color term correction. The latter takes into account the fact that MegaCam filters do not perfectly correspond to their SDSS counterparts, but differ somewhat in bandpass and transmission. This implies that the convolution of a given stellar spectrum with a given transmission filter will not provide exactly the same results in the MegaCam and in the SDSS photometric systems; this difference in the response will depend on the features of the spectrum itself (a redder and a bluer spectrum will have a different response on the two filters).

To perform this calibration, I did not use a specific sample of standard stars in the field of view, but instead selected an ensemble of around 3 000 stars, among CFHT targets in the region, with tabulated SDSS photometry from the seventh SDSS Data Release (Abazajian et al. 2009), to statistically link instrumental magnitudes to SDSS magnitudes.

The photometric calibration procedure consists in solving a set of equations similar to the following:

$$u_{CFHT} = u_{SDSS} + u_c\,(u_{SDSS} - g_{SDSS}) + u_0 \tag{2.1}$$

$$g_{CFHT} = g_{SDSS} + g_c\,(g_{SDSS} - r_{SDSS}) + g_0 \tag{2.2}$$

$$r_{CFHT} = r_{SDSS} + r_c\,(r_{SDSS} - i_{SDSS}) + r_0 \tag{2.3}$$

$$i_{CFHT} = i_{SDSS} + i_c\,(r_{SDSS} - i_{SDSS}) + i_0 \tag{2.4}$$

In Eqs. 2.1–2.4, m_{CFHT} are the instrumental magnitudes, m_{SDSS} are the magnitudes in the SDSS system, m_0 are zero-point offsets between intrumental and CFHT magnitudes, and m_c are the color term coefficients. To derive m_c and m_0, the magnitude difference between CFHT and SDSS systems is plotted in a diagram against the SDSS color, as indicated in the Equation of interest, for the whole sample of objects common to the MegaCam and the SDSS catalogs; zero-point offset and color terms are then derived as a linear fit to the main data point distribution.

Objects in the CFHT catalog were matched to their SDSS counterparts using TOPCAT (matching radius = 1 arcsec; only best symmetric matches retained). At this step, I took into account only sources with a complete CFHT *ugri* set and that matched the magnitude limits for 95% detection repeatability for point sources defined for the SDSS photometric survey (Abazajian et al. 2004). In addition, to avoid contamination by color outliers to our derived calibration relationships, I compared the SDSS color distribution across our ensemble of stars with the SDSS dwarf color loci tabulated in the literature (Covey et al. 2007; Lenz et al. 1998), and selected the subsample of objects whose colors were consistent with these expected ranges ($-0.5 \lesssim u-g \lesssim 3.0$, $-0.6 \lesssim g-r \lesssim 2.0$, $-0.4 \lesssim r-i \lesssim 2.5$, from early O-type to late M-type field stars) . We referred our calibration analysis to the results published in the study of Regnault et al. (2009), which deals with the photometric calibration of the extensive 3-year dataset acquired with MegaCam for the CFHT Supernova Legacy Survey (Astier et al. 2006). Those authors notably provide color transformations between the SDSS and MegaCam magnitudes, with the caveat that the relationship derived for the i-band is not valid for data obtained later than June 2007, due to the accidental breakage and subsequent replacement of the i-band filter in use at MegaPrime. In u, g and r (Eqs. 2.1–2.3), we found the color trends predicted by Regnault et al.'s relationships to well adapt to our data point distribution; hence, we adopted their tabulated values for u_c, g_c and r_c, combined with a zero-point offset (u_0, g_0 and r_0, respectively) determined as the intercept of the linear fit to our data. In the i-band (Eq. 2.4), we did not find any significant color dependence in $i_{CFHT} - i_{SDSS}$ for our data; Eq. 2.4 then simplifies to $i_{CFHT} = i_{SDSS} + i_0$, with i_0 being the median offset between MegaCam and SDSS i-band magnitudes.

The system of equations 2.1–2.4, complete with the appropriate parameters, describes how to transform SDSS magnitudes into instrumental MegaCam magnitudes. The correct prescriptions to perform the opposite conversion are thus obtained by inverting this system of equations. The resulting conversion parameters are reported in Table 2.4.

Filter	m_0	m_c
u	-0.63	-0.211
g	-0.51	-0.155
r	0.00	-0.030
i	-0.02	0.000

Table 2.4: Zero-points and color coefficients obtained for the calibration of instrumental CFHT magnitudes to SDSS magnitudes (Eq. 2.1–2.4).

The procedure detailed above describes the photometric calibration carried out for the NGC 2264 *ugri* mapping dataset. Similarly, *u*- and *r*-band data obtained for the monitoring survey were calibrated to the SDSS system. The calibration analysis was again performed on a statistical ensemble of about 3 000 field stars common to the CFHT and SDSS surveys, selected as described previously. In this case, I took as reference the calibrated $u\,r$ photometry from the first CFHT survey. To ascertain the presence of offsets and/or color dependencies in the light curve magnitudes relative to SDSS-calibrated magnitudes, I investigated the distribution of residuals between median light curve magnitudes (from Feb. 2012) and single-epoch calibrated magnitudes (from Dec. 2010) as a function of median light curve magnitudes, both in *r* and in *u* (that is, $r_{\,lc\_med} - r_{\,2010\_cal}$ vs. $r_{\,lc\_med}$, and similarly for the *u*-band). A narrow horizontal sequence centered on zero was found in the *r*-band, which indicates that the preliminary automatic calibration derived within the Elixir reduction pipeline already provided a correct calibration to the SDSS system; conversely, both a zero-point offset and a non-zero slope (indicative of a color-dependence in the offset) were detected on the diagram for the *u*-band. I then derived a calibration relationship for the *u*-band, accounting for both terms, as a linear fit to the data point distribution on the $u_{\,lc\_med} - u_{\,2010\_cal}$ vs. $u_{\,2010\_cal} - r_{\,2010\_cal}$ diagram. The resulting calibration equation is (see Venuti et al. 2014):

$$u_{\,lc\_med} - u_{\,2010\_cal} = -0.1343\,(u_{\,2010\_cal} - r_{\,2010\_cal}) - 0.1009 \tag{2.5}$$

2.3 CSI 2264: a synthesis

CFHT observations provide the first tight monitoring of mid-term variability at short wavelengths for a large population of several hundreds of young stars. The photometry is globally accurate up to a few hundredths of a mag, and the relative accuracy rises up to order of mmag for brighter objects.

By combining infrared, optical and UV photometry, we are able to probe the various emission components of the young stellar object (from the inner disk, to the stellar photosphere, to the accretion shocks at the surface of the star), if present; this information is synthetized in the spectral energy distribution (SED) of the object. SEDs are sampled through the definition of colors in a multiwavelength dataset, that is, flux ratios at two different wavelengths or passbands; the values of these indices reflect the properties of the central object as well as the presence of circumstellar material (e.g., the infrared color excess revealing the presence of a disk) and the physics and dynamics of the processes that govern the evolution of the object (e.g., UV color excess in presence of disk accretion).

Figure 2.4 illustrates an example of the variety, wide wavelength and time coverage, precision and cadence of the dataset available on individual objects from the CSI 2264 campaign.

The scientific exploitation of the CSI 2264 project started in early-2012, soon after all observing runs associated with the campaign were completed. In these first three years, a number of new, significant results have already been issued concerning the physics of young stars; a dozen refereed publications were released, and a similar number are currently in preparation.

The exquisite cadence and photometric accuracy provided by space-borne telescopes enabled spectacular progress in our description of time domain behavior of YSOs, on timescales ranging from fractions of hours to several weeks (Cody et al. 2014). If the light curves of disk-free WTTS exhibit predominantly regular, periodic flux variations, which result from geometric modulation by dark surface spots, the panorama associated with CTTS is considerably more varied and complex. As described in Sect. 1.4, earlier studies (e.g., Herbst et al. 1994; Alencar et al. 2010) have divided the variability patterns exhibited by YSOs into three main groups: periodic (spot-

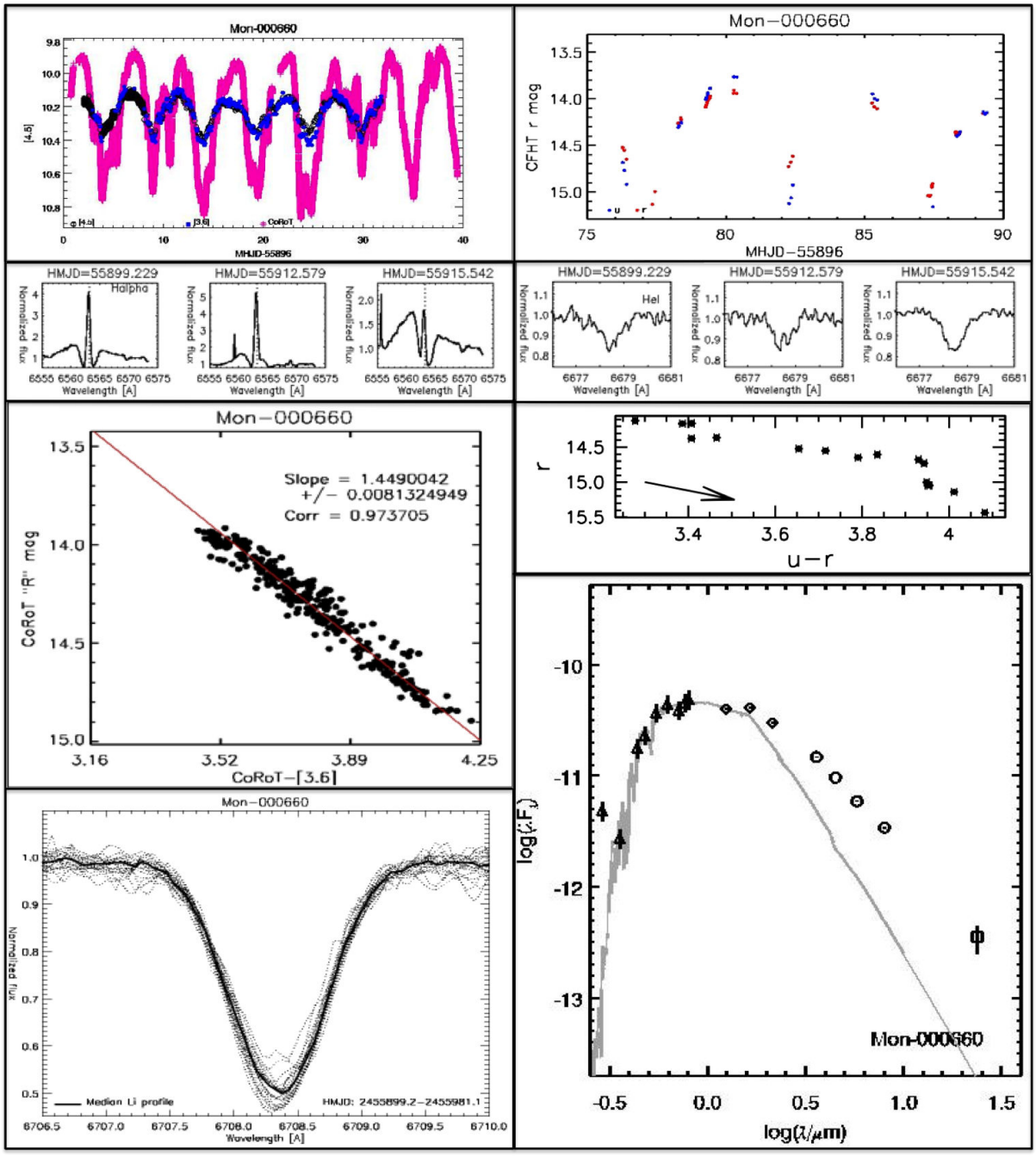

Figure 2.4: An example of the multiwavelength dataset available for young stars from the CSI 2264 campaign. The figure represents CSIMon-000660 (nomenclature from Cody et al. 2014), a K4-type, disk-bearing member of NGC 2264 which displays an AA Tau-like nature (for a detailed analysis of this object, see Fonseca et al. 2014; also, Fonseca et al., in preparation). Panels on the left side of the Figure show, from top to bottom: *CoRoT* (magenta), IRAC 3.6 μm (blue) and IRAC 4.5 μm (black) light curves (all light curves are centered on the mean IRAC 4.5 μm magnitude); three epochs of Hα spectra obtained with FLAMES; *CoRoT* magnitude and corresponding $CoRoT - IRAC\,4.5$ color at each observing epoch; single-epoch (dotted) and median (solid line) Li profiles. Panels on the right side of the Figure show, from top to bottom: MegaCam r (red) and u (blue) light curves (centered on the mean r-band magnitude); three epochs of He I spectra; r vs. $u - r$ color variation trend; SED of the system, reconstructed from CSI 2264 plus literature data (triangles = CFHT photometry; "+" = Johnson/Cousins literature photometry; diamonds = 2MASS photometry; circles = single-epoch IRAC photometry; square = single-epoch MIPS photometry). From http://csi2264.ipac.caltech.edu

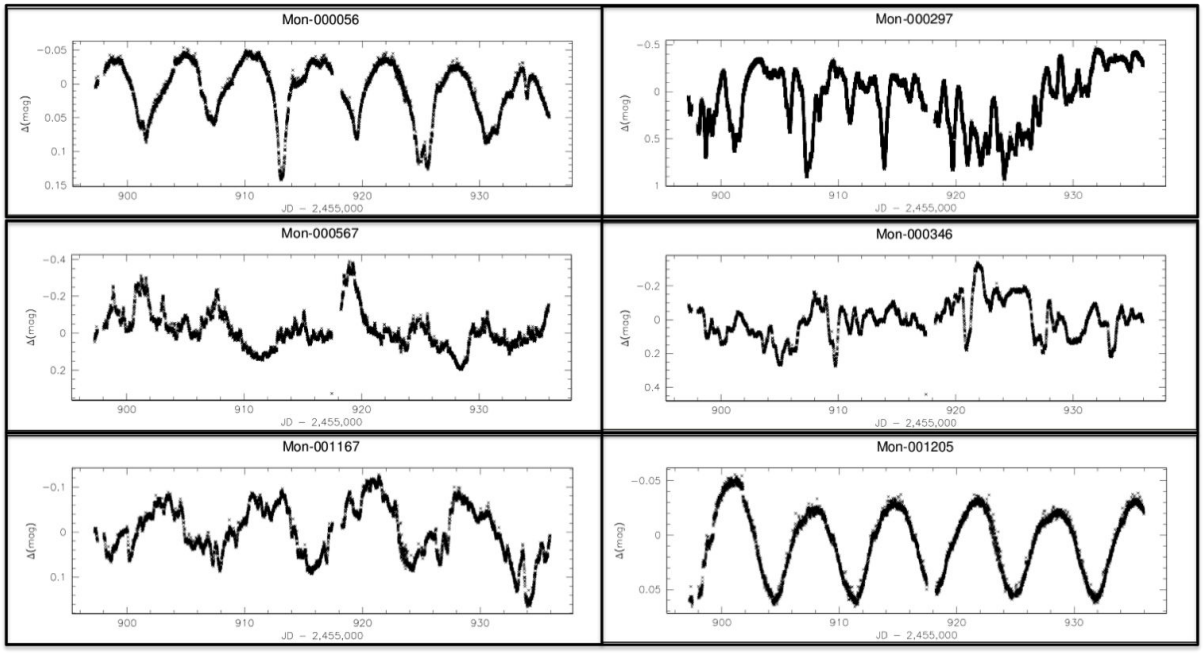

Figure 2.5: Examples of different variability types identified among disk-bearing NGC 2264 members from *CoRoT* time series photometry within the CSI 2264 campaign. Panels show in the order (from left to right, from top to bottom): quasi-periodic dipper; aperiodic dipper; burster; stochastic star; quasi-periodic object; strictly periodic light curve.

dominated); aperiodic (irregular, often reconducted to variable accretion luminosity); and flat-topped with large flux dips, which in some cases occur periodically (as for AA Tau; Bouvier et al. 2007a). Based on the new CSI 2264 *Spitzer* and *CoRoT* data, Cody et al. (2014) were able to perform a more systematic census of light curve morphology among CTTS. The authors identified seven light curve morphology classes (see Fig. 2.5 for a few examples), each presumably associated with different physical processes and/or geometric effects. These comprise:

- *quasi-periodic variables*: light curves exhibiting repeating patterns that either change in shape from cycle to cycle or display lower-amplitude stochastic behavior on top of a periodic pattern;

- *dippers*: light curves characterized by transient optical fading events, which may in some cases recur periodically, although with changes in depth and/or shape from one cycle to the next;

- *bursters*: light curve characterized by sudden, rapid (0.1-1 day) rises in flux, followed by decreases on comparable timescales, superimposed on a baseline flux that varies more slowly on a longer term (a few to several days);

- *stochastic behavior*: light curves which exhibit prominent brightness changes, either fading or brightening, on a variety of timescales;

- *strictly periodic*: spotted-like light curves, where the flux variations recur on a definite pattern with no appreciable morphological changes from one cycle to the other;

- *long timescale behavior*: light curves which exhibit variability that grows or declines systematically all along the monitored time interval.

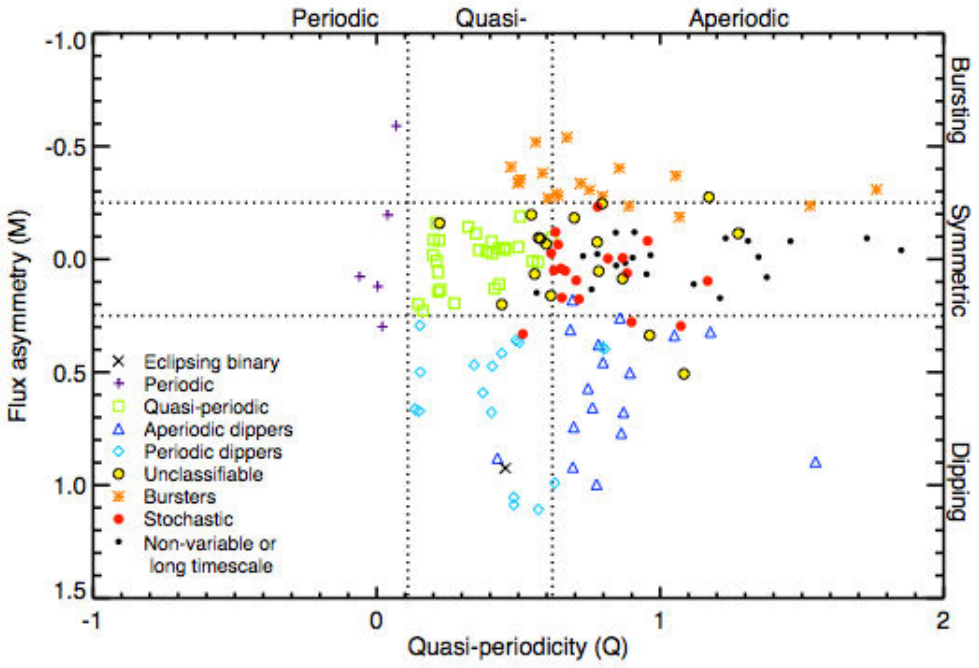

Figure 2.6: Light curve morphology classes, as divided by the quasi-periodicity (Q) and flux asymmetry (M) parameters for optical light curves obtained with *CoRoT* in the disk-bearing sample of NGC 2264 members. Color coding indicates the variability classification chosen by eye, before statistical assessment. Adapted from Cody et al. (2014).

This variability classification scheme was first developed by visual scanning of the full light curve set. The extent and accuracy of the *CoRoT* sample then enabled the authors to define a quantitative metrics to sort light curves automatically. The metrics is based on two parameters: Q, or quasi-periodicity, which assesses the degree of periodicity in the light curve pattern; and M, which measures the degree of asymmetry in the light curve (i.e., whether the typical luminosity state is closer to the bright mag end, or to the faint mag end, or is roughly equidistant from the upper and lower edges of the mag range). As illustrated in Fig. 2.6, the adoption of the Q-M metrics enables to quantitatively retrieve the different morphology classes sorted upon visual examination of the light curves. This metrics hence provides an efficient statistical tool for light curve classification.

Among the newly identified types of YSO variables, the class of *stochastic accretion bursters* (Stauffer et al. 2014) is especially noteworthy. This comprises about 25 cluster members, and provides the first observational evidence for young stars whose accretion occurs in an unstable regime, dominated by Rayleigh-Taylor instabilities at the disk-magnetosphere interface. This mechanism, predicted by magnetohydrodynamical models (Kulkarni & Romanova 2008), causes the disk matter to accrete onto the star in the form of tongues which penetrate equatorially between the magnetic field lines, eventually turning into small-scale funnel flows following the field lines in the proximity of the star. Contrary to stable funnel-flow accretion, where the disk matter accretes onto the star close to the magnetic poles, such instability-driven tongues of matter impact the stellar surface much closer to the equator. A few tongues at a time can develop and reach the stellar surface; each of them produces a hot spot at the impact with the stellar surface, and they evolve rapidly on the inner disk dynamical timescale. As a result, light curves of objects dominated by this unstable accretion mechanism display short-lived flux bursts

that follow each other in a chaotic pattern.

In spite of the detailed theoretical characterization, the moderate amplitudes predicted for the accretion bursts (typically in the range of ∼5–10% of the quiescent value) and the short lifetimes (∼1 day) severely hamper their identification from ground-based campaigns beyond a general assessment of their irregular behavior. The CSI 2264 campaign was the first to possess the precision, cadence and duration required to unambiguously identify those mechanisms, and a suitable wavelength coverage to explore and confirm their nature. Light curves belonging to this variability type in our sample were first selected by eye; subsequent analysis of their UV excesses from the MegaCam data (Venuti et al. 2014) proved that these objects are among the strongest accretors in the region. This is well consistent with the theoretical prediction for the Rayleigh-Taylor instabilities to be associated with high accretion rates (Kulkarni & Romanova 2008).

The class of *dippers* represents a significant fraction (over 20%) of the CTTS population in the cluster. These objects present extinction events due to partial eclipsing of the stellar surface by circumstellar material. About half of them, described in detail in McGinnis et al. (2015), qualify as AA Tau analogs, that is, they display a definite periodicity in the occurrence of the flux dips, although these vary in shape and/or amplitude from cycle to cycle. Dips are often irregularly shaped and may exhibit substructures in the minima; in some cases, they can disappear from the light curve for one cycle, and reappear in the following one. This kind of variability is interpreted as arising from periodic occultations of part of the stellar surface by an inner disk warp (Bouvier et al. 2007a); this is located at or near the disk co-rotation radius and is spatially associated with the accretion columns resulting from the interaction between an inclined magnetosphere and the inner disk.

A second group of dippers detected in our sample of stars includes objects which show no obvious periodicity in the extinction events (McGinnis et al. 2015). A possible interpretation of this different behavior from AA Tau-like stars lies in different accretion scenarios for the two groups of objects, unstable in the first case, stable funnel-flow-like in the second case. McGinnis et al. also show that a star may undergo a transition from the periodic AA Tau-like behavior to the aperiodic variable extinction model, or vice versa, on a timescales of a few years or less.

A third, newly identified morphologic group among light curves associated with variable extinction events is that of short-duration, periodic dippers (Stauffer et al. 2015). Nine objects in the sample of CTTS are assigned to this new class. These differ from the AA Tau analogs in the properties of the dips, which are relatively narrow, shallower than in the AA Tau-like light curves and nearly Gaussian-shaped. Such dips may be superposed either or a relatively flat continuum, or on sine-wave light variations, presumably linked with other physical mechanisms. Periods for the extinction events fall in the range 3–11 days, consistent with dust near the Keplerian co-rotation period. The light curve properties for these objects are interpreted in terms of clumps of material located in or near the inner disk wall; these may be determined by either a disk warp due to interaction with the stellar magnetic field, or by dust entrained in funnel-flow accretion columns which arise close to the inner disk wall. These clumps of material pass through the line of sight to the star at certain rotational phases, hence producing the observed flux dips.

The variety in light curve morphologies identified among CTTS is likely associated with as many different accretion regimes. Accretion rate ($\dot{M}_{acc}$) measurements inferred from the UV excess diagnostics (Venuti et al. 2014) or from the Hα EW (Sousa et al. 2015) show that accretion bursters consistently exhibit the largest accretion rates across the sample; dippers are found to be associated with somewhat lower though conspicuous accretion regimes, and spot-like systems tend to distribute at more moderate values of $\dot{M}_{acc}$ as well (see Fig. 3.13 in Chapter 3 of this manuscript). Comparison of the UV excess measurements with the α_{IRAC} index (which

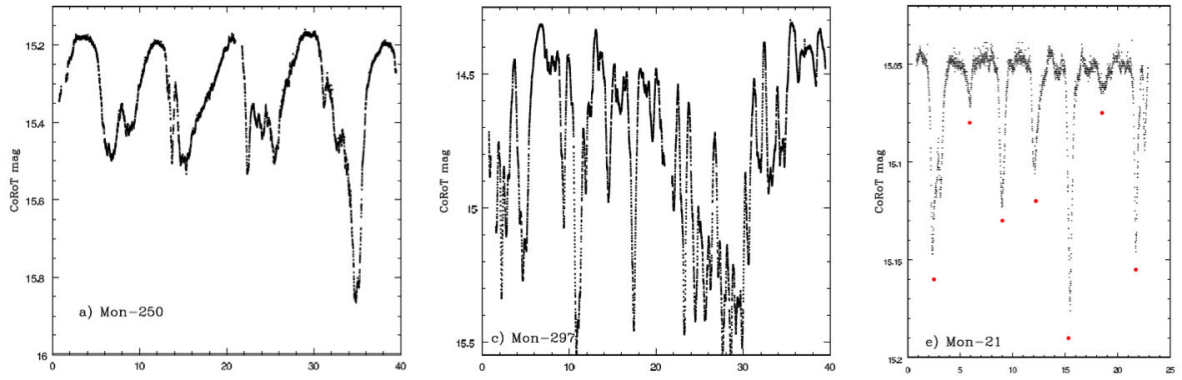

Figure 2.7: Illustration of the three different types of dipper-like light curves identified: AA Tau analog (left panel), aperiodic variable extinction object (middle panel), and narrow-dip object (right panel).

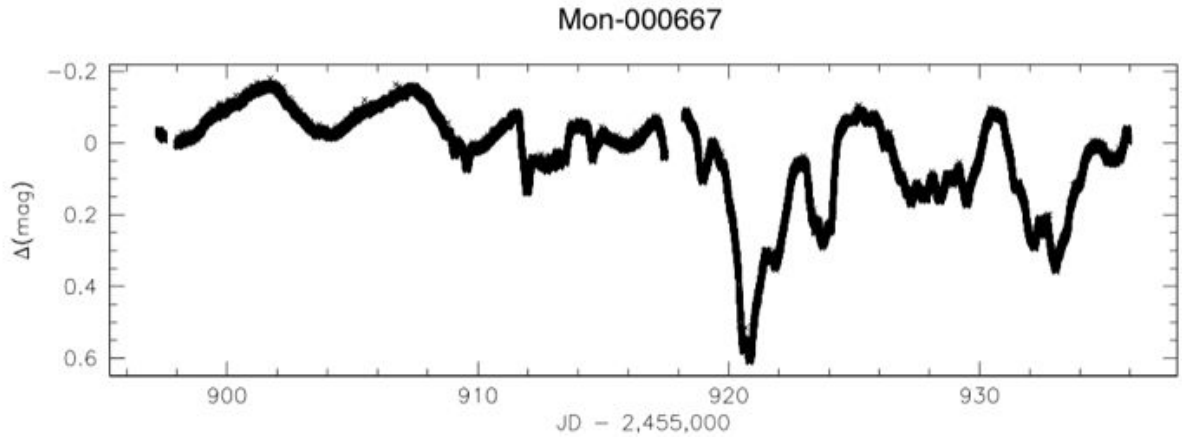

Figure 2.8: *CoRoT* for CSIMon-000667, an object that appears to transit from a periodic, spot-like light curve to a dipper-like light curve, at the same periodicity, on a timescale of a few rotational cycles.

is defined as the slope of the SED between 3.6 μm and 8 μm; Lada et al. 2006; Teixeira et al. 2012) shows that accretion and disk evolution are intimately related, with the strongest accretors having the dustiest inner disks. Analyses of the Hα line profile time variability (Sousa et al. 2015) suggest that light curves with periodic behavior may be associated with stable accretion regimes, whereas unstable accretion may dominate in the case of aperiodic, irregular light curves. Transitions from one state to the other on a timescale of a few years is not uncommon (as discussed by Sousa et al. 2015 and McGinnis et al. 2015, based on a subsample of objects, from the CSI 2264 *CoRoT* run, that were already observed in the 2008 NGC 2264 *CoRoT* run and are reported in Alencar et al. 2010). Such transitions may occur even on much shorter (weeks) timescales, as documented for at least one object (Fig. 2.8) included in our 2011 campaign.

2.4 Specific contribution from this thesis

As discussed in the Introduction, the UV excess diagnostics is one of the most direct probes of the accretion rate onto the star. CFHT observations of NGC 2264 have provided a first extensive mapping of a whole young cluster at short wavelengths, and homogeneous variability monitoring of its several hundred members on timescales from hours to a couple of weeks. The analysis of this dataset represented the core of my thesis work, reported here.

The first part of the study was devoted to explore the census of the cluster at short wave-

lengths, characterize the UV color excess as a diagnostics of accretion, and use it to derive a global picture of accretion properties across the region and to investigate the variability of the accretion process. This analysis was aimed at addressing four main points: i) what is the dependence of the mass accretion rate on stellar parameters such as mass and evolutionary age? ii) what is the origin of the dispersion in accretion rates at a given stellar mass? iii) how variable are mass accretion rates on timescales relevant to stellar rotation? iv) of the observed variability, what fraction is intrinsic and what fraction is due to geometric modulation effects? Results from this analysis were published in Venuti et al. (2014) and are reported in detail in Chapter 3 of the present manuscript.

The second part of the study was focused on exploring the diversity of photometric variability behaviors among accreting and non-accreting cluster members. I used various indicators to statistically map the levels of variability associated with CTTS and WTTS in the region, and analyzed their photometric amplitudes and color variations to investigate the nature and properties of the dominant variability features in each group, notably in a spot-modulated description of stellar variability. I then examined the different amounts of variability detected in the UV on various timescales (hours, days, years) to probe the dynamics and time variability of the accretion process in CTTS. Results from this part of the analysis were published in Venuti et al. (2015) and are described and discussed in Chapter 4 of this thesis.

In the third part of my work, I investigated the connection between the accretion process and the rotation properties for young stars. I analyzed the set of light curves obtained with the *CoRoT* satellite to measure the photometric periods of CTTS and WTTS in the sample and derive the period distribution across the cluster. I examined its properties with reference to the CTTS or WTTS status of cluster members, in order to assess the difference in rotation properties between the two groups and evaluate its significance. I then compared these results with information on the UV excess of the sources, in the disk-locking scenario. This part of the analysis is reported in Chapter 5 of the thesis; a publication encompassing these aspects (Venuti et al. 2015b) is currently in preparation.

Chapter 3

Mapping the different accretion regimes in NGC 2264

Contents

In this chapter, I derive and examine a statistical picture of the properties of accretion in the NGC 2264 cluster. I use the diagnostics of the UV excess, characterized on the colors of non-accreting cluster members, to determine an estimate of the average mass accretion rate for individual CTTS in the region, and measure its variability on day timescales. I thus obtain a map of the diverse accretion properties across the cluster and its hundreds of disk-bearing members. I investigate the statistical dependence of the average accretion rate on stellar parameters like mass

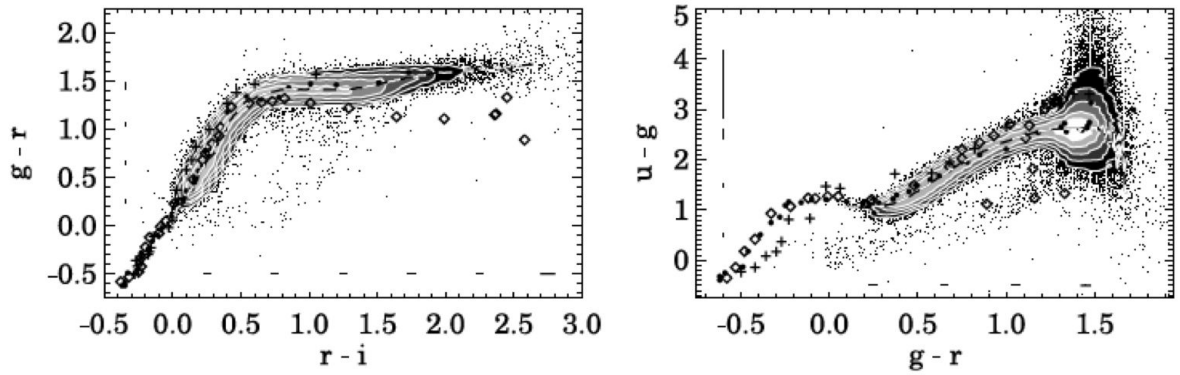

Figure 3.1: Color loci of point sources in the SDSS sample on the $(g-r,\ u-g)$ and $(r-i,\ g-r)$ diagrams (from Covey et al. 2007). Small black dots correspond to individual sources; contours show source density, starting from 10 000 objects per square magnitude and increasing by a factor of 3 between contours. The dashed line indicates the location of the median stellar locus.

and age, and explore the diversity in accretion regimes exhibited by young stars in NGC 2264, and a possible connection with an intrinsic evolutionary spread among cluster members. An Appendix to this chapter, consisting of the publication issued from the main results of this part of the work, is included in the manuscript (Appendix B).

3.1 The colors of young stars at short wavelengths

Color indices, or colors, are very informative regarding the nature of the observed young stellar systems. Optical colors provide indications on the photospheric temperature, hence spectral type, of the object; bright UV colors may indicate the presence of hot, overluminous regions on top of the stellar surface; IR colors enable investigation of the dusty circumstellar environment. Contrary to apparent magnitudes, colors do not depend on the distance to the objects; these can then be more immediately compared to characterize the physical properties of different stellar groups, with the caveat that a displacement toward redder colors on a color-color diagram may be caused by interstellar and/or circumstellar extinction.

3.1.1 The color loci of field stars in the SDSS system

In order to investigate the photometric properties of young stars, it is of interest to define the photospheric color properties expected for main-sequence (MS) stars.

Covey et al. (2007) analyzed a sample of over 300 000 little extincted ($A_r < 0.2$) point sources, detected during the earliest stages of the SDSS survey, to map the dwarf color loci in *ugri* filters (Fig. 3.1). They calculated synthetic colors using spectral standards from the compilation of Pickles (1998) and derived an empirical scale of SDSS colors as a function of spectral type. An independent scale was proposed by Kraus & Hillenbrand (2007); this is derived by assembling a set of empirical SED models for members of the open cluster Praesepe and then fitting those models to derive a scale of colors and absolute magnitudes as a function of spectral type.

In Fig. 3.2, we compare the color distribution of point sources detected in the MegaCam field with the reference color sequences for solar-metallicity dwarfs compiled by Covey et al. (2007) and Kraus & Hillenbrand (2007). The color loci defined by the bulk of field stars are found to match closely those defined in Covey et al. (2007), illustrated in Fig. 3.1.

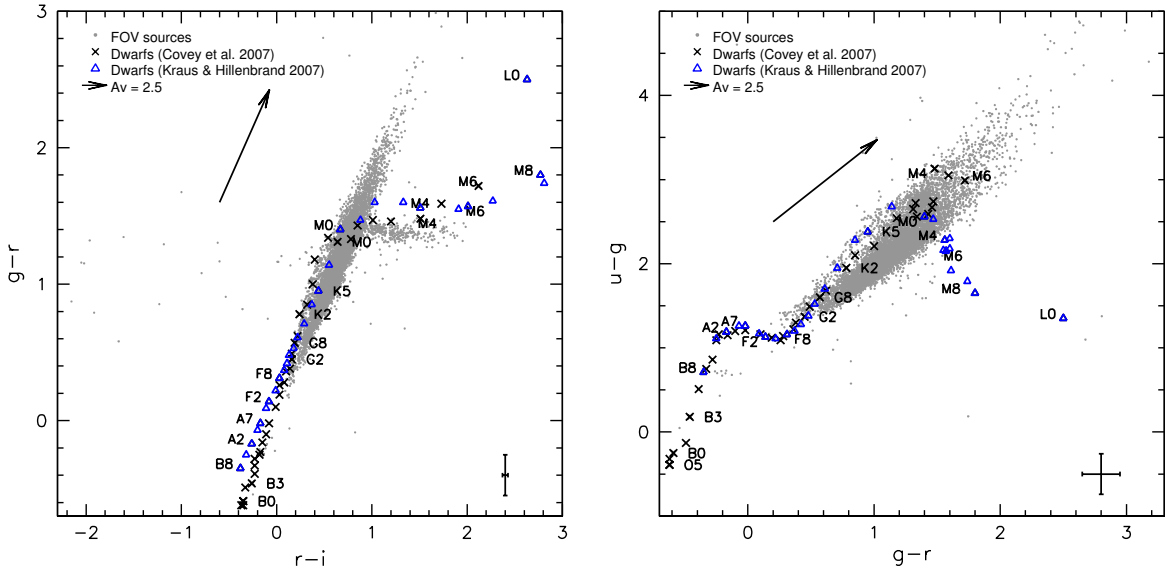

Figure 3.2: $g-r$ vs. $r-i$ (left) and $u-g$ vs. $g-r$ (right) color-color diagrams for objects monitored at CFHT. Empirical dwarf color sequences from Covey et al. (2007) and Kraus & Hillenbrand (2007) are shown as black crosses and blue triangles, respectively. The reddening vector is traced based on the reddening parameters in the SDSS system provided by the Asiago Database on Photometric Systems (ADPS; Fiorucci & Munari 2003). Typical $\pm 3\sigma$ photometric uncertainties are indicated in the bottom right corner.

In Fig. 3.2a, earlier-type field stars are located along the diagonal ellipse: foreground or slightly reddened objects define the lower (bluer) part of the distribution, while more extincted objects and background stars trace the continuation[1] of the distribution, along the direction of the reddening vector, above the horizontal branch at $g-r \sim 1.4$. M-type stars are predominantly located on the horizontal branch at a constant $g-r$ of about 1.4; this property is due to the strong TiO bands present in their spectra (Finlator et al. 2000). Their $r-i$ color, on the other hand, varies strongly with spectral subclass.

Similarly, a progression of increasing spectral types and reddening effects can be observed from left to right along the ellipse in Fig. 3.2b; M-type stars are expected to concentrate along the vertical slice centered on $g-r \sim 1.4$ (as indicated by the empirical color – spectral type sequences overplotted to the data point distribution), while reddened early to K-type stars populate the right end of the elliptical distribution.

An offset of a few tenths of a mag is observed between the mean locus of field stars in our survey and the sequences of Covey et al. (2007) and Kraus & Hillenbrand (2007). This offset cannot be explained with imprecisions in our calibration. A possible reason for this discrepancy may lie in a metallicity lower than solar standards for the bulk of field stars probed here. Several studies have determined a negative metallicity gradient from the center to the outer regions of the Galaxy disk (Δ[Fe/H]/ΔR $\simeq -0.07$ dex/kpc; e.g., Bergemann et al. 2014). Metal-poorer stars are less affected from the line-blanketing effect, and this translates to bluer $u-g$ colors (Covey et al. 2007; Ivezić et al. 2008).

Two interesting loci of color outliers relative to the main point distribution can be identified

[1]This upper part of the distribution, nearly parallel to the reddening vector, at $g-r > 1.5$ is not observed on the left panel of Fig. 3.1 due to the strict constraints on A_r adopted in Covey et al.'s (2007) study for the selection of the stellar sample.

on Fig. 3.2.

The first includes the tens of objects located to the left (i.e., blueward) of the standard locus in $r-i$ on Fig. 3.2a. For all these objects, I checked the position and properties (radial profile plot, contour plot) of the corresponding point source on the field images using the Image Reduction and Analysis Facility (IRAF) tool (Tody 1993). While, for a few of these sources, the anomalous value of $r-i$ may reflect issues in the photometry extraction (such as bad pixels in the aperture, source falling partly onto CCD gaps, mildly saturated source, or presence of two blended sources), this does not apply to the majority of them. The most likely explanation for these objects is that they are highly variable, and the inferred $r-i$ color is spurious due to the large epoch difference between the r-band and i-band photometry (over one year elapsed between the ugr and the i-band mappings of the region, as discussed in Sect. 2.2.2 and reported in Table 2.2). Main-sequence field stars are not expected to vary significantly from one observing epoch to the other, beyond the characteristic photometric noise; therefore it is plausible to assume that this region of the diagram may be primarily populated by young cluster members. If the spurious colors are due to combining uncorrelated r- and i-band measurements for strongly variable sources, we would expect to observe a similar phenomenon to the right of the main body of the distribution as well. Indeed, some color outliers can be located below the horizontal branch on the diagram; it should be noted that the horizontal color branch itself could mask some of these cases on the right side of the diagram.

The second interesting locus is defined by the point dispersion at $0.5 \leq g-r \leq 2.0$, below the main body of the color distribution, on Fig. 3.2b. Objects located in this region of the diagram display $u-g$ color excesses (i.e., bluer colors) with respect to the bulk of field stars. These color excesses are presumably linked with the YSO accretion activity, manifest at UV wavelengths with a flux excess compared to the photospheric emission.

3.1.2 Colors and UV excess of young stars

The photometric properties observed for MS stars on the SDSS diagrams provide guidance for exploring the color signatures of young stars. I then selected all known young cluster members in the CFHT NGC 2264 catalog, sorted them according to their WTTS (no evidence of disk) or CTTS (disk-accreting) status, and overplotted them to the color diagrams on Fig. 3.2.

To identify cluster members amidst the population of the region, we used a wide collection of photometric/spectroscopic data available in the literature from various surveys of the cluster (see Cody et al. 2014). We selected objects that satisfied one or more of the following criteria: i) Hα emission from narrow-band photometry and variability from the data of Lamm et al. (2004) and following their criteria; ii) X-ray detection (Ramírez et al. 2004; Flaccomio et al. 2006) and photometric data consistent with the cluster locus on the (I, R-I) diagram (see Flaccomio et al. 2006) when R,I photometry is available; iii) Hα emission from spectroscopy (Hα EW $>$ 10 Å[2], Hα width at 10% intensity $>$ 270 km s^{-1}); iv) radial velocity member according to Fűrész et al. (2006); v) member according to Sung et al. (2008) (cf. criteria enumerated earlier) and Sung et al. (2009) (classification as Class I, Class II, or flat SED based on the mid-infrared excess from *Spitzer*/IRAC observations)[3].

This first selection allowed us to retrieve a sample of around 700 known cluster members from the CFHT source catalog, using a radius of 1 arcsec to match literature objects with their

[2]This is the threshold commonly adopted for the Hα EW as an accretion diagnostics (Herbig & Bell 1988), although White & Basri (2003) discuss a more robust, spectral type-dependent classification scheme.

[3]The classification scheme is based on the value of the α_{IRAC} indicator, defined in Sect. 2.3. Following Teixeira et al. (2012), Class I sources have $\alpha_{IRAC} \geq 0.5$; flat spectrum sources have $0.5 \geq \alpha_{IRAC} \geq -0.5$; Class II sources (optically thick disks) have $-0.5 \geq \alpha_{IRAC} \geq -1.8$.

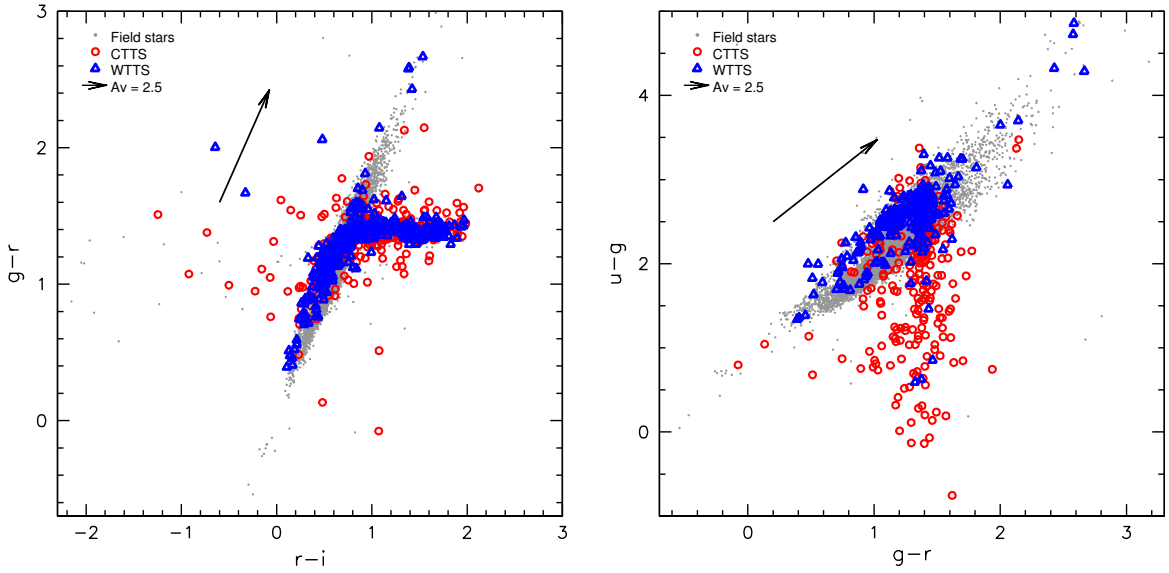

(a) **(b)**

Figure 3.3: $g-r$ vs. $r-i$ (left) and $u-g$ vs. $g-r$ (right) color-color diagrams for NGC 2264 members monitored at CFHT. Field stars, non-accreting cluster members (WTTS) and accreting cluster members (CTTS) are depicted as grey dots, blue triangles and red circles, respectively. The reddening vector is traced based on the reddening parameters reported in the ADPS (Fiorucci & Munari 2003).

CFHT counterpart. About ∼60% of this starting sample of 700 members are classified as WTTS (that is, they do not display any evidence of disk either in the Hα line or in the IR properties).

Optical and UV color properties for cluster members are plotted on top of the reference dwarf color distributions in Fig. 3.3.

WTTS trace a color sequence that nicely overlaps the locus defined by field stars, both in redder (Fig. 3.3a) and in bluer (Fig. 3.3b) filters. The agreement between WTTS and dwarf color distributions in Fig. 3.3a indicates that little foreground extinction affects the photometry of cluster members, with the exception of a few tens of objects distributed along the reddened part of the diagram.

CTTS distribute along the same color sequence as WTTS in redder filters (Fig. 3.3a), albeit with a somewhat larger scatter around the typical spectral type-dependent values. A few CTTS populate the region of the diagram at smaller (bluer) values of $r-i$, to the left of the main color sequence; as discussed in Sect. 3.1.1, their position on the diagram likely reflects multi-year variability, which is evidently more common in the CTTS than the WTTS. Conversely, accreting and non-accreting stars define two clear distinct distributions on the $(g-r,\ u-g)$ diagram in Fig. 3.3b, with the former located at smaller (i.e., bluer) $u-g$ values compared to the main color locus defined by dwarfs.

Similar distinctive features are observed on the $(u-r,\ r)$ color-magnitude diagram of the region, shown in Fig. 3.4. The WTTS population clearly traces the cluster sequence on the diagram, while CTTS appear broadly scattered to the left (smaller, i.e. bluer, $u-r$ values) as a result of their u-band excess, indicative of active accretion activity, compared to WTTS.

Two main conclusions can be drawn from this preliminary analysis of CTTS/WTTS color loci:

1. CTTS and WTTS members do differentiate in the SDSS colors on the basis of photometric accretion signatures at short wavelengths (UV flux excess);

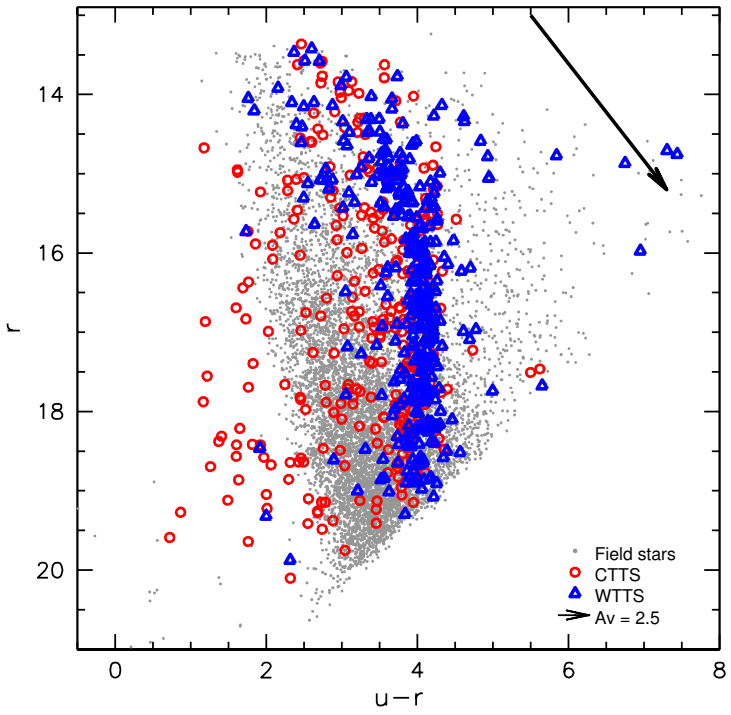

Figure 3.4: $(u-r, r)$ color-magnitude diagram for NGC 2264 members monitored at CFHT. Field stars, WTTS and CTTS are depicted as grey dots, blue triangles and red circles, respectively. The reddening vector is traced based on the reddening parameters reported in the ADPS (Fiorucci & Munari 2003).

2. the UV excess linked with accretion, detected in the u-band, does not affect significantly the observations in filters at longer wavelengths[4], as emphasized by the substantial agreement of the CTTS and WTTS color sequences in Fig. 3.3a and the color saturation at $g-r \sim 1.4$, a behavior common to field stars.

Based on this preliminary exploration of photometric properties at short wavelengths for different groups of stars, we are now in the position to perform a new membership and population study of NGC 2264, from a specifically accretion-driven perspective. This analysis has the twofold purpose of investigating the presence, in the large CFHT FOV, of additional objects that are new CTTS candidate members, and of re-examining the classification of known members. In both cases, the study will rely on the identification and subsequent analysis of color outliers relative to their current classification status.

3.1.3 UV excess vs. different accretion diagnostics

Before using the UV excess indicator to map accretion activity across the cluster population, it is of interest to assess its degree of coherence with other commonly adopted diagnostics of

[4]Some residual color excess in the g-band is observed for a number of CTTS, as evinced in part from Fig. 3.3a; however, colors observed for the majority of CTTS in g, r and i follow closely the photometric properties defined by WTTS, which indicates that the flux excess linked with accretion is primarily detected in the u-band. Another argument in support of this interpretation follows from the UV excess measurement (Sect. 3.4.1): if noticeable flux excess was on average still detected in the g-band, the color excess, $E(u-g)$, measured on the $u-g$ color ought to be systematically smaller (i.e., less negative) than that measured on $u-r$; this, however, is not observed (cf. Fig. 3.12).

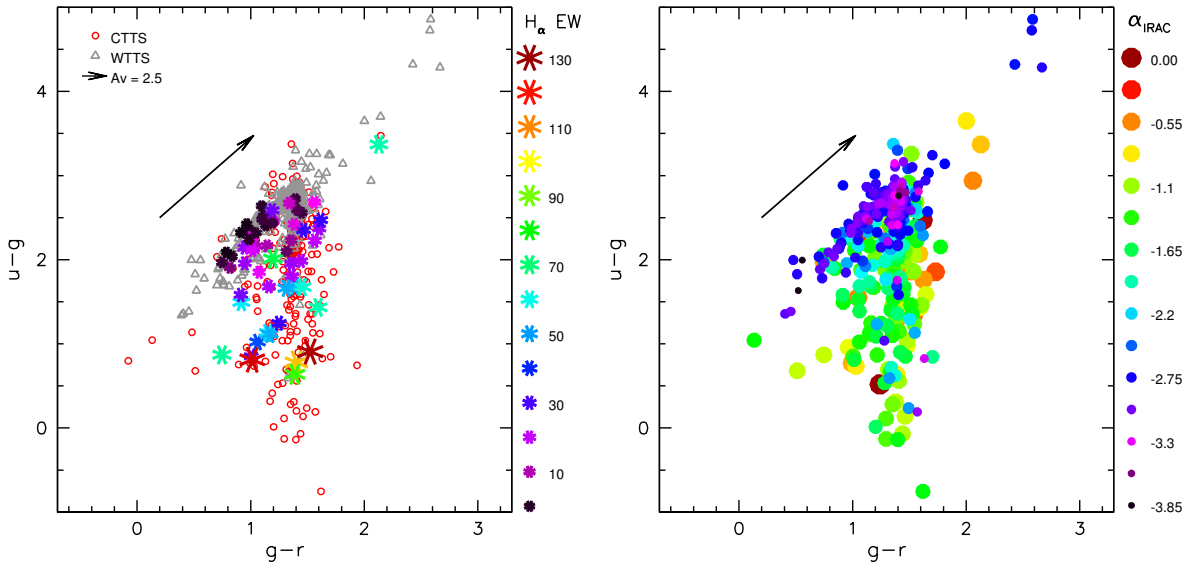

(a) **(b)**

Figure 3.5: UV excess is compared to different accretion diagnostics. In panel (a), information on the $u-g$ and $g-r$ colors for NGC 2264 members are combined with measurements of the Hα EW. Asterisks mark members for which Hα EW is available from the CSI 2264 campaign (see text). Asterisk colors and sizes are scaled according to the value of Hα EW. Panel (b) illustrates a version of the $(g-r,\ u-g)$ diagram of cluster members where colors and sizes of symbols are scaled according to the value of α_{IRAC} from the data of Teixeira et al. (2012).

accretion. This will also enable a more robust definition of the accretion-dominated color regions on the diagrams.

In Fig. 3.5, we compare the color excesses on $u-g$ to the Hα EW (panel (a)) and to the α_{IRAC} (panel (b)) indicators. Values of Hα EW reported in Fig. 3.5a were measured from VLT/FLAMES spectra obtained during the CSI 2264 campaign and are analyzed in Sousa et al. (2015); values of α_{IRAC} reported in Fig. 3.5b were derived in Teixeira et al. (2012).

Both panels in Fig. 3.5 show a good agreement between the UV excess measured on the $(g-r,\ u-g)$ diagram and different accretion/disk indicators. In Fig. 3.5a, small, black or dark purple asterisks (corresponding to objects with Hα EW $<$ 10 Å) are predominantly located on the WTTS color locus, while larger values of Hα EW are more commonly found among objects distributed at bluer $u-g$ colors. Similarly, in Fig. 3.5b, small, purple to ultramarine dots (corresponding to $\alpha_{IRAC} \lesssim$ -2.5, indicative of stars with naked photosphere according to the classification scheme proposed by Teixeira et al. 2012) are predominantly located on the normal $u-g$ color locus, while objects showing a UV excess (and thus actively accreting stars) are typically associated with α_{IRAC} larger than -2 (indicative of thick disk objects).

Hence, although there is inevitably a boundary region on the diagram, close to the lower edge of the WTTS color distribution, where WTTS and CTTS appear mingled in photometric properties, we can clearly define a threshold line, on $u-g$ vs. $g-r$, below which objects exhibit a UV excess and qualify most likely as accreting CTTS.

3.2 A UV census of the NGC 2264 young stellar population

3.2.1 New CTTS candidates in NGC 2264

As discussed in the previous sections, a most interesting locus to identify accreting members is the data point dispersion below the main body of the color distribution in Fig. 3.3b. There, the UV excess displayed by CTTS can be easily detected and measured with respect to the colors of WTTS; these trace the sequence of expected photometric properties, as a function of spectral type, for young stars, in the absence of accretion. As can be noted on the diagram, the reference color sequence defined by WTTS is nearly parallel to the reddening vector for spectral types earlier than ∼M0; therefore, the color excess estimates obtained for these objects will be essentially unaffected by the visual extinction A_V. For later spectral types, the color sequence traced by WTTS turns down, and saturates at $g-r \sim 1.4$ (as best observed on Fig. 3.3a). This implies that any UV excess estimate derived for M-type stars by taking as reference the extrapolation of the WTTS color trend from earlier spectral types will be a systematic overestimate. I address this point in more detail in Sect. 3.4.1.

To minimize contamination from non-accreting and field stars, I traced a straight line, parallel to the reddening vector, which borders the accretion-dominated area below the lower envelope of the dwarf color locus (as illustrated in Fig. 3.6); I then selected as new CTTS candidates all the objects lying in this region and marked as field stars. Before confirming their selection, all these objects were cross-checked on the CFHT field images with IRAF, in order to discard those sources whose flux measurements could be affected by detection issues (e.g., close to the detection limit, presence of a close-by source, partial projection of the source on CCD gaps or bad pixel rows).

A second group of new CTTS candidates was extracted from the diagram in Fig. 3.3a, namely among the color outliers located to the left of the main color distribution and, to a smaller extent, below the horizontal branch. As discussed earlier, the atypical position of these objects on the diagram is likely due to a strong variable nature, which renders the $r-i$ color, obtained by combining two photometric sets acquired at a large epoch difference, spurious. CTTS are the primary suspects in case of conspicuous variability signatures among the stellar population probed here; the assumption that most objects with spurious $r-i$ values are indeed CTTS is corroborated by the many known accreting members of the cluster among the sample of color outliers on the diagram. As done before for CTTS candidates selected based on their UV excess on Fig. 3.3b, all selected objects were photometrically checked on the field images prior to being confirmed in the list of new candidates.

The two diagrams in Figs. 3.3a and 3.3b represent the most important tools used for our analysis of population. A limitation to the candidate extraction performed on the $u-g$ vs. $g-r$ diagram lies in the poor sensitivity to moderate UV excesses in M-type stars, as a result of the color saturation in $g-r$ for this spectral class. To circumvent this effect, we introduced an additional color-color diagram, $u-g$ vs. $r-i$ (see Appendix B). This takes the shape of a "transition" diagram between ($g-r$, $u-g$), where the $u-g$ color excess distinctive of CTTS stands out relative to the main WTTS color distribution, and ($r-i$, $g-r$), where late-type objects are located on a distinct branch from earlier-type stars and separate well on $r-i$. Therefore, it provides a greater sensitivity to the UV excess for spectral types ≥M0. The analysis of this diagram allowed us to identify a number of additional, late-type CTTS candidates, whose properties were inspected on the *ugri* images of the region to ensure accurate photometry extraction.

At the end of this analysis, 50 new CTTS candidate members were identified on the various diagrams. Most of the new candidates are spatially located on the periphery of the cluster or

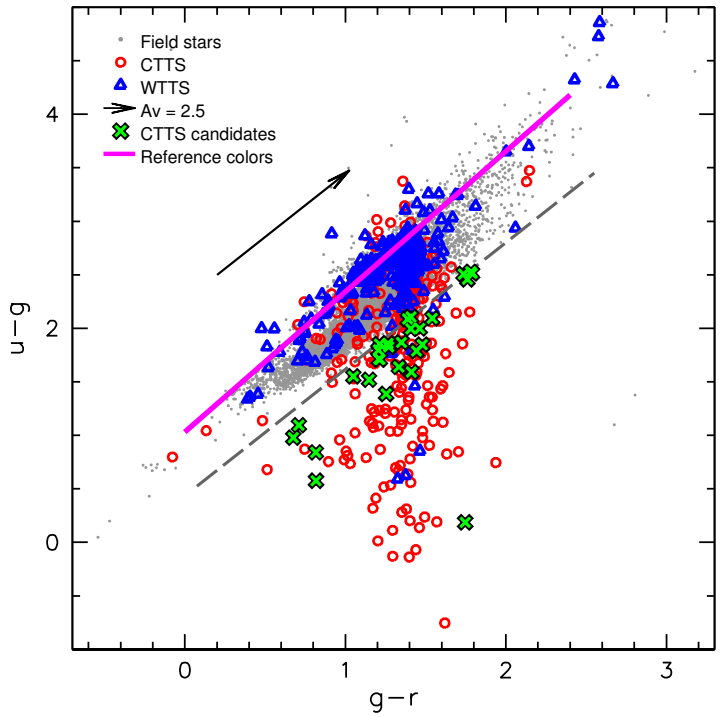

Figure 3.6: Selection of new CTTS candidates from the $(g-r,\ u-g)$ diagram. The grey dashed line traces a conservative boundary separating the accretion-dominated region of the diagram from the color locus of non-accreting stars (see text). Field stars, WTTS and known CTTS are depicted as grey dots, blue triangles and red circles, respectively; the new CTTS candidates selected from this diagram are marked as green crosses. The purple line fitting the upper envelope of the WTTS distribution traces the reference sequence of photospheric colors that has been adopted for measuring the UV excess of accreting stars (see Sect. 3.4.1).

beyond (see Fig. 11 of Venuti et al. 2014 in Appendix B). This provides evidence for a more extended spatial distribution of the PMS population associated with NGC 2264, and attests to the presence of actively accreting members far from the original sites of star formation.

In this first selection of new candidate members, I focused on those objects, labeled as "field stars", which populated the accretion-dominated regions of the color-color diagrams. In fact, another interesting group of "color outliers" can be identified on the same diagram regions, namely the objects, classified as WTTS from information gathered in previous surveys, whose colors fell generally within the UV-bright regions (for example, the small group of blue points located below the normal dwarf locus in Fig. 3.3b). I then explored the photometric properties of these putative WTTS in our several diagrams and selected a group of 19 stars which qualify as CTTS based on their CFHT colors. This re-classification from WTTS to CTTS does not necessarily imply that the previously attributed status was erroneous, but may as well reflect a long-term (∼years) variability in the accretion activity of the objects (see, e.g., Littlefair et al. 2004).

The results of this analysis, with a complete list of newly identified CTTS candidates and of known cluster members whose status varied from WTTS to CTTS, were reported in Table A.1 and Table A.2, respectively, of Venuti et al. (2014) (a full copy of the publication is enclosed to the present manuscript in Appendix B).

This revised census of accreting members we infer for NGC 2264 likely encompasses all

objects with strong UV excess, and hence a significant amount of accretion. However, diagrams in Figs. 3.3b and 3.4 display a non-negligible overlap between the distributions in colors of CTTS and WTTS. This implies that our diagnostics is not as sensitive to the weak accretion regimes. Hence, we do identify some new CTTS, but we might be missing a number of lower accretors, showing a smaller UV excess that cannot be easily separated from the color properties of WTTS or field stars.

3.2.2 Field contaminants in the NGC 2264 sample

The r vs. $u-r$ diagram (Fig. 3.4) has been so far left out of the discussion. A direct search for new candidate members on this color-magnitude diagram would not be feasible, as intrinsic colors and distance-dependent reddening effects combine in a broad distribution of photometric properties for field stars which overlap those observed for known cluster members, accreting and not, across most of the color range of interest. However, once an object is known to be a cluster member from other pieces of information, CTTS and WTTS can be observed to statistically separate on the diagram, with the former located blueward of the sequence defined by the latter. Hence, this diagram provides an additional test bench for investigating the nature of individual objects and color outliers.

As already noted on Fig. 3.3b, we can identify on Fig. 3.4 a group of putative non-accreting members with inferred $u-r$ colors bluer than expected. I investigated the position of these objects on different color-magnitude diagrams (g vs. $u-g$, i vs. $u-i$), and in several cases a bluer than expected nature was confirmed on all of them. Oddly enough, these objects populate the thin lower branch of the WTTS distribution, below the main WTTS locus, on the lower part of the dwarf locus in Fig. 3.3b ($u-g$ vs. $g-r$ diagram). Little spectroscopic information is available for this group of stars; contrary to what is expected for stars with noticeable accretion, the level of variability detected for many of these objects during our monitoring does not exceed the photometric noise sequence, defined, as a function of magnitude, by field stars in our survey (see Venuti et al. 2015, also in Appendix C, and Chapter 4 of this manuscript). In addition, several of these putative members would be located close to or onto the MS-turnoff (or below) in the HR diagram of the region (Fig. 3.11). We therefore suspect at least a part of these objects to possibly be misclassified young dwarfs instead (see, e.g., Smith et al. 2014 for a recent study proposing that strong active chromospheres in young dwarfs may determine bluer than expected colors for these objects). A list of objects with questioned membership, of the relevant CFHT photometry and of the original selection criteria is reported in Table A.3 of Venuti et al. (2014) (see Appendix B).

Another interesting group of objects in Fig. 3.4 is the sample of WTTS displaced redward of the main cluster sequence. Most of these objects appear significantly reddened through all CFHT photometric diagrams; in several cases, they display little variability. While contamination by field stars might be partly reflected in the observed properties, most of the objects in this stellar group would actually look like very young, or equivalently overluminous, objects on the HR diagram of the region (i.e., they are located on the upper right envelope of the data point distribution in Fig. 3.11). This would rather suggest binarity and/or earlier (i.e., more embedded) evolutionary status as possible explications of the distinctive properties of these objects.

3.3 Derivation of individual stellar parameters

The final sample of PMS stars in NGC 2264 from the CFHT survey amounts to 757 objects, inclusive of the already known members retrieved on MegaCam images and of the new CTTS candidates identified from CFHT data (Sect. 3.2). This is the final ensemble of objects explored

for the study presented in this thesis.

Part of these objects were included in previous studies of NGC 2264, and individual estimates of parameters such as reddening, stellar mass and radius exist for them in the literature. However, this collected information is necessarily not homogeneous in source or method, and may result in biases or inconsistencies when analyzing the complete sample. In order to obtain a set of internally consistently derived stellar parameters, I performed an extensive investigation of individual stellar properties across the whole sample of objects, using multiband photometry obtained during our campaign as well as literature data at different wavelengths.

The following subsections detail the procedure adopted to this purpose; the resulting compilation of calibrated CFHT photometry and stellar parameters (spectral type, extinction, bolometric luminosity, mass, radius) for the 757 objects in our sample was provided to the astronomic community as a set of two tables appended to Venuti et al. (2014).

3.3.1 Individual A_V estimates

A direct estimate of individual A_V for late-type (M-type) stars was derived from the color properties displayed on the $g-r$ vs. $r-i$ diagram (Fig. 3.3a). There, as discussed before, M-type stars distribute on a narrow sequence at a constant $g-r$ value of about 1.4, which departs from the color locus defined by earlier-type stars and is nearly perpendicular to the reddening vector. The lower envelope of field stars on the branch defines the zero-reddening color locus for M-type stars; an estimate of A_V for these objects can then be derived by measuring the distance, along the reddening direction, between their actual position on the diagram and the zero-reddening locus, as illustrated in Fig. 3.7a. This procedure has the advantage of relying solely on observed quantities, without involving the comparison with an external reference sequence that would intrinsically introduce an additional source of uncertainty on the result.

This technique cannot be applied to objects which, for a given reason[5], are located below the lower envelope of the horizontal branch; no direct estimate of A_V can be derived for them on this diagram. Similarly, a direct A_V measurement for earlier-type stars on this diagram is prevented by the fact that they define a color sequence nearly parallel to the reddening direction; nevertheless, this diagram can still provide useful indications on these objects to check the consistency of A_V values derived from different data and discard largely off estimates[6].

I derived an independent estimate of individual A_V across our sample by exploring the color properties of the objects on a J-H vs. H-K diagram (Fig. 3.7b). Photometry in the J,H,K_S bands is available for most objects in our sample from the 2 Micron All Sky Survey (2MASS; Skrutskie et al. 2006). In this case, two external sequences were used to define the reference color loci for A_V measurements. I adopted the dwarf color sequence in JHK$_S$ filters compiled in Covey et al. (2007) as the reference for photospheric colors for WTTS, while for CTTS I compared the observed colors with the infrared locus defined in Meyer et al. (1997) in the standard CIT system (Elias et al. 1982) and transformed onto the 2MASS photometric system as in Covey et al. (2010)[7]. The procedure for measuring A_V relative to these reference color sequences is then similar to the one adopted on the $g-r$ vs. $r-i$ diagram and is illustrated in Fig. 3.7b.

[5]These might be M-type objects with residual color excess on $g-r$, or strongly variable objects with spurious $r-i$ colors due to the large epoch difference between r-band and i-band observations.

[6]For instance, for the WTTS located on the reddened color locus, at approximately the same $g-r$ as the object circled in green, it is not possible to establish from this diagram whether its A_V amounts to 2 or 3 magnitudes (unless prior knowledge of its spectral type is available), but we can affirm that it falls in the group of the most extincted objects probed in our study.

[7]The actual equations for the Meyer et al.'s 1997 locus in the 2MASS system, derived for the study of Covey et al. (2010), were kindly made available to us by Kevin Covey and are the following:
H-K$_S$ = 0.2+x*0.1, x = {0, 1, ..., 9};
J-H = 0.58*(H-K$_S$)+0.52

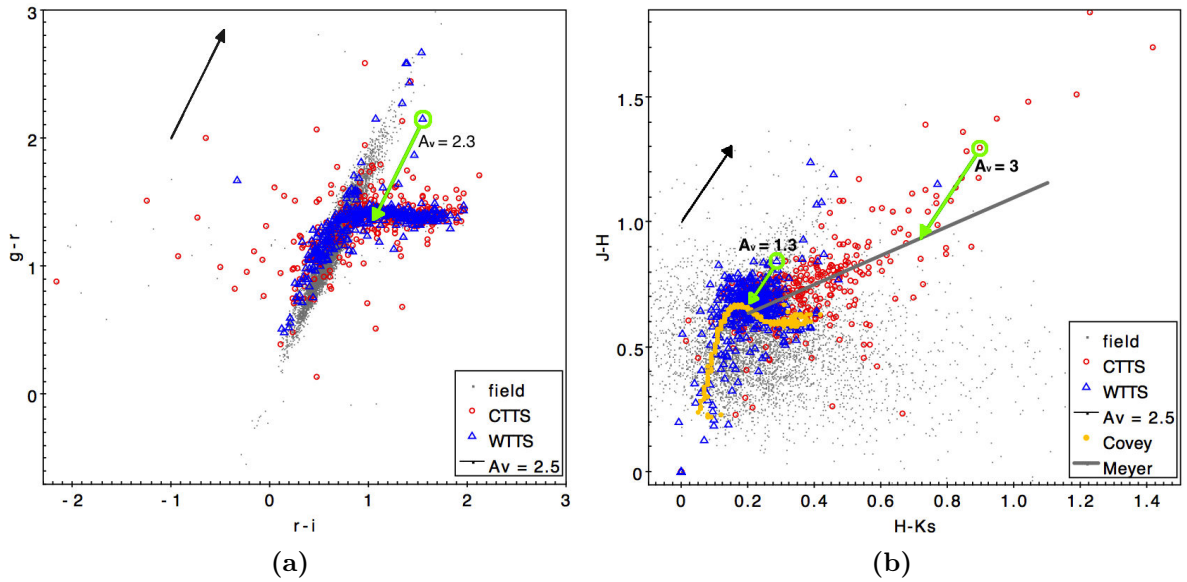

Figure 3.7: Illustration of the procedure adopted to derive an A_V estimate for individual objects based on their position of the $g-r$ vs. $r-i$ diagram (panel (a)) or on the J-H vs. H-K_S diagram (panel (b)). In the first case (panel(a)), a direct measurement of A_V is possible only for M-type stars, which are photometrically located on the horizontal branch at nearly constant $g-r$, almost perpendicular to the reddening vector. The lower edge of the branch defines the zero-reddening color sequence for M-type stars. Each object located at larger $g-r$ colors is displaced blueward parallel to the reddening vector until it reaches the lowermost envelope of the dwarf distribution on the branch, as illustrated by the green arrow on the diagram. The corresponding amount of reddening is then measured and extracted as an A_V estimate. A similar procedure is adopted in the near-infrared (panel (b)), but the reference color sequences are traced by the locus defined in Meyer et al. (1997) for CTTS and by the compilation of dwarf colors extracted from Covey et al. (2007) for WTTS.

Additional A_V estimates for a part of these sources are available from previous optical studies or literature data. Rebull et al. (2002) provide A_V for about 90 sources in our sample; individual extinction is investigated by measuring the color excess on R-I relative to the expected colors based on the spectral type of the objects. B,V,R,I photometry, collected from earlier surveys, is available for a broader sample of cluster members than that investigated in Rebull et al. (2002); we then adopted a similar procedure to derive A_V from color excess measurements on (in order of preference) R-I, V-I or B-V. A different method for deriving A_V is implemented in Cauley et al. (2012) for a smaller group of objects (about 30) common to our sample: in this case, an estimate of A_V is obtained by fitting the stellar spectra with spectral templates.

Individual A_V estimates can be fairly uncertain, and values derived for the same objects from different authors/methods can vary by a few to several tenths of a mag. Among the several derivations summarised in the above discussion, the A_V estimates obtained from the $g-r$ vs. $r-i$ diagram, when available, were favored, as this is the only method that involves a simple comparison with photometric properties of objects observed in the same conditions and characterized in a similar fashion as the sample we are interested in.

In the absence of a direct A_V estimate from CFHT photometry, all available A_V derivations were examined and compared, and their consistency with color properties displayed on the CFHT diagrams was checked to discard any possible discrepant estimates. We then averaged the various A_V values retained from the different methods to obtain a final estimate to be associated with the individual object under exam.

To estimate the typical uncertainty on our derived A_V values, we measured the amount of

dispersion between results yielded by different A_V derivation methods for common objects. We found that different A_V estimates for the same objects are typically consistent within a few tenths of a mag. This then provides an order of magnitude for the expected accuracy on the A_V values adopted in this study.

3.3.2 Spectral types and effective temperatures

Spectral type is known from spectroscopy for around 50% of young stars in our sample, and was retrieved, in order of preference, from the studies of Dahm & Simon (2005), Rebull et al. (2002) or Walker (1956).

For the remaining objects, I derived a photometric estimate of spectral type from dereddened colors in CFHT optical bands ($g-r$ and $r-i$). I adopted the empirical spectral type–color scale tabulated in Covey et al. (2007) as a reference to match the observed colors with the corresponding spectral type. As noted on Fig. 3.2, there appears to be a small offset between the reference color sequence and the median locus of stars obtained from CFHT photometry in the NGC 2264 field. To remedy this mismatch, I selected a subsample of WTTS members with known spectral type, earlier than M0, and used their dereddened photometry to recalibrate Covey et al.'s (2007) spectral type–color sequence onto our photometric data. The correction introduced consisted of shifting the sequence by 0.1 mag toward bluer colors on $g-r$.

For each object, the $g-r$ and $r-i$ colors were then compared with the empirical scale, and the appropriate spectral type was selected as the one whose corresponding $g-r$ and $r-i$ in the table provide the closest match to both the observed $g-r$ and $r-i$. In the case where the observed colors fell in the range between two tabulated spectral types, the intermediate class (or subclass) was adopted as a spectral type estimate for the corresponding objects. For some objects, it occurred that the spectral type estimate suggested by the observed $g-r$ did not correspond to the spectral type estimate that would be deduced from the observed $r-i$, but the two would be several subclasses apart. In those cases, the indication from $g-r$ was favored over $r-i$ for earlier-type objects, located below the knee at spectral type $\sim$ K5 in the color distribution on Fig. 3.3a, since different subclasses in this spectral range are better distinguished in $g-r$ than in $r-i$; conversely, the information from $r-i$ was favored in the case of later-type objects, which fall close to or into the region at nearly constant $g-r$ on the diagram.

Spectral types were converted to effective temperatures T_{eff} following the scale of Cohen & Kuhi (1979), built on the results of the eight-color photometric survey of Johnson (1966) for stars earlier than M0 and of Johnson (1965) for M-type stars. In Fig. 3.8, I compare this scale to other spectral type – T_{eff} calibrations available in the literature and often adopted for T Tauri stars.

Kenyon & Hartmann (1995) adopt a spectral type – T_{eff} scale mainly based on the work of Schmidt-Kaler (1982), where, starting from direct interferometric measurements of stellar diameters, scales between spectral types and radii, and then surface brightnesses and spectral types, are obtained by interpolation. This scale, such as Cohen & Kuhi's, is calibrated onto luminosity class V objects. The two scales are in fairly good agreement for early-type stars (differences in T_{eff} for a given spectral type in the two scales amount to $\lesssim 1\%$ of the temperature estimate), while somewhat larger differences, of order $\sim$100 K, are registered between the two scales for later-type (>M1) stars (where T_{eff} estimates in Kenyon & Hartmann 1995 are systematically higher than those tabulated in Cohen & Kuhi 1979).

In their study of the young cluster IC 348, Luhman et al. (2003) develop a new spectral type – T_{eff} conversion scale. This follows Schmidt-Kaler (1982) for spectral types of M0 and earlier, while for later spectral types it revises the scale of Luhman (1999); in the latter, late-type PMS stars are described as having intermediate luminosities between those of dwarfs and giants,

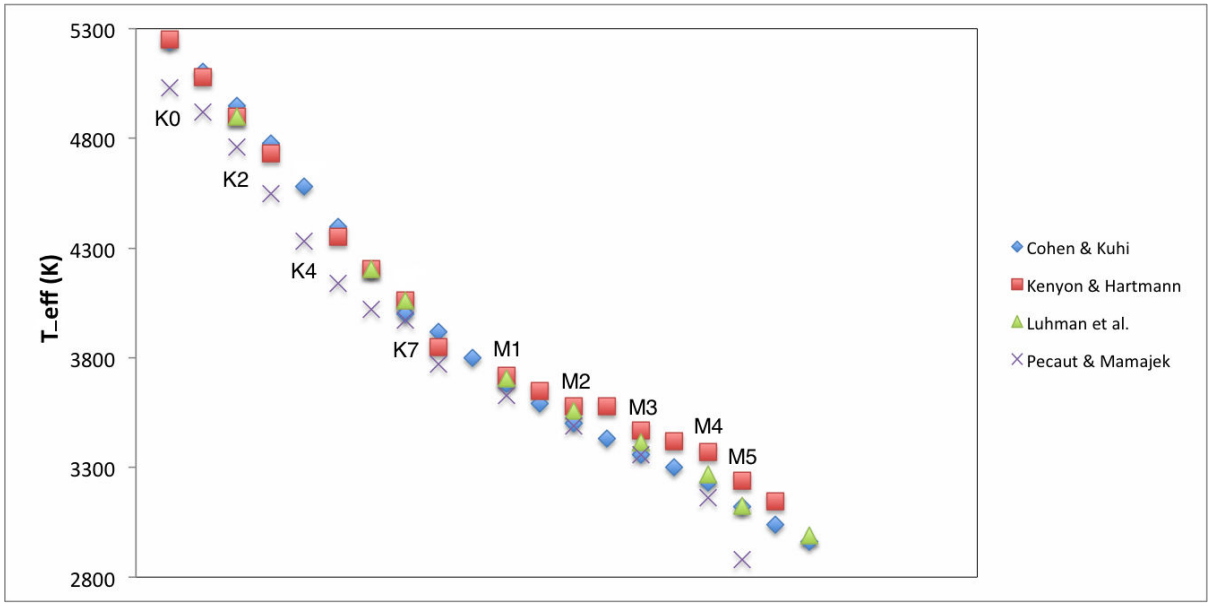

Figure 3.8: Comparison of different spectral type – effective temperature scales adopted in the literature for young stars. For each spectral subclass, ordered along the x-axis from K0 to M6, T_{eff} estimates deduced from four different scales are compared: Cohen & Kuhi (1979, blue diamonds), Kenyon & Hartmann (1995, red squares), Luhman et al. (2003, green triangles), and Pecaut & Mamajek (2013, violet crosses). For M-type stars, temperatures tabulated for intermediate subclasses in some of the considered scales are also shown.

and their T_{eff} scale is obtained by placing these objects on a HR diagram and allowing their temperatures to vary to adjust the sequence to the theoretical isochrones from Baraffe et al.'s (1998) evolutionary models. Luhman et al.'s (2003) scale compares well with those by Cohen & Kuhi (1979) and Kenyon & Hartmann (1995) for early-type stars; for late, M-type stars, it provides T_{eff} estimates which are again close to those in Cohen & Kuhi (1979) (differences are of the order of 1–2%) and lower than those in Kenyon & Hartmann (1995).

Hence, from this comparison we conclude that the scale proposed in Cohen & Kuhi (1979) is about equivalent to combining Kenyon & Hartmann's (1995) scale for spectral types down to M0 and that of Luhman et al. (2003) for later spectral types; I selected the former reference (i.e., Cohen & Kuhi 1979) for this study because it provides a single, uniform and well sampled scale.

More recently, Pecaut & Mamajek (2013) have proposed a new spectral type – T_{eff} scale, specifically calibrated to PMS objects. This is obtained by fitting observed multiband photometry for members of nearby young clusters, associations and moving groups to synthetic spectra from the library of Allard et al.'s (2012) BT-Settl models. As can be observed in Fig. 3.8, this new scale is in fairly good agreement with previous scales in the K7-M4 spectral range, whereas new T_{eff} estimates for early K-type stars and for very late-type ($\gtrsim$M5) stars are significantly lower than those in Cohen & Kuhi (1979) (differences amount to $\sim$200 K, or about 5% of the temperature estimate).

Fig. 3.9 illustrates how predicted colors from the BT-Settl model isochrone at 3 Myr compare to the actual photometric properties observed for NGC 2264 WTTS members on the r vs. $g-r$ (Fig. 3.9a) and on the $g-r$ vs. $r-i$ (Fig. 3.9b) diagrams. On the color-magnitude diagram in Fig. 3.9a, WTTS trace a well-defined cluster sequence. The 3 Myr isochrone from the BT-Settl evolutionary models, brought to a distance of 760 pc and reddened by $A_V = 0.4$ mag (typical A_V measured across the cluster), does not provide a satisfactory fit to the cluster locus, and

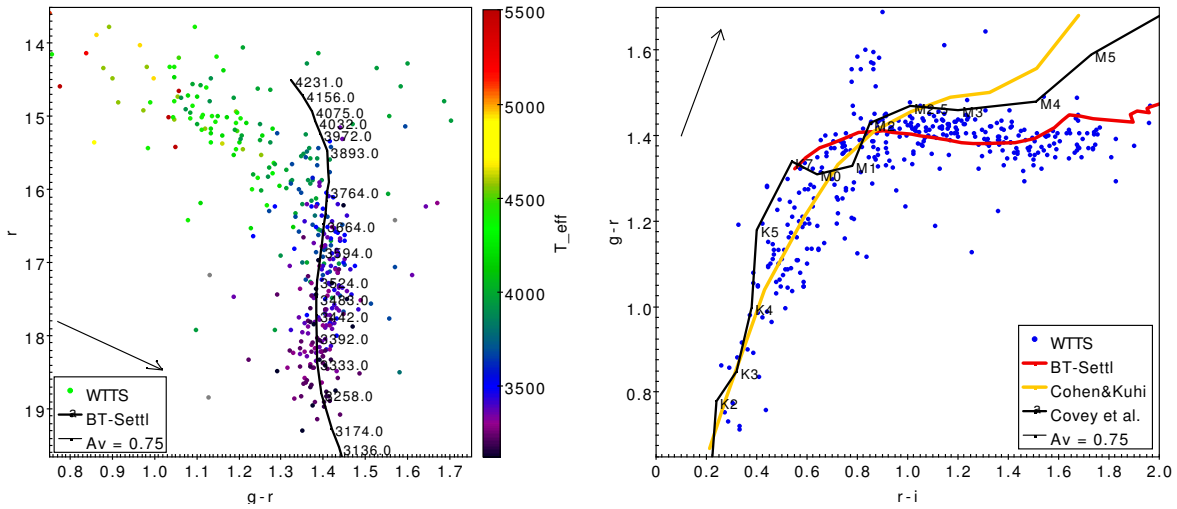

Figure 3.9: Photometric properties observed for WTTS in NGC 2264 are compared to the theoretical predictions deduced from BT-Settl models (Allard et al. 2012), at 3 Myr, in SDSS filters. In panel (a) (r vs. $g-r$ color-magnitude diagram), the model isochrone (solid black line), brought to a distance of 760 pc and assuming a typical A_V of 0.4 mag, is overplotted to the cluster sequence defined by WTTS members (different colors indicate different effective temperatures, following the scale in the side axis). Points along the isochrone are labeled according to model T_{eff}. In panel (b), observed $g-r$ and $r-i$ colors for cluster members (blue dots) are compared to the expected color sequence based on the BT-Settl model (red line). The empirical color sequences from Covey et al. (2007) (black line) and from the tables of Johnson (1965, 1966) (yellow line), on which the spectral type – T_{eff} scale by Cohen & Kuhi (1979) is based, are also shown for comparison purposes. As the original color tables for the compilation of Johnson (1965, 1966) are in the UBVRI photometric system, UBVRI to SDSS transformation equations from Bilir et al. (2005) were used to convert B-V and R-I colors to $g-r$ and $r-i$.

the discrepancy is especially marked for temperatures above 3 700 K (roughly corresponding to spectral types earlier than M1) and for very late spectral types (later than ∼M4). At both ends, the model track is displaced at redder colors than the actual cluster locus. Similar conclusions can be drawn from the color-color diagram in Fig. 3.9b. The color sequence built from the model track appears to depart somewhat from the actual color sequence traced by cluster members in the K-spectral type range, whereas a better fit to the color locus of early-type stars appears to be provided by colors reported in the tables of Johnson (1965, 1966)[8], on which the conversion scale from spectral type to T_{eff} adopted in Cohen & Kuhi (1979) is based. The offset in color between the model track and the sequence of members amount to about 0.1-0.2 mag, which corresponds approximately to the distance in $g-r$ between two consecutive subclasses for K-type stars (see Table 3 of Covey et al. 2007).

Since the spectral type–T_{eff} scale of Pecaut & Mamajek (2013) departs from previously adopted scales mainly in the K-spectral type regime and for very late-type stars, and since these are specifically the regions where models on which Pecaut & Mamajek's scale is based appear to provide a poorer fit to the observed color loci of young stars in NGC 2264, we decided to not adopt this most recent determination of the conversion between spectral types and effective temperatures, but to retain the scale from Cohen & Kuhi (1979).

[8]On the contrary, these tables appear to provide a poorer fit to the color locus of M-type stars on the diagram in Fig. 3.9b. This likely originates in a non-optimal calibration of the UBVRI-to-SDSS transformations, which fails to reproduce the $g-r$ color saturation observed at these spectral types.

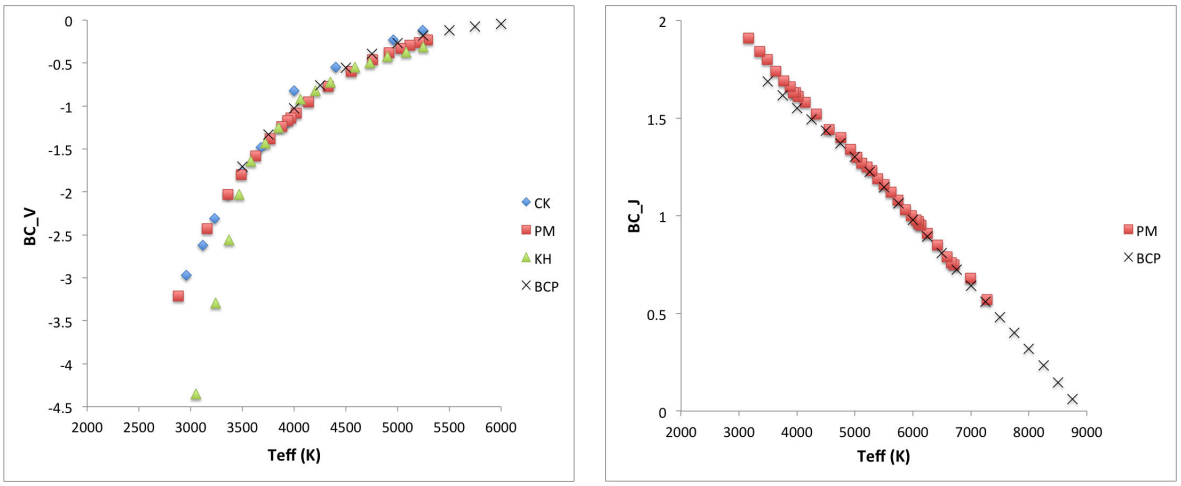

(a) (b)

Figure 3.10: Comparison of various effective temperature – bolometric correction scales from different authors, in the V-band (panel (a)) and in the J-band (panel (b)). Blue diamonds indicate the scale from Johnson (1965, 1966); red squares correspond to the scale retrieved from Pecaut & Mamajek (2013); green triangles mark the scale adopted in Kenyon & Hartmann (1995); black crosses show the scale deduced from the model-based compilation of Bessell et al. (1998) with log g = 4.

3.3.3 Bolometric luminosities

I derived bolometric magnitudes for our objects from 2MASS J-band photometry, because measurements of the stellar flux in this filter are not significantly "contaminated" by disk emission (which peaks at longer wavelengths), nor by accretion luminosity (more important at shorter wavelengths); in addition, extinction affects optical magnitudes more than near-infrared magnitudes, and stellar atmosphere models developed in the J-band are typically better constrained than at optical wavelengths, due to the numerous line opacities at the latter (see discussion by Kenyon & Hartmann 1990).

To convert J-band magnitudes to bolometric magnitudes, I adopted a distance to the cluster of 760 pc and used a scale of T_{eff}–dependent bolometric corrections BC_J derived as follows. I collected a number of T_{eff}–BC scales available in the literature from various authors and methods: Johnson (1965, 1966), Pecaut & Mamajek (2013), Kenyon & Hartmann (1995), and Bessell et al. (1998). In Fig. 3.10, we compare those different scales, both in the V-band (Fig. 3.10a) and in the J-band (Fig. 3.10b). These scales appear to be consistent with one another, in the sense that, at a given value of T_{eff}, similar BC values would be predicted by different scales (with the exception of the BC_V values associated with late M-type stars in the scale from Kenyon & Hartmann (1995), which depart from the trend traced by the other compilations in Fig. 3.10a). Therefore, I used the T_{eff} – BC scales, in the J-band, extracted from Pecaut & Mamajek (2013) and Bessell et al. (1998)[9], shown in Fig. 3.10b, to define an analytical T_{eff}-to-BC_J calibration as a fit to those two scales. The analytic conversion relationship obtained is the following:

$$BC_J = a + b\,T_{eff} + c\,T_{eff}^2 + d\,T_{eff}^3\,, \tag{3.1}$$

where $a = 2.927$, $b = -3.47 \times 10^{-4}$, $c = 8.76 \times 10^{-9}$, $d = -6.82 \times 10^{-13}$.

J-band photometry from the 2MASS survey is available for all but a few tens of objects in our sample. In these cases, bolometric luminosities L_{bol} were estimated by using an empirical

[9]Bessell et al. (1998) do not provide the BC_J values explicitly; I derived them from the tabulated BC_V values and the corresponding V-K and J-K colors.

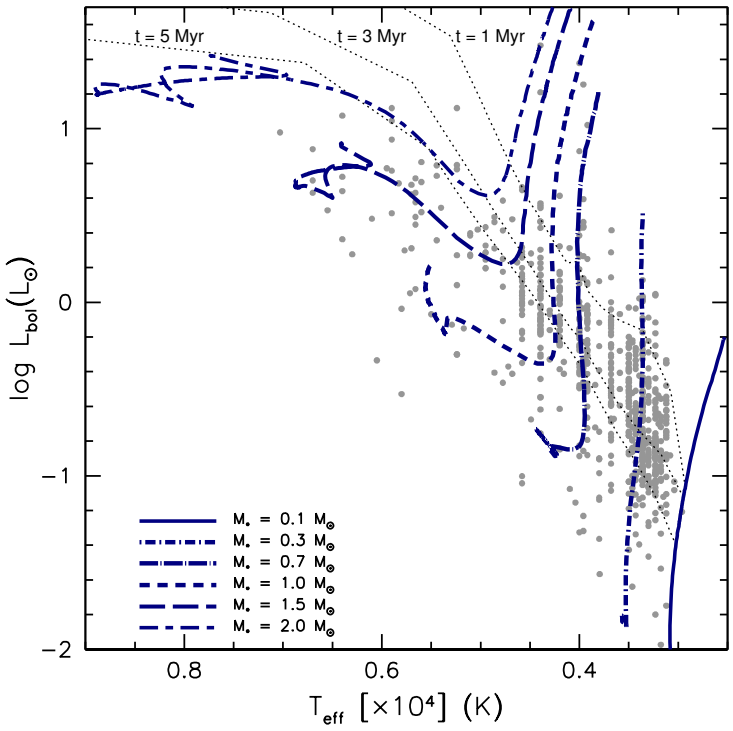

Figure 3.11: HR diagram for NGC 2264 members. Mass tracks and isochrones from Siess et al.'s (2000) models are plotted over the point distribution.

calibration derived between the L_{bol} values obtained for objects with J-band photometry and the corresponding, dereddened r-band magnitudes.

3.3.4 Stellar masses and radii

I used effective temperatures and bolometric luminosities, calculated as detailed in Sect. 3.3.2 and 3.3.3, respectively, to build the HR diagram of the region. This is illustrated in Fig. 3.11.

I then derived mass estimates for individual objects by interpolating their positions on the HR diagram with mass tracks from the PMS model grid of Siess et al. (2000)[10], assuming solar metallicity. These model tracks were favored over other commonly adopted evolutionary models for PMS stars, such as the isochrones of Baraffe et al. (1998), because they provide uniform coverage of the whole range of bolometric luminosities of interest here (while, for instance, Baraffe et al.'s model tracks extend to substellar mass regimes, which are not probed in this study, but not to mass regimes higher than $\sim$1.5 $M_{\odot}$). It is important to keep in mind that the mass estimates inferred will be dependent, to some extent, on the specific choice of reference model tracks: the value of stellar mass derived from the models of Baraffe et al. (1998) for a given object on the HR diagram may exceed by a factor of $\sim$50% the estimate inferred, for the same object, from Siess et al.'s (2000) models.

As can be seen on Fig. 3.11, members probed in our study span the mass range from $\sim$0.1 to $\sim$2 $M_{\odot}$, although about half of them are concentrated in the lower-mass regime ($<$0.5 $M_{\odot}$).

[10] I used the online tool at http://www.astro.ulb.ac.be/$\sim$siess/pmwiki/pmwiki.php/WWWTools/HRDfind; given the L_{bol}–T_{eff} coordinates of the object on the diagram, this program explores the grid of models at the metallicity chosen by the user to find the best fit to the observational data, and outputs the corresponding stellar parameters. In cases when no solution was provided by this automated tool, I inferred an estimate of the mass of the object of interest by visually interpolating between the two closest mass tracks on the HR diagram.

Stellar radii were determined from the estimates of L_{bol} and T_{eff} as

$$R_\star = \sqrt{\frac{L_{bol}}{4\pi\sigma T_{eff}^4}}$$

where σ is the Stefan-Boltzmann constant.

An order-of-magnitude estimate for the typical uncertainty on the derived $R_\star$ values is obtained from the uncertainty on the bolometric luminosity L_{bol}, which in turn is estimated through propagation of the uncertainties on J-band photometry, individual A_V and bolometric corrections. This yields $\Delta R_\star \sim 0.1\, R_\star$. The accuracy on stellar mass $M_\star$ is assumed to be of the order of 0.05 $M_\odot$, which corresponds to half the distance between two consecutive mass tracks in Siess et al.'s (2000) model grid.

3.4 UV excess and mass accretion rates

3.4.1 Measuring the UV flux excess

As discussed in the Introduction, measuring the flux excess at short wavelengths for CTTS provides one of the most straightforward diagnostics of the accretion luminosity, and hence of the mass accretion rate onto the star, since it arises from the shock formed at the impact of the accretion column onto the stellar surface.

The u-band flux excess is simply given by

$$F_u^{exc} = F_u^{obs} - F_u^{intr}, \tag{3.2}$$

where F_u^{obs} is the measured flux in the u-band, and F_u^{intr} is the intrinsic amount of flux that would be expected from that source, based on its spectral type, in the absence of additional emission components.

Due to their intense chromospheric activity, T Tauri stars are intrinsically overluminous at short wavelengths compared to MS dwarfs; this property is common to accreting (CTTS) and non-accreting (WTTS) objects. To disentangle the two emission components and obtain a "clean" estimate of the UV excess linked to accretion, I defined an internal reference color sequence, which follows the distribution of WTTS on color-color and color-magnitude diagrams, and measured the color excess of CTTS with respect to this sequence.

The color excess is hence determined as the difference between the observed stellar colors for CTTS and the expected colors, at the appropriate magnitude or spectral type, based on the photometric properties of their non-accreting counterparts (which take into account both the photospheric and chromospheric contributions):

$$E(u-m) = (u-m)_{obs} - (u-m)_{phot+chrom} \tag{3.3}$$

where m, in our case, is alternatively the g-band or r-band photometry (as detailed in the following).

As discussed earlier, based on the comparison of the photometric properties observed for the samples of CTTS, WTTS and field stars, we expect the accretion luminosity to impact predominantly the emission in the u-band, with no significant contribution, on the average, at redder filters; therefore, the color excess of Eq. 3.3 translates mainly to a flux excess on the u-band: $E(u) \simeq E(u-m)$. This can then be straightforwardly converted to an estimate of the u-band excess luminosity (L_u^{exc}).

$E(u-g)$

I measured the UV color excess of accreting stars in two different ways, from the analysis of either the $u-g$ vs. $g-r$ diagram (as detailed in the present subsection) or of the r vs. $u-r$ diagram (as detailed in the next subsection).

In the first case (Fig. 3.3b), I defined the reference color sequence as a straight line nearly parallel to the reddening vector and which follows the upper part of the WTTS distribution on the diagram. This reference line is shown in fuchsia on Fig. 3.6 and has equation

$$(u-g) = 1.312\,(g-r) + 1.03 \tag{3.4}$$

$E(u)$ is thus measured as

$$E(u) = (u-g)_{obs} - (u-g)_{ref}\,, \tag{3.5}$$

where $(u-g)_{ref}$ is the reference (i.e., expected) color, computed from Eq. 3.4 at the observed $g-r$.

The reference color sequence adopted is in good agreement with the WTTS color locus for spectral types earlier than M0. In this spectral range, the method implemented here for measuring the UV excess has the advantage of providing a nearly A_V–independent $E(u-g)$ estimate. For M-type objects, the approximation of the WTTS color locus as a line, in continuity with the trend observed at earlier spectral types, is no longer valid due to the fact that the real color sequence turns down on the diagram and saturates at a constant $g-r$, whereas the extrapolated reference sequence keeps increasing in $g-r$ and $u-g$. Hence, adopting the same reference sequence across the whole spectral range of interest causes a systematic overestimation (that is, more negative values) of $E(u)$ for M-type stars.

In order to correct for this bias, I measured the average displacement of the bulk of M-type stars below the reference color line, which amounts to about 0.2 mag. I then systematically added this quantity to the $E(u)$ measurements obtained for this group of objects.

$E(u-r)$

On the r vs. $u-r$ color-magnitude diagram (Fig. 3.4), WTTS trace a well-defined cluster sequence over the whole range of magnitudes. I then dereddened the u, r photometry and defined a sequence of reference colors as follows:

- I divided the magnitude range into bins of 0.5 mag;
- inside each bin, I applied an iterative $3\,\sigma$-clipping routine to compute the typical $u-r$ color, and corresponding dispersion, among WTTS included in that mag bin (results are reported in Table 3.1);
- I computed an analytic description of the WTTS color locus, $(u-r) = f(r)$, as a least-squares polynomial fit to the (r-mag, $(u-r)_{med}$) sequence derived as detailed in the previous point and listed in Table 3.1.

The UV excess is then defined as

$$E(u) = (u-r)_{obs} - (u-r)_{ref}\,, \tag{3.6}$$

where $(u-r)_{ref}$ is the reference color at brightness r_{obs}.

As can be observed on Fig. 3.4, at the brighter mag end the WTTS sequence is not well defined, due to the small number of objects with magnitudes in this range and to the large

r-mag (bin center)	$(u-r)_{med}$	σ
14.75	3.619	0.28
15.25	3.814	0.27
15.75	3.976	0.20
16.25	4.007	0.19
16.75	4.052	0.11
17.25	4.038	0.14
17.75	4.027	0.16
18.25	4.041	0.13
18.75	3.960	0.05

Table 3.1: Typical color locus, as a function of magnitude, traced by WTTS on the r vs. $u-r$ diagram, and measure of the WTTS dispersion in color around this average locus.

scatter in color; hence, in this case, I restricted the UV excess analysis to objects fainter than 14.5 in r.

Measuring the UV excess from u, r photometry, collected during the monitoring survey in Feb. 2012, is advantageous because it allows us to derive both a global picture of accretion in NGC 2264 from the average photometry, and a variability range for the UV excess on a timescale of a few weeks, obtained in a homogeneous fashion by measuring $E(u-r)$ at each observing epoch during the monitoring.

Unlike the first method adopted for measuring the UV excess (on $u-g$), the derivation of $E(u-r)$ from the color-magnitude diagram is potentially affected by issues with dereddening; a variation of 0.5 mag on A_V would translate to a variation of 0.35 mag in $u-r$, which, although not huge, might make the distinction between a low and a moderate accretion regime. In order to assess how the two sets of color excesses compare, I plotted the $E(u-r)$ values measured at the mean light curve state against the $E(u-g)$ values derived from Dec. 2010 single-epoch photometry; I could then ascertain the consistency of the global distribution with the equality line on the diagram. This indirectly supports the idea that the excess luminosity linked to accretion manifests primarily in the u-band, with no significant contribution, on the average, to the flux detected at the redder wavelengths probed here.

The distribution of $E(u-r) - E(u-g)$ residues (Fig. 3.12) appears to peak at slightly positive ($\sim$0.1) values for stars with spectral types later than M0, which means that slightly larger (i.e., more negative) values of UV excess are measured from the diagram in Fig. 3.3b than on Fig. 3.4. This may indicate that the correction to the measured $E(u-g)$ introduced *ad hoc* for M-type stars does not account entirely for the offset between the reference color sequence adopted and the actual WTTS color distribution in this spectral range. Conversely, the $E(u-r) - E(u-g)$ distribution for K-type stars appears to be centered around zero. The width of the distributions in $E(u-r) - E(u-g)$ reflects at least partly the epoch-to-epoch variability in colors and luminosity characteristic of these young stars; indeed, a difference of a few $\times$0.1 mag on the color excess may be expected, due to stellar variability, when we compare the average photometric properties of the system with those measured at a random epoch. A more extensive discussion of the typical amounts of variability observed for TTS in our sample is deferred to Sect. 3.5.2 and to Chapter 4. The distribution in $E(u-r) - E(u-g)$ for K-type stars in Fig. 3.12 appears to be broader than that for later-type stars; this may be a result of the larger dispersion around the typical WTTS color locus measured for earlier-type stars (see Table 3.1).

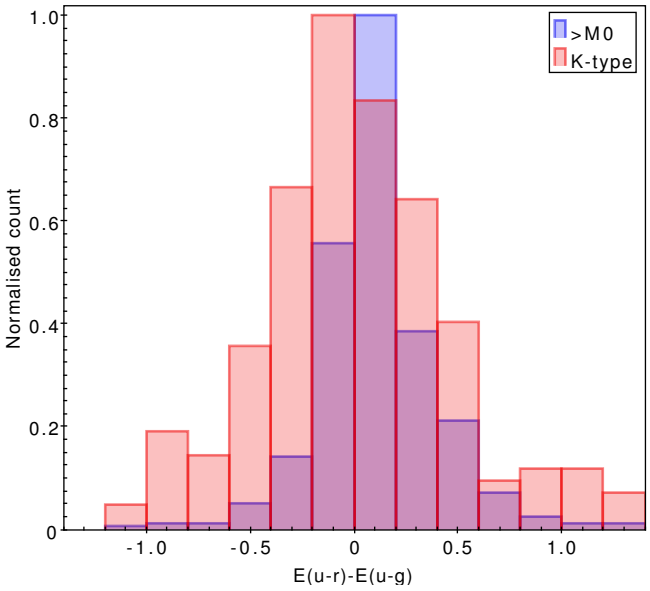

Figure 3.12: Distribution of measured $E(u-r) - E(u-g)$ residues for K-type stars (red) and late M-type stars (blue). The heights of histogram bars are normalised to the highest count in the respective distributions.

From color excess to u-band excess luminosity

Eq. 3.2 provides a definition of the flux excess in the u-band as a function of the observed flux and of the intrinsic flux (photospheric + chromospheric). If we explicit it in terms of magnitudes, this becomes:

$$F_u^{exc} = F_{u,0} \cdot 10^{-u_{obs}/2.5} - F_{u,0} \cdot 10^{-u_{intr}/2.5}, \tag{3.7}$$

where u_{obs} is the (dereddened) apparent u-band magnitude of the object, u_{intr} is the expected magnitude based on photospheric + chromospheric emission and $F_{u,0}$ is the SDSS u-band zero-point flux ($F_{u,0} = 3767.2$ Jy[11], or $F_{u,0} = 3.175{\times}10^{-8}$ W/m^2 when performing the conversion from Jansky to S.I. units using the filter parameters defined in Fukugita et al. 1996, $\lambda_u^{eff} = 3557$ Å).

In Eq. 3.7, u_{intr} can be rewritten as $u_{intr} = (u-m)_{intr} + m_{intr}$. In the assumption that the accretion luminosity does not impact significantly the magnitudes detected at wavelengths redder than u in our photometry, we can consider $m_{intr} \simeq m_{obs}$. The expression for u_{intr} hence becomes:

$$u_{intr} = (u-m)_{intr} + m_{obs}\,, \tag{3.8}$$

where $(u-m)_{intr}$ is the reference color at brightness m_{obs}.

The reference (or expected) color in Eq. 3.8 can be rewritten in terms of the observed color and the color excess $E(u-m) \simeq E(u)$:

$$(u-m)_{intr} = (u-m)_{obs} - E(u). \tag{3.9}$$

If we then combine Eqs. 3.7, 3.8 and 3.9, we obtain:

[11]Specification from http://svo2.cab.inta-csic.es/svo/theory/fps3/index.php?mode=browse&gname=SLOAN

$$F_u^{exc} = F_{u,0} \cdot 10^{-0.4\,u_{obs}} - F_{u,0} \cdot 10^{-0.4(m_{obs}+(u-m)_{obs}-E(u))} = \\ = F_{u,0} \cdot 10^{-0.4\,u_{obs}} - F_{u,0} \cdot 10^{-0.4(u_{obs}-E(u))} = \\ = F_{u,0} \cdot 10^{-0.4\,u_{obs}} \left(1 - 10^{+0.4\,E(u)}\right) \quad (3.10)$$

I followed Eq. 3.10 to derive the u-band flux excess across the whole sample and then converted F_u^{exc} to the excess luminosity L_u^{exc} using a distance to the cluster of 760 pc.

3.4.2 From u-band excess luminosity to total accretion luminosity

The u-band excess luminosity L_u^{exc}, derived as detailed in the above discussion, represents a single component of the total excess emission over the whole spectrum. To properly characterize the accretion properties, it is necessary to also take into account the flux excess at unobserved wavelengths, i.e., to apply a bolometric correction to the flux excess measured in the UV. This requires characterizing the emission spectrum of the accretion spot, relative to the stellar photosphere, for different temperatures, and comparing this ratio to the amount of excess flux detected in the u-band.

In the following, I adopt a simple phenomenological approach to study the relationship between the L_u^{exc} and the total accretion luminosity L_{acc}. In a basic picture, I approximate the emission spectrum from the spot as a blackbody spectrum at an effective temperature T_{spot}. Similarly, stellar emission is described as a blackbody emission at the photospheric temperature T_{phot}. This assumption is not strictly correct, because a blackbody model does not account for the presence of absorption lines and the resulting line-blanketing effect in stellar spectra. Therefore, while this approximation may be sufficient to reproduce the main emission features of a hot, ∼8 000–10 000 K spot, it may yield an overestimate of the photospheric flux level expected, for a given temperature, in the wavelength range of interest.

Be F^{phot} the flux emitted by the star according to its photospheric temperature, and F^{spot} the flux corresponding to the distribution of accretion spots, which extends over a fraction a of the stellar surface $\mathcal{A}$. The luminosity excess L^{exc} linked to accretion, measured over the photospheric luminosity, is then the difference between the total emission from the spot distribution and the emission that would arise from a portion of the stellar photosphere of the same surface extension as the spot distribution:

$$L_{exc} = a\,\mathcal{A}\,(F^{spot} - F^{phot}) \quad (3.11)$$

In terms of blackbodies, this becomes the difference between a blackbody flux density at $T=T_{spot}$ and a blackbody flux density at $T=T_{phot}$, both integrated over the same area.

We are interested in knowing what fraction of this excess luminosity is detected in the u-band. This corresponds to the inverse of the ratio r between the total excess luminosity, defined as in Eq. 3.12, and the convolution of this excess luminosity with the u-filter bandpass:

$$r = \frac{L^{exc}}{L_u^{exc}} = \frac{a\,\mathcal{A}\,(F^{spot} - F^{phot})}{a\,\mathcal{A}\,(F_u^{spot} - F_u^{phot})} \quad (3.12)$$

This ratio r is independent of the actual size of the spot distributions, and can hence be evaluated without any assumptions on the filling factor.

For a blackbody at temperature T, the spectral radiance per unit wavelength is expressed by Planck's law

$$B_\lambda(T) = \frac{2hc^2}{\lambda^5} \frac{1}{\exp(\frac{hc}{\lambda kT}) - 1} \ , \tag{3.13}$$

while the total radiance is given by Stefan-Boltzmann's law

$$B(T) = \frac{\sigma T^4}{\pi} \ . \tag{3.14}$$

In this picture, the ratio r of total-to-observed flux excess in the u-band, which corresponds to the corrective factor to be introduced to derive the total L_{exc}, i.e., the accretion luminosity L_{acc}, from L_u^{exc}, is given by the following expression:

$$r = \frac{\sigma T_{spot}^4 - \sigma T_{phot}^4}{\pi \int_u \left(B_{T_{spot}}(\lambda) - B_{T_{phot}}(\lambda)\right) d\lambda} \ , \tag{3.15}$$

where the integration is performed over the u-band window.

L_u^{exc}–to–L_{acc} conversion

In order to investigate the relationship between L_u^{exc} and L_{acc}, I selected a subsample of 44 CTTS, which cover the spectral type range M3.5:K2 (or equivalently the mass range ∼0.2–1.8 $M_\odot$) and whose variability, monitored in the u-band (λ_{eff}=3557 Å) and r-band (λ_{eff}=6261 Å) at CFHT, is likely accretion-dominated. By this second criterion, I refer to the results of extensive spot modeling I performed on the simultaneous $u + r$ variability amplitudes measured for all objects in our sample, following the approach of Bouvier et al. (1993). This analysis, reported in more detail in Chapter 4 (and published in Venuti et al. 2015), was aimed at assessing what are the dominating features of variability displayed by individual objects. Accretion-dominated sources in this context were identified as well-represented variables in terms of a surface spot distribution a few to several $\times 10^3$ K hotter than the stellar photosphere, with reasonably small uncertainties on the derived spot parameters.

For each of the selected objects, I adopted T_{phot} corresponding to its spectral type in Cohen & Kuhi's (1979) scale (see Sect. 3.3.2) and the individual T_{spot} estimate inferred from spot models. This latter corresponds, by construction, to the color temperature of the spot distribution that best reproduces the simultaneous flux variations observed at optical and UV wavelengths, or in other words, the one that best describes the observed λ-dependence in the luminosity contrast between the spot distribution and the stellar reference emission level. Individual T_{spot} values I derived across our sample cover a wide range, with a mean around ∼6500 K, a spread of ∼2000–3000 K at a given stellar temperature and nominal T_{spot} that can reach up to ∼9000–11 000 K and down to ∼5000 K.

For each object, I derived the ratio r of Eq. 3.15 through numerical integration[12] of $B(\lambda)$ in the spectral range 3257–3857 Å (which corresponds to an interval centered on the the effective wavelength λ_{eff} and of amplitude equal to the FWHM defined for the SDSS u-band filter in Fukugita et al. 1996). An estimate of the uncertainty on the value of r was derived from the uncertainty on the T_{spot} value deduced from the models (see Sect. 4.3.2), following the rules of error propagation.

Typical values of r derived for our sample indicate that, on average, the fraction of excess flux which is detected in the u-band amounts to about 10% of the total. This value obviously depends on the effective temperature of the spot distribution. While, for a typical photosphere

[12]Newton-Cotes trapezoidal rule

(T_{phot} ∼4 000 K), 12% of the excess emission of a 10 000 K spot is observed in the u-band, this percentage reduces to ∼10% for a 7 000 K spot and to less than 8% for a 6 000 K spot. A weaker dependence in the ratio r is observed on the photospheric temperature T_{phot}: for a spot distribution at a fixed temperature of 8 000 K, 11% to 12% of the flux excess produced will be detected in the u-band, whether the star is a late-M (T_{phot} ∼3 000 K) or an early-K (T_{phot} ∼5 000 K).

For each of the objects in the subsample analyzed at this step, I computed the accretion luminosity L_{acc} as $L_{acc} = r L_u^{exc}$, where r depends on the photospheric temperature of the star and on its estimated spot temperature, as indicated above, while L_u^{exc} is the excess luminosity measured in the u-band as described in Sect. 3.4.1.

The resulting point distribution in $\log(L_u^{exc}/L_\odot)$ vs. $\log(L_{acc}/L_\odot)$ is illustrated in Fig. 14 of Venuti et al. (2014) (Appendix B of this manuscript). Error bars are associated with L_{acc} values reflecting the uncertainty on the r factor. Data points are observed to trace a linear trend, with L_{acc} increasing with L_u^{exc}. I then defined a general L_u^{exc}–to–L_{acc} calibration relationship, to be extended to the whole sample, as a least-squares fit to the locus defined by this distribution on the diagram. The resulting calibration is the following:

$$\log\left(\frac{L_{acc}}{L_\odot}\right) = (0.97 \pm 0.03)\ \log\left(\frac{L_u^{exc}}{L_\odot}\right) + (1.09 \pm 0.07) \tag{3.16}$$

Errors on the parameters of the fit were derived by standard propagation of the uncertainties on L_{acc} (Taylor 1997).

On the correlation between UV excess luminosity and total accretion luminosity

The existence of a direct correlation between the flux excess observed in the U-band and the total accretion luminosity L_{acc} for CTTS was first discussed in the study of Gullbring et al. (1998). That result was based on a sample of 26, mostly late-K or early-M CTTS; for these objects, the authors measured the excess emission from spectra covering the λ-window from 3200 to 5400 Å, then modeled the excess spectrum with a slab model to estimate a correction for the unobserved excess component, and eventually used the observed spectra to synthetize a U-band magnitude, compute the corresponding flux excess, and investigate the relationship between the latter and the total accretion luminosity previously derived. This comparison showed that the two quantities are well correlated, which is not surprising since the excess emission likely dominates the observed flux at wavelengths < 4500 Å.

This correlation result was supported by complementary theoretical effort in Calvet & Gullbring (1998), who presented a more detailed model of the excess emission spectrum, as the sum of an optically thick component arising from the heated photosphere below the shock, plus an optically thin component produced in the preshock and postshock regions.

These first studies on the L_U^{exc}–L_{acc} correlation explored stars in the mass range 0.25–0.8 $M_\odot$ and with accretion rates between 10^{-9} and 10^{-7} $M_\odot$/yr. Rigliaco et al. (2012) analyzed a sample of 12 stars in σ Ori with masses between 0.08 and 0.3 $M_\odot$ and accretion rates between 10^{-11} and 10^{-9} $M_\odot$/yr, and concluded that a significant correlation between the excess luminosity measured in the UV and the accretion luminosity L_{acc} persists at much lower luminosities than the range for which the relationship had been originally derived.

In Venuti et al. (2014) (Appendix B of this manuscript), we compared Gullbring et al.'s (1998) L_U^{exc}–L_{acc} calibration with the relationship derived as discussed earlier in this subsection (see Fig. 14 of the paper). We found that the parameters which define the two calibrations are consistent within the uncertainties, although a systematic displacement of our calibration line above that defined in Gullbring et al. (1998) is observed (the difference between the two ranges

from a factor of $\lesssim$2 to 4). This difference is smaller than, or of about the same order as, the typical uncertainties on the accretion rate measurements ($\sim$0.5 dex). The two calibration lines, taken together, appear to delimit the range of model predictions, for varying filling factors and accretion column energy flux, depicted in Fig. 10 of Calvet & Gullbring (1998). In the paper, we discuss how the different assumptions adopted in the two approaches, namely on the effective spot temperature, may contribute to determine this shift between the two calibrations. Since the two relationships, although being distinct, are still somewhat consistent with one another, it appears of interest to explore what kind of impact a different choice in the calibration might have on the physical information deduced from the data. We then resolved to adopt our own derived calibration (Eq. 3.16) to infer L_{acc} estimates from the measured L_u^{exc}, and at the same time take Gullbring et al.'s (1998) relationship into consideration for comparison purposes on the final results.

3.4.3 Mass accretion rates

If we assume that the accretion energy is reprocessed entirely into the accretion continuum (cf. Herczeg & Hillenbrand 2008), the mass accretion rate $\dot{M}_{acc}$ can be derived from L_{acc} as

$$\dot{M}_{acc} = \left(1 - \frac{R_*}{R_{in}}\right)^{-1} \frac{L_{acc} R_*}{G M_*} \sim 1.25 \, \frac{L_{acc} R_*}{G M_*}, \tag{3.17}$$

where $M_\star$ and R_* are the parameters of the central star, R_{in} is the inner disk radius and we are assuming that the accretion funnel originates at the truncation radius of the disk, at $R_{in} \sim 5\,R_*$ (Gullbring et al. 1998).

In Fig. 3.13, I show the distribution of mass accretion rates, as a function of stellar mass, obtained for the disk-bearing population of NGC 2264. This sample includes 236 objects, which are confirmed members of the cluster and were classified as CTTS based on one or more of the disk diagnostics listed in Sect. 3.1.2. The range in stellar mass spanned by those objects extends from $\sim$0.1 $M_\odot$ to $\sim$1.5 $M_\odot$.

Accretion rate values in Fig. 3.13 were obtained from the measurement of $E(u-r)$ on the diagram in Fig. 3.4, and correspond to the average photometry (i.e., median UV excess state) monitored on a timescale of two weeks. The measured WTTS dispersion in color about the reference sequence (see Table 3.1) was used to define a mag-dependent confidence threshold for UV excess detection. Objects were defined to possess a significant UV excess, indicative of accretion, above the photospheric+chromospheric level if their $u-r$ colors are at least $1\,\sigma$ bluer, i.e. smaller, than the typical location, at the corresponding brightness range (first column of Table 3.1), on the WTTS sequence. The σ value reported in the third column of Table 3.1 thus represents the minimum amount of UV excess that an object must exhibit, depending on its r-band magnitude, to be considered a robust indicator of accretion activity. For objects with $u-r$ comprised between $(u-r)_{ref}$ (second column of Table 3.1) and $(u-r)_{ref} - \sigma$ (second minus third column in Table 3.1), it is not possible, a priori, to evaluate the relevance of spurious contributions (i.e., chromospheric activity) to the apparent UV excess. Hence, for disk-bearing objects whose measured UV excess is less than the corresponding boundary value, no direct estimate of the actual $\dot{M}_{acc}$ can be inferred from this diagnostics, but only an upper limit to it, computed at the UV excess detection threshold. Objects for which only an upper limit to $\dot{M}_{acc}$ was derived are indicated as down-headed arrows on the diagram.

As can be noticed both on Table 3.1 and on Fig. 3.13, lower UV excesses are more easily detected on later-type stars; this simply reflects a selection effect due to the contrast between the spot distribution and the stellar photosphere, which is more favorable for lower T_{phot}.

As done in the case of $E(u-g)$ and $E(u-r)$, I compared $\dot{M}_{acc}$ estimates that would be derived for the same objects from the two diagnostics (see Fig. 15 of Venuti et al. 2014) and could ascertain that the two distributions are on average consistent, within a small mass-dependent offset likely reflecting a residual overestimation of the $(u-g)$ color excess from Fig. 3.6. A certain amount of scatter around the equality line can be observed on the diagram; as noted in the case of Fig. 3.12, variability is likely to contribute to the scatter observed within ± 0.25 dex around the line (see Sect. 3.5.2).

3.5 Accretion regimes in NGC 2264

3.5.1 The $\dot{M}_{acc} - M_{\star}$ relationship

Accretion rate estimates, derived as detailed in Sect. 3.4.3 and above, span three orders of magnitude for NGC 2264 members in the 0.1 to 1.5 $M_{\odot}$ mass range (Fig. 3.13). The strongest accretion regimes detected correspond to rates of $\sim 10^{-7}$ $M_{\odot}$/yr; on the other side of the $\dot{M}_{acc}$ distribution across the cluster, we find objects accreting at rates as low as 10^{-10} $M_{\odot}$/yr and a number of non-detections (about 20% of the CTTS sample).

An important question that arises from the analysis of such diagrams as Fig. 3.13 is whether a definite relationship between the typical $\dot{M}_{acc}$ and the mass $M_{\star}$ of the central object can be assessed. This is of interest to understand and develop more accurate models of the mechanisms that govern the disk accretion process in young stars (see, e.g., the discussion in Hartmann et al. 2006), as well as to investigate a possible dependence of this trend on the initial conditions of the parent protostellar core (e.g., Dullemond et al. 2006).

An appraisal of the actual trend in $\dot{M}_{acc}$ vs. $M_{\star}$ is hampered by two factors: the typically observed large spread in $\dot{M}_{acc}$ at any given value of $M_{\star}$ (which can extend over up to two orders of magnitude, as illustrated in Fig. 3.13; see also, e.g., Hartmann et al. 2006; Natta et al. 2006; Rigliaco et al. 2011; Manara et al. 2012), and the presence of censored data at the low-$\dot{M}_{acc}$ end (upper limits at the detection threshold). In the following, I address this second aspect, in the perspective of determining a robust estimate of the $\dot{M}_{acc} - M_{\star}$ relationship; the nature of the spread in $\dot{M}_{acc}$ about the general trend will be explored in later sections.

Measuring correlation in the presence of censored data

The issue of whether observational inferences on the $\dot{M}_{acc}$–$M_{\star}$ relationship may be significantly affected by incompleteness of the data at low accretion regimes was first raised by Clarke & Pringle (2006). In their analysis, the authors referred to the study of Natta et al. (2006), who performed a homogeneous accretion survey for about a hundred disk members of ρ Ophiuchi. Results of Natta et al. (2006) showed that a strong correlation is present on the average between $\dot{M}_{acc}$ and $M_{\star}$; however, they also showed that the estimated upper limits in $\dot{M}_{acc}$ for non-detections distribute along the lower envelope of the $\dot{M}_{acc}$ distribution defined by objects which accrete above the detection threshold, and scale with $M_{\star}$ in approximately the same way. A similar situation is observed here in Fig. 3.13. Approaches to the problem which consist in either neglecting the upper limits for the analysis of correlation, or in considering them in the same manner as actual detections, in principle do not enable disentangling the two contributions (detections vs. upper limits) to the overall trend and hence assessing the reality of the measured correlation between $\dot{M}_{acc}$ and $M_{\star}$.

Techniques of survival analysis can be applied for a more rigorous statistical treatment of the problem. Here I adopt a generalization of Kendall's τ test for correlation to the case of censored data (Feigelson & Babu 2012; Helsel 2012).

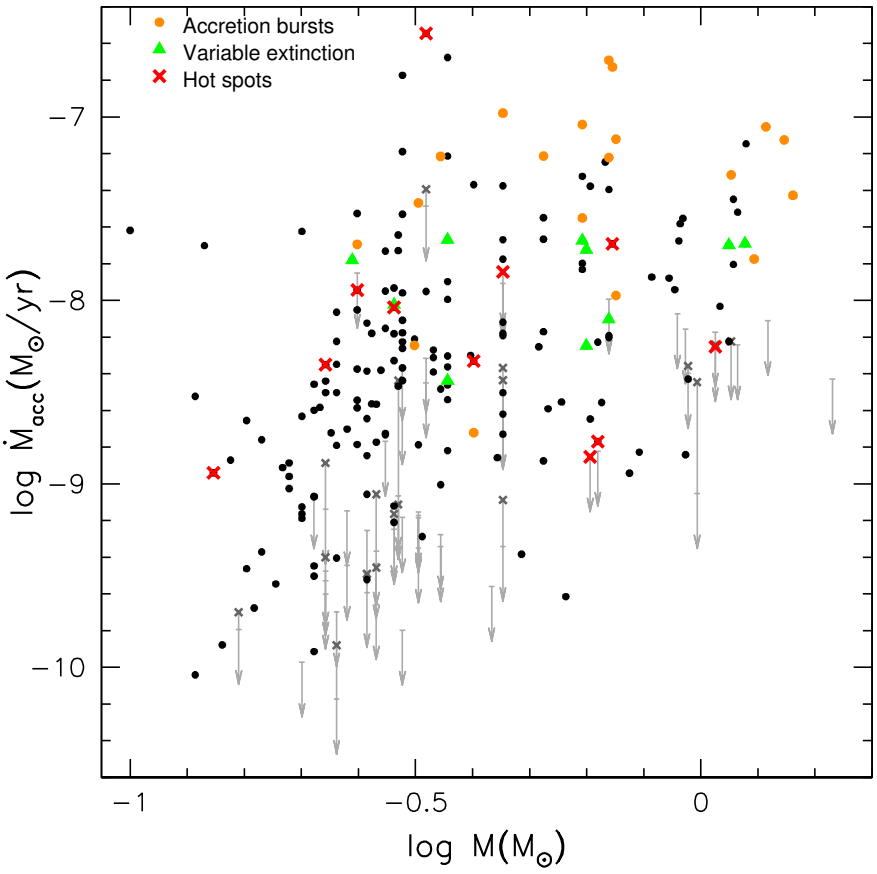

Figure 3.13: $\dot{M}_{acc}$ distribution as a function of stellar mass for the population of NGC 2264 accreting members observed at CFHT. Upper limits are shown for those objects that fall below the estimated confidence threshold for accretion detection (see text). For some objects, no significant $\dot{M}_{acc}$ has been detected at the median state of the system, but they do show a significant accretion activity (i.e., above the detection level) at the brightest state; in these cases, an upper limit is placed at the detection threshold, while a grey cross marks the maximum $\dot{M}_{acc}$ actually detected. Orange dots and green triangles mark two subgroups of objects dominated respectively by stochastic accretion bursts (Stauffer et al. 2014) and variable extinction from a rotating inner disk warp (McGinnis et al. 2015). Red crosses identify a subgroup of objects whose light curves are suggestive of hot spot modulation (see, e.g., Fig. 20 of Stauffer et al. 2014).

Two different types of incompleteness affect our data: *ties* (objects at the same value of $M_\star$ but different $\dot{M}_{acc}$)[13] and *left censoring* (upper limits in $\dot{M}_{acc}$, i.e. objects that fall below the detection threshold).

The starting idea of the test is straightforward. If a significant correlation (either positive or negative) is present in a sample of data points, then a definite interrelationship is to be observed statistically between variations on the x-axis and on the y-axis (either they are concordant in sign, that is, an increase in x corresponds to an increase in y and vice versa, when a positive correlation links one variable to the other, or they are discordant in sign, in case of anticorrelation). The test is then structured as follows: we have a starting sample of N points, which are either detections or upper limits; these can be paired in N (N-1)/2 different ways; for each of these pairs, we measure the slope of the line connecting the two points on the diagram (Fig. 3.13) and retain the information on the sign of the angular coefficient; we then ask ourselves how many times a positive slope is measured among all pairs versus how many times a negative slope is measured, and whether the difference between these two numbers is significant and symptomatic of a definite correlation between the two variables.

Fig. 3.14 illustrates the different possibilities when pairing two data points and how these are considered for the test. A pair of data points having the same $M_\star$-value will be counted as a tie (no slope defined), and, similarly, a pair of upper limits will correspond to an indeterminate relationship; upper limits will uniquely contribute a definite relationship when paired with actual detections at higher $\dot{M}_{acc}$-value.

If n_C is the total number of concordant pairs and n_D is the total number of discordant pairs identified, the statistical correlation coefficient τ is defined as:

$$\tau = \frac{n_C - n_D}{n_{tot}} \tag{3.18}$$

where n_{tot} is the total number of pairs[14].

ln this picture, upper limits have the effect of lowering the likelihood of a correlation, if this is present in the data, as they introduce a number of indeterminate relationships among the tested pairs. Conversely, no correlation will be found in a pure sample of upper limits, even though these trace a well-defined trend, because the number of pairs with a definite relationship will be zero.

In the null hypothesis of no correlation, τ follows a normal distribution centered on zero and with variance

$$\sigma^2 = \frac{2(2N+5)}{9N(N-1)}$$

(in the case where all pairs are included in n_{tot} for the computation of τ); the ratio $Z = \tau/\sigma$ will hence provide an estimate of the significance of the correlation/non-correlation result.

[13]These cases arise because the mass determination from positioning the objects on the HR diagram and comparing them with model tracks does not return a continuous distribution in values with large precision, but rather a discrete distribution with a precision of order 10^{-2} at most.

[14]If all pairs are assumed to be equally informative regarding the trend investigated, n_{tot} corresponds simply to the total number of available pairs, N (N-1)/2. Feigelson & Babu (2012) define n_{tot} as the number of effective pairs, i.e. the pairs for which a slope can be defined:

$n_{tot} = \sqrt{\left(\frac{N(N-1)}{2} - n_{ties\_X}\right)\left(\frac{N(N-1)}{2} - n_{ind\_Y}\right)}$

This considers that indeterminate relationships do not contribute to the actual information on the correlation/anticorrelation trend, but rather introduce a lack of information which results in weakening the statistics. In the analysis presented here, I applied both definitions for the computation of τ; either choice does not change appreciably the result I derive.

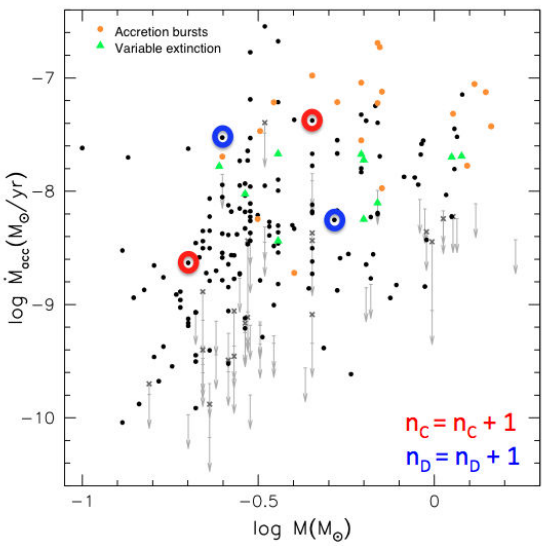

(a) Pairing of two detections at different $M_\star$.

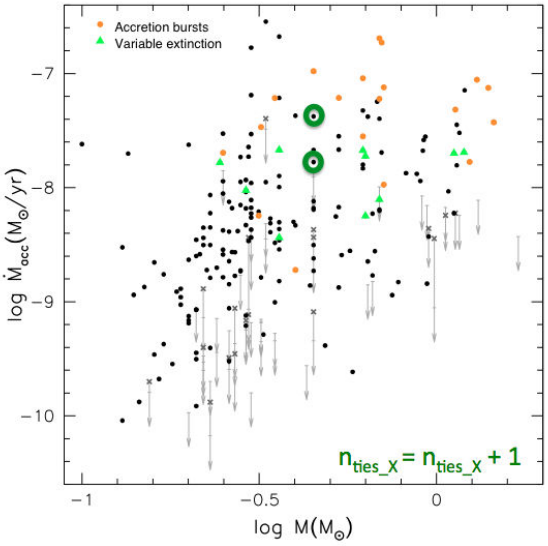

(b) Pairing of two data points at the same $M_\star$.

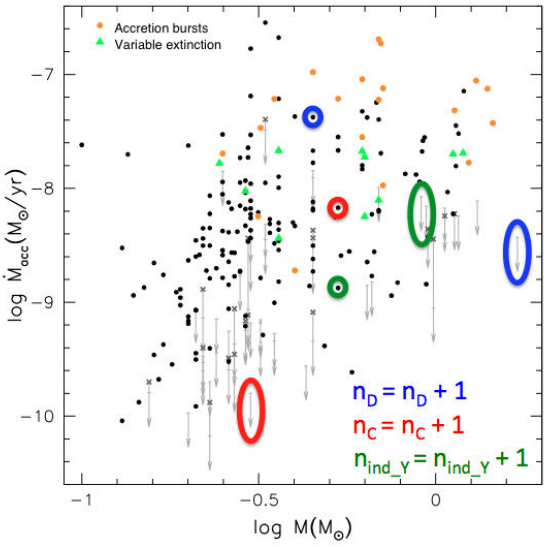

(c) Pairing of one detection and one upper limit.

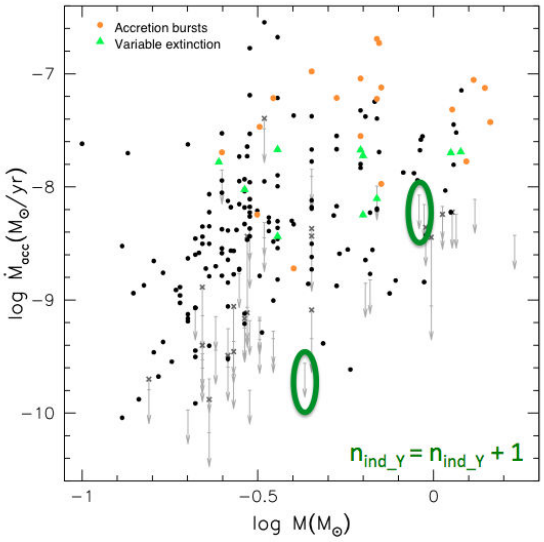

(d) Pairing of two upper limits.

Figure 3.14: Implementation of the Kendall's τ test for correlation to the $\dot{M}_{acc}$ vs. $M_\star$ data point distribution in Fig. 3.13. Panels (a) through (d) illustrate the different possible cases when pairing two objects on the diagram. In the first case (panel (a)), two actual detections are paired; these can either determine a positive slope (and hence contribute to the total number of concordant pairs, n_C, as for the pair marked in red on the image), or be connected by a line with negative slope (and hence contribute to the counter of discordant pairs, n_D; this is illustrated by the pair highlighted in blue). Panel (b) shows an example of two paired objects (either detections or upper limits) which are a tie in $M_\star$; in these cases, no relationship between the two points can be defined, and these are included in a first group of indeterminate relationships, n_{ties_X}. In panel (c), the different possible situations which involve pairing a detection with an upper limit (not a tie in $M_\star$) are examined. When the upper limit is lower than the $\dot{M}_{acc}$ detection it is paired with, we still have a definite relationship (either concordant, as the pair marked in red, or discordant, as that marked in blue), because the actual $\dot{M}_{acc}$ of the non-detection can be smaller than the upper limit estimate, but not larger. Conversely, when the upper limit is paired with a detection at lower $\dot{M}_{acc}$ (as in the case marked in green on the image), a definite relationship cannot be determined, because we have no information on how small the non-detected $\dot{M}_{acc}$ is (and hence whether this is larger or smaller than the $\dot{M}_{acc}$ detected for the paired object); these cases then contribute to a second group of indeterminate relationships, n_{ind_Y}. In panel (d), a pair of two non-detections is considered; these will always contribute to the group of indeterminate relationships.

In our sample, we measure $\tau \sim 0.28$ and $\sigma \sim 0.04$; this hence suggests that a significant correlation is present and appears to hold across the whole mass range studied here to the $> 6\,\sigma$ level.

To test the solidity of this result, I built random distributions of $\dot{M}_{acc}$ values, which were subsequently analyzed for correlation, as follows. I took our true sample of objects, displayed in Fig. 3.13; each of these objects has an individual $\dot{M}_{acc}$ detection threshold defined depending on its brightness, as described in Sect. 3.4.3. For each of these objects, I generated a random value of $\dot{M}_{acc}$, extracted uniformly from the range [-10.5, -6.5] (which corresponds to the range of values in $\log \dot{M}_{acc}$ spanned by actual detections in our sample). These randomly assigned $\dot{M}_{acc}^{test}$ values throughout the sample are compared to individual detection thresholds $\dot{M}_{acc}^{th}$; if $\dot{M}_{acc}^{test}$ is larger than $\dot{M}_{acc}^{th}$ for a given object, this is considered as a detection; in the opposite case, it is considered as an upper limit at $\dot{M}_{acc}^{th}$. This random accretion rate is associated to the true $M_\star$ parameter derived for the object.

I then applied the Kendall's τ test for correlation to the newly built distribution of $\dot{M}_{acc}^{test}$ vs. $M_\star$ (or $\dot{M}_{acc}^{th}$ for objects considered as non-detections), and extracted the corresponding τ. I repeated the whole procedure 100 times in order to define an expected distribution of τ values for a sample where, by construction, no $\dot{M}_{acc}$–$M_\star$ correlation other than the trend associated with upper limits is present. The τ distribution inferred from these 100 iterations is peaked around τ=0.00 (no correlation) with a σ of 0.04; this supports the conclusion, derived from the true data point distribution in Fig. 3.13, that an intrinsic correlation is observed in our data to a significance of $> 6\,\sigma$, and that the trend in the upper limit distribution does not affect this result. Similar conclusions are presented in Ercolano et al. (2014), who adopt a different statistical approach to revise the issue of $\dot{M}_{acc}$–$M_\star$ correlation in the presence of upper limits.

Incidentally, I also performed a correlation analysis of the $\dot{M}_{acc}^{test}$ vs. $M_\star$ distribution with either discarding upper limits or treating them as actual detections; with these assumptions, I derived a probability of over 99% that a correlation trend is present in the purposedly flat generated distribution. This suggests that caution must be exercised in the analysis of samples where large fractions of data points are censored, although the difference in result between neglecting or properly accounting for censored data may not be critical when censoring affects a smaller fraction of observational points[15].

I then inferred a statistical estimate for the slope α of the $\log(\dot{M}_{acc})$–$\log(M_\star)$ correlation following the approach of Akritas-Theil-Sen nonparametric regression (see Feigelson & Babu 2012):

1. I derived a first guess for the slope from a least-squares fit to the data distribution and explored a range of ± 0.5 around this first estimate with a step of 0.005;

2. for each value α_{test}, I subtracted the $\alpha_{test} \times \log(M_\star)$ trend from the initial $\log(\dot{M}_{acc})$ distribution and repeated the Kendall's τ computation procedure on the distribution of residues thus inferred.

The best fitting trend is the one that, subtracted to the point distribution, produces τ=0; I then derived an estimate of the uncertainty around α as the interval of values that correspond to $-\sigma < \tau < \sigma$.

The result I obtain from data in Fig. 3.13, where $\dot{M}_{acc}$ estimates are derived from the measured $E(u-r)$, is:

[15]Even in our case, where censoring affects about 20% of objects, the two approaches yield similar results. A slightly larger fraction of upper limits, about 30–35%, is instead generated in the test sample with uniform distribution in $\dot{M}_{acc}$.

$$\dot{M}_{acc} \propto M_{\star}^{1.5\pm0.2} \tag{3.19}$$

Similarly, I repeated this analysis on the $\dot{M}_{acc}$ estimates inferred from $E(u-g)$ measurements; this yields

$$\dot{M}_{acc} \propto M_{\star}^{1.3\pm0.2} \tag{3.20}$$

The two trends are consistent within $1\,\sigma$; the smaller exponent in Eq. 3.20 compared to Eq. 3.19 may reflect the small, mass-dependent offset between the $\dot{M}_{acc}$ distributions inferred from the two methods (as observed on Fig. 15 of Venuti et al. 2014). I then estimate the final result as $\alpha = 1.4 \pm 0.3$.

A slope of 1.7±0.2, instead of the estimate in Eq. 3.19, would be inferred if we converted $E(u-r)$ to L_{acc} values following the prescription of Gullbring et al. (1998) instead of Eq. 3.16. The two estimates are still consistent within $1\,\sigma$; this comparison illustrates that a (small) uncertainty on the true slope may be determined by external factors such as the L_u^{exc}–L_{acc} conversion.

The value of α in the $\dot{M}_{acc} \propto M_{\star}^{\alpha}$ relationship

While it appears established that a global correlation exists between $\dot{M}_{acc}$ and $M_{\star}$ in young stars, the actual shape of such a relationship is still controversial.

Muzerolle et al. (2003b) was one of the first studies to explore the correlation trend between $\dot{M}_{acc}$ and $M_{\star}$. Those authors probed a composite sample of about 50 objects distributed in mass between 0.04 and 1 $M_{\odot}$, and inferred a correlation result with $\alpha = 2$. Similar results were obtained by Calvet et al. (2004) (who expanded the sample of Muzerolle et al. 2003b to larger $M_{\star}$ by adding a sample of nine objects with masses between 1.5 and 4 $M_{\odot}$, and found a value of $\alpha = 1.95$ over the whole mass range); Muzerolle et al. (2005) (who expanded the sample of Muzerolle et al. 2003b and Calvet et al. 2004 toward lower masses, down to 0.015 $M_{\odot}$, and extracted $\alpha = 2.1$); Mohanty et al. (2005) (who extrapolated the relationship further to substellar mass regimes by adding a sample of objects, from various young clusters, with $M_{\star}$ between 0.15 and 0.01 $M_{\odot}$ to samples investigated earlier); Natta et al. (2006) (who explored a sample of a hundred of objects in ρ Ophiuchi, with masses between 0.03 and 2.5 $M_{\odot}$, and inferred $\alpha = 1.8 \pm 0.2$); Herczeg & Hillenbrand (2008) (who enlarged the sample considered in Muzerolle et al. 2005 in the Taurus region and derived $\alpha = 1.87 \pm 0.26$); Alcalá et al. (2014) (who considered a sample of 36 objects in the Lupus star-forming region, with masses between 0.08 and 1.3 $M_{\odot}$, and measured $\alpha = 1.8 \pm 0.2$).

On the other hand, somewhat smaller values of α, although often consistent, within the uncertainties, with the various estimates enumerated earlier, were proposed in several recent studies. For instance, Rigliaco et al. (2011) examined an ensemble of about 100 disk-bearing objects in σ Ori, with masses between 0.06 and 1 $M_{\odot}$, and inferred a value of $\alpha = 1.6 \pm 0.4$. Biazzo et al. (2012) analyzed a sample of 40 members of the Chamaeleon II star-forming region, whose masses are distributed between 0.1 and 1 $M_{\odot}$, and derived $\alpha = 1.3 \pm 0.4$. Barentsen et al. (2011) studied a population of 158 accreting stars in the region IC 1396, with masses in the range 0.2–2 $M_{\odot}$, and inferred a $M_{\star}$–$\dot{M}_{acc}$ relationship with $\alpha = 1.1 \pm 0.2$. The estimate of α derived in the present study, on the mass range ∼0.1–1.5 $M_{\odot}$, is positioned in this second group of values, somewhat shallower than the $\alpha \sim 2$ estimates albeit compatible with several of them.

The studies summarized earlier differ in the accretion diagnostics adopted, in the intrinsic properties of the stellar samples probed and in statistical extent; these differences may have an impact on the range of α values deduced from the comparison of their results. However, taken at

face values, these results seem to indicate that a steeper dependence of $\dot{M}_{acc}$ on $M_\star$ is measured when a significant fraction of the stellar sample considered for the analysis is in the substellar mass regime, whereas shallower α values are typically associated with higher mass regimes. This trend appears to be valid in the mass range from ∼0.01 to a few $M_\odot$; a stronger correlation may again be observed in the intermediate mass regime (∼1–10 $M_\odot$), as discussed in Ercolano et al. (2014).

Some evidence of a mass dependence in α may in fact be present in our data (Fig. 3.13). The correlation result described above refers to the homogeneous sample as a whole. While the relationship we infer seems to be robust across the whole sample, this likely provides a general, average information on the global trend of $\dot{M}_{acc}$ with mass, not a punctual description of the trend. For instance, little mass dependence seems to characterize the upper envelope of the $\dot{M}_{acc}$ distribution above $M_\star$∼0.25 $M_\odot$ (see also Hartmann et al. 2006). I attempted a more detailed investigation of the observed $\dot{M}_{acc}$ vs. $M_\star$ relationship by separating our sample in two, similarly populated, mass bins ($M_\star \leq 0.3\,M_\odot$ and $M_\star > 0.3\,M_\odot$), and repeating the correlation analysis in each of them individually. In both subgroups, I found some evidence of correlation, albeit with different values and significance levels: a correlation with a slope of 3.3±0.7 was inferred, to the $4\,\sigma$ level, in the lower-mass group, while a correlation with a slope of 0.9±0.4 was obtained for the higher-mass group with a significance of $2.4\,\sigma$. These results might suggest that the dependence of $\dot{M}_{acc}$ on $M_\star$ is indeed not uniform across the whole $M_\star$-$\dot{M}_{acc}$ range, but shallower at higher masses and higher accretion rates (consistent with inferences presented earlier from the comparison of α estimates obtained by different authors). However, these results on the mass dependence in the $M_\star$–$\dot{M}_{acc}$ relationship, obtained from the analysis of small subsamples of objects, are supported by a more limited statistics, and hence are necessarily more uncertain, than the assessment of a general correlation trend observed across the whole sample.

3.5.2 Accretion variability

A prominent feature of the data point distribution in Fig. 3.13 is the large dispersion in $\dot{M}_{acc}$ values at each $M_\star$; this spread typically extends over two orders of magnitude around the average trend. Similar dispersion properties on the $\dot{M}_{acc}$ vs. $M_\star$ diagram were already observed, e.g., in Muzerolle et al. (2005) for a composite sample of young stars from different regions, and by Natta et al. (2006), Rigliaco et al. (2011), and Manara et al. (2012) from the analysis of single clusters (ρ Ophiuchi, σ Ori, and the Orion Nebula Cluster, respectively)[16].

Part of the dispersion may in principle be a reflection of the huge photometric variability exhibited by T Tauri stars, both on short-term (hours) and mid-term (days) timescales (see, e.g., Ménard & Bertout 1999, for a review of the characteristic timescales of variability in TTS). Short-term variability may affect the $\dot{M}_{acc}$ estimates for individual objects, but it typically represents only a second-order component in the variability pattern of TTS (see Chapter 4 for a detailed discussion on the amount of variability detected in the UV on different timescales). On the other hand, mid-term variability, which includes both the geometric effects linked to stellar rotation and the intrinsic accretion variability on characteristic hot spot lifetimes, might effectively blur the $\dot{M}_{acc}$ distribution inferred from single-epoch mapping of the region, since each object is then observed at an arbitrary phase.

[16] Alcalá et al. (2014) and Manara et al. (2015) have recently explored the $\dot{M}_{acc}$–$M_\star$ relationship in the Lupus and ρ Ophiuchi regions, respectively, and have inferred significantly smaller estimates of the $\dot{M}_{acc}$ dispersion, restricted to an interval of about 1 dex around the average $\dot{M}_{acc}$–$M_\star$ trend. Both these studies are based on the analysis of VLT/X-Shooter spectra from ∼330 to 2500 nm, which enable simultaneous characterization of a large number of emission lines and accurate determination of stellar parameters, although they encompass more limited samples of accreting objects (a few tens) than other studies mentioned above.

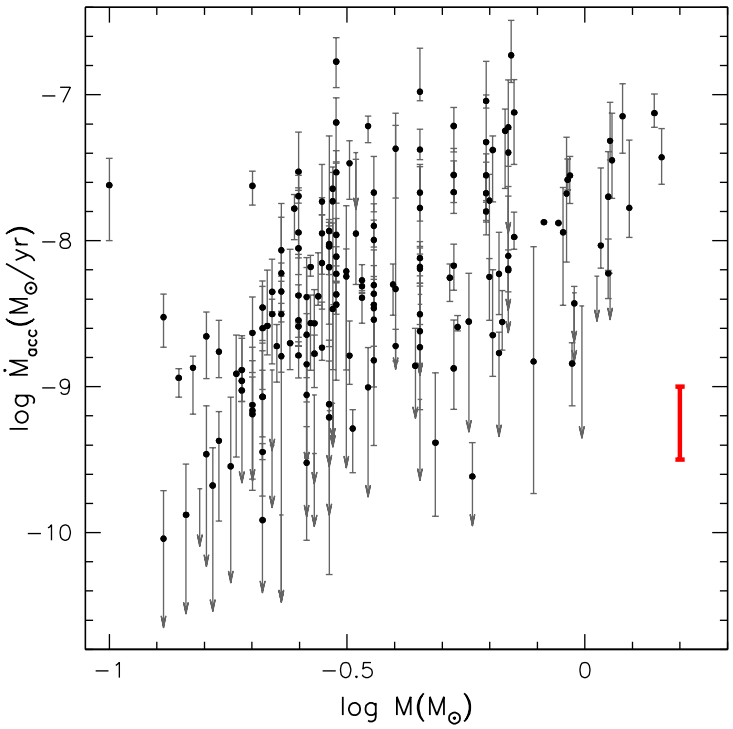

Figure 3.15: Variability of the mass accretion rates observed for NGC 2264 members over the 2-week long CFHT monitoring. Black dots correspond to the median $\dot{M}_{acc}$ measured for each object (see Fig. 3.13). For each object, the relevant variability bar is displayed, corresponding to the difference between the maximum and the minimum $\dot{M}_{acc}$ detected during the monitoring. A typical variability bar is shown in red.

In order to assess the contribution of mid-term variability to the $\dot{M}_{acc}$ spread, I considered separately each observing epoch acquired at CFHT during the u, r monitoring (Sect. 2.2.2). For each of them, obtained in photometric conditions[17], I measured the $E(u-r)$ and corresponding $\dot{M}_{acc}$, following the procedure described in Sect. 3.4. This allowed me to define a range of variability to be associated with the average $\dot{M}_{acc}$, displayed as dots for individual objects in Fig. 3.13.

These variability bars are combined with average $\dot{M}_{acc}$ values in Fig. 3.15. Each variability bar encompasses all values of $\dot{M}_{acc}$ detected for the corresponding object during the monitoring (i.e., it connects the highest and the lowest detected $\dot{M}_{acc}$). CTTS which are non-detections in accretion (and hence upper limits on Fig. 3.13) were not considered for this step of the analysis and are not shown in Fig. 3.15. In some cases, objects fall below the $\dot{M}_{acc}$ detection threshold at certain epochs (although being detections in $\dot{M}_{acc}$ at the average state); for these objects, the lower end of the variability bar on Fig. 3.15 is an upper limit at the detection threshold.

Variability properties are not uniform across the sample. The detected amplitudes of variability in $\dot{M}_{acc}$ range from small fractions to ∼1 order of magnitude (Fig. 3.16). Table 5 of Venuti et al. (2014) lists the average variability properties detected in three different mass bins. No clear trends emerge with stellar mass or mass accretion rates; the average amount of variability detected over a timescale of two weeks (which correspond to ∼2-3 rotational cycles for most of the objects; see Affer et al. 2013) is of 0.5 dex, as illustrated in Fig. 3.15. A few objects on the

[17]These typically amount to 16-17 measurements per object, distributed over a period of two weeks; for further details on how photometric nights were selected, see Chapter 4.

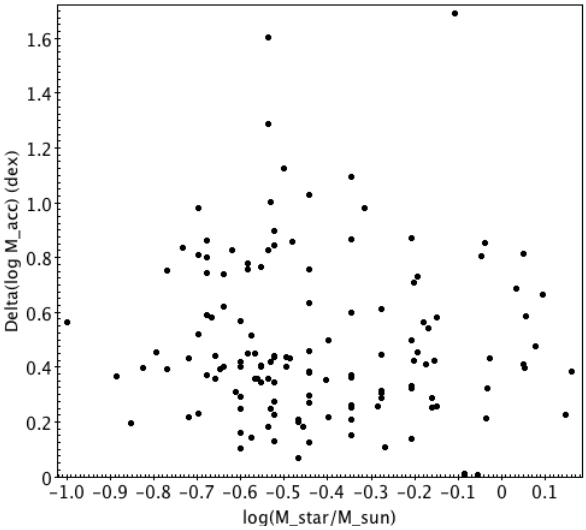

Figure 3.16: Amplitudes of variability, in dex, measured around the average $\dot{M}_{acc}$ for individual objects are shown as a function of stellar mass $M_\star$.

diagram display significantly lower variability; these may be sources observed in a pole-on configuration. The (a)symmetry of individual variability bars, albeit potentially affected by the specific temporal sampling, may reflect the way accretion proceeds onto the central object, as well as the dominant features of the system. Variability bars throughout the sample are statistically found to be symmetric around the median $\dot{M}_{acc}$ (i.e., $\log \dot{M}_{acc}^{max} - \log \dot{M}_{acc}^{med} \simeq \log \dot{M}_{acc}^{med} - \log \dot{M}_{acc}^{min}$), which indicates that the typical state of the systems also corresponds to their mean luminosity state. A strongly asymmetric bar, with $\dot{M}_{acc}^{med}$ close to $\dot{M}_{acc}^{min}$ and large ($\log \dot{M}_{acc}^{max} - \log \dot{M}_{acc}^{med}$), would instead indicate that the system is typically found it the low-luminosity state, with occasional strong flux bursts.

The typical 0.5 dex variability on $\dot{M}_{acc}$, that we find here on timescales of a few weeks, compares well with the results obtained in other surveys of accretion variability. Costigan et al. (2014) explored the $\dot{M}_{acc}$ variability, from the Hα EW diagnostics, for a sample of 15 T Tauri and Herbig Ae stars, on timescales varying from $\lesssim$hour to days. They derived $\dot{M}_{acc}$ variability ranging from 0.04 to 0.4 dex on timescales of days, while typical variations observed on timescales of hours are a factor of $\sim$4 smaller. Comparison with measurements obtained at a distance of years for a subset of objects allowed the authors to conclude that variability on the longer term is of the same order as that detected on day timescales. Similarly, Nguyen et al. (2009) and Fang et al. (2013) explored the $\dot{M}_{acc}$ variability, on timescales of months, from spectroscopic diagnostics for several tens of T Tauri stars in the regions Taurus-Auriga+Chamaeleon I and L1641, respectively. The first derived $\dot{M}_{acc}$ and monitored its variations from measurements of Hα 10% width and Ca II flux, and inferred a median variability estimate amounting respectively to 0.65 dex and 0.35 dex. The second measured the amount of accretion from the full width of the H_α line at 10% intensity, and inferred a typical $\dot{M}_{acc}$ variability of $\sim$0.6 dex.

All these studies show that $\dot{M}_{acc}$ variability on timescales from months to years is consistent with that observed on days timescales[18], which in turn amounts to $\sim$0.5 dex. This variability range is significantly smaller than the typical spread, of about 2 dex, observed at a given $M_\star$; hence, this spread cannot take origin from $\dot{M}_{acc}$ variability, at least that monitored on timescales

[18]This is also confirmed, in the case of NGC 2264, by the comparison between our results and the single-epoch U-band accretion survey performed, for a smaller sample of objects, by Rebull et al. (2002) (see Fig. 13 of Venuti et al. 2014).

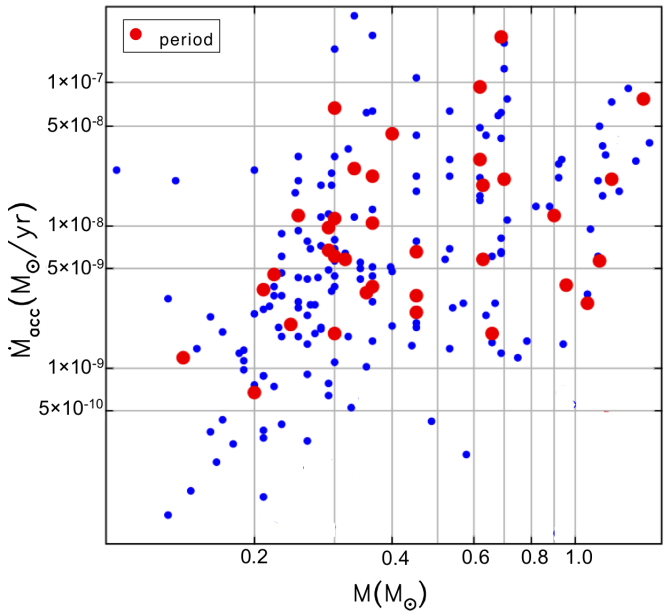

Figure 3.17: Distribution in $\dot{M}_{acc}$ vs. $M_{\star}$ of the subsample of objects, with known rotational period, whose UV excess light curve is examined to infer an estimate of the intrinsic variability–to–modulated variability ratio in the detected $\dot{M}_{acc}$ variability.

up to years.

$\dot{M}_{acc}$ variability: intrinsic vs. modulated

The amount of variability measured on $\dot{M}_{acc}$ takes contribution from both intrinsic accretion variability (non-steady accretion, hot spot evolution) and geometric effects linked with rotational modulation.

Assessing which contribution is predominant, on the average, on the timescales monitored here is of interest to better understand and characterize the dynamics of the accretion process onto the star. In order to investigate this point, I selected a subsample of objects, detections in $\dot{M}_{acc}$ on Fig. 3.13, whose rotational period is known and derived in the recent study of Affer et al. (2013), based on the light curves obtained with the *CoRoT* satellite during a previous campaign held in March 2008. I further imposed the condition that the period should be small enough to be able to retrieve more than one rotational cycle over the monitored time span, to trace the variations in UV excess at a given phase from one cycle to the other.

The distribution of objects in this subsample on the $\dot{M}_{acc}$ vs. $M_{\star}$ diagram is shown in Fig. 3.17. These span the range in $M_{\star}$ and $\dot{M}_{acc}$ fairly well; no members at the lowest accretion regimes detected ($\dot{M}_{acc} \leq 5 \times 10^{-10}$ $M_{\odot}$/yr) are included in the subsample, but this is due to the fact that those sources are too faint to be detected with *CoRoT*, and hence were not present in the Affer et al.'s (2013) sample.

Details on the procedure adopted to measure the contributions of instrinsic and of modulated variability to the total variability detected on the UV excess, and hence on $\dot{M}_{acc}$, are illustrated in Sect. 4.3 of Venuti et al. (2014). In brief, for each object, I folded the UV excess light curve in phase at the period extracted from Affer et al. (2013); I then measured the average rms scatter in UV excess values on hour timescales (i.e., obtained during the same observing night) and on days timescales (by dividing the phase range in bins of 0.05 and measuring, in each phase bin, the rms scatter among UV excess values detected at different rotational cycles). These two components (variability on hour timescales and variability from cycle to cycle) define the intrinsic variability

associated with $\dot{M}_{acc}$. I then summed up these two contributions, in the assumption that they are mutually independent, and compared their sum to the variability amplitude displayed in the UV excess light curve.

Results of this analysis show that rotational modulation determines, on the average, the most important contribution (up to ∼75%) to the variability range measured around the median $\dot{M}_{acc}$ on week timescales. Hence, for typical variability amplitude of about 0.5 dex in $\dot{M}_{acc}$, instrinsic accretion variability is expected to contribute on average only for about 0.15 dex. This estimate is consistent with the lower envelope of the $\Delta \log(\dot{M}_{acc})$ distribution in Fig. 3.16. In this picture of modulated variability, and assuming a homogeneous phase sampling, we would expect the typical $\dot{M}_{acc}$ state to correspond to the average luminosity state, with symmetric variability bars around it; this is well consistent with what we observe statistically across the sample.

3.5.3 Different accretion regimes/mechanisms

The discussion in Sect. 3.5.2 shows that variability on timescales of hours to years does not contribute significantly to the large spread in $\dot{M}_{acc}$ detected at a given value of $M_\star$ on Fig. 3.13. Hence, this spread appears to have a physical origin, which may be looked for in a variety of accretion regimes that co-exist within the same young stellar population, as well as in an effective evolutionary spread among cluster members. I address the first point in this section; the second point will be discussed in Sect. 3.5.4.

In Sect. 2.3, I introduced two morphologically distinct classes of disk-bearing objects in NGC 2264, which together represent an important fraction of the accreting population of the cluster.

The first class regroups those objects whose light curves are dominated by stochastic accretion bursts (Stauffer et al. 2014). These types of light curves had been predicted theoretically, e.g., by Kulkarni & Romanova (2008), but no supporting observational evidence could be achieved prior to our CSI 2264 campaign due to the high time resolution and photometric accuracy needed in order to resolve their characteristic flux bursts. Light curves belonging to this class appear as a stochastic sequence of short-lived luminosity bursts, superimposed over a less varying flux continuum; these bursts are interpreted to originate in an unstable accretion regime, dominated by Rayleigh-Taylor instabilities at the disk-magnetosphere boundary (Kulkarni & Romanova 2008) or by magnetorotational instabilities which modulate the accretion rate from the inner disk (Romanova et al. 2012). Stauffer et al. (2014) estimated a typical frequency of about a dozen bursts distributed over a period of 30 days, or a few bursts per rotational cycle. Analysis of our CFHT data showed that sources of this kind are among the objects with the largest UV excesses in our sample (see Fig. 4 of Stauffer et al. 2014). Indeed, stochastic bursters are found to populate the upper boundary of the $\dot{M}_{acc}$ distribution in Fig. 3.13, with a median accretion rate of $\sim 7 \times 10^{-8}$ $M_\odot$/yr measured across the group. This is well consistent with the theoretical predictions presented in Kulkarni & Romanova (2008), who assess that high accretion rates are a necessary condition for instabilities to develop. Variability bars around the median $\dot{M}_{acc}$ for this group of objects tend to be asymmetric, with larger amplitudes in the upper bar than in the lower bar, albeit with a broad scatter of values. This is consistent with the picture of an object with typical luminosity state in a "flat" minimum, interspersed by short-lived flux bursts.

At somewhat lower though significant[19] accretion rates in Fig. 3.13, we find the representatives of the second class of CTTS defined in Sect. 2.3, that is, objects whose light variations are dominated by fading events linked to variable circumstellar extinction (McGinnis et al. 2015).

[19]The average mass accretion rate measured across the variable extinction group, although being noticeably lower than that associated with the accretion burst group, is nevertheless larger than the average measured across the whole CTTS population probed here.

Their light curves exhibit an almost flat or slowly varying maximum interspersed by flux dips, which can reach depths of ∼1 mag and often present substructures in the minima. Such flux dips are associated with extinction events, due to circumstellar material that eclipses the stellar photosphere, in a geometric configuration where the star+disk system is seen at high inclinations (or almost edge-on). For a part of these objects, labeled AA Tau's after the prototype of the class (Bouvier et al. 1999, 2003, 2007a), these flux dips occur periodically; these are interpreted as arising from an inner disk warp spatially associated with the accretion columns formed in the interaction between an inclined magnetosphere and the inner disk. Objects which are part of this class typically display smaller UV excesses than stochastic bursters, and have typical mass accretion rates a factor of ∼3 lower, or about 2×10^{-8} $M_{\odot}$/yr. Again, variability bars measured around the median $\dot{M}_{acc}$ across this group of objects tend to be asymmetric, but contrary to the accretion burst group, the imbalance is in favor of the lower bar. This matches the picture of an object whose typical state is closer to the maximum luminosity state, interspersed by prominent flux diminutions.

McGinnis et al. (2015) suggest that the two distinct subclasses in the group of extinction-dominated objects, that is, objects with periodic, AA Tau-like flux dips vs. objects dominated by aperiodic extinction events, may be associated with two different accretion regimes. Namely, an aperiodicity in the circumstellar extinction events may indicate that accretion is ongoing in an unstable regime (e.g., Kurosawa & Romanova 2013), whereas an AA Tau-like behavior may correspond to a stable, funnel-flow accretion mode in which matter flows from the inner disk to the star surface in two high-density funnel streams, located opposite to each other, which follow the field lines along the shortest paths from the inner disk to the magnetic poles, in an inclined magnetosphere geometry (Kurosawa et al. 2008). In the latter picture, the accreting material is deposited on the star close to the magnetic poles, which would imply that an association is expected between the occultation events linked with the rotating accretion columns and hot accretion spots at the stellar surface. This property is indeed observed for several such objects in our sample, for which the measured EW in the Li I line increases for increasing brightness, hence suggesting that larger veiling, associated with the excess emission produced in the accretion shock, is observed at the epochs when the obscuration occurs (McGinnis et al. 2015).

In Fig. 3.13, I highlight, for comparison purposes, the accretion properties of objects belonging to a third light curve morphology class: those that present symmetric, periodic light curve variations suggestive of rotational modulation by hot spots (three examples of which are illustrated in Fig. 3.18). Stauffer et al. (2014) discuss some arguments in favor of their light variations being dominated by hot (rather than cold) spots: these objects exhibit Hα EW larger than the defining threshold for CTTS; they do not lie in the Class III-dominated regions of color-color diagrams in *Spitzer*/IRAC bands; in most cases, they display a significant UV excess. Based on the metrics that I will discuss in Chapter 4 to characterize the variability properties of WTTS and CTTS in the CFHT sample, we can add that many of these objects show $u - r$ color signatures consistent with hot spots and their $u + r$ variability amplitudes are best represented in terms of a hot spot distribution. The distribution in $\dot{M}_{acc}$ of these objects on Fig. 3.13 is overall consistent with that defined by variable extinction objects, with typical accretion rate of $\sim 10^{-8}$ $M_{\odot}$/yr, close to that measured across the variable extinction group. These properties suggest that hot spotted stars and AA Tau-like objects exhibit the same (stable) accretion regime. This association further indicates that the difference in light curve morphology between the two classes may simply be driven by inclination effects: when the systems are seen at low inclinations, hot accretion spots close to the magnetic poles are on sight, and these determine the characteristic pattern of luminosity modulation as the star rotates; conversely, high inclinations bring inner disk structures into view, which translate to periodic occultations of the stellar surface and AA Tau-type light variations.

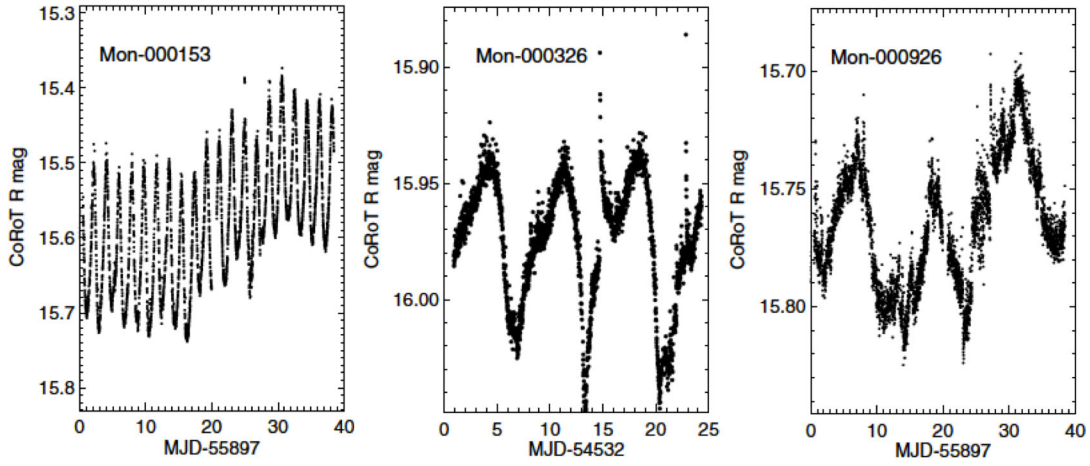

Figure 3.18: Three examples of light curves for NGC 2264 accreting members whose luminosity variations appear to be driven by geometric modulation from hot spots (from Stauffer et al. 2014).

3.5.4 Evolutionary spread across the cluster

In Sect. 3.5.3, I discussed how the huge spread in $\dot{M}_{acc}$, observed at any given value of $M_\star$, may reflect a variety of accretion regimes within the cluster, with unstable accretion prevailing at higher mass accretion rates and steady accretion mechanisms at more moderate accretion rates. Another factor that may effectively contribute to the observed $\dot{M}_{acc}$ spread is a non-negligible age spread, or equivalently evolutionary spread, across the cluster.

A number of studies have indicated that NGC 2264 has a hierarchical structure (see Sect. 2.1), with regions of active, current star formation embedded in a more widespread population of somewhat older stars (Sung et al. 2009). Embedded protostars co-exist with a rich sample of Class II/Class III objects and several OB stars; an age spread of a few to several Myr is generally recognized to be present within the cluster.

An estimate of individual ages for members of the cluster is typically inferred from their position on the HR diagram. When young cluster populations are represented on a HR diagram (as can be observed for NGC 2264 in Fig. 3.11), they often determine a large spread in luminosity, which is commonly interpreted as an indicator of age spread across the cluster. Age estimates for individual objects are then inferred by comparison with evolutionary PMS model tracks[20]. The distribution in accretion rates for CTTS cluster members can then be investigated as a function of age, to study any connection between the two variables.

This is illustrated in Fig. 19 of Venuti et al. (2014), for different mass bins. The median $\dot{M}_{acc}$ appears to define a clear anticorrelation trend with stellar age, with a decrease of about two orders of magnitude over a time span of ∼10 Myr. A fit to the $\dot{M}_{acc}$ vs. age distribution (for $M_\star \leq 1$ M$_\odot$) yields the relationship:

$$\dot{M}_{acc} = t^{-1.51}\,, \tag{3.21}$$

in agreement with previous estimates for the functional form of the decline of $\dot{M}_{acc}$ with age (Hartmann et al. 1998).

Age estimates inferred from isochrone fitting on the HR diagram are however quite uncertain and subject to systematics. For instance, lower ages appear to be more likely associated with more massive, hence more luminous, objects than with lower-mass objects in the sample.

[20] As discussed in Sect. 3.3, we adopt here the model grid of Siess et al. (2000)

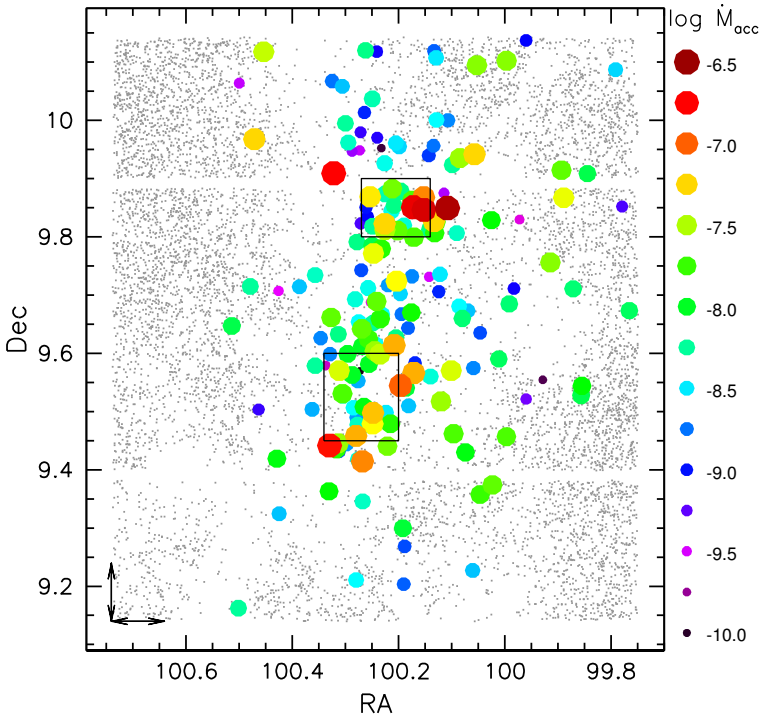

Figure 3.19: Spatial mapping of accretion properties in NGC 2264. Small grey dots indicate the distribution of field stars, large dots indicate accreting cluster members. Only objects with an actual $\dot{M}_{acc}$ detection are shown. Symbol colors and sizes are scaled according to the value of $\dot{M}_{acc}$. The black boxes mark the regions of maximum stellar density in the cluster (from Lamm et al. 2004). Double arrows mark a physical distance of 1.5 parsecs.

Moreover, recent studies (Baraffe et al. 2009) have suggested that the luminosity spread on a HR diagram typical of young clusters may actually not correspond to an actual age spread, but simply be the result of the individual episodic accretion history, whose dynamics may mimic an age spread of up to a few Myr for coeval stars.

More unbiased and less controversial indications on a possible age spread among accreting cluster members can be obtained from characterizing their spatial distribution in relation to the measured $\dot{M}_{acc}$. This may also provide interesting information on the evolution dynamics of the cluster. An illustration of this analysis is shown in Fig. 3.19. CTTS are indicated as large dots on the (RA, Dec) diagram of the cluster; colors and sizes of the dots are scaled according to the value of $\dot{M}_{acc}$. Most accretors appear projected onto the cluster; a part of the population of accreting or mildly accreting members are instead located on the peripheral regions. This diagram provides evidence for a non-homogeneous spatial distribution of objects in the various accretion regimes: the strongest accretors tend to be concentrated close to the two known active sites of star formation within the cloud, located at a distance of a few parsecs one from the other, while the population of more moderate accretors tends to be more evenly distributed throughout the whole cluster. The halo of members is spread over a region of few parsecs around the star-forming sites.

This non-homogeneous distribution of mass accretion rates may be the product of sequential star formation: the youngest stars, likely the most actively accreting, are indeed expected to distribute more compactely close to their birth sites, while dynamical evolution over a few Myr (the average age of the cluster) can explain displacements up to a few parsecs relative to

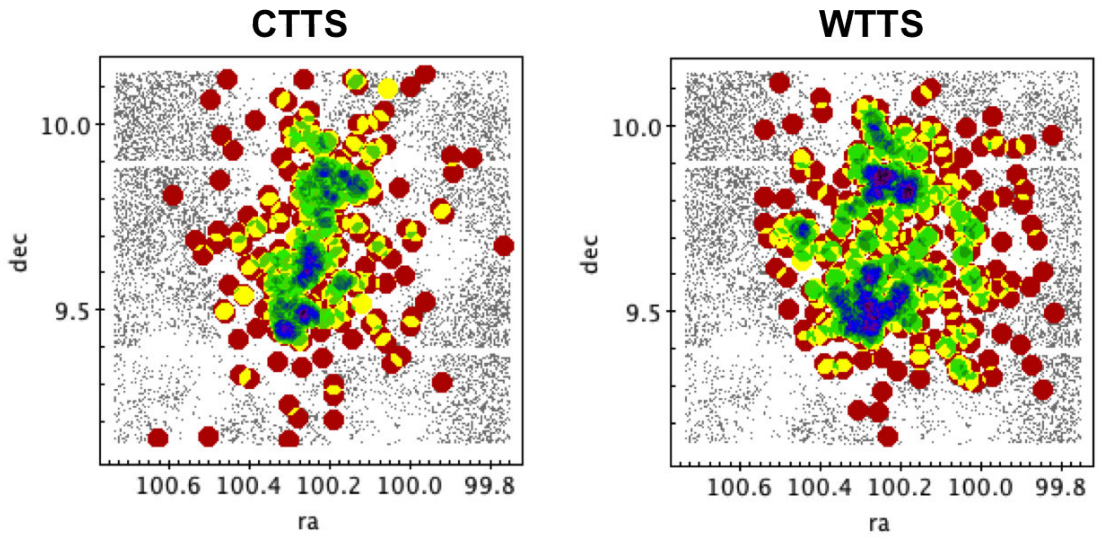

Figure 3.20: Density maps of the spatial distribution of CTTS (left panel) and WTTS (right panel) cluster members across the region. Color gradation from red to violet marks increasing number density. Field stars are shown as small grey dots in the background.

the original location where stars were formed[21]. If this is the case, the distribution of $\dot{M}_{acc}$ also reflects the presence of an intrinsic age spread within the region, hence corroborating the interpretation in terms of a time evolution over different ages.

An interesting contribution to this discussion would arise from a comparison of the spatial distribution of CTTS to that of WTTS across the region. If WTTS are on average more evolved than CTTS, then we would expect them to be statistically more widespread around the star-forming sites than CTTS. This comparison is shown in Fig. 3.20. For both populations (CTTS and WTTS), the highest concentrations of objects are found projected close to the two known active sites of star formation within the cloud. This can be understood if we assume that, after formation, young stars dynamically evolve isotropically from their birth sites. However, it can be observed that WTTS are distributed more uniformly, and across a wider area, around the star formation poles than CTTS, which are instead more concentrated in the inner regions of the cluster. This would support the idea that the spatial distribution of members statistically reflect their evolutionary status.

I adopted the statistical method of the "minimum spanning tree" (Prim 1957) to investigate further and quantify the spatial compactness of "younger" cluster members (on a model-based age scale) relative to older ones. This method consists in computing the minimum path-length required to connect all points of a given sample in a network of direct point-to-point links with no closed loops. Shorter path-lengths will hence identify more compact populations. Details on this analysis for the NGC 2264 CTTS population were reported in Sect. 5.4 of Venuti et al. (2014) (see Appendix B of this manuscript). We did recover some hints of a more compact spatial distribution for younger members than for older ones; however, the statistics at the lower and higher age ends in our sample is not sufficiently large to extract conclusive evidence from this analysis. On the other hand, the clumpy structure of the cluster, with at least two separate poles of star formation activity a few parsecs away, translates intrinsically to somewhat larger intra-cluster distances and more complex cluster evolution, which is reflected in the path-length measured with the minimum spanning tree approach.

[21]Typical expected velocities for young stars relative to the center of mass of the stellar system amount to ∼1 km/s, or 1 pc/Myr (see, e.g., Bate 2009).

Useful indications on the evolutionary state of the systems can be derived from the α_{IRAC} index. This is compared to the $\dot{M}_{acc}$ measurements, for different mass bins, in Fig. 20 of Venuti et al. (2014). The two quantities are statistically correlated, in the sense that larger values of α_{IRAC}, indicative of dustier inner disks, typically correspond to larger accretion rates; conversely, the average accretion rates decrease as disks become more evolved, although a significant spread is associated with this global trend in each mass group.

3.6 Conclusions

In this chapter, I have presented the results of an extensive photometric investigation of accretion properties in the young open cluster NGC 2264. This chapter provides an expansion of the study published in Venuti et al. (2014). The analysis was based on 4-color (u, g, r, i) single-epoch photometry and on two-week-long $u + r$ monitoring of the cluster obtained at the CFHT with the instrument MegaCam. The survey encompassed a population of about 750 young cluster members, about 40% of which display evidence of disk accretion. To ensure internal consistency, I performed an extensive determination of stellar parameters for the whole sample, using CFHT photometry as well as additional archival data at different wavelengths.

I investigated accretion properties by characterizing and measuring the UV flux excess distinctive of CTTS relative to non-accreting young stars (WTTS). This excess is primarily detected in the u-band. I compared this diagnostics with others commonly adopted proxies of accretion (Hα emission, IR excess) and could ascertain their consistency. From a UV excess-related perspective, I performed a new membership study of the cluster on various color-color and color-magnitude diagrams, which enabled me to identify 50 new candidate members with signatures of accretion. Several of these are spatially located in the periphery of the cluster.

An empirical conversion was used to derive accretion luminosities and mass accretion rates $\dot{M}_{acc}$ from the measured UV excess. $\dot{M}_{acc}$ values detected across the CTTS population of the cluster were found to vary from $\lesssim 10^{-10}$ M$_\odot$/yr to $> 10^{-7}$ M$_\odot$/yr over the mass range 0.1–1.5$M_\star$. The average $\dot{M}_{acc}$ statistically correlates with $M_\star$; I applied a rigorous statistical technique to evaluate correlations in presence of censored data (upper limits) and derived $\dot{M}_{acc} \propto M_\star^{1.4\pm0.3}$. This relationship is determined and appears to be robust over the whole mass range explored in this study, although some indications of a mass dependence in the actual $\dot{M}_{acc}$–M$_\star$ correlation (steeper in the M$_\star < 0.3$ M$_\odot$ regime, shallower at larger masses) may be deduced from the data.

A significant feature of the $\dot{M}_{acc}$ vs. $M_\star$ distribution inferred here is the large spread in $\dot{M}_{acc}$ detected at any given stellar mass, which extends up to over 2 dex. I show that little contribution to the spread in the $\dot{M}_{acc}$ vs. $M_\star$ distribution arises from $\dot{M}_{acc}$ variability, which is found to amount to ∼0.5 dex on the average, on days to months timescales; hence, the spread in $\dot{M}_{acc}$ observed has another physical origin.

One possible contribution to the measured spread may arise from a variety of accretion regimes at play in different systems across our sample. Unstable accretion regimes, driven by instabilities at the magnetosphere-disk boundary, are found to be dominant at the largest $\dot{M}_{acc}$. These manifest as short-lived, stochastic accretion bursts. In contrast, stable, funnel-flow accretion regimes, with a steady behavior over many rotational cycles, are found at more moderate accretion rates and are likely responsible for the well-behaved, hot spotted light curves as well as for AA Tau-like objects, depending on the viewing angle to the systems.

The observed dispersion in $\dot{M}_{acc}$ could also result from an age spread in the cluster. Indeed, the strongest accretors are found to be predominantly located close to the active sites of star formation within the cluster, which suggests that they are comparatively younger than objects which accrete in more moderate regimes. The latter are more uniformly distributed across the region, which suggests that they have evolved dynamically from their original birth sites.

Chapter 4

The UV variability of young stars in NGC 2264

Contents

In this chapter, I investigate and chacterize the variability signatures at short wavelengths that pertain to different types of YSO variables. I first concentrate on the photometric variability exhibited on day timescales (mid term); I examine different indicators to map the level of variability across the sample of objects, and explore the connection between photometric behavior and accretion activity in the CTTS group. I adopt a spot-modulated description of mid-term variability to account for the different amplitude ranges and color variation trends across the sample, and derive a statistical depiction of the main variability features specific to CTTS as opposed to WTTS. Finally, I compare the amount of variability on day timescales to that measured on shorter (hours) and longer (years) timescales, to investigate the dynamics and timescales of interest for the accretion process. An Appendix to this chapter, consisting of the publication issued from this part of the work, is included in the manuscript (Appendix C).

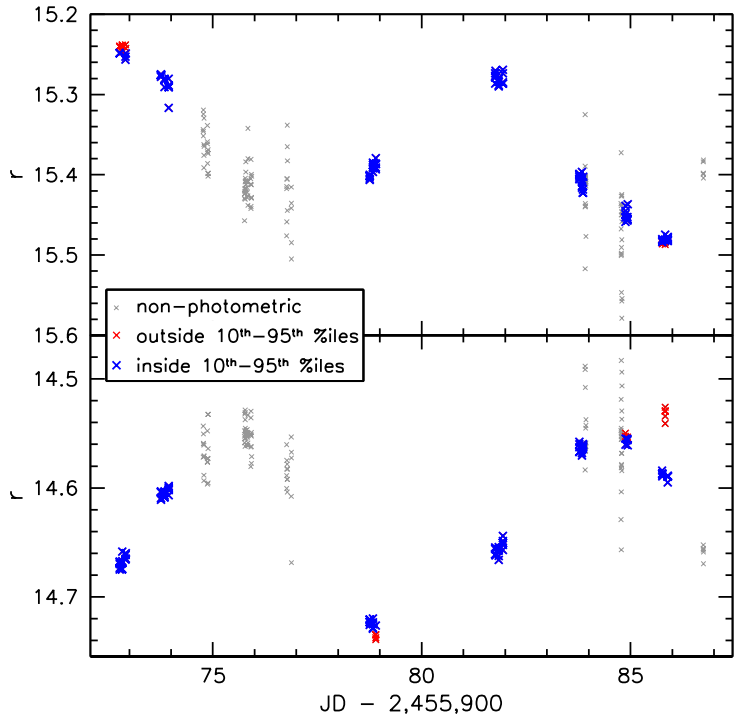

Figure 4.1: Two examples of CFHT r-band light curves for two WTTS members of NGC 2264. Different colors identify different sets of light curve points, discussed in the text: gray indicates observations obtained in non-photometric nights or sequences, which were rejected for the present analysis; red corresponds to light-curve points brighter than 10^{th} percentile or fainter than 95^{th} percentile in magnitude; blue marks data points comprised between the two aforementioned percentile levels.

4.1 A closer look at photometric variability in the CFHT sample

Fig. 4.1 shows two examples of r-band light curves obtained for two WTTS members of NGC 2264 in the CFHT/MegaCam survey. As discussed in Sect. 2.2.2, the CFHT observations consisted of a simultaneous monitoring of u-band and r-band variability that extended over 11 nights during a 14-day-long instrument run, from February 14 to 28, 2012. This ensured adequate time sampling to reconstruct the variability pattern exhibited by objects in the field on a timescale of a couple of weeks, which corresponds to two or three rotational periods for a typical cluster member (Affer et al. 2013). In addition, on each night of observations the region was imaged repeatedly (typically three pointings per night spaced by one or two hours), to probe the short-term variability. Each observing sequence was composed of five dithered exposures in the u-band and five dithered exposures in the r-band.

While several nights during the observing run were photometric, a few were somewhat cloudy. This results in poorer signal-to-noise ratio for observations obtained during these nights relative to those with good observing conditions, and, consequently, in a larger scatter among measurements from different dithered exposures within single observing sequences (as illustrated in Fig. 4.1, for the observing epochs highlighted in grey). Since this would impact the analysis of variability in the light curves, we decided to isolate all data points obtained in non-photometric conditions and discard them from the start.

To identify the observing sequences that were obtained in poorer conditions, I examined the full ensemble of about 8 000 field stars detected in the MegaCam FOV. For each of these and

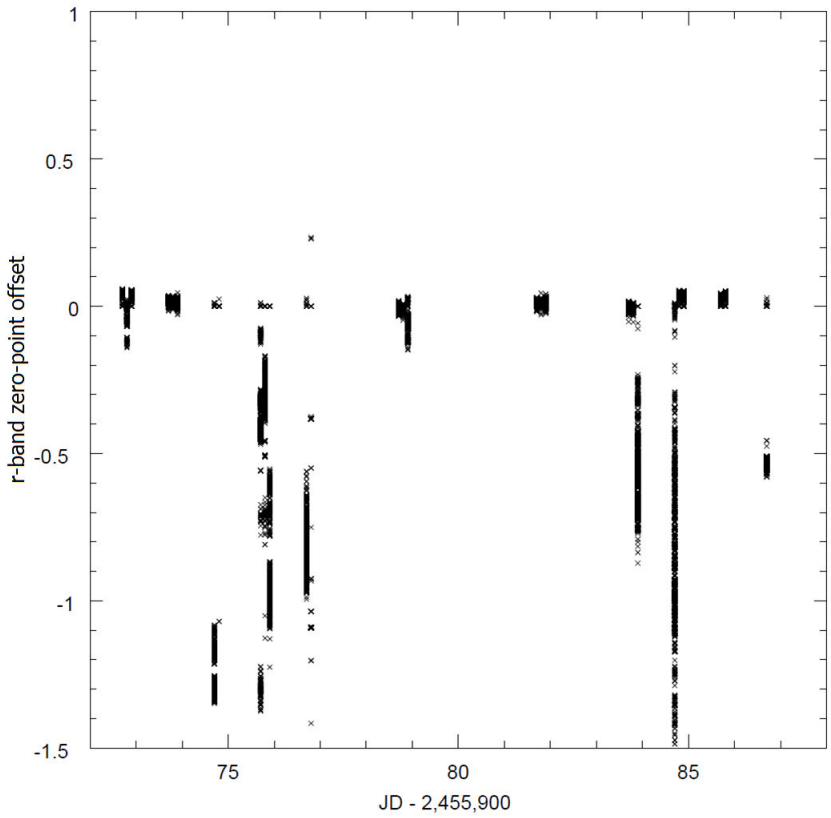

Figure 4.2: Distribution of median zero-point offsets relative to the master frame, for each observing epoch, across the population of field stars detected in the MegaCam FOV. Each point on the diagram corresponds to the median zero-point offset estimated for a single star in the corresponding observing sequence. Each vertical stripe of points is referred to a single observing sequence (for a typical night of observations, e.g. Julian Date = 2 455 972, three observing sequences were on average performed, e.g. J.D. = 2 455 972.7 – 2 455 972.8 – 2 455 972.9, which then determine a set of three stripes close to each other before J.D. = 2 455 973 on the diagram).

for each observing sequence, I computed the average zero-point offset relative to the master frame; I then computed the median zero-point offset associated with the full light curve and measured the difference between zero-point offsets for individual observing sequences and the median zero-point offset for the source in the whole monitoring.

The results of this procedure are illustrated in Fig. 4.2 for the r-band (a similar analysis was performed in the u-band). In several cases, the distribution of residues between single-sequence zero-point offsets and median zero-point offsets across the full sample of objects appears to be concentrated close to zero on the diagram, which indicates that the corresponding observing epoch was obtained in typical observing conditions. On the other hand, at some epochs (e.g., nights on J.D. from 2 455 974 to 2 455 976, values truncated at the unity), the zero-point offset residues measured for most stars in the field are largely negative. This indicates that the corresponding observations were carried out through clouds. Furthermore, on a few dates of observations (e.g., J.D. = 2 455 983 or 2 455 984), observing conditions appear to have evolved during the night, with clear sky for some of the observing sequences obtained on those dates, and poor transparency for some others.

The analysis of the diagram in Fig. 4.2, and of its analogue in the u-band, allowed us

to identify a number of observing sequences, performed in non-photometric conditions, that were rejected. Table 1 of Venuti et al. (2015) (whose full text is reported in Appendix C of this manuscript) provides a detailed list of all the observing epochs, obtained during the CFHT/MegaCam monitoring survey of NGC 2264, which were retained for the study of variability presented in the following. These amount to 18, acquired on 7 nights distributed throughout the two-week-long instrument run.

A $5\,\sigma$-clipping routine was adopted to discard occasional largely discrepant spurious points. Our time series photometry takes contribution from two different timescales of variability: i) the short-term ($\lesssim$hours), which is dominated by short-lived events (like flares or bursts), and ii) the mid-term ($\sim$days, or of the order of the rotation period of cluster members), which is dominated by geometric effects of rotational modulation. In my study, I will focus primarily on the latter timescales; discussions earlier in Sect. 1.4.1 and 3.5.2 indicate that this is a most interesting standpoint to investigate the dynamics of the processes that govern the physics of these young stars, at least on baselines of up to several years. In order to smooth out the contribution from short-term variability, and to reduce the impact of photometric noise on the detected amplitudes of variability, I computed the 10^{th} and 95^{th} percentile levels on the magnitude-ordered light curve and disregarded all data points which fell either at brighter magnitudes than the 10^{th} percentile or at fainter magnitudes than the 95^{th} percentile. These cut levels were determined upon visual examination of the full statistical sample of light curves. A typical CFHT light curve in our dataset is composed of about 100 points (about twenty observing sequences, with five dithered exposures, hence five light curve points, per sequence). Therefore, for a modulated light curve with period of about 4 days, for which we detect about three minima and maxima, neglecting all points with magnitude fainter than the 95^{th} percentile translates to removing slightly more than one point per observed minimum. Since all dithered exposures in a given observing sequence were obtained consecutively, these are spaced by a few minutes at most; hence, the scatter among measurements from dithered exposures that are part of the same observing sequence, on the low-luminosity state, likely reflects photometric noise only. Thus, applying this 95^{th} percentile filter enables reducing the contribution from photometric noise to the observed variability amplitudes. A more severe threshold (10^{th} percentile) was adopted at the brighter mag end; this choice was aimed at properly omitting flares, which typically affect a couple consecutive observing sequences (rise and/or decline on timescales of hours).

These selective levels were implemented in an automated routine to process the full sample of light curves. The results of this analysis are illustrated in Fig. 4.1 for two examples of WTTS light curves among NGC 2264 members. At the end of the routine, I visually inspected similar diagrams for all individual objects, to ascertain accurate point selection. In a few tens of cases, this automatic routine introduced a bias on the measured amplitudes; this could happen, for instance, when light-curve minima or maxima occurred close to non-photometric nights (discarded), or when a given set of data points was correctly discarded in one filter but not in the other, due, e.g., to different scatter properties associated with the same observing sequence in the two bands. For these cases, the point selection was corrected by hand.

Light curves processed as detailed above constitute the dataset analyzed for the variability study presented in the following.

4.1.1 Measuring the variability of CTTS and WTTS: light curve rms

A first map of variability properties for different groups of stars across the sample can be obtained by measuring the light-curve dispersion around the average photometric level. Non-variable stars are expected to be associated with flat light curves, with only weak, stochastic fluctuations around their mean brightness due to the photometric noise that affects every measurement. On

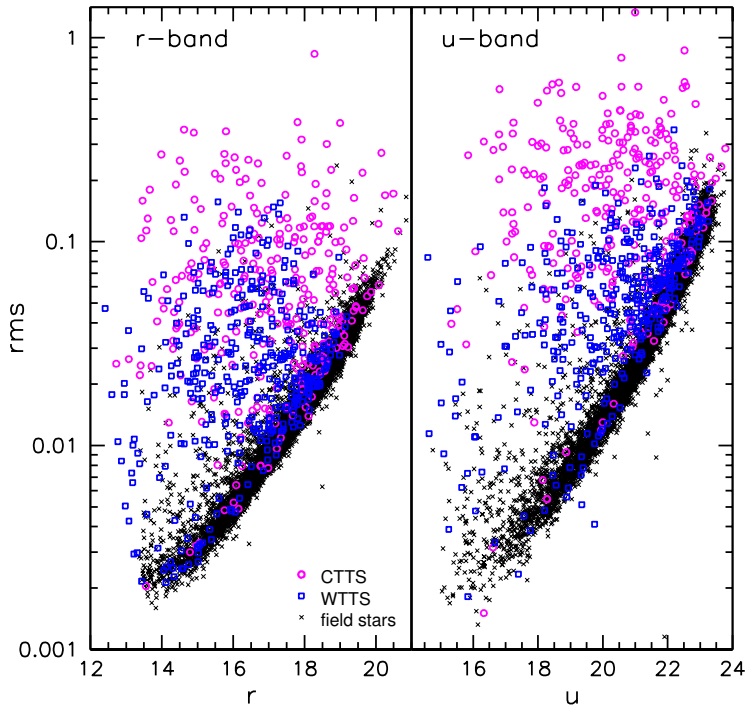

Figure 4.3: r-band (left panel) and u-band (right panel) light-curve dispersion as a function of magnitude for different groups of monitored objects: field stars (black crosses), accreting NGC 2264 members (CTTS; magenta circles), and non-accreting members (WTTS; blue squares).

the other hand, light curves of intrinsically variable stars are expected to exhibit a significantly larger root-mean-square (rms) variation than that expected for photometric noise.

In Fig. 4.3, the rms variability level exhibited by young members of NGC 2264 is compared to that of main-sequence dwarfs in the field. Cluster members are further distinguished in CTTS and WTTS, following the classification scheme discussed in Sect. 3.1.2 and 3.2.

The light curve rms measured for field stars as a function of magnitude defines both in r and in u the photometric noise level at a given brightness. We fitted an exponential curve to the lower envelope of the field star distribution, both in u and in r, to derive an analytic expression of the photometric noise as a function of magnitude, with equations:

$$err_u = 0.0033 + \exp\left(0.847\,u - 20.99\right) ; \tag{4.1}$$

$$err_r = 0.0031 + \exp\left(0.804\,r - 18.54\right) . \tag{4.2}$$

These provide an estimate of the lowest, magnitude-dependent, noise component expected to affect our photometry.

In each (m, rms_m) diagram, the young stars exhibit a distinct level of intrinsic variability over the photometric noise sequence; furthermore, accreting and non-accreting members tend to occupy statistically distinct though overlapping regions, with a median rms value 2.5 times higher for the first group than for the second, and increasing in both cases from the r to the u band. A two-sample Kolmogorov-Smirnov test (Press et al. 1992), aimed at comparing the distribution in rms of accreting members to that of non-accreting objects both in u and in r, attests to the significantly different nature of the two populations with respect to the property investigated, with a probability for the null-hypothesis of 10^{-24} in r and 10^{-37} in u. For fainter objects, the

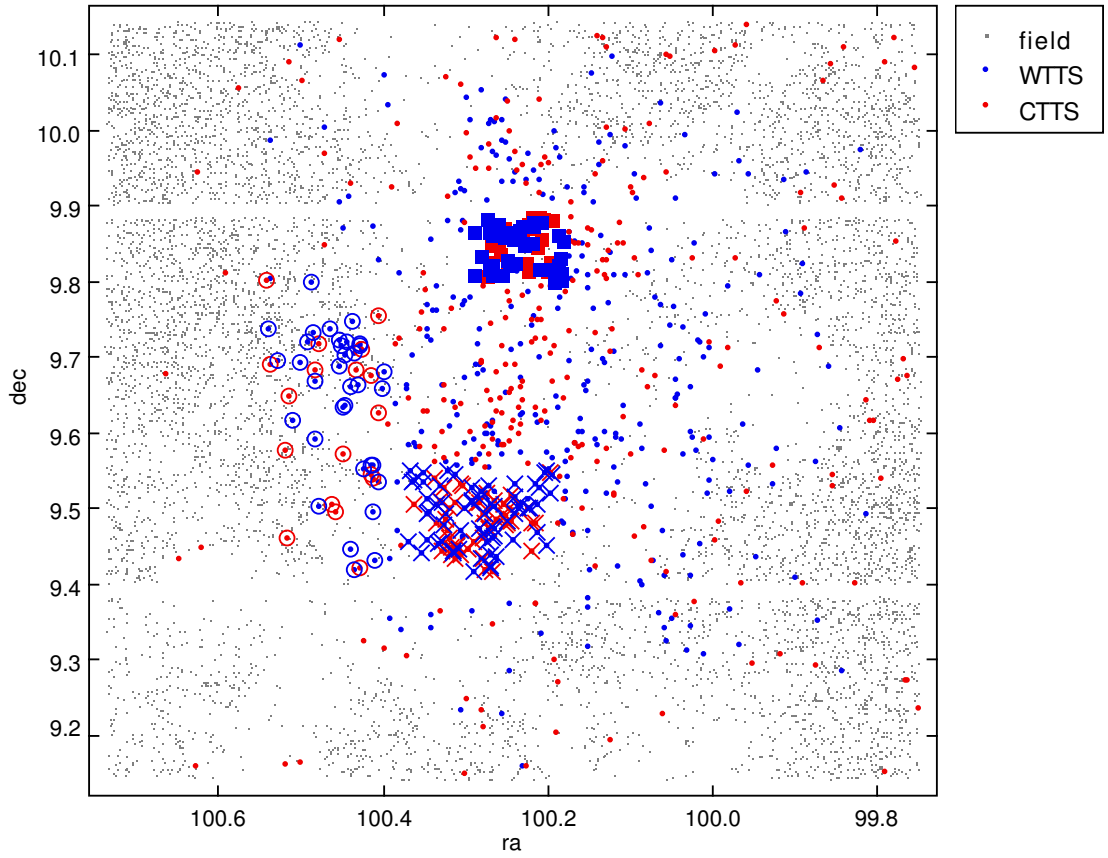

Figure 4.4: Selection of three sub-fields, in the NGC 2264 region, to test any association between the level of *rms* variability measured for WTTS/CTTS and the spatial location of the objects in the cluster. Blue indicates WTTS members, red indicates CTTS members; field stars are marked as small grey dots. The two sub-fields dotted with crosses or squares are projected onto the two known active sites of star formation within the cluster (or equivalently the regions with the highest concentration of variable objects in the cluster, from Lamm et al. 2004), while circles mark cluster members located in the selected sub-field on the peripheral area of the molecular cloud associated with the cluster.

photometric noise that affects the light-curve measurements becomes more important, especially in the u band, which results in a certain degree of overlapping between the loci of variable and non-variable stars.

One might wonder whether the spatial association with nebulosity might affect the level of *rms* variability detected for these objects, notably for CTTS. It is reasonable to assume that disk-bearing objects, supposedly in an earlier stage of stellar evolution, are statistically more embedded and concentrated in regions of the sky with bright nebulae, compared to other stars in the field. This might introduce an additional component of *rms* scatter in their light curves, due to variable seeing, that would artificially increase the level of "variability" measured for these objects relative to WTTS or field stars at the same brightness, especially for fainter objects and in the u-band.

In order to test this, I selected three small areas on the NGC 2264 field (as illustrated on Fig. 4.4). Two of these are projected onto the active sites of star formation in the cluster, while the third encompasses a more peripheral region. I then pinpointed all CTTS and WTTS that fell in each of these sub-fields, and adopted a Kolmogorov-Smirnov (KS) test to compare i) the distribution in rms_u of CTTS to that of WTTS inside each sub-field, and ii) the distributions in rms_u detected for separate groups of CTTS, located in different areas within the region (and

similarly for WTTS).

For the following discussion, I will refer to the northern subfield projected onto the cluster (marked with squares on Fig. 4.4) as F_1, to the southern subfield projected onto the cluster (crosses on Fig. 4.4) as F_2, and to the subfield selected on the periphery of the cluster (circles on Fig. 4.4) as F_3. Results of the KS test to compare how CTTS vs. WTTS distribute in rms_u inside fields F_1 and F_2 indicate that the null hypothesis of two samples extracted from the same parent distribution is rejected to a p-value of 5×10^{-5} and 6×10^{-9}, respectively. In both subfields, the CTTS population exhibits significantly higher variability than the WTTS population. In F_3, the result of the test indicates that the null hypothesis is rejected to a significance level of 5%, but not to a significance level of 1% (p-value = 0.02).

When applying the KS test to compare the distributions in rms_u of CTTS from fields F_1 and F_2, the null hypothesis is retained with a p-value of 0.6; hence, the two subgroups of CTTS display the same statistical variability properties. A borderline result is instead obtained when comparing the CTTS populations in F_1 and F_3 and in F_2 and F_3, with a p-value of 0.04.

However, when comparing the distributions in rms_u of the WTTS populations in the different subfields among themselves, no statistical differences are detected through the KS test: p-values of 0.7, 0.98 and 0.9 are obtained for the F_1 vs. F_3, F_1 vs. F_2, and F_2 vs. F_3 cases, respectively. This indicates that the distribution in variability properties derived for WTTS is independent of their spatial location in the field. This suggests that nebulosity has no significant impact on the variability level we measure across our sample: if this were not true, we would expect its impact to affect both the CTTS and the WTTS populations in a similar way. We would then expect to observe significant differences in rms_u distributions when comparing WTTS from fields F_1 or F_2 with those extracted from the area F_3. Since this is not observed, we may then conclude that the rms measurements are not significantly affected by the nebulosity component. The more ambiguous result obtained when comparing the variability properties of CTTS and WTTS in F_3, or those of CTTS from F_1 or F_2 with CTTS from F_3, may then perhaps be interpreted in evolutionary terms, with CTTS members located in peripheral regions being statistically older, and hence more similar to WTTS, than those more embedded in the cluster (see also discussion in Sect. 3.5.4).

4.1.2 Measuring the variability of CTTS and WTTS: Stetson's index J

A more accurate variability tracer applied to homogeneous and contemporaneous multiwavelength datasets is the index J defined in Stetson (1996). This measures the amount of correlated variability monitored in two different filters; this variability indicator hence suffers significantly lower contamination from stochastic noise. To compute the value of J for a given source, each point in the u-band light curve is biunivocally paired with the closest r-band epoch (that is, the first u-band exposure in a given observing sequence is paired with the first r-band exposure obtained in that same sequence and so on). Since each observing sequence was composed of five dithered exposures in u and five dithered exposures in r, obtained consecutively, paired u-band and r-band measurements are at an average separation of 10 to 15 minutes; these can thus be considered simultaneous compared with the timescale of days investigated here. For a given object in our sample, Stetson's variability index is defined as

$$J = \frac{\sum_{i=1}^{n} w_i \, \mathrm{sgn}(P_i)\sqrt{|P_i|}}{\sum_{i=1}^{n} w_i} \, , \tag{4.3}$$

where:

- i is the time index across the series;

- n is the total number of simultaneous u, r observation pairs (typically 98, distributed over two weeks);
- w_i is a weight, associated to the contribution from the i^{th} pair to the sum, defined as (see also Fruth et al. 2012)
$$\exp\left\{-\frac{\mathrm{abs}\left[t_i(u)-t_i(r)\right]}{<\mathrm{abs}[t(u)-t(r)]>}\right\} ,$$
where t_i is the time of the i^{th} measurement and $<\mathrm{abs}\,[\mathrm{t(u)\text{-}t(r)}]>$ is the mean temporal separation between paired measurements[1];
- sgn is the sign function;
- P_i is the product of the normalized residuals of two paired observations,
$$\left(\sqrt{\frac{n}{n-1}}\right)^2\left(\frac{u_i-<u>_\sigma}{\sigma_i(u)}\right)\left(\frac{r_i-<r>_\sigma}{\sigma_i(r)}\right) ,$$
where $<u>_\sigma$ and $<r>_\sigma$ are the error-weighted mean magnitudes in u and r light curves, u_i and r_i are the measurements corresponding to the i^{th} observation pair in the time series and $\sigma_i(u)$ and $\sigma_i(r)$ are the instrumental errors associated to the i^{th} observation pair.

A spurious variability component, merely due to random noise, is expected to statistically average to zero throughout the whole time series. Conversely, in the assumption that variability observed in the optical and in the UV for these young stars originates from the same process, a definite correlation is expected to exist between u-band and r-band behavior for a truly variable star; this would result in values of J significantly different from zero.

Fig. 4.5 shows the J distribution for cluster members and field stars in our survey. Field stars are predominantly located on a narrow, horizontal sequence centered on J=0, independent of the brightness of the objects. Table 4.1 lists the typical J and rms dispersion around this value measured, as a function of magnitude, on the field star locus in Fig. 4.5. To derive this reference J-value sequence, I divided the magnitude range into bins of 0.5 mag, and then applied an iterative $3\,\sigma$-clipping routine, in each bin, to compute the typical J value and the corresponding σ. A larger mag bin, of 1 magnitude instead of 0.5, was adopted at the bright end of the distribution to account for the fact that this brightness regime is less populated than the fainter ones. The lower statistics available at brighter magnitudes is also reflected in the larger uncertainty associated with the measurement of the typical J in this mag bin, as deduced from Table 4.1.

A low percentage of field stars ($\sim$3%) shows a significant amount of variability, attributable either to occasional spurious points or to an intrinsic variable nature (e.g., binaries, pulsators, active stars). Among NGC 2264 members, about 63% show clear variability above the J sequence traced by field stars at the $3\,\sigma$ level (75% at $1\,\sigma$ level); this percentage rises to 72% (81%) when considering the accreting members alone. As for Fig. 4.3, CTTS display a significantly higher level of variability than WTTS; the typical J value measured across the first groups is three to four times larger than that measured in the second group. Fewer CTTS with high values of J are detected at fainter magnitudes compared to brighter magnitudes. This might be a bias due to the fact that fainter objects are typically affected by more conspicuous photometric noise, as illustrated in Fig. 4.3, and hence measurements of the intrinsic variability level through the J index analysis may be more difficult in these cases.

[1]This weight is introduced to account for the actual time distance between paired measurements, which can vary slightly along the time series. In the weighted sum, pairs built using points closer in time will then contribute more to the total than those which combine more distant measurements.

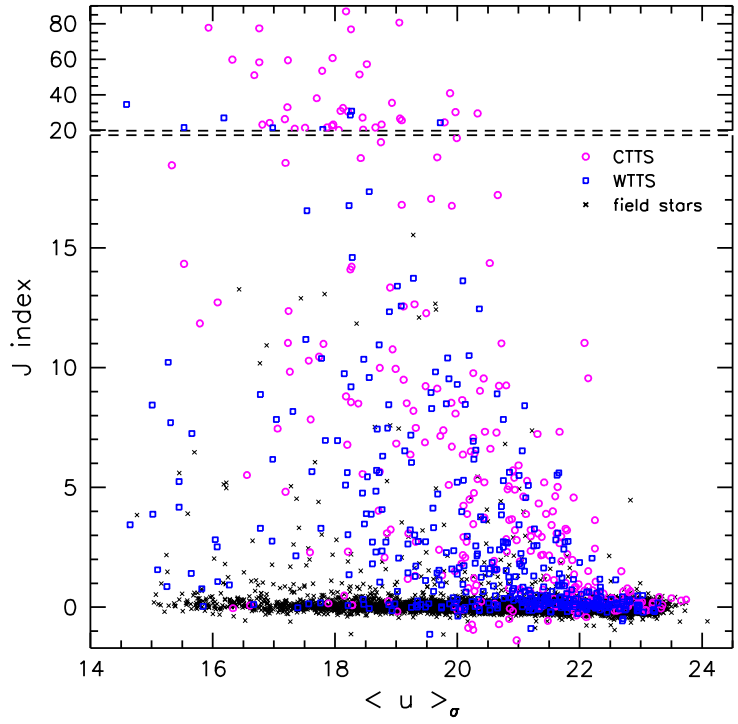

Figure 4.5: Stetson's (1996) J index of correlated UV/optical variability as a function of u-band magnitude for different groups of monitored objects: field stars (black crosses), accreting NGC 2264 members (CTTS; magenta circles), and non-accreting members (WTTS; blue squares).

u-mag (bin center)	J index	σ
15.50	0.20	0.20
16.50	0.10	0.20
17.25	0.03	0.13
17.75	0.04	0.13
18.25	0.04	0.17
18.75	0.04	0.13
19.25	0.02	0.12
19.75	0.03	0.13
20.25	0.02	0.14
20.75	0.02	0.13
21.25	0.02	0.13
21.75	0.02	0.14
22.25	0.02	0.14
22.75	0.02	0.14
23.25	0.01	0.15

Table 4.1: Typical value of Stetson's (1996) index J, and corresponding rms dispersion, measured, as a function of magnitude, for MS stars in the MegaCam FOV.

I used the J-index diagnostics to select a "clean" sample of variable cluster members, i.e. those objects which exhibit a definite level of photometric variability above the noise sequence traced by field stars. Truly variable stars were selected upon having J at least $3\,\sigma$ larger than the typical value, at the corresponding brightness, on the dwarf locus in Fig. 4.5 (see reference values listed in Table 4.1). Flux variations for sources which exhibit lower variability than this threshold are potentially noise-dominated.

Objects selected above the non-variable star sequence amount to 215 CTTS and 212 WTTS. These constitute the sample of variable members that I will explore in the following to investigate the connection between the observed signatures of photometric variability and the physics of these young stars, with special consideration for the accretion process.

4.2 The imprints of disk accretion in UV variability

4.2.1 A comparison between UV excess and u-band variability

Sect. 4.1 illustrates that CTTS are statistically more variable than WTTS. This is true in the optical, but especially evident at shorter wavelengths (u-band). This enhanced UV variability suggests that disk accretion mechanisms, which are distinctive of CTTS with respect to WTTS and whose signatures can be most directly detected in the UV, play a primary role in determining the luminosity variation pattern observed for these objects. Insights on the dynamics of accretion and star-disk interaction may hence be obtained from a detailed characterization of the monitored variability signatures.

In Fig. 4.6, I investigate the connection between the intensity of accretion and the level of UV variability, by comparing the UV excess measurements, derived from the $u-r$ colors of the objects as detailed in Sect. 3.4.1, to the u-band rms measured on the light curves for variable cluster members. The rms_{obj} reported on the y-axis is an estimate of the intrinsic level of rms variability in the light curve, computed as $rms_{obj} = \sqrt{rms^2_{meas} - rms^2_{noise}}$, where rms_{meas} is the actual rms dispersion measured around the average light curve brightness and rms_{noise} is the photometric error estimate derived from Eq. 4.1–4.2. $E(u-r)$ measurements are reported on the diagram for both the CTTS and WTTS samples[2], for comparison purposes. In the latter case, the UV excess definition has no straightforward interpretation, but it provides an estimate of the scatter in color of WTTS around the reference sequence.

The existence of any significant correlation relationship between UV color excess and u-band rms variability, both in the WTTS and CTTS groups, was probed by means of a Spearman's non-parametric, rank correlation test (Press et al. 1992). This test provides a measure of how well the trend among the data can be described in terms of a monotonic function: abscissa and ordinate of each data point are replaced with the values of their ranks among the ordered series of x-values and y-values in the whole sample of N elements; Spearman's correlation coefficient ρ is then defined as Pearson's correlation coefficient between the ranked variables. To assess the significance of the result, the ρ value is translated to the variable $t = \rho\sqrt{(N-2)/(1-\rho^2)}$, which follows approximately Student's distribution (e.g. Abramowitz & Stegun 1972) with N-2 degrees of freedom under the null hypothesis.

Little, if any, indication of correlation is obtained from the test for the population of WTTS. Conversely, direct evidence of a correlation between the accretion process and the level of photometric variability exhibited at short wavelengths is inferred from the distribution of accreting

[2] As discussed in Sect. 3.4.1, the reference color sequence built for measuring the color excess of accreting stars on $u-r$ is ill-defined on the bright end, due to the limited population and to the large data point scatter in this region of the r vs. $u-r$ diagram. For this reason, only objects fainter than 14.5 in r are displayed on Fig. 4.6.

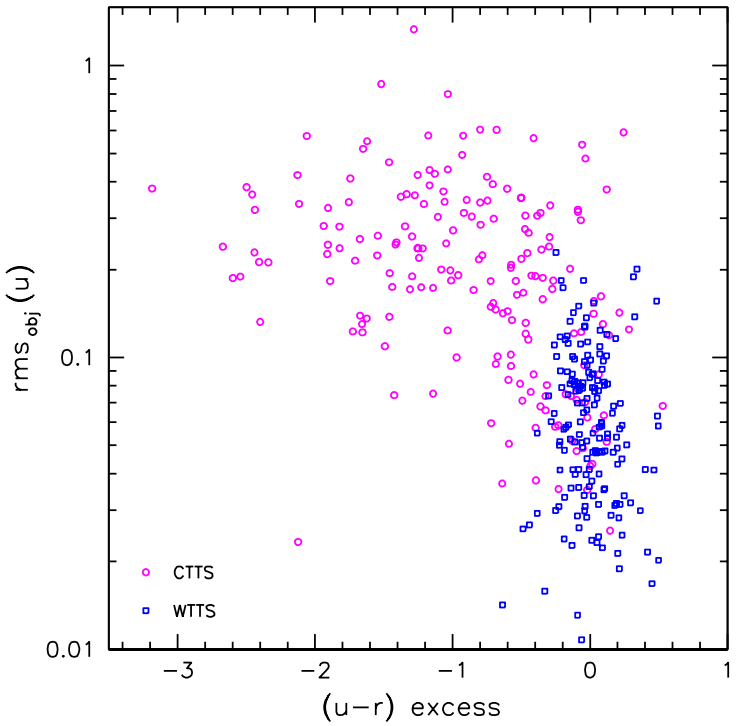

Figure 4.6: UV excess measurements (see Sect. 3.4.1) are compared to the level of u-band rms variability detected for CTTS (magenta circles) and WTTS (blue squares) in NGC 2264. Objects displayed are all selected as significantly variable using the J-index indicator (see text). The UV excess increases from right to left on the diagram.

objects on this diagram. The bulk of the CTTS are located at a higher u-band rms level than the WTTS, as already observed on Fig. 4.3, and higher rms values correspond, on average, to higher (i.e., more negative) UV excesses. This correlation result is estimated to be significant to the $6\,\sigma$ level.

4.2.2 Time evolution on the r vs. $u-r$ diagram of the cluster

An interesting depiction of photometric variability on week timescales for NGC 2264 members, combined with information on their UV colors, is provided in Fig. 4.7. This illustrates how the position of the different cluster members on the r vs. $u-r$ color-magnitude diagram of the region evolves on timescales of days due to their variability.

Relative to Fig. 4.6, this diagram introduces a new dimension in characterizing the variability nature for these young stars – how the colors of the systems vary as these transit from the brightest to the faintest state. Single-band variability amplitudes provide some indication on the intensity of the contrast between the stellar photosphere and the source of variability, which is to some extent revealing of the nature of the dominating variability features (amplitudes above a few tenths of mag are unlikely to originate in rotational modulation by cold spots). However, as illustrated in Sect. 4.3, the same global traits of variability may be common to otherwise well-distinguished physical scenarios (e.g., modulation by cold or hot surface spots); these cases can then be identified from the analysis of their "differential color variations", that is, of how the observed variability amplitudes change with wavelength (Vrba et al. 1993).

On Fig. 4.7, a significant number of CTTS display markedly bluer colors than the corresponding location on the cluster sequence traced by WTTS, as a result of the distinctive UV

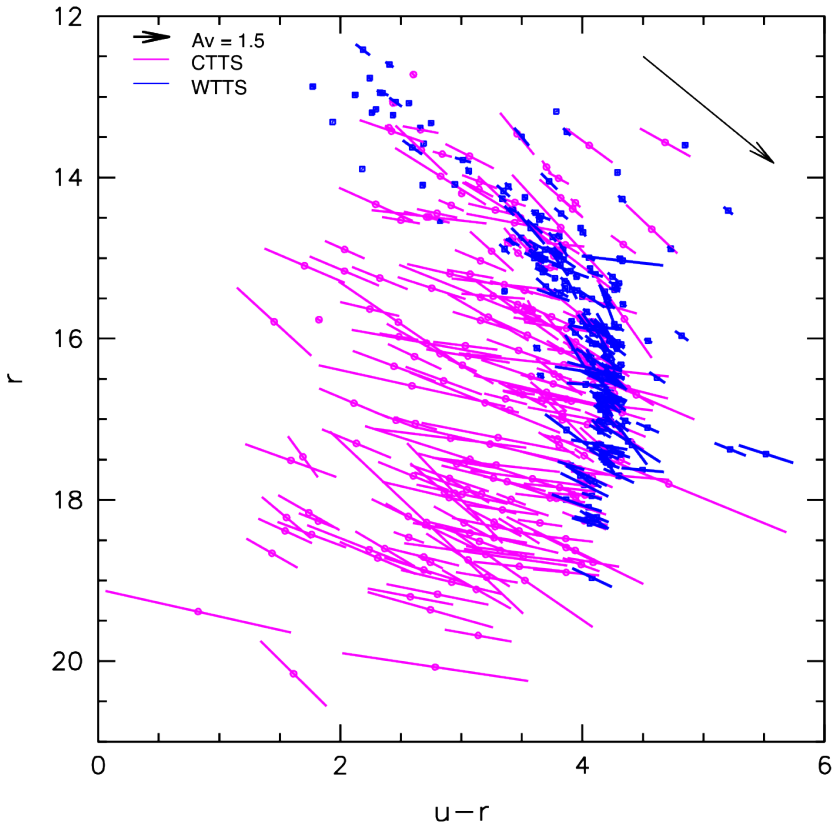

Figure 4.7: Monitoring of color and magnitude variations on the $(u-r, r)$ diagram for CTTS (magenta) and WTTS (blue) in NGC 2264 on a timescale of weeks. Circles and squares indicate the average photometric properties displayed by WTTS and CTTS, respectivey. A variability bar is associated with each object: the center of the bar is located at the color and r-band magnitude of the object at the median luminosity state, while the amplitudes along $u-r$ and r mark the total amount of variability detected during the CFHT monitoring (i.e., $(u-r)_{max}-(u-r)_{min}$ and $r_{max}-r_{min}$ over the $10^{th}-95^{th}$ percentiles range, respectively). The effects of reddening on the diagram are traced by the black arrow in the top right corner (Fiorucci & Munari 2003).

excess linked with ongoing disk accretion. In addition, as already illustrated in Fig. 4.6, high UV excesses are typically associated with strong variability, whereas a significantly lower level of variability, both in magnitude and in color, is observed on the same timescales for non-accreting objects.

Beyond the statistical inference on a global connection between accretion and UV variability that can be drawn from Fig. 4.7, the diagram provides evidence for a strong diversity in the actual picture of variability observed for individual objects. This is reflected in the range of slopes associated with variability bars among both WTTS and, especially, CTTS. Different color signatures are expected to correspond to different physical scenarios. This point is illustrated in the following section.

4.2.3 Exploring the color signatures of different physical scenarios

I selected four members of NGC 2264, each of which is a specimen of a different type of YSO variables, as indicated by their properties and light curve morphology. Fig. 4.8 compares brightness and color variation trends for these four objects.

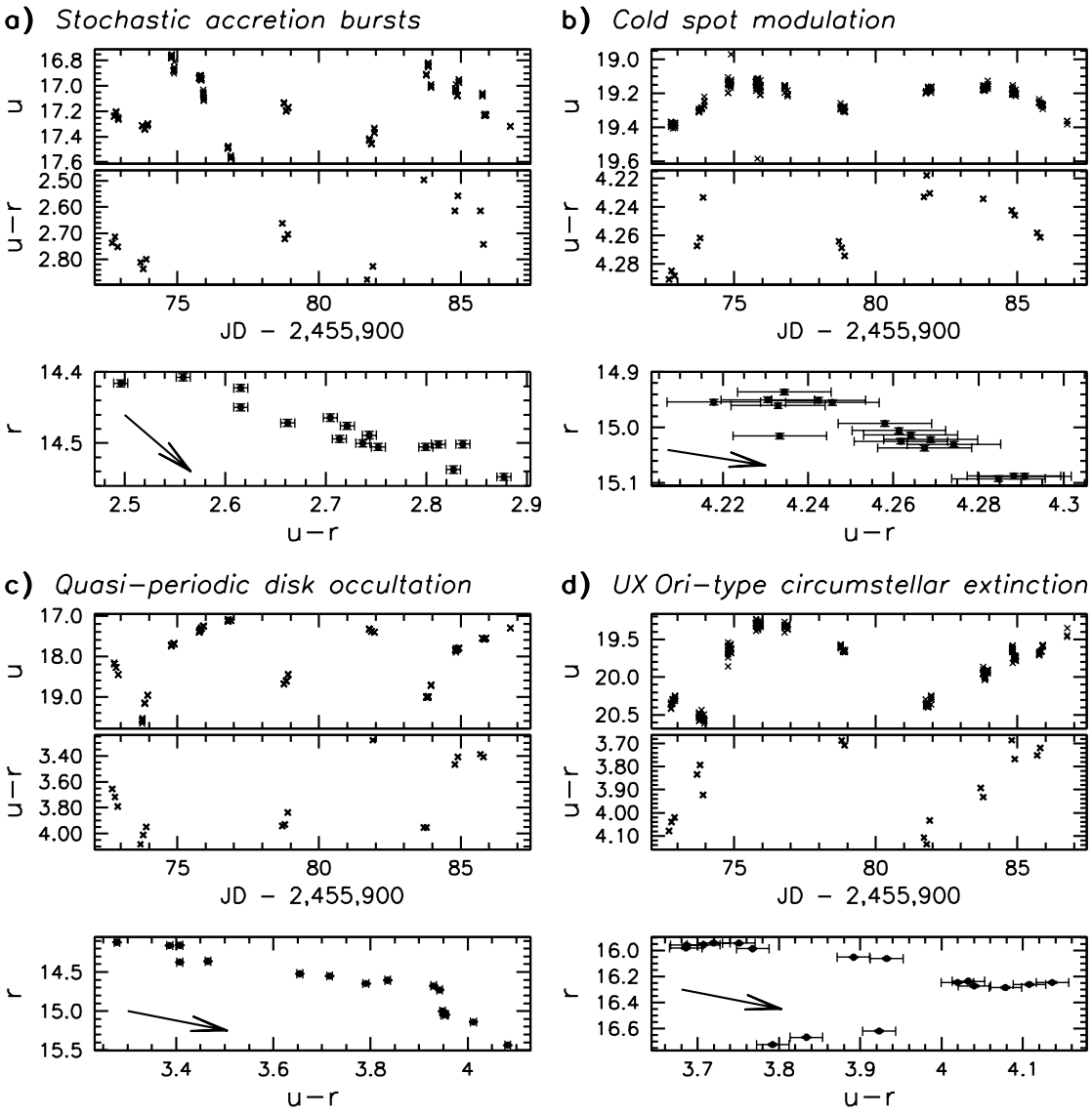

Figure 4.8: u-band light curve, $u-r$ light curve, and r vs. $u-r$ variations for four objects of different types in NGC 2264: a) a representative of the stochastic accretion bursters (Stauffer et al. 2014) class; b) a prototypical WTTS; c) an AA Tau-like CTTS (McGinnis et al. 2015); d) an aperiodic dipper. Light curves report all flux measurements obtained from the monitoring campaign for a better overview of the variability pattern, but only observing sequences obtained in photometric conditions (see Sect. 4.1 of this manuscript and Table 1 of Venuti et al. 2015) are retained for the color analysis. Each point in the r vs. $u-r$ diagram for a given object corresponds to the average $u-r$ color and r-band magnitude measured from a single observing sequence; error bars are associated with each point based on the lowest rms level detected for field stars at the corresponding brightness (see Fig. 4.3). The effects of interstellar reddening are traced as a vector in the bottom left quarter of each (r, $u-r$) diagram.

Panel a) shows an example of a stochastic accretor (Stauffer et al. 2014), whose variability is dominated by short-lived, stochastic accretion bursts. The color light curve nearly retraces the features of the magnitude light curve, as the system becomes consistently bluer for increasing brightness. The same global property (system bluer when brighter) is observed for case b), which depicts a WTTS member whose variability is produced by rotational modulation of cold magnetic spots. Cases b) and a) are distinguished by both i) the amplitudes of variations, especially in color, and ii) the slope of the average r vs. $u-r$ trend (as can be deduced when comparing the direction traced by data points with the slope of the reddening vector, which is the same in each plot). This latter property is particularly meaningful, as it provides an indicator of how steeply the spot/photosphere contrast varies from redder to bluer wavelengths; the more vertical the overall trend in the r vs. $u-r$ diagram, the greyer the luminosity variations (except limb-darkening color effects).

A more complex trend is observed for case c), which illustrates the brightness and color variations of a CTTS member with AA Tau-like nature (Alencar et al. 2010; McGinnis et al. 2015), i.e., a system, observed at high inclination, whose main variability features are driven by quasi-periodic occultations of part of the stellar surface from an inner disk warp. The global behavior is similar to that observed for spotted-like variables, and the system is found to be bluer at phases of larger brightness. However, the r vs. $u-r$ diagram for this object reveals the presence of two separate contributions of different nature to the overall variability profile: one with color signatures as expected for accretion spots (segment at linear increase of $u-r$ with r, with slope consistent with that shown in panel a)) and the other displaying grey brightness variations (segment flat in $u-r$), which is indicative of opaque material that crosses the line of sight to the source. These behavior changes occur within only two weeks and average to a global $\Delta r/\Delta(u-r)$ slope consistent with that traced by the reddening law. Complex and phase-varying color behavior is well documented in the case of AA Tau itself (Bouvier et al. 2003). The alternation of phases of colored and grey magnitude variations for these objects may indicate non-uniform extinction properties across the occulting screen (e.g., more opaque at the center and optically thin at the edges). Furthermore, increased veiling at the epochs of maximum accretion shock visibility (i.e., close to the occultation event, in the assumption that the inner disk warp is located at the base of the accretion column) may determine a sudden transition of the system between different color regimes.

Another interesting behavior is shown in panel d). As in the previous case, the variability of this system is dominated by circumstellar extinction; the system generally becomes redder when fainter, with the exception of the first segment of the light curve, where a decrease in luminosity down to the minimum level detected is accompanied by a marked decrease in $u-r$ (i.e., bluer colors). Again, two different components can be distinguished on the r vs. $u-r$ diagram of the object. At first, the system becomes redder as it proceeds from the phase of maximum luminosity to a mean brightness state, with an overall trend consistent with what is expected for an accreting source; however, as the brightness drops below a certain level, the system is suddenly found to depart from the previous color trend, and gets bluer until it reaches the phase of minimum brightness recorded. This effect is reminiscent of the UX Ori phenomenon (Herbst et al. 1994): when the direct stellar emission along the line of sight is considerably screened by an intervening material, a significant fraction of the light that reaches the observer is actually contributed by scattered light from the circumstellar disk; since the scattering law is more efficient at shorter wavelengths, this process results in bluer colors for the system at the lowest luminosity phases. This interpretation assumes that the system is observed at high inclinations (i.e., close to the plane of the disk), so that structures in the inner disk may play an effective role in obscuring the photosphere along the line of sight; McGinnis et al. (2015) show that this is likely the case for most objects in our sample whose light curve morphology appears

to be dominated by circumstellar extinction effects.

4.2.4 A global picture of color variability for different YSO types

Variability bars shown on Fig. 4.7 are obtained from individual $(u-r, r)$ diagrams, similar to those reported in Fig. 4.8, as the main diagonal of the rectangular box that encloses all observational points for a given object. Although this averaged tracer may result in a loss of "punctual" information (notably in cases such as panels c) and d) of Fig. 4.8), it provides an efficient probe for extensive comparison of the main observational signatures pertaining to different groups of objects, fairly robust even in the case of fainter sources, for which deriving a detailed picture of color variability is hampered by conspicuous photometric noise.

Individual amplitudes and slopes may vary broadly among cases that share the same physical origin, reflecting intrinsic object-to-object differences in the relative surface extent and temperature contrast provided by the intervening layer (see discussion in Appendix A of Venuti et al. 2015 around the properties observed for a subsample of WTTS, all of the same spectral type). Nevertheless, we would expect to observe noticeable differences between typical color-magnitude trends for distinct variable groups, driven by well-distinguished mechanisms. In order to test this, I selected good representatives of the WTTS, stochastic bursters (Stauffer et al. 2014) and AA Tau-like (McGinnis et al. 2015) classes, specific examples of which are detailed and discussed in Fig. 4.8. This selection favored objects, in each group, that showed the largest variability amplitudes in CFHT bands, or equivalently were the least affected by photometric noise and hence provided the clearest depiction of characteristic variability features. Amplitudes in color and in magnitude for these objects are compared in Fig. 4.9. WTTS show the smallest amplitudes, and remarkably little color variations as the system moves from the brightest to the faintest state. Bursters show magnitude variations that are similar to those displayed by WTTS in the r-band, but are associated with significantly larger color variations; this indicates that the gradient of photometric amplitude with wavelength is significantly steeper for this group of objects than for WTTS. In the case of the AA Tau's, the largest variability amplitudes are observed, and the average $\Delta r/\Delta(u-r)$ slope detected on a timescale of a couple of weeks is found to be consistent with the slope expected for interstellar extinction. A significant degree of overlapping is observed between the slope fans pertaining to AA Tau's and to WTTS.

These relative trends, derived for a chosen sample of comparatively bright sources, are confirmed when analyzing the color slopes for the whole sample of variable NGC 2264 members, WTTS or CTTS, with a particular focus, among the latter, on objects showing either a stochastic burster or an AA Tau-like nature. The distribution in $\Delta r/\Delta(u-r)$ slopes derived for these different groups is illustrated in Fig. 4.10; median slope and statistical dispersion inferred from these distributions are listed in Table 3 of Venuti et al. (2015) (Appendix C of this manuscript). The CTTS group shows on average a smaller slope than the WTTS group; this difference is more marked when considering accretion-dominated objects alone. AA Tau-like objects and WTTS are found to display similar ranges of values in slopes, in turn consistent with the interstellar extinction slope.

4.3 A spot model description of YSO variability

As discussed by several authors over the past few years (e.g. Venuti et al. 2014; Costigan et al. 2014; Grankin et al. 2007, 2008), baselines of days to weeks appear to be the leading timescales for YSO variability (at least up to several years). A major fraction of this variability originates, on average, from the effect of luminosity modulation by surface inhomogeneities on the stellar

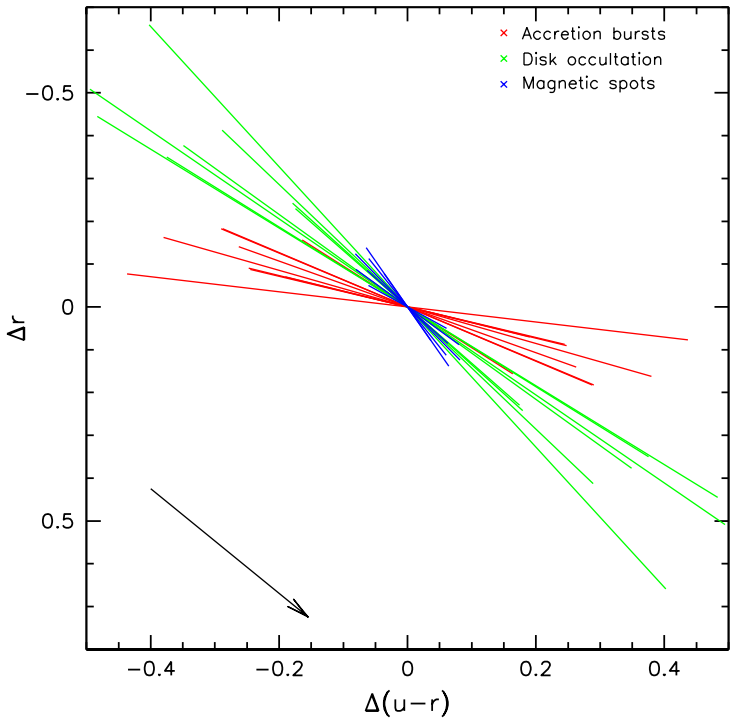

Figure 4.9: Comparison of photometric amplitudes and $\Delta r/\Delta(u-r)$ slopes observed for representative objects of three different types of NGC 2264 members (stochastic accretors, WTTS, and AA Tau-like stars) whose variability is driven by accretion bursts (red lines), cold magnetic spots (blue lines), or disk occultation (green lines), respectively. Luminosity increases from the bottom up along the y-axis and objects become bluer from right to left along the x-axis.

rotation period. This is clear for the well-behaved, periodic light curves typical of WTTS, but also appears to be the case for accreting objects, as discussed in Sect. 3.5.2.

Interesting indications on the properties and dominating features of individual objects can thus be inferred by attempting to reproduce the observed multiwavelength variability signatures with spot models. In this picture, the variability is assumed to arise from a region (single spot or spot distribution) of different temperature at the stellar surface, whose emission modulates the observed luminosity of the star while it rotates.

Fig. 4.11 provides a schematic view of the main features of the photometric variability expected from a surface spot distribution. Independently of the nature of the spot distribution at the stellar surface (cooler or hotter than the photosphere), a spot-dominated variability scenario is characterized by the following qualitative properties:

- the systems appear to be redder at fainter states;
- the amplitudes of variability detected are larger at shorter wavelengths.

Spot parameters (notably temperature and fractional area coverage relative to stellar photosphere) are, then, uniquely determined by the rate at which the observed amplitudes decrease toward longer wavelengths (Vrba et al. 1993): in particular, hot spots are associated with a steeper decrease in amplitude of variability for increasing wavelengths than cold spots (Bouvier et al. 1993).

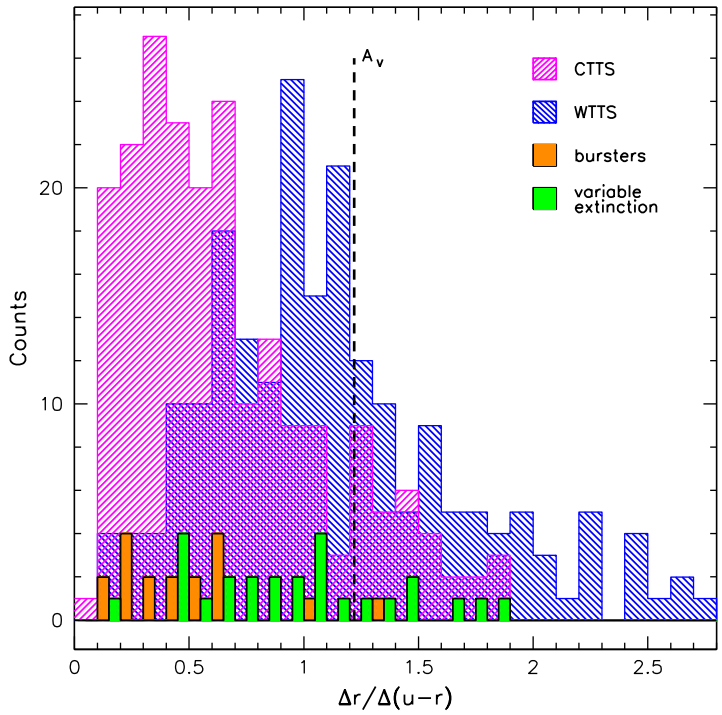

Figure 4.10: Histograms of $\Delta r/\Delta(u-r)$ amplitude ratios are compared for WTTS (blue), all CTTS (magenta), accretion-burst-dominated CTTS (orange), and circumstellar extinction-dominated CTTS (green). Histogram bars for bursters and the variable extinction group are shifted by -0.025 and 0.025, respectively, relative to the bin center and are placed side by side for a better visual comparison of the overall distributions. The slope predicted by the interstellar extinction law is shown as a black dashed line.

4.3.1 Formulation of the spot model

Several studies, including extensive photometric monitoring and spectropolarimetric observations of individual objects (e.g. Donati et al. 2010), have shown that the surface of TTS is likely covered by multiple spots or spot groups, whose geometry is poorly constrained. To circumvent this deficit and investigate the main global features (temperature, size) of the spot distribution at the stellar surface, I follow here the approach of Bouvier et al. (1993) and adopt a spot model that does not introduce any assumptions on the number and shape of spots at the stellar surface. The model assumes, however, i) uniform temperature for all spots at the stellar surface, and ii) blackbody distribution for stellar and spot emission.

Let:

- α be the angle between the local normal to the surface and the line of sight;
- $S(\lambda)$ the specific intensity of the immaculate photosphere at the stellar disk center;
- $S'(\lambda)$ the specific intensity of the spotted region at the stellar disk center;
- μ the linear limb-darkening coefficient;
- R the stellar radius;
- D the distance to the observer;
- θ the colatitude coordinate on the rotating star;

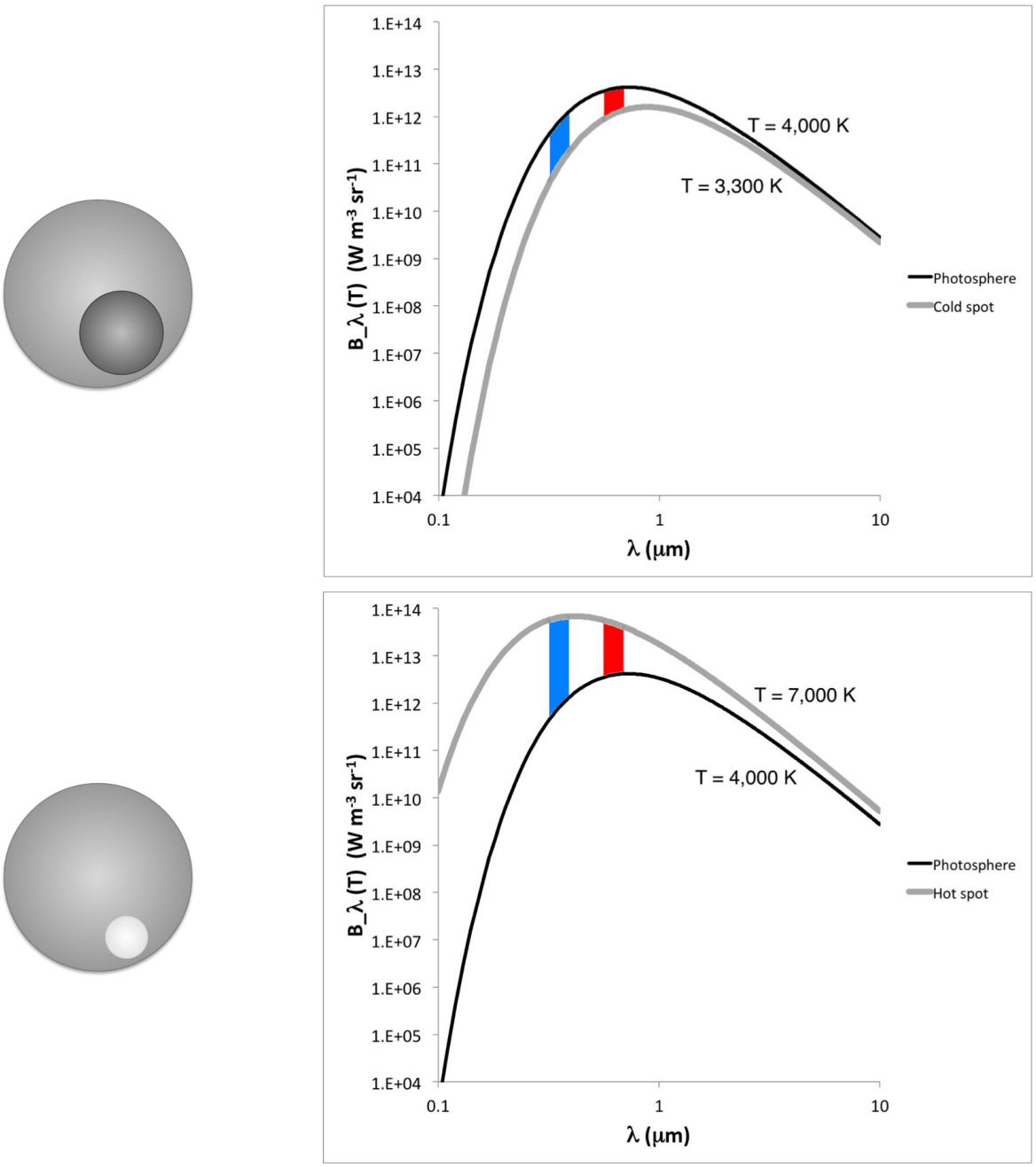

Figure 4.11: Schematic illustration of the wavelength-dependence in the spot-to-photosphere luminosity contrast for cold (upper panel) and hot (lower panel) spots at the stellar surface. The sketch in the upper left panel represents a star with a dark, colder-than-photosphere spot, which covers 20% of the stellar disk. In the diagram in the upper right panel, the emission spectra from unit areas of stellar photosphere and of spot distribution are approximated as black-body emission spectra at typical temperatures of 4 000 K (black curve) and 3 300 K (grey curve), respectively. The brightest state of the system occurs at the phase of minimum spot visibility; since the spot is cooler than the photosphere, the spot emission peaks at longer wavelengths than the photospheric emission, and thus the light variations exhibited by the object during the full rotational cycle will be stronger in the u-bandpass (area shaded in blue) than in the r-bandpass (area shaded in red). The lower left panel shows a sketch of a star with a hot, bright surface spot which extends over 5% of the stellar disk. The emission spectra per unit area for a photosphere at T = 4 000 K and a hot spot at T = 7 000 K, in the black-body approximation, are illustrated in the lower right panel. In this case, the system is at its brightest state when the spot is at maximum visibility; since the spot is hotter than the photosphere, its emission peaks at shorter wavelengths than the photospheric emission, and thus the variability amplitudes monitored for the object will again be stronger in the u-band than in r-band.

- ϕ the longitude coordinate on the rotating star;
- i the pitch angle between the star rotation axis and the line of sight;
- L the stellar luminosity.

For each point at the stellar surface, the angle α can be expressed as a function of the coordinates and of the inclination i as

$$\cos\alpha = \sin i \sin\theta \cos\phi + \cos i \cos\theta$$

and the differential element of projected area on the stellar surface is given by

$$dA = R^2 \cos\alpha \sin\theta d\theta d\phi.$$

If we assume the same linear limb-darkening law for stellar photosphere and spot distribution, the flux received from the spot is given by

$$f' = \left(\frac{R}{D}\right)^2 S'(\lambda) \iint_{spot} (1 - \mu + \mu\cos\alpha)\cos\alpha \sin\theta d\theta d\phi. \tag{4.4}$$

Similarly, the flux received from the immaculate photosphere is given by

$$f = \left(\frac{R}{D}\right)^2 S(\lambda) \int_{-\pi/2}^{\pi/2}\int_{0}^{\pi} (1 - \mu + \mu\cos\alpha)\cos\alpha \sin\theta d\theta d\phi = \pi \left(\frac{R}{D}\right)^2 S(\lambda)\left(1 - \frac{\mu}{3}\right). \tag{4.5}$$

A similar expression to Eq. 4.4, where $S'(\lambda)$ is replaced by $S(\lambda)$, defines the amount of flux that would be contributed from the region of the photosphere covered by spots, if these were not present:

$$f'' = \left(\frac{R}{D}\right)^2 S(\lambda) \iint_{spot} (1 - \mu + \mu\cos\alpha)\cos\alpha \sin\theta d\theta d\phi. \tag{4.6}$$

The ratio between Eq. 4.6 and Eq. 4.5 corresponds to the ratio G(λ) of effective projected area covered by spots to effective stellar disk surface:

$$G(\lambda) = \frac{S(\lambda)(R/D)^2 \iint_{spot} (1 - \mu + \mu\cos\alpha)\cos\alpha \sin\theta d\theta d\phi}{S(\lambda)(R/D)^2 \iint_{unspotted\ star} (1 - \mu + \mu\cos\alpha)\cos\alpha \sin\theta d\theta d\phi} =$$

$$= \frac{\iint_{spot} (1 - \mu + \mu\cos\alpha)\cos\alpha \sin\theta d\theta d\phi}{\pi\,(1 - \mu/3)} \tag{4.7}$$

The λ-dependence in G(λ) is contained in the limb-darkening coefficients $\mu \equiv \mu(\lambda)$.

The value of G(λ) varies as the star rotates, due to non-uniform spot distribution at the stellar surface. If $G_{max}(\lambda)$ and $G_{min}(\lambda)$ indicate respectively the effective fraction of stellar disk surface covered by spots at the phase of maximum/minimum spot visibility, the amplitude of variability for the spotted light curve is defined as (see Vogt 1981 and Torres & Ferraz Mello 1973):

$$\Delta m(\lambda) = -2.5 \log\left\{\frac{1 - G_{max}(\lambda)\,(1 - S'(\lambda)/S(\lambda))}{1 - G_{min}(\lambda)\,(1 - S'(\lambda)/S(\lambda))}\right\}. \tag{4.8}$$

Eq. 4.8 can be rewritten as (Bouvier et al. 1993)

$$\Delta m(\lambda) = -2.5 \log\left\{1 - G_{eq}(\lambda)\left(1 - S'(\lambda)/S(\lambda)\right)\right\}, \tag{4.9}$$

where

$$G_{eq}(\lambda) = \frac{G_{max}(\lambda) - G_{min}(\lambda)}{1 - G_{min}(\lambda)\,(1 - S'(\lambda)/S(\lambda))}. \tag{4.10}$$

G_{eq} represents a lower limit to the effective fraction of star surface coverage by spots: $G_{eq} \leq G_{max} \leq A_{spot}/A_{stellar\ disk}$.

From Eq. 4.7, G_{eq} can be rewritten as

$$G_{eq}(\lambda) = \frac{G'_{eq}}{\pi\,(1 - \mu(\lambda)/3)}\ , \tag{4.11}$$

where $G'_{eq}/\pi \equiv \mathcal{F}_{eq}$ is the ratio of projected spotted area to stellar disk surface. Eq. 4.9 thus becomes

$$\Delta m(\lambda) = -2.5 \log \left\{ 1 - \left(1 - \frac{S'(\lambda)}{S(\lambda)} \right) \frac{\mathcal{F}_{eq}}{(1 - \mu(\lambda)/3)} \right\}. \tag{4.12}$$

In the blackbody approximation for star and spot emission spectra, $S'(\lambda)/S(\lambda)$ corresponds to

$$\frac{S'(\lambda)}{S(\lambda)} = \frac{\exp\left(hc/(\lambda k T_{eff})\right) - 1}{\exp\left(hc/(\lambda k T_{spot})\right) - 1}\ , \tag{4.13}$$

where T_{eff} is the effective temperature of the star. By substituting Eq. 4.13 into Eq. 4.12, we finally obtain:

$$\Delta m(\lambda) = -2.5 \log \left\{ 1 - \left[1 - \frac{\exp\left(hc/(\lambda k T_{eff})\right) - 1}{\exp\left(hc/(\lambda k T_{spot})\right) - 1} \right] \frac{\mathcal{F}_{eq}}{(1 - \mu(\lambda)/3)} \right\}. \tag{4.14}$$

This is the equation that defines the spot model adopted. It contains two free parameters, the effective temperature T_{spot} and the surface extent $\mathcal{F}_{eq}$ of the spot distribution. Photospheric temperature T_{eff} and limb-darkening coefficients $\mu(\lambda)$ have assigned value for a given object, deduced from tabulated scales, based on its spectral type. The values of the two free parameters are obtained from the model by fitting the amplitudes defined in Eq. 4.14 to the observed photometric amplitudes at different wavelengths.

The limitations of this model and the implications of the assumptions are discussed extensively in Bouvier et al. (1993). The approach pursued allows us to circumvent the poor knowledge of the spot geometry at the stellar surface, sacrificing the information on the spot location at the stellar surface to that on effective temperature and surface extension of the spot distribution. While the accuracy on individual spot parameters is limited by the simplifications introduced in the model, the picture adopted provides an efficient tool to statistically map the main variability features (hot/cold spot nature, temperature and surface contrast) specific to different groups of objects.

4.3.2 Implementation of the model

In order to find the (T_{spot}, $\mathcal{F}_{eq}$) pair that provides the best spot model description to the variability properties observed for a given object, I explored a two-dimensional grid, ranging from 1000 K to 10 000 K in T_{spot} and from 0.1% to 90% in $\mathcal{F}_{eq}$, with a step of 5 K in T_{spot} and of 0.002% in $\mathcal{F}_{eq}$. This parameters space range was enlarged in cases where the best solution fell at the edge of the domain explored. For each point of the grid, the theoretical amplitudes

Δm defined as in Eq. 4.14 were computed and their agreement with the observed variability amplitudes was estimated through the χ^2 statistics; the best solution (i.e., the best pair of spot parameters T_{spot}–$\mathcal{F}_{eq}$) is defined as the one that minimizes the χ^2.

Photospheric temperatures T_{phot} that appear in Eq. 4.14 were inferred for each object in our sample from their spectral types, following the scale of Cohen & Kuhi (1979) (as discussed in Sect. 3.3.2). Linear limb-darkening coefficients were deduced from the compilation of Claret & Bloemen (2011), computed in the SDSS bands using ATLAS plane-parallel atmosphere models (Castelli & Kurucz 2004), and assuming solar metallicity and $\log g = 4$. Limb-darkening coefficients tabulated for spectral type M2 were uniformly extended to later spectral types, which are not sampled in the reference compilation at the metallicity and gravity values adopted.

The robustness of the result and the associated uncertainty were evaluated by investigating how stable this "best" solution is relative to small variations of the input "observed" amplitudes. Spot model predictions are typically affected by a degree of degeneracy between different spot parameters, notably between T_{spot} and $\mathcal{F}_{eq}$ (see, e.g., Walkowicz et al. 2013); a given set of amplitudes could in principle be reproduced either in terms of more extended surface spots with a modest temperature difference relative to the stellar photosphere, or of a smaller spot distribution whose effective temperature is more markedly different from the temperature of the star. The procedure I adopted to derive an estimate of the uncertainty on spot model results for individual objects consists of the following steps:

1. I took the u-band and r-band amplitudes (amp_u, amp_r) and the associated error bars err_u, err_r (defined as $err_m = \sqrt{2\sigma_m^2}$, where σ_m is the photometric error estimate obtained from the brightness of the star and the prescription in Eq. 4.1 or Eq. 4.2, respectively);

2. I used the rejection method for generating random deviates within a normal distribution (Press et al. 1992) to produce 200 random ($amp_u^{test}, amp_r^{test}$) pairs, where amp_m^{test} is extracted from a Gaussian distribution centered on amp_m with standard deviation err_m;

3. for each of the randomly generated (u, r) amplitude pairs, I ran the spot model in Eq. 4.14, and computed the parameters of the spot distribution that best reproduces this simulated pair of variability amplitudes;

4. the spot models results for each of the random amplitude pairs were used to build a T_{spot} and a $\mathcal{F}_{eq}$ distribution, whose mean and standard deviation were extracted as a best value and a corresponding uncertainty, respectively.

4.3.3 A global picture of spot properties for TTS in NGC 2264

An overview of the different nature of modulated variability exhibited by accreting and non-accreting members of NGC 2264 is provided in Fig. 4.12 (see also Bouvier et al. 1995). This compares the u-band and r-band amplitudes for different classes of members to cool (upper panel) and hot (lower panel) spot model predictions, computed assuming, for illustration purposes, a typical photospheric temperature of 4000 K and varying spot temperatures (between a few hundred K and a few thousand K different from T_{phot}) and filling factors (from 0.1 to 60% of the stellar surface).

A first interesting feature of these two diagrams is that u-band variability amplitudes are always larger than r-band amplitudes. This is consistent with expectations in the spot description of modulated variability. WTTS typically display lower variability amplitudes than CTTS, $\lesssim 0.4$ mag in r and 0.5 mag in u. Cool spot model tracks, depicted in the upper panel of Fig. 4.12, span the WTTS locus over the entire amplitude range fairly well; this suggests that, in most cases, WTTS variability can be convincingly reproduced in terms of cool magnetic spots, having

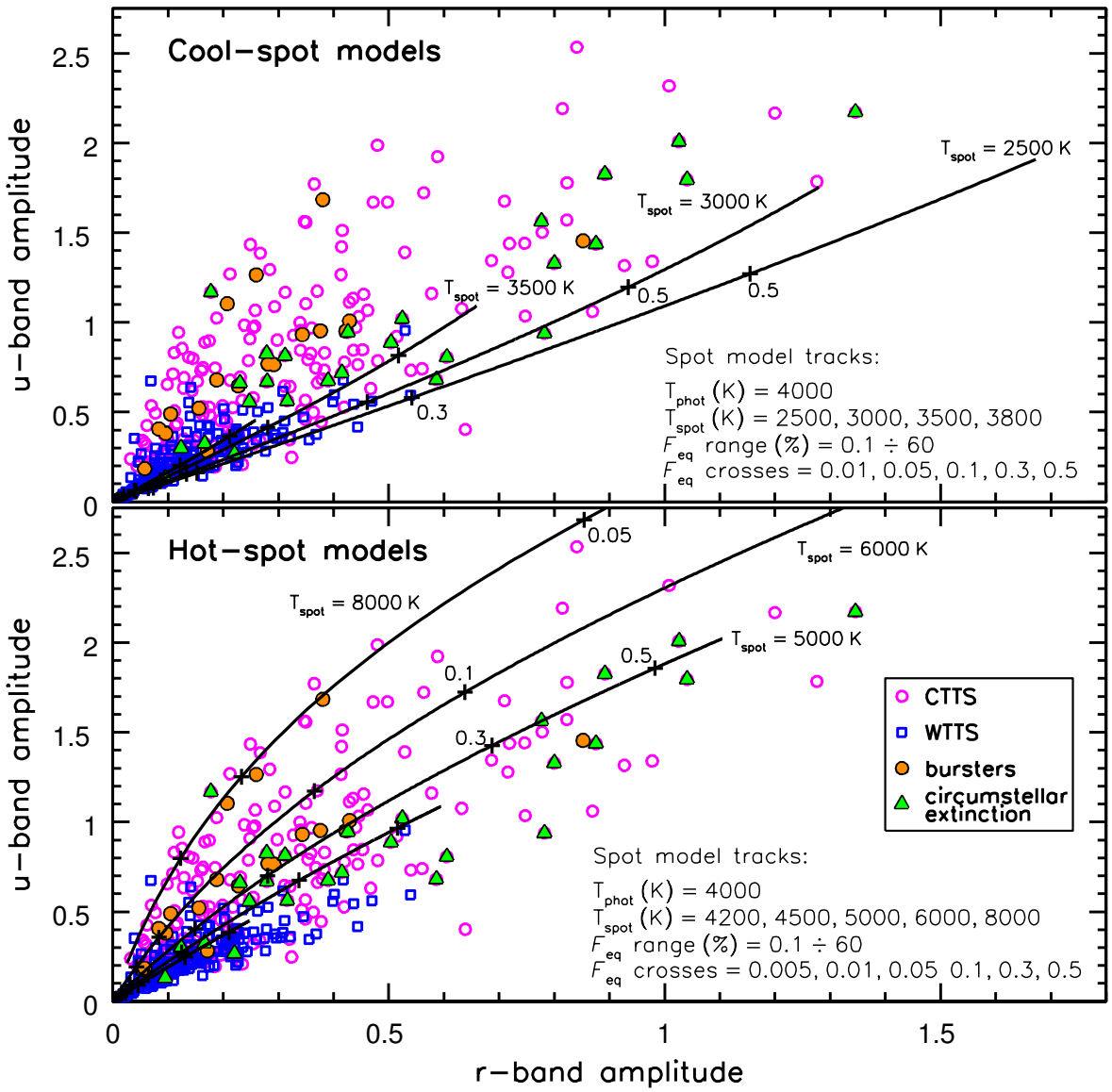

Figure 4.12: u- and r-band variability amplitudes observed for WTTS (blue squares) and CTTS (magenta circles) are compared to cool (upper panel) and hot (lower panel) spot model predictions. Model tracks are traced assuming a fixed photospheric temperature T_{phot} of 4000 K (corresponding to a K7 star). Each model track corresponds to a different spot temperature T_{spot}: in the upper panel (cool spots), four different T_{spot} values are considered, ranging from 200 K to 1500 K lower than T_{phot}; in the lower panel (hot spots), five different T_{spot} values are explored, ranging from 200 K to 4000 K above the photospheric temperature. Along each track, $\mathcal{F}_{eq}$ varies from 0.1% to 60%; reference values of the spot-to-star surface ratio are marked with crosses for clarity. For CTTS, two additional subclasses are highlighted: objects dominated by stochastic accretion bursts (Stauffer et al. 2014, orange dots) and objects dominated by circumstellar extinction (McGinnis et al. 2015, green triangles), either quasi-periodic (AA Tau-like objects) or aperiodic.

a temperature of ∼500-1000 degrees lower than T_{phot} and covering up to ∼30% of the stellar surface. Fig. 11 of Venuti et al. (2015) shows that variability amplitudes observed for WTTS, both in r and in u, tend to decrease for increasing stellar mass; this may indicate that the spot distribution at the surface of more massive stars is typically less extended and/or more uniform than magnetic spots found at the surface of lower-mass (i.e., later-type) objects, as is the case for MS dwarfs. No evidence for any trend of photometric amplitudes with stellar mass is instead observed in the CTTS group.

A smaller fraction of WTTS are located in the region of the diagram dominated by hot spots; enhanced chromospheric activity may explain the photometric properties observed for some of these objects, while others might actually be accreting stars at levels too low to be detected. A non-negligible overlap exists between the distributions in amplitudes of WTTS and CTTS; this attests to the more complex picture of CTTS variability, that likely ensues from a combination of accretion/star-disk interaction – related effects and of underlying WTTS-like magnetic activity. However, a more significant fraction of CTTS is observed to exhibit larger variability amplitudes than WTTS and, at a given value of amp_r, the bulk of accreting members is located at larger u-band amplitudes than their non-accreting counterparts. Cool spot model predictions are not able to reproduce the color variability of objects located in this part of the CTTS distribution; a better fit to their photometric amplitudes is provided by hot spot model tracks in the lower panel of Fig. 4.12. Temperature differences between hot spots and stellar photosphere range from $\lesssim$1000 K to several thousand Kelvin. The hot spot distributions that best describe the properties of individual objects are typically found to extend over a lesser fraction of the stellar surface compared to that covered by cool spots in non-accreting sources; surface coverage amounts, in the former case, to ∼5–10% for spots 2000 K–hotter than the stellar photosphere and down to a few percent for the hottest spots.

4.3.4 The different nature of modulated variability for CTTS vs. WTTS

Fig. 4.13 synthesizes the main features of the spot properties inferred, case by case, for the populations of CTTS and WTTS in NGC 2264, using the model described in Sect. 4.3.1.

Three distinct loci can be identified on this diagram. The first, located to the right of the red line (i.e., at positive values of T_{phot} - T_{spot}), below $\mathcal{F}_{eq} = 40\%$, is the main locus populated by WTTS. In most cases, the best spot solution suggests a surface spot distribution ∼500 K colder than the stellar photosphere, extending over ∼10–30% of the stellar surface. A small number of CTTS are also located in this region of the diagram, with properties consistent with those deduced for WTTS, which suggests that cool spots of magnetic origin are still a primary cause of modulated variability in these cases.

The second locus is located to the left of the red line (i.e., at negative values of T_{phot} - T_{spot}) and is the locus primarily populated by CTTS. Spot distributions that best reproduce the observed photometric amplitudes in individual cases are typically ∼1000 – 2000 K hotter than the stellar photosphere, with a tail of objects for which temperature differences of over 3000 – 4000 K are predicted by spot model results. Although the $T_{spot} - \mathcal{F}_{eq}$ degeneracy in spot model results may play a non-negligible role in the anticorrelation between these two quantities, observed to a certain extent both to the left and right of the red line in Fig. 4.13, a significant difference between the distributions of CTTS and WTTS in $\mathcal{F}_{eq}$ can be detected, with the former being largely located below 5–10%, while the latter are mainly comprised between 5–10% and 30%, as discussed earlier. Objects whose variability is dominated by stochastic accretion bursts are good representatives of this category (amplitudes reproduced with hot spot distributions), of which they span the whole range of model results.

The third locus in the diagram is the point distribution around the T_{phot} - $T_{spot} = 0$ line, above $\mathcal{F}_{eq} = 40\%$. This is mainly populated by CTTS. These objects stand out for the small

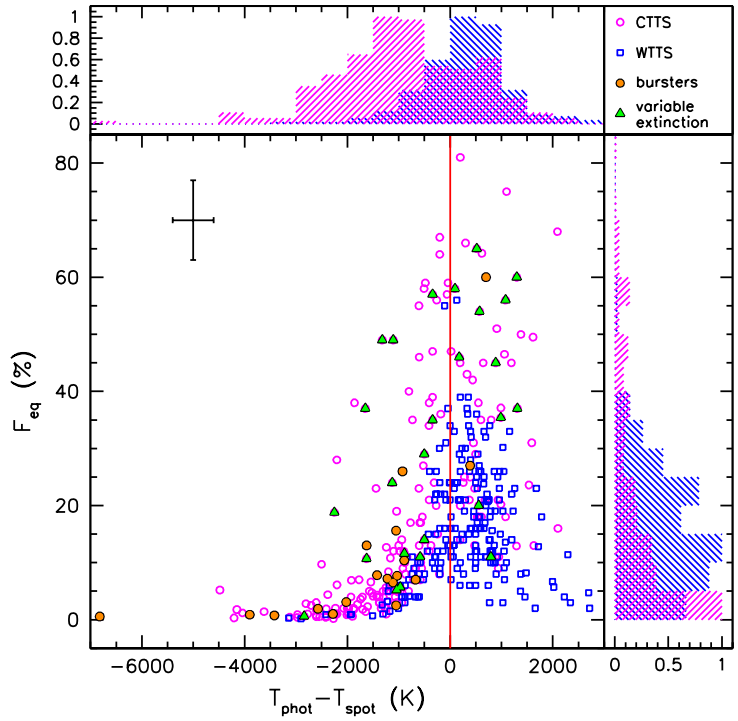

Figure 4.13: Best spot model solutions for CTTS (magenta circles) and WTTS (blue squares) in NGC 2264 are statistically compared. A typical error bar is shown as a black cross in the upper left corner of the diagram. Error estimates result from the uncertainties on the photometric amplitudes, following the procedure described in Sect. 4.3.2, plus a lower order correction accounting for uncertainties on the photospheric temperature (T_{phot}) and on the shape of the limb-darkening coefficients $\mu(\lambda)$. The red vertical line marks the zero-value temperature difference between stellar photosphere and spot distribution. For CTTS, objects dominated by stochastic accretion bursts are marked in orange, while green triangles correspond to AA Tau-like objects. Histograms shown in side panels at the top and to the right of the diagram compare the CTTS (magenta) vs. WTTS (blue) distribution in spot properties (temperature difference relative to the stellar photosphere and percentage of surface covered, respectively). The heights of histogram bars are normalized to the highest channel count in each distribution.

temperature difference between photosphere and best spot model and for the corresponding high value of $\mathcal{F}_{eq}$, significantly higher than the typical values for WTTS or CTTS. This suggests that for this subgroup of objects, spot models are ill-suited to describe the observed amplitudes and color properties, and hence other components may be dominating the observed variability. This conclusion is supported by several AA Tau-like objects in this group, whose variability is known to be dominated by quasi-periodic disk occultation and whose color properties are markedly different from those observed for WTTS or accretion-dominated objects (Fig. 4.9).

4.4 Timescales of variability for the accretion process

Throughout the chapter, I have focused on exploring the properties of UV variability on timescales relevant to stellar rotation. In this Section, I will compare this picture of mid-term variability with what we observe on shorter (hours) and longer (years) timescales. This is instrumental in achieving a more complete description of YSO dynamics.

The short timescales (hours) show on average little variability compared to the amount measured on mid-term timescales (days/weeks). Episodic flares are detected for a few tens of objects in our sample during the monitored time span; these typically determine an increase in flux comparable to, or a few times larger than, the average emission level of the system in the u-band, and fade out on timescales of a few hours.

If we exclude flaring activity, only low-level luminosity variations are observed on hour timescales. To estimate a typical amount of short-term variability, I computed the average rms scatter of u-band measurements obtained at different epochs within single nights (see Sect. 2.2.2 and Sect. 4.1, notably Fig. 4.1) across our sample. CTTS are typically found to display an rms variability of 0.06 mag on these time baselines, corresponding to barely 8-9% of the amplitudes measured on timescales of days. Similar results are obtained for the WTTS group, with typical short-term rms variability of 0.025 mag, or about 10% with respect to the corresponding mid-term variability amplitudes in the u-band.

This result for CTTS is well consistent with the analysis reported in Sect. 3.5.2, which showed that up to ∼75% of the UV variability detected for typical CTTS on week timescales is simply due to geometric effects of rotational modulation. Of the remaining fraction linked with intrinsic variability, a larger contribution can be attributed to cycle-to-cycle variations (possibly related to accretion spot evolution), while a smaller component is statistically contributed on hour-long timescales, which is more sensitive to unstable, stochastic behaviors in the accretion process.

In order to evaluate the impact of mid-term timescales on long-term (years) variations, I compared u-band photometry obtained during the CFHT/MegaCam monitoring survey of Feb. 2012 with single-epoch photometry obtained in Dec. 2010 (Sect. 2.2.2). In the hypothesis that mid-term timescales dominate TTS variability on longer baselines, then it is reasonable to assume that, if we had information on mid-term variability around the Dec. 2010 observing epoch for objects in our sample, this would be a close reproduction of the light curve variation patterns exhibited by those same objects in Feb. 2012. Hence, the photometric measurement from the snapshot survey of Dec. 2010 ($u_{\,2010}$) should simply correspond to the luminosity state of the system at a random phase on the light curve of the object reconstructed from 2012 monitoring. If this assumption is correct, then we can measure the absolute difference between $u_{\,2010}$ and the median light curve magnitude from Feb. 2012 $\left(u^{\,med}_{\,2012}\right)$, and should expect this difference to be statistically smaller than (or comparable to) half the variability amplitude $amp_{\,u}$ of the light curve from Feb. 2012[3]. Conversely, if other variability mechanisms are predominant on year-long

[3]This is true for approximately symmetric light curves around the typical luminosity state, but not necessarily for strongly asymmetric light curves, where the object is most often found close to the minimum or maximum

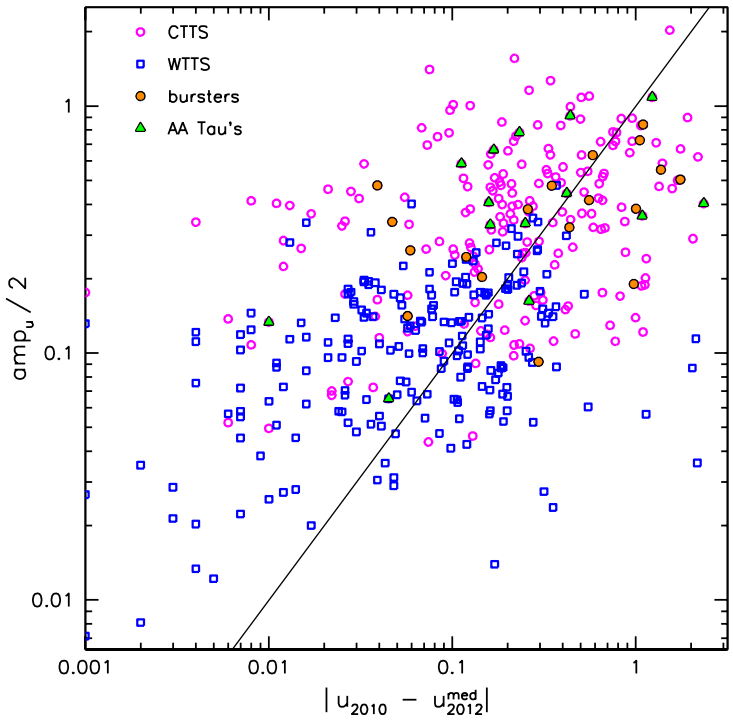

Figure 4.14: u-magnitude differences between single-epoch photometry in December 2010 and median light curve photometry in February 2012 are compared to the semi-amplitudes of u-band light curves from February 2012 monitoring for WTTS (blue squares), CTTS (magenta circles), and CTTS accretion-dominated (orange dots) and extinction-dominated (green triangles) subgroups. The equality line is traced in black to guide the eye.

timescales, then we expect to measure $|u_{2010} - u^{med}_{2012}|$ values which are on average larger than $amp_u/2$.

Fig. 4.14 illustrates the comparison between the $|u_{2010} - u^{med}_{2012}|$ and $amp_u/2$ quantities, measured for all variable members considered in this study. A clear offset along the equality line is observed between the WTTS and the CTTS groups in the diagram, with the latter group located at significantly higher variability amplitude values, consistently with the fact that they are statistically more variable than WTTS. However, there are no significant differences between the WTTS and the CTTS groups in the indicator of interest here, that is, the $|u_{2010} - u^{med}_{2012}|/(amp_u/2)$ ratio. Both groups distribute in clouds of similar properties about the equality line on the diagram, with mean ratio of 0.8 (i.e., typical epoch-to-epoch difference that can be fully accounted for by mid-term variability) and comparable *rms* scatter. This suggests that similar timescales or mechanisms (notably rotational modulation) are responsible for the long-term variations observed in the two cases. No significantly different behaviors are observed for stochastic accretors or AA Tau-like objects in this respect. A small group of WTTS can be located well below the main locus at large epoch-to-epoch mag variations; corrupted photometry is most likely responsible for the atypical location of these objects on the diagram[4].

brightness level with episodes of strong flux increase or fading, respectively. However, the analysis reported in Sect. 3.5.2 indicates that roughly symmetric variations around the typical state of the systems are indeed more commonly observed across our sample.

[4]In spite of being relatively bright, these few objects exhibit atypically low variability and their $u-r$ colors from 2012 data are atypically red, both relative to the reference WTTS locus and to the colors exhibited by these same stars at the 2010 observing epoch. In addition, they are located spatially close together and have hence all

For the CTTS group, I additionally probed the stability of u-band variability on longer timescales (>10 years) by comparing the UV excess luminosity measured and monitored in our survey (Venuti et al. 2014 and Chapter 3 of this thesis) with values measured in a similar, single-epoch U-band survey of NGC 2264 performed by Rebull et al. (2002). Results of this comparison are shown in Fig. 13 of Venuti et al. (2014). Again, we observe that median UV excess luminosities from 2012 and single-epoch measurements from Rebull et al.'s study distribute around the equality line with an rms scatter consistent with the typical amount of variability detected on a timescale of a couple of weeks.

These results suggest that the mid-term timescale is the leading timescale for YSO variability, at least up to baselines of several years. The similarity of WTTS and CTTS in this respect also suggests that the typical dynamics of the accretion process on CTTS is intrinsically stable over timescales of years, although it may display a variable nature in the shorter term. In other words, single accretion events may be shorter-lived, and the dynamics of interaction between disk and stellar magnetosphere may lead to rapidly evolving surface spots (on timescales of a few rotational cycles or less) and irregular light curve morphology. However, the averaged spot properties, indicative of the intensity of mass accretion onto the star and of the mechanisms that regulate the process, can persist over timescales of years. Similar conclusions were presented by Grankin et al. (2007).

4.5 Conclusions

In this chapter, I have explored the properties of photometric variability for several hundred CTTS and WTTS members of NGC 2264 at UV wavelengths. The analysis was focused on simultaneous monitoring in the optical (r-band) and in the UV (u-band) on a timescale of two weeks, with multiple measurements per observing night. This enabled investigation of the nature of different types of YSO variables by characterizing the intensity of light variations and the color variability.

The CTTS and WTTS populations are found to be statistically distinct in various variability metrics on mid-term timescales (comparable to stellar rotation periods). The former exhibit significant higher variability than the latter, both in the optical and, even more markedly, in the UV. A global correlation appears to hold between the amount of variability exhibited by CTTS and the accretion process, with large UV excesses being statistically associated with high variability. Amplitude ranges and color variations monitored for WTTS are best reproduced in terms of cool surface spots linked with magnetic activity, which modulate the luminosity of the star as it rotates. Hot-spot models are instead required to account for the stronger variability and steeper amplitude increase from the optical to the UV observed for typical CTTS.

Although being statistically distinct, the populations of CTTS and WTTS are observed to display a non-negligible overlap in photometric behaviors on the various photometric diagrams analyzed here. Some CTTS, classified as such based on evidence of circumstellar disk, exhibit photometric properties consistent with objects that lack disk signatures, and vice versa. This suggests that a continuum of intermediate behaviors are possible between the state of a "classical" T Tauri and that of a diskless, weak-lined T Tauri star. Indeed, the distribution in $\dot{M}_{acc}$ derived for the disk-bearing population of the cluster in Chapter 3 indicates that a broad variety of accretion regimes coexist within the same stellar population, which may be linked to the presence of an evolutionary spread among cluster members. Similarly, some sources classified as WTTS by our criteria might actually be objects with low undetected accretion or in "quiescent" state.

been extracted from a single CCD on the MegaCam plate, which was possibly affected by calibration problems during the 2012 run, as assessed by comparing the average photometric properties observed for non-variable field stars on this CCD at the 2010 and 2012 epochs.

The comparison of the amount of UV variability displayed on timescales of weeks with that detected on much longer timescales, for both the CTTS and WTTS groups, indicates that it is rotational modulation on day timescales which dominates the picture of YSO variability over several hundred periods (i.e., years). This suggests that the underlying physical processes (namely magnetic activity in WTTS and disk accretion in CTTS) have a relatively stable nature on the long term, which translates to persistent averaged spot properties at the stellar surface, although disk accretion can exhibit more erratic behavior in the shorter term.

Chapter 5

The accretion–rotation connection in young stars

Contents

In this chapter, I present some preliminary results of a study of periodicity and rotation properties for TTS members in NGC 2264, which I have performed in the second part of my PhD thesis work, based on the set of optical light curves obtained with the *CoRoT* satellite during the CSI 2264 campaign. Notably, I will focus here on the aspects of this analysis which are connected with the study of the accretion process in young stars and of its impact on their early evolution. I first introduce the technique adopted to detect and extract the periodic signal component from the light curves, if present; I then illustrate the period distribution inferred for the whole cluster and explore the difference between WTTS and CTTS. This will allow me to discuss the connection between rotation and accretion properties in the context of the disk-locking scenario. A more complete analysis of periodicity and rotation in NGC 2264 will be presented in a forthcoming paper (Venuti et al. 2015b, in preparation).

5.1 Photometric period determination

As discussed in Chapter 4, the surface of young stars looks far from homogeneous, but a significant fraction of it (up to a few tenths) is covered by unevenly distributed spots of different temperature relative to the photosphere. As the star rotates, different portions of the stellar surface cross the observer's line of sight to the star; this determines a modulation effect in the detected luminosity. If the lifetimes of surface spots are longer than the timescales of interest, a

definite periodic trend will appear in the light curves[1]. Hence, a photometric estimate of the rotation period of the star can be derived by investigating and extracting the periodic component of its light curve, in the assumption that this modulation arises indeed from photospheric spots (and not, for instance, from concentrations of material at some Keplerian orbit in the disk, in the case of CTTS).

Several methods have been proposed in the literature to extract a periodic component from a time-ordered series of signal measurements. Some, more analytic, consist in decomposing the signal in waves at a given frequency; others, more geometric or empirical, are based on a comparative examination of the morphology of different segments of light curve, in units of trial period. In my study, I adopted 3 different methods to search for periodic signals in our sample of light curves: the Lomb-Scargle periodogram (LSP), the auto-correlation function (ACF) and the string-length method (SL). A brief description and comparison of advantages and disadvantages of these methods is provided in Sect. 5.1.1, while details on their application to the analysis presented here are provided in Sect. 5.1.2.

5.1.1 Period-search methods used in this study

Lomb-Scargle periodogram

This approach (Scargle 1982; Horne & Baliunas 1986) is a revised version of the discrete Fourier transform method; it is applicable to datasets with uneven temporal sampling and is invariant to a shift of time origin. The method is equivalent to least-squares fitting of sinusoidal waves at a test frequency ω to the observed light curve: the power spectrum of the light curve is reconstructed by varying the test frequency ω in the range of investigation.

The definition of the periodogram is

$$P_m(\omega) = \frac{1}{2}\left\{ \frac{\left[\sum_j m_j \cos\omega\,(t_j-\tau)\right]^2}{\sum_j \cos^2\omega\,(t_j-\tau)} + \frac{\left[\sum_j m_j \sin\omega\,(t_j-\tau)\right]^2}{\sum_j \sin^2\omega\,(t_j-\tau)} \right\}, \tag{5.1}$$

where m_j is the observation at time t_j, $\{m_j \equiv m(t_j),\, j = 1, 2, ..., N\}$ and τ is defined as

$$\tan(2\omega\tau) = \frac{\sum_j \sin 2\omega t_j}{\sum_j \cos 2\omega t_j}. \tag{5.2}$$

For our application, $P_m(\omega)$ is normalized to the total variance σ^2 of the light curve to obtain

$$P_{\mathcal{N}}(\omega) = \frac{P_m(\omega)}{\sigma^2}. \tag{5.3}$$

Autocorrelation function

Contrary to the LSP method, the ACF method (McQuillan et al. 2013) does not introduce any assumptions on the shape of the light curve.

The method is based on the self-similarity of different segments of periodic light curves at the same phase. It consists in exploring a range of trial periods and computing, for each of them, the auto-correlation coefficient r_k of the light curve at lag k, where k is the tested period P in units of time cadence Δt ($P = k\Delta t$):

$$r_k = \frac{\sum_{i=1}^{N-k}(m_i - \overline{m})(m_{i+k} - \overline{m})}{\sum_{i=1}^{N}(m_i - \overline{m})^2}, \tag{5.4}$$

[1]This is true unless the object is too faint (amplitude dominated by photometric noise) or it is seen in a pole-on configuration (hence the same portion of the stellar surface will always be on sight).

where m_i is the magnitude at time t_i, m_{i+k} is the magnitude at time $t_i + P$, $\overline{m}$ is the average light curve magnitude and N is the total number of light curve points (equally spaced in time with step Δt).

The auto-correlation function is reconstructed by plotting r_k as a function of P. When the P value tested matches the actual periodicity of the light curve, similar behaviors relative to the typical luminosity state $\overline{m}$ are expected at epochs i and $i + k$, hence resulting in large values of r_k and a maximum in the ACF; conversely, small values of r_k are found if matched epochs i and $i + k$ are out of phase.

String-length method

As for ACF, the SL method (Dworetsky 1983) does not introduce any assumptions on the shape of the light curve. The method explores a range of trial periods; for each P, light curve points are ordered in phase and a string-length parameter L is defined as the sum of the lengths of line segments that connect successive points of the phased light curve on the (m, ϕ) diagram:

$$L = \sum_{i=1}^{N-1} \sqrt{(m_i - m_{i-1})^2 + (\phi_i - \phi_{i-1})^2} + \sqrt{(m_1 - m_N)^2 + (\phi_1 - \phi_N + 1)^2}\,, \qquad (5.5)$$

where i is the index running on the phase-ordered light curve.

A preliminary rescaling of the observed magnitude range to the phase range is needed so that variations on the two variables have equal weight in the computation of L.

The best period P is the one that minimizes the value of L, while large L values will be found when the light curve is phased with an arbitrary period, hence resulting in a scattered cloud of points with no specific pattern on the phase diagram.

Comparison of the different methods

Figure 5.1 illustrates the results yielded by the different period search methods for a case of NGC 2264 WTTS member with multiple spots at the stellar surface, which determine a non-sinusoidal light curve with multiple flux minima/maxima during a single period.

The LSP method generally ensures more accurate period measurement than ACF and SL, as it is less sensitive to spurious points and long-term trends; in addition, it provides a straightforward estimate of the uncertainty on the derived periodicity, by measuring the Gaussian width of the highest peak in the periodogram. On the other hand, the explicit assumption that the periodic luminosity component can be described in terms of sine curves may be in contrast with the actual light curve shape observed for these young stellar objects. Moreover, this analytic approximation may lead to incorrect period identifications in cases such as that in Fig. 5.1, since the method will try to fit one sine curve to each minimum-maximum pair.

The ACF technique, which takes into account the actual shape of the light curve, allows more reliable identification of the peak corresponding to the true periodicity (as shown in Fig. 5.1); however, the need for an even time binning and for adopting a ΔP step for period investigation that is the same as (or a multiple of) the light curve Δt limits the accuracy of the extracted period value compared with the accuracy that can be achieved, with the same binning, from the corresponding peak in the periodogram.

The SL technique combines the advantages of being conceptually straightforward, directly related to the actual variability pattern of the light curve, and of being applicable to any temporal sampling; as a downside, due to the greater sensitivity to spurious points and long-term trends, the overall SL curve as a function of P tends to be more noisy than resulting diagrams from other methods, notably at shorter period values.

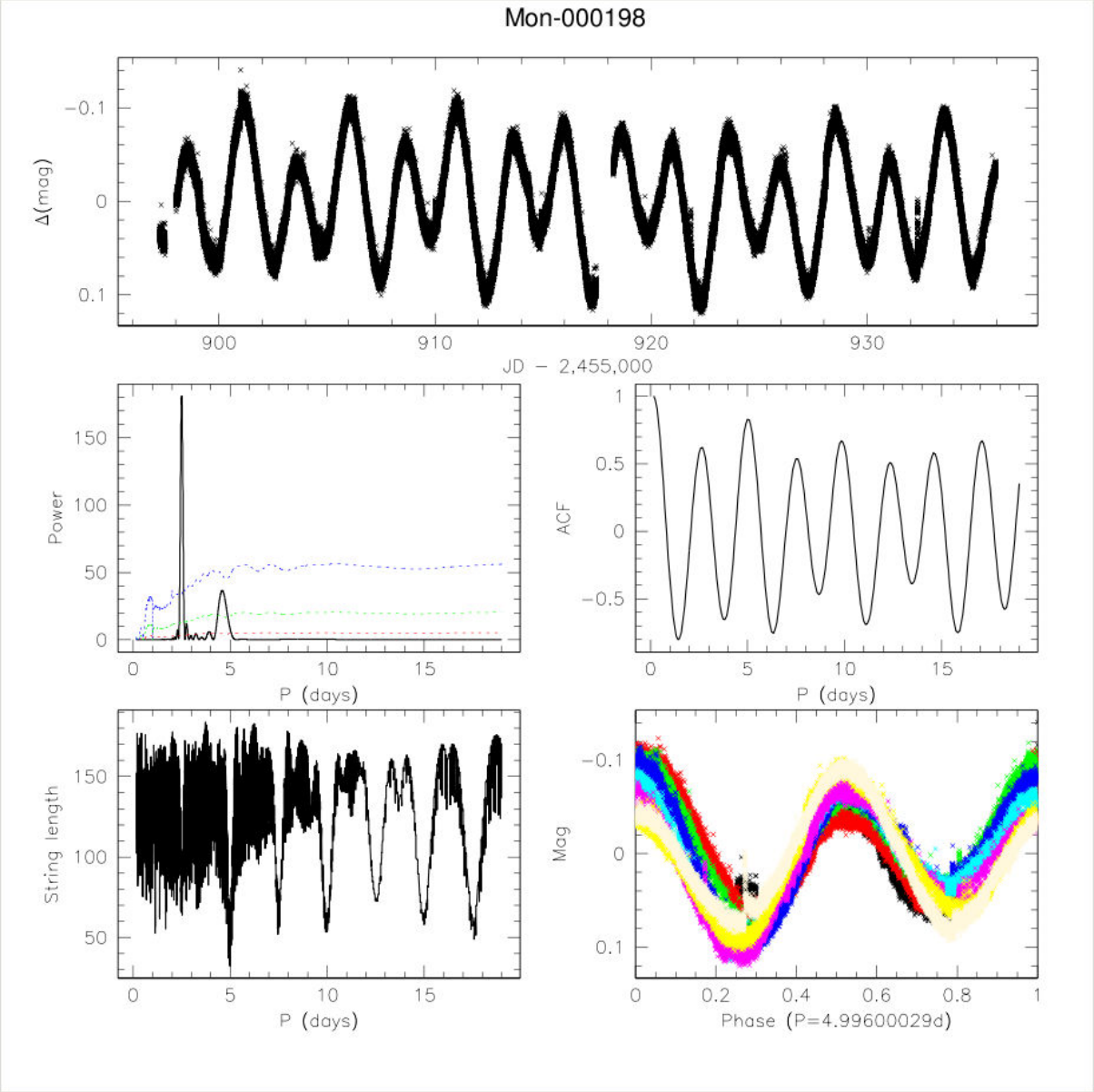

Figure 5.1: Period analysis for a multi-spotted WTTS member of NGC 2264. The original light curve after removal of spurious points is shown in the upper panel; results from the periodogram analysis are reported in the middle left panel; the auto-correlation function is illustrated in the middle right panel; results from the string-length method are shown in the lower left panel; the phased light curve with the final period is displayed in the lower right panel. Red, green and blue dotted curves in the middle left panel correspond respectively to the mean, mean+3 σ and mean+10 σ periodogram computed for light curves dominated by stochastic mag fluctuations about the mean (see Sect. 5.1.2). Due to the fact that the light curve "unit" (light variation pattern corresponding to one rotational cycle) has two minima, the periodogram analysis errouneously reports the half-period as best periodicity of the light curve; on the other hand, the correct periodicity is indicated by both the other methods.

The above discussion illustrates that each of these methods, which provide a different approach to the issue of periodicity in light curves, has its own advantages and limitations. A comparative analysis of the resulting diagrams from these three methods hence enables more robust period determination.

5.1.2 Implementation of the period-search routine

The rotation analysis performed here was based on the set of optical light curves obtained with the *CoRoT* satellite during the CSI 2264 campaign. A description of this dataset and of its preliminary reduction was provided in Sect. 2.2.1.

Cluster members were primarily identified among *CoRoT* targets based on spatial coordinate matching with the member list built as described in Chapter 3 of this thesis and reported in Venuti et al. (2014). A matching radius of 1 arcsec was adopted to identify sources common to that list of members and the list of *CoRoT* targets; only best (i.e., closest) matches were retained. Additional probable members, not included in the CFHT sample (mainly objects falling outside the CFHT/MegaCam field of view or brighter than the magnitude range explored), were selected from the CSI 2264 master catalog of the cluster (see Cody et al. 2014). The complete sample of members analyzed for periodicity consists of 502 objects, distributed in mass between ∼0.1 and 2 $M_{\odot}$.

Light curve processing and period extraction

Prior to the period search analysis, *CoRoT* light curves were rebinned to 2 h. The choice of this time step was on one side motivated by the 1.7 h-long orbital period of the *CoRoT* satellite, smoothed out in this new data binning (see also Affer et al. 2012, 2013); this also represents a suitable choice in terms of computation efficiency. To ascertain that this rebinning does not introduce a significant bias in the period detection for fast rotators, I computed the expected break-up velocity $\mathcal{V}$ for all sources in the sample with estimated mass $M_{\star}$ and radius $R_{\star}$ from Venuti et al. (2014) (available for 86% of the objects here investigated for periodicity). This comparison showed that, for the vast majority of objects, the minimum possible rotational period expected is longer than 2 h : less than 1% of the considered objects have $\mathcal{V} > 2\pi R_{*}/2\,h$, while about 9% have $\mathcal{V} > 2\pi R_{*}/4\,h$ (where 4 h is the smallest period that can be investigated according to the time step defined). Hence, it is reasonable to assume that the time step adopted for rebinning the light curves will not affect the results significantly.

Rebinned light curves were then investigated for periodicity. Each light curve was examined three times, using at each step a different technique among those listed in Sect. 5.1.1. I explored a range of periods from 0.4 h (i.e., twice the data sampling) to 19 days (i.e., half the total duration of the time series). The upper limit of the period range selection ensues from the assumption that a periodic behavior can be identified reliably only if this is repeated at least twice during the monitored time; however, I occasionally investigated possible longer periods in case some evidence of a significant periodicity above 19 days is shown in the light curve and/or in the results of the period search routine in the 0.17–19 days range. A step dP of 0.1 h was adopted to explore the period range with the LSP and the SL methods, while dP was set to the step of the rebinned time series for the ACF method.

At the end of the automated routine, I visually inspected and compared the period diagrams derived from each of the LSP, ACF and SL methods; I selected the best period as the one toward which indications from the three diagnostic tools converge. I used the ACF and SL diagrams as the primary reference to locate the correct periodicity, for the reasons explained in Sect. 5.1.1; I

then extracted the exact period value from the peak displayed in the periodogram at the position predicted from the other two methods.

In case no significant features are present in the LSP diagram at this location, the period value was extracted from the SL diagram; this latter usually provides period estimates which are more accurate than those derived from the ACF and in very good agreement with those extracted from the LSP diagram, as I could ascertain by performing an extensive comparison of period values measured from different methods for "easy" cases of periodic variables (spotted light curves). SL minima are typically more noisy than LSP peaks, as can be seen in the example in Fig. 5.1; to circumvent this issue, when SL results were adopted to determine the exact period value, I measured the position of each minimum in the SL period diagram and defined the extracted period as the average distance between successive minima.

Period validation

In order to obtain a first indication on the significance of periodogram peaks, I adopted the following procedure (see also Affer et al. 2013; Flaccomio et al. 2005; Eaton et al. 1995). I segmented the original light curve in blocks of 12 h, shuffled them and reassembled them in a random order. Every potential periodicity longer than the time length of the segments is destroyed in the process, hence resulting in a test light curve where the main contribution to variability arises from stochastic fluctuations. The periodogram analysis was then performed on this "stochastic" light curve and the whole routine was iterated 1 000 times. The noise periodogram was thus defined point by point as the mean power measured across the 1 000 simulations at the given ω value, while the variance measured across the 1 000 simulations was used to define confidence levels above the mean. The true periodogram of the source was then compared to these curves in order to get an indication of the confidence associated with the period detection/non-detection. This is illustrated in the middle panel of Fig. 5.1. It is important to note that the confidence levels estimated with this procedure might be somewhat optimistic: indeed, the nature of T Tauri stars is intrinsically variable on characteristic timescales beyond the periodic component linked to stellar rotation. This implies that, when we reshuffle the 12 h-long blocks, this characteristic variability component is destroyed together with the rotational modulation, which potentially results in underestimating the spurious "noise" component that affects the periodogram analysis for the true light curve. At any rate, the measured "false alarm probability" provides an useful indication as a relative scale to assess the robustness of individual period estimates throughout the sample.

A better statistical indicator of the degree of periodicity in the light curve is the parameter Q introduced in Cody et al. (2014). This measures how well a periodic trend at the period extracted can describe the original light curve. Q is defined as

$$Q = \frac{\left(rms^2_{resid} - \sigma^2\right)}{\left(rms^2_{raw} - \sigma^2\right)}\,, \tag{5.6}$$

where σ is the photometric uncertainty, rms_{raw} is the level of rms scatter in the original light curve, and rms_{resid} is the level of rms scatter in the light curve after subtraction of the periodic trend (which is reconstructed by generating a smoothed phase-folded curve and overlaying it to the original light curve, repeating it once per period). Q therefore measures how close the light curve points are to the systematic noise floor before and after subtraction of the phased trend from the light curve. Following the scheme of Cody et al. (2014), $Q < 0.11$ indicates strictly periodic light curves, $0.11 < Q < 0.61$ corresponds to quasi-periodic light curves, and $Q > 0.61$ indicates likely aperiodic light curves, with spurious period determination.

Table 5.1: Morphology types in the light curve sample of NGC 2264 members.

Morphology class	*Count*	*% tot.*
Burster	21	4.2
Dipper	37	7.4
Spotted	187	37.3
Multi-periodic	34	7.2
Eclipsing binary	3	0.6
Stochastic	22	4.4
Long-timescale variable	3	0.6
Non-variable	82	16.3
Others	114	22.7

A careful visual inspection of period diagrams and phase-folded light curves was performed to reinforce the statistical period validation based on the Q metrics. This is especially useful to decide on borderline cases or to select the correct periodicity in case of multiple peaks, as well as to check the accuracy of periodogram estimates (imprecise values will translate to offsets between different cycles in the phase-folded light curve). For all objects in the sample, I examined diagrams similar to that shown in Fig. 5.1 for a single example, and sorted them by eye into periodic at a given period or aperiodic, independently of the associated Q. I then compared this visual classification to the statistical classification, to confirm the periodic/aperiodic nature of objects for which the two approaches agree (nearly 80% of the total) and select the contradictory cases. For the latter, a final decision was taken upon further visual inspection. In order to limit biases deriving from the subjective character of such eye-based analyses, I provided a few of our collaborators (namely Jérôme Bouvier at IPAG, Ann Marie Cody at NASA Ames Research Center and John Stauffer at Spitzer Science Center) with the same diagnostic diagrams that I derived and used for the period extraction, and asked them to visually inspect those diagrams and list what sources they thought were periodic or aperiodic. I then put all results together and assigned or discarded a period estimate to a given source with a certain degree of confidence based on the coherence of these different classification schemes.

5.2 Results

In this and the next section of this chapter, I will illustrate the main results, from the periodicity analysis of the *CoRoT* sample, which are relevant to characterizing the properties of CTTS as opposed to WTTS and studying their connection with the accretion process.

Table 5.1 lists the different classes of light curve morphology identified in the complete *CoRoT* sample (CTTS+WTTS) and their respective frequency: bursters and dippers (defined in Sect. 2.3); spotted (periodic or quasi-periodic modulation presumably linked with surface spots); multi-periodic (beat-like light curves or showing two or more independent frequencies of modulation); eclipsing binaries; stochastic; long-timescale variables; non-variable (flat light curves); non-sorted light curves (unclassifiable variable type or affected by, e.g., temperature jumps).

A definite periodic signal is detected for 272 objects (single periodicity) + 3 EBs + 34 objects (multiple periods), i.e., for 62% of the objects in our sample. Among WTTS, a periodicity frequency of about $70\% \pm 9\%$ is detected; among CTTS, the frequency is of about $58\% \pm 6\%$.

The uncertainty on the period values, measured from the average width of a Gaussian fit to the periodogram peaks, is estimated as

$$err_P = 0.0096 \times P^2 \,, \tag{5.7}$$

where P is expressed in days. This hence amounts to $err_P \sim 0.15$ days for periods of the order of 4 days and $err_P \sim 1$ day for periods of the order of 10 days.

We can assume that, for objects for which a single periodicity is determined from the analysis, this corresponds to the rotation period of the star. In the following, I will then focus on the sample of single-period objects to explore the properties of rotation throughout the NGC 2264 cluster.

5.2.1 Period distribution for NGC 2264: CTTS vs. WTTS

Figure 5.2 shows the period distribution inferred for the population of the cluster.

Although *CoRoT* light curves extend over a time span of 38 consecutive days, hence enabling investigation of periods of up to about twenty days, the vast majority of periodic cluster members exhibit periodicity below 13 days. The period distribution of the cluster is bimodal, with one first peak at around 1.5 days and a second taller and broader peak at around 3-4 days, with a slowly-declining tail of longer periods.

A closer analysis of periods measured across the populations of CTTS and WTTS, separately, indicates that the first peak in the global period distribution is mostly determined by cluster members which lack disk signatures; very few fast rotators are found among CTTS. WTTS also define a second, broad peak around P∼4 days, with possible sub-structuring (one peak around 3.5 days and another around 5-5.5 days). The period distribution obtained for CTTS, on the other hand, is nearly flat with very few counts in the period range 0.5–2.5 days; it displays a peak of objects with periods around 3-3.5 days (close to the position of the second peak feature for WTTS) and then a long tail of slower rotators, similarly to what observed for WTTS.

This comparison suggests that distinct rotation properties are observed for disk-bearing and disk-less young stars, with the first rotating on average more slowly than the second (that is, if a fast rotator is found among young cluster members, this is most likely a WTTS rather than a CTTS). A Kolmogorov-Smirnov (K-S) test (Press et al. 1992) applied to the two populations yields a probability of only 4×10^{-3} that the corresponding distributions in period are extracted from the same parent distribution. This result is consistent with the findings of, e.g., Affer et al. (2013) and Cieza & Baliber (2007) in the NGC 2264 cluster (namely, statistically different rotational distributions for CTTS and WTTS, with the latter rotating faster than the former). This would support the idea that the presence of an accretion disk interacting with the central object has an impact on the rotation period of the star. As the systems evolve and circumstellar disks are dissipated, more and more diskless stars in the cluster will spin up as they contract, thus contributing to build the peak of fast-rotating sources which is observed in the distribution in Fig. 5.2 (see, e.g., the study of Vasconcelos & Bouvier 2015, who investigated the rotational evolution of young stars through numerical simulations).

5.2.2 Mass dependence?

Some studies have reported evidence of a significant mass dependence in the period distribution for young stars (see, e.g., the discussion in Herbst et al. 2007). Namely, while a bimodal period distribution is observed for higher-mass objects ($\geq$0.4 $M_\odot$), with the first peak of fast rotators centered around P∼1–2 days and the second peak at about 4–7 days, the distribution inferred for lower-mass objects only displays a single peak of fast rotators.

To test this effect, I divided the sample in three mass groups ($M_\star < 0.4$ $M_\odot$; $0.4 \leq M_\star \leq 1.0$ $M_\odot$; $M_\star > 1.0$ $M_\odot$), and compared the distributions of periods derived in each of them, both

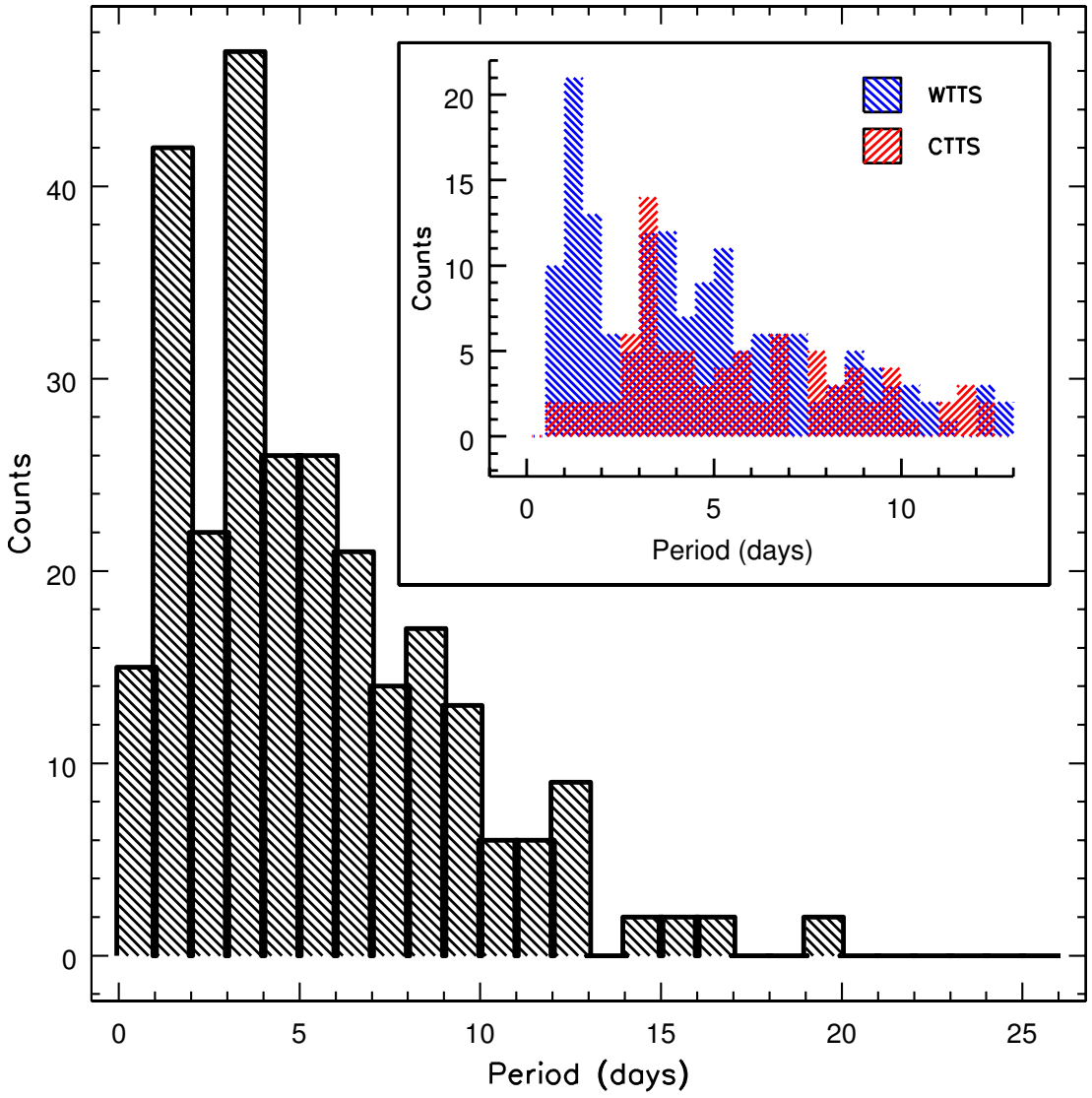

Figure 5.2: Period distribution for NGC 2264 members (shaded in black). Only objects with a single periodicity detected are considered to build this histogram. The box to the right of the complete period distribution shows a zoom of the 0–13 day period range, with illustration of the separate contributions from CTTS (shaded in red) and WTTS (shaded in blue) members of the cluster.

for CTTS and WTTS.

This is illustrated in Fig. 5.3. The limited statistics in each of the three mass groups, for WTTS and CTTS separately, does not allow accurate inferences to be extracted from this diagram; however, some indications of an evolution in shape from the upper panel (lower-mass regimes) to the lower panel (higher-mass regimes) might be present. The period distribution for WTTS at $M_\star < 0.4$ $M_\odot$ appears to display one significant peak at 1–2 days, while the population of slower rotators distributes fairly uniformly in the period range from 3 to 9 days. At intermediate masses (middle panel of Fig. 5.3), new peaks around P$\sim$4 days appear in the distribution, in addition to the peak of fast rotators; in the higher-mass regime ($M_\star > 1.0$ $M_\odot$), the period distribution for WTTS displays two well-defined peaks at 1–1.5 days and 3.5–4 days. The population of CTTS with period detections is more limited than that of WTTS, which reduces the statistics even more severely when dividing the sample in three mass groups; however, on Fig. 5.3, it can be observed that the few fast rotators detected among CTTS are concentrated at masses below 1 $M_\odot$; no fast rotators appear in the higher-mass sample.

Another global illustration of rotational periods vs. stellar mass in NGC 2264 is shown in Fig. 5.4. As noticed earlier, very few CTTS with periods shorter than 2 days are detected; a higher concentration of fast rotators relative to the total population at a given mass is observed for lower-mass objects ($\lesssim 0.5$ $M_\odot$).

To evaluate quantitatively the difference between the period distributions observed in different mass ranges, I compared CTTS and WTTS in the upper panel of Fig. 5.3 ($M_\star < 0.4$ $M_\odot$) with those in the lower panel of the same diagram ($M_\star > 1.0$ $M_\odot$) by means of a K-S test.

No conclusive evidence can be drawn from this analysis. When considering only CTTS, the K-S test returns a normalized probability of 0.2 that the two groups are extracted from the same parent distribution; a probability of 0.4 is obtained from a similar analysis for WTTS. When considering WTTS and CTTS together (that is, comparing the whole PMS population in the upper panel of Fig. 5.3 with that in the lower panel of the diagram), a p-value of 0.12 is obtained that periods for TTS in the lower mass range and those detected in the higher mass range derive from the same parent distribution.

5.2.3 Are CTTS periods similar in nature to WTTS periods?

As discussed in Artemenko et al. (2012), rotation periods detected for CTTS may not always derive from modulation effects by surface inhomogeneities, but also be associated with concentrations of material at some Keplerian orbit in the disk, which periodically cross the line of sight to the star.

The rotational period of a star is given by

$$P = \frac{2\pi R_\star}{v} \equiv \frac{2\pi R_\star \sin i}{v \sin i} \tag{5.8}$$

where v is the tangential velocity and $v \sin i$ is the projected rotational velocity, measured from spectroscopic observations (i being the inclination of the system, i.e., the angle between the rotation axis and the line of sight to the observer).

A simple way to check whether disk Keplerian periods may affect significantly the period distribution derived for CTTS consists in inverting Eq. 5.8 to derive an estimate of $\sin i$ for all objects with period determination and $R_\star$ and $v \sin i$ estimates in our sample. If the period measured is photometric, then we would expect to obtain $\sin i \leq 1$; if the period actually corresponds to some Keplerian orbit in the disk, the actual radial distance of the orbit from the stellar surface will be larger than the stellar radius, and hence using this latter in the equation for $\sin i$ will yield spurious $\sin i > 1$. Conversely, no such effect should be present among WTTS,

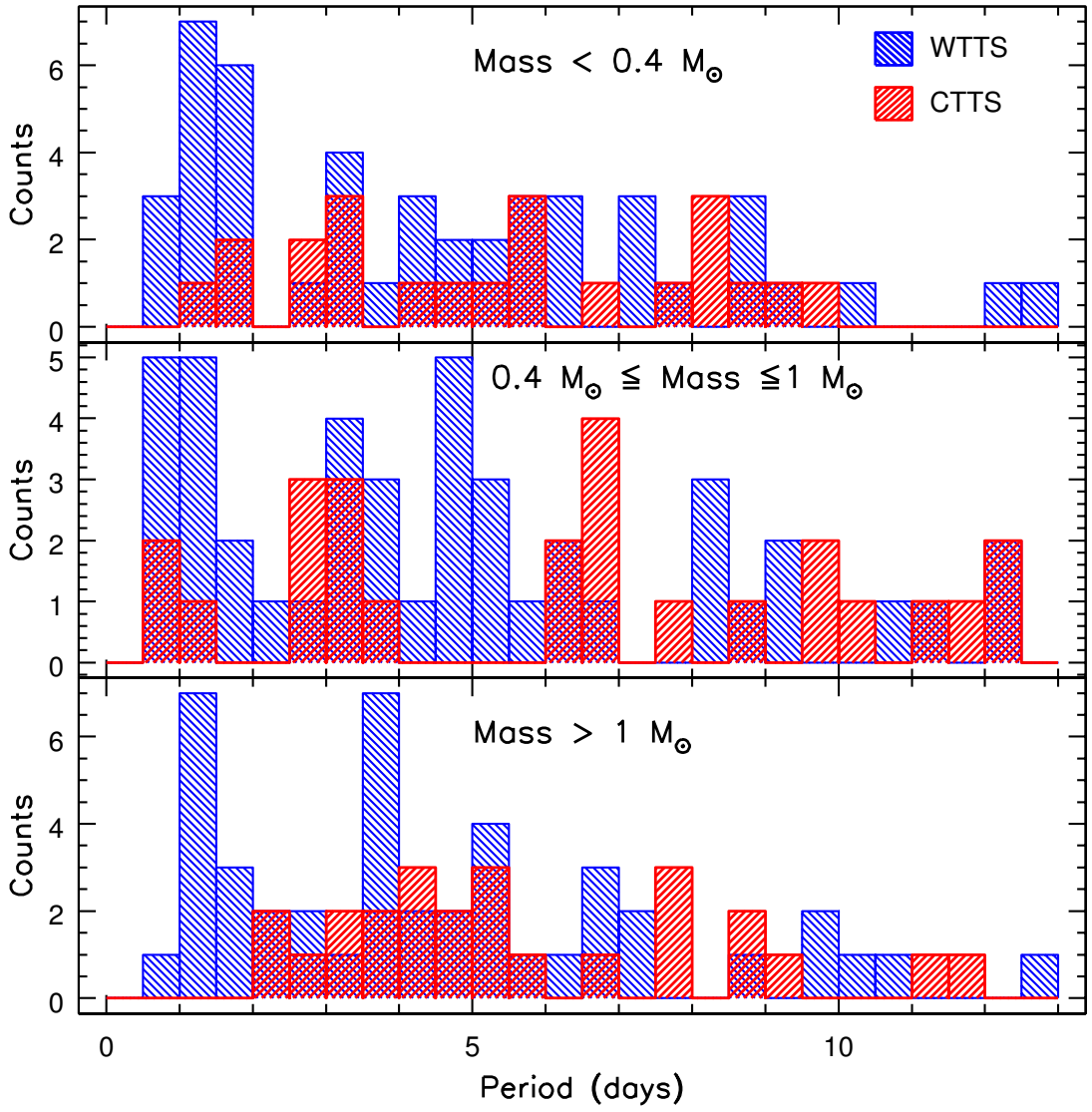

Figure 5.3: Period distributions inferred, for CTTS (red) and WTTS (blue), in each of three different mass regimes: $M_\star < 0.4$ $M_\odot$; $0.4 \leq M_\star \leq 1.0$ $M_\odot$; $M_\star > 1.0$ $M_\odot$. Only objects with a single period detected are considered for the diagram.

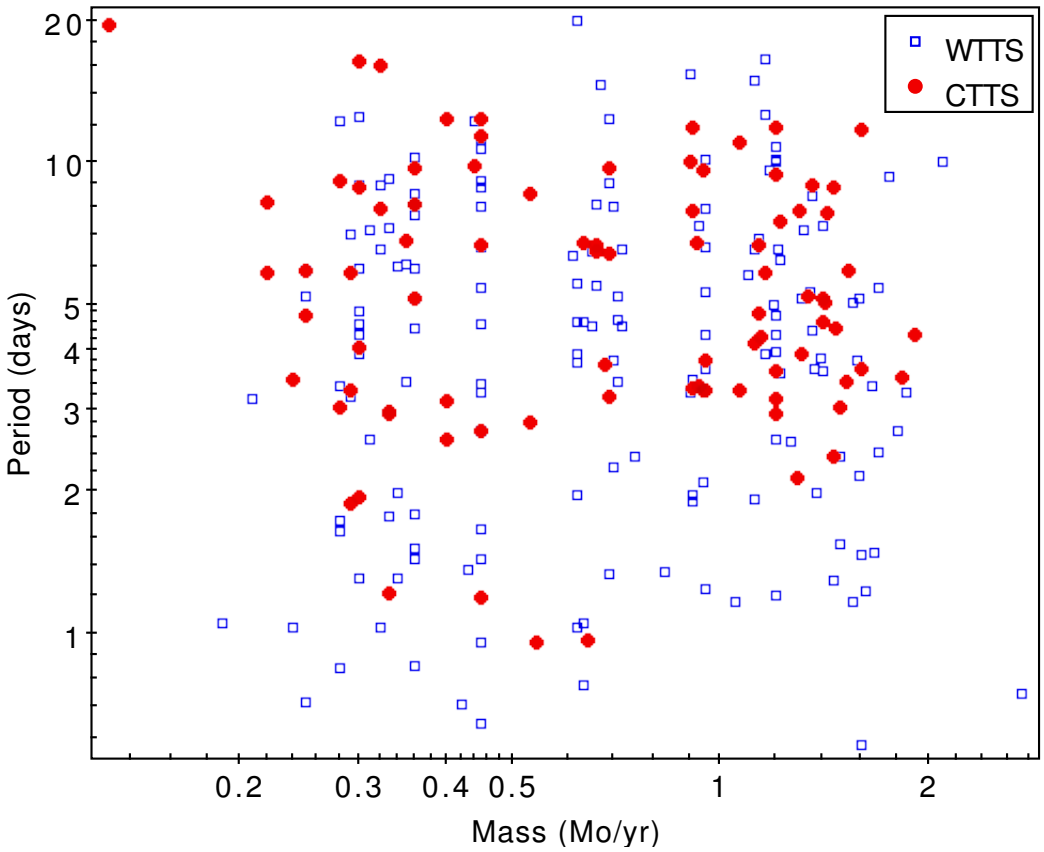

Figure 5.4: Periods of rotation, as a function of stellar mass, for CTTS (red dots) and WTTS (blue squares) in NGC 2264.

and the periods measured for these objects are expected to truly be photospheric. Hence, values of $\sin i$ systematically smaller than 1 should be expected to be found when repeating the same exercise for diskless cluster members.

The results of this computation for NGC 2264 members (CTTS and WTTS separately) are illustrated in Fig. 5.5. The values of $R_\star$ used for the computation are those computed as described in Sect. 3.3.4, while $v \sin i$ values are retrieved from the study of Baxter et al. (2009). Values of $\sin i$ are calculated as (Artemenko et al. 2012)

$$\sin i = 0.0195\, Pv \sin i / R_\star\,, \tag{5.9}$$

where P is expressed in days, $v \sin i$ in km s^{-1}, and $R_\star$ in solar radii.

For a part of the objects probed here, values of $\sin i > 1$ are obtained from this analysis. In the case of CTTS, this might indicate that the period detected from the light curve is actually not the axial rotation period, but a Keplerian period in the disk. However, similar properties are obtained for the distribution in $\sin i$ values of WTTS objects as well. This would suggest that the large values of $\sin i$ measured for some members are rather due to (or affected by) uncertainties on the parameters that intervene in the computation of the inclination. Hence, no evidence for a significantly different nature of CTTS periods compared to WTTS is derived from this analysis.

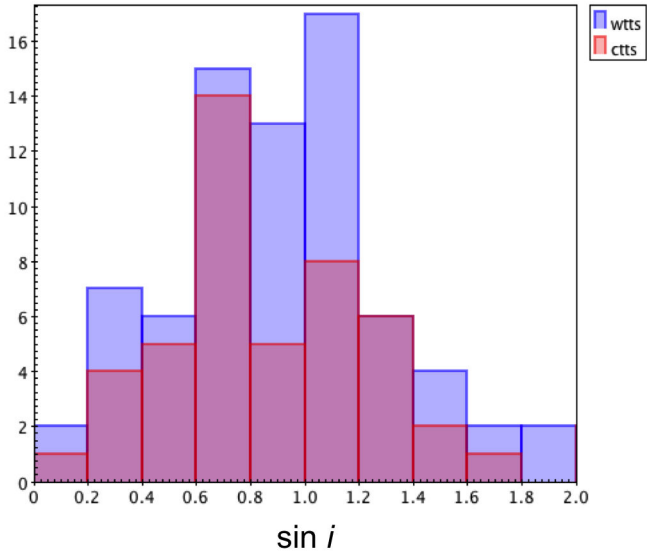

Figure 5.5: Distributions in $\sin i$ for CTTS (red) and WTTS (blue) objects in NGC 2264. The values of projected rotational velocities $v \sin i$ used for estimating the inclinations to the systems are retrieved from the study of Baxter et al. (2009).

5.3 The accretion–rotation connection

As illustrated in Sect. 1.3.2, the mechanism of interaction between young stars and their circumstellar disks is thought to be responsible for braking the central objects and thus preventing them from spinning up in the early phases of their evolution. This scenario, called "disk-locking", was developed since the first pictures of magnetospheric accretion in young stars (Königl 1991), which postulated a star-disk coupling through the stellar magnetosphere. It was later supported by a number of observational studies (e.g., Rebull et al. 2002; Herbst et al. 2002; Cieza & Baliber 2007) which showed that the frequency of objects with near-infrared excess (indicative of dusty inner disk) increases with rotation period, although no definite consensus has yet been reached on the effectiveness of this mechanism to brake the stars.

The period distribution derived for CTTS and WTTS in this study, presented in Sect. 5.2.1, provides evidence of distinct rotational behaviors for accreting and non-accreting stars: the second exhibit a prominent peak of fast rotators (P$\sim$1.5 days), while very few fast rotators are detected among the first group. This is consistent with the idea that circumstellar disks have a braking effect on young stars; after inner disks are cleared, these are not longer coupled and the central object can start spinning up as it contracts toward the ZAMS.

Measurements of the UV excess provide a more direct diagnostics of mass accretion onto the star than the detection of near-IR excess. In 2006, Fallscheer & Herbst used the UV excess to investigate a connection between the accretion properties and the rotation properties for about a hundred of objects in NGC 2264. They reported empirical evidence in support of the disk-locking paradigm: slowly rotating stars were more likely to have large UV excesses than rapidly rotating stars.

In Fig. 5.6, I show the distribution of UV excesses vs. rotational periods for the wider sample of NGC 2264 members probed in this study. UV excess measurements are obtained as discussed in Sect. 3.4.1 of this manuscript. This plot does confirm that a statistic association exists between rotation periods and UV excess (and, hence, accretion). WTTS, whose "UV excess" distribution reflects the scatter around the reference color sequence (as illustrated in Sect. 3.4.1), populate the diagram on the whole range of periods, with two broad concentrations between 0.5–2 days

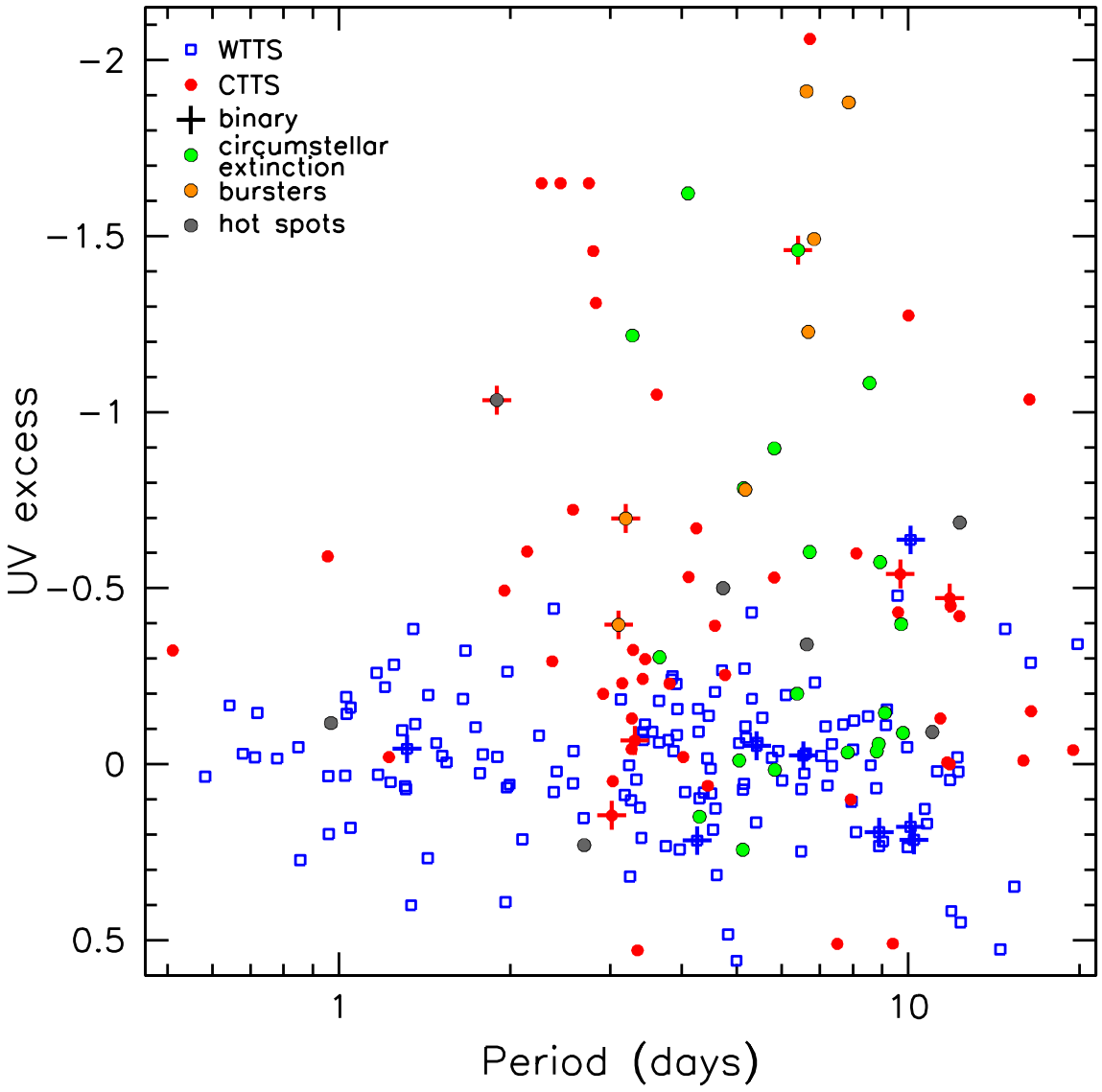

Figure 5.6: Distribution of UV excess vs. rotation periods for NGC 2264 members. UV excesses are computed as described in Sect. 3.4.1; the UV excess increases from bottom to top along the y-axis. CTTS are indicated as red dots on the diagram; WTTS are marked as blue squares. Among CTTS, objects with a circumstellar extinction-dominated light curve are marked in green, objects dominated by stochastic accretion bursts are marked in orange and objects with a hot spot-dominated light curve are marked in grey. Crosses indicate the objects in the sample which are known binary systems.

and around 5 days, and are distributed nearly horizontally around UV excess∼0. A clear dearth of accreting objects (UV excess $\lesssim$ -0.5) with short periods (P $\lesssim$ 2 days) appears on the diagram; CTTS distribute at periods longer than 2 days across the whole range of UV excess. A number of CTTS are found to populate the WTTS locus at longer periods on the diagram. Interestingly, many of these objects belong to the variable extinction group. This may indicate that the accretion shock is partly screened by intervening material in these systems, hence yielding lower apparent UV excesses.

5.4 Conclusions

In this chapter, I have illustrated some preliminary results on the analysis of rotation properties in the NGC 2264 cluster, and their connection with the accretion process. Periodicity was investigated from the set of light curves obtained with the *CoRoT* satellite during the CSI 2264 campaign; three different methods of period search and extraction (Lomb-Scargle periodogram, auto-correlation function, string-length method) were employed to detect periodic signals in the time series photometry.

Assuming that the photometric periods detected arise from luminosity modulation by inhomogeneities at the stellar surface (and hence really correspond to the rotation period of the star), a bimodal period distribution is reconstructed for the NGC 2264 cluster. The first peak in the distribution is located around periods of ∼1.5 days (fast rotators), while the second, broader, peak is located around P∼4 days. The population of fast rotators mostly comprises diskless stars (WTTS) in the cluster; very few CTTS are found to rotate at rates faster than 2 days. Conversely, the peak in the distribution at longer periods is defined by both CTTS and WTTS members. Some hints of a possible mass dependence in the period distribution, with lower-mass stars showing a single peak at short rotation periods and higher-mass stars distributing in period in a bimodal fashion, may be conveyed from the data, although no conclusive statistical evidence could be derived from our sample.

Definite evidence for a connection between the presence of circumstellar disks and the rotation properties of the central objects is inferred from this analysis. Rotation rates for CTTS are on average slower than those measured across the WTTS group, and the period distribution for disk-bearing sources shows a single peak around 3.5–4 days. Analysis of the distribution of UV excess vs. rotation rates indicates that large UV excesses are typically associated with long periods; this is consistent with the disk-locking scenario. On the other hand, the period distribution for WTTS members is found to be bimodal, with a prominent peak of fast rotators and a second, smaller peak at intermediate rotation rates (at approximately the same location as the period peak in CTTS), with a long tail toward longer periods. The presence of both fast and slower rotators among WTTS may reflect a variety in the evolutionary state of the objects, which implies that these have been released from their circumstellar disks at different epochs. WTTS distributed at slower rotation rates may have dissipated their inner disks more recently, and hence have not yet had the time to spin up significantly. As evolution progresses, disk-free objects contract toward the ZAMS and increase their rotation speed to conserve angular momentum, thus migrating toward the fast rotation regimes.

Chapter 6

Conclusions and perspectives

6.1 Case of study: a brief recap

In the course of this thesis, I have explored the variety and time evolution of the accretion process in young stars, from an observational perspective. My study focused on a sample of over 750 T Tauri stars, accreting (CTTS) and not (WTTS), in the star-forming region NGC 2264. This was the target of a large-scale monitoring program, the *Coordinated Synoptic Investigation of NGC 2264* (CSI 2264), commenced in December 2011; the program involved simultaneous monitoring of YSO variability across the cluster with several telescopes, with the aim of obtaining broad wavelength coverage (from the X-rays to the mid-IR) on timescales ranging from sub-hours to several weeks. Such large-scale surveys are critical to our understanding of the physics and evolution of PMS stars. Exploring the wavelength domain in YSO variability enables simultaneous characterization of the different emitting regions in a young stellar object, which provides strong constraints on the nature of these sources. Exploring the time domain in YSO variability allows us to determine the characteristic timescales of the physical processes at play and to investigate their dynamics. Moreover, statistical studies of large homogeneously characterized populations enable exploration of how the properties of the different processes vary as a function of stellar parameters (e.g., mass and age), which is connected to their evolution.

In the context of the CSI 2264 project, I took charge of the analysis of observations performed at the Canada-France-Hawaii Telescope (instrument MegaCam), which consisted of a deep 4-band (u, g, r, i) mapping of the region and of two-week-long monitoring of the variability of about 9 000 sources in the field of view at UV (u-band) and optical (r-band) wavelengths. The primary motivation for this dataset was to probe and monitor the distinctive UV excess that CTTS exhibit relative to the intrinsic colors of non-accreting young stars, from which mass accretion rates can be derived for all disk-bearing sources in the cluster. The simultaneity between the u-band and r-band observations enabled investigation of the variations in color as the sources transit from the brightest to the faintest luminosity states; this allows us to distinguish between different physical scenarios and therefore map the diverse nature of variability among cluster members. Light curves trace the flux variations on timescales from hours (several measurements during the same night) to several days; comparison of the amount of variability detected on those two timescales, in combination with the results of similar surveys performed at distant epochs, was analyzed to identify the leading timescales of variability observed on both accreting and non-accreting sources. In the picture of modulated variability, rotation periods can be determined photometrically from repeated patterns in the light curves; in the last part of the thesis, and using the time series photometry obtained over a period of 40 consecutive days with the *CoRoT* satellite, as part of the CSI 2264 campaign, I carried out a periodicity analysis for CTTS and WTTS in the region, to explore the connection between the accretion process and

rotation properties.

In Sect. 6.2, I summarize the main results obtained from the thesis work outlined in the above; Sect. 6.3 illustrates some points for further analysis.

6.2 Main points of this work

6.2.1 Different accretion regimes coexist within the cluster

A broad variety of accretion regimes is detected in the PMS population of NGC 2264. The strongest accretors in the region have measured $\dot{M}_{acc} \sim 10^{-7}$ $M_\odot$/yr; on the opposite side of the distribution in accretion rates, objects are found at $\dot{M}_{acc} \sim 10^{-10}$ $M_\odot$/yr or fall below the detection threshold. In between these two ends, cluster members trace a continuum of intermediate states.

A definite correlation is derived between the average $\dot{M}_{acc}$ and stellar mass $M_\star$ ($\dot{M}_{acc} \propto M_\star^{1.4\pm0.3}$) over the range 0.1–1.5 $M_\odot$. The data point distribution suggests that the functional form of this dependence itself may be mass-dependent, with the lower-mass objects exhibiting a steeper correlation of the average $\dot{M}_{acc}$ with $M_\star$. Similarly, the steepness of the correlation appears to vary, on the $\dot{M}_{acc}$ vs. $M_\star$ plane, from the lower to the upper edge of the distribution in $\dot{M}_{acc}$; in particular, a weaker correlation is found for the highest accretion regimes.

The global $\dot{M}_{acc}$ vs. $M_\star$ distribution inferred for the whole disk-bearing population of the cluster displays a large spread in $\dot{M}_{acc}$ values at any given stellar mass. This spread may extend over two orders of magnitude. This feature cannot simply be explained with uncertainties on the stellar parameters used for the computation of the accretion rates, that have been derived for all objects in the sample in a homogeneous and internally self-consistent way. Similarly, stellar variability, at least on timescales of weeks, is found not to impact this spread significantly: the typical variability range on $\dot{M}_{acc}$ measured in this study amounts to ∼0.5 dex, that is, considerably smaller than the spread observed.

6.2.2 $\dot{M}_{acc}$ reflect a diversity in accretion mechanisms and cluster evolution

Different accretion regimes may be associated with a diverse nature of the accretion process onto the star. Unstable regimes, where Rayleigh-Taylor instabilities at the disk-magnetosphere boundary are predominant, manifest as stochastic bursts of accretion at typically high $\dot{M}_{acc}$; objects undergoing this process populate the upper boundary of the $\dot{M}_{acc}$ vs. $M_\star$ distribution. At somewhat lower accretion rates, objects appear to be dominated by stable, funnel-flow accretion, where material from the inner disk organizes in two main accretion streams, at roughly opposite phases, resulting from the interaction of the disk with an inclined dipole. When the systems are seen at low inclinations (i.e., close to the rotation pole), their light variations appear to be dominated by hot surface spots at the accretion shocks; at high inclinations (i.e., for systems seen almost edge-on), the same accretion mechanism likely produces AA Tau-like light curves, where the most prominent light variations are associated with periodic fading events due to a rotating inner disk warp that partly occults the stellar photosphere.

The wide range in $\dot{M}_{acc}$ spanned by the disk population of NGC 2264 may also reflect the history of formation and dynamical evolution of the cluster. The strongest accretors are observed to be predominantly located close to the two sites, across the region, where star formation activity is still ongoing; this suggests that, on average, these objects have been formed more recently than other cluster members, and hence did not yet have time to dynamically evolve far from the birth sites. More moderate accretors are instead distributed more evenly across the cluster area, within radii of a few parsecs from the two poles of star formation. Comparison with the spatial distribution of WTTS shows that the latter are even more broadly scattered; this may indicate

that disk-free objects are on average dynamically older than disk-bearing members, albeit with a significant degree of overlapping between CTTS and WTTS properties.

6.2.3 Variability in young stars has a broadly assorted nature

Mapping of variability features at short wavelengths across the cluster yields statistically different results for CTTS and WTTS. The first group exhibits higher levels of variability than the second; in both cases, variability amplitudes are larger in the UV than in the optical, but this λ-dependence is steeper in the case of CTTS than for WTTS. These color properties are consistent with a broad variability scenario where WTTS are dominated by cold magnetic spots and CTTS are dominated by hot accretion shocks. Typical spot parameters found across the two groups are $\Delta T \equiv T_{phot} - T_{spot} \approx 500 \div 1000\,\mathrm{K}$ and surface coverage $\mathcal{F}_{eq} \approx 10 \div 30\%$ for WTTS, and $\Delta T \approx -2000\,\mathrm{K}$ and $\mathcal{F}_{eq} \approx 1 \div 5\%$ for CTTS. The distributions of variability properties found for CTTS and WTTS display a significant overlap, which indicates that accretion and magnetic-related features combine in varying proportions in individual objects.

Somewhat different color signatures pertain to variability types which are dominated by circumstellar extinction in systems seen almost edge-on. Out of the eclipse phases, these objects exhibit color variations consistent with hot spots at the stellar surface; however, when flux dips occur, strong luminosity decreases are observed which are not accompanied by any substantial color change (grey occultation). When the system is less luminous, at the faintest states of the systems, a effect of blueing (color becoming bluer as the luminosity drops) may be detected, due to the light scattered off the disk plane.

6.2.4 Timescales of days dominate the variability of WTTS and CTTS

Short-lived events like chromospheric flares or bursts of accretion may determine a considerable increase in luminosity over short timescales (hours); however, a statistical investigation across the whole sample of young stars in NGC 2264 shows that variability on hour-long timescales (i.e., at different epochs within a single night) typically represents a small percentage ($\lesssim 10\%$) of that detected on day-long timescales, and may thus be explained as the fraction of the variation trend exhibited on day timescales which is accomplished during a single night[1]. This result is the same for CTTS and for WTTS.

If we compare the flux measurements obtained at epochs a few years apart ("long-term" timescales), the amount of variability detected is comparable to that measured when comparing two epochs at a distance of days ("short-term" timescales). This result suggests that variability on timescales of a few to several ($\lesssim 10$) years, at least, mainly reflects the variability trend on day timescales. Again, no difference is found between CTTS and WTTS in this respect: in both groups, the amount of variability on the long term can be typically accounted for by variability on the mid term. This would indicate that, in both groups, similar effects (namely geometric modulation of luminosity over a rotation cycle) dominate the observed variability pattern from mid-term to long-term timescales.

The strong impact of modulated variability on the $\dot{M}_{acc}$ variations monitored over a few rotational cycles is assessed in this study by folding the UV excess light curve in phase with the rotational period of the objects and measuring the UV excess variations, in a given phase bin, both within a single night and from one cycle to the next. The sum of these two components typically accounts for less than 25% of the total amplitude of variability; this indicates that modulated variability alone contributes up to 75% of it.

[1] Indeed, if we consider a typical rotation period of 4 days and a nightly observation window of 6 hours, during that night we would expect to detect an amplitude of variability which is roughly 1/8 of the total modulated amplitude.

The fact that, independently of the accretion status, rotational modulation dominates the variability on baselines of up to years suggests that the main features of accretion are typically stable on such timescales. Hot spots at the stellar surface likely form and evolve on much shorter timescales, as suggested by the distinctive irregular profiles of their light curves, with stochastic small-scale substructures overimposed on the main pattern. However, the absence of a significant variability above that contributed by day timescales on the longer term indicates that the dnamics of the accretion process is "self-consistent" on years or more, that is, the mechanisms which regulate the mass transfer from the inner disk to the star repeat themselves in a similar fashion, with resulting long-term stability in the averaged accretion properties of a given system.

6.2.5 Disks have an impact on the rotation properties of young stars

WTTS and CTTS exhibit statistically distinct rotation properties. The first define a bimodal period distribution, with a first peak of fast rotators (P$\sim$1.5 days) and a second peak at more moderate rotation rates (P$\sim$4 days). CTTS, instead, have lower spin rates on average than WTTS: their period distribution shows a single peak around P$\sim$3.5–4 days, with almost no fast rotators below P$\sim$2 days and a long tail toward longer periods.

The absence of CTTS with short rotation periods likely reflects the mechanism of star-disk coupling in early stellar evolution. In the disk-locking scenario, the interaction at the star-magnetosphere boundary acts like a brake onto the star, imposing constant angular velocity and preventing it from spinning up during the disk phase. A comparison between the rotation properties and the accretion properties of NGC 2264 members shows that, indeed, a connection between disk accretion and rotation is observed, with large UV excesses being typically associated with long periods. At later stages of PMS stellar evolution, after the star has been released from the inner disk (dissipated via accretion onto the central object, mass ejection, photoevaporation and/or other mechanisms), it can start spinning up as it contracts toward the ZAMS, eventually merging with the population of fast rotators among WTTS, on timescales of a few Myr.

6.3 Perspectives

Our understanding of the accretion process in young stars has made enormous progress over the last decades, thanks to the wealth of observational constraints brought by both large-scale and individual surveys, and to the parallel development of more sophisticated models of the dynamics of early stellar evolution. Nevertheless, several issues remain to be explored.

Small-scale structures and variability features in the light curves of CTTS often appear to be irregular and short-lived. However, results presented in this thesis and in earlier studies indicate that the typical amplitudes of photometric variations associated with a given object on timescales of days tend to be preserved on timescales of years, and are dominated by modulation effects linked with stellar rotation. This would suggest that the main accretion features on a typical object tend to repeat themselves on the longer term. A question that may arise is what mechanism actually regulates disk accretion onto the star. Instabilities in the disk may determine inward transport of material at irregular rates; however, the flux of material at the star-disk interaction interface becomes governed by the stellar magnetosphere, and this latter may act like a dam which determines the amount of material that can be conveyed to the star. Magnetically-driven mass ejections from the system may then intervene in the regulation of the disk accretion process, by carrying away material in excess of the quantity actually channeled in the accretion columns.

A related issue is characterizing the time-dependence and evolution of disk accretion. This is critical to achieve a more profound understanding of the physics of disk evolution, and also to set

the time frame for planetary formation. Studies of disk lifetimes based on the IR excess frequency in various young clusters of differing ages cannot fully address this issue, as they do not provide any clues to the time-dependence of mass accretion rate in circumstellar disks. To address this point, we have started a campaign of photometric survey of several young clusters and star-forming regions, whose average ages span the range between 1-2 Myr and 20 Myr (that is, the range of interest for disk lifetimes as inferred from IR-based studies). Homogeneous u, g, r, i mapping was obtained for each of these clusters at CFHT with the instrument MegaCam between semesters 2014A and 2014B (programs 14AF17 and 14BF17, respectively; P.I. = L. Venuti). An analysis similar in scope to that presented in this thesis for NGC 2264 will be performed on each cluster to derive a global picture of accretion as a function of age. The adoption of average cluster ages to define the age scale for $\dot{M}_{acc}$ evolution will enable us to circumvent the issue of poorly constrained individual ages for cluster members, which limits the reliability of intra-cluster studies of $\dot{M}_{acc}$ evolution based on intrinsic age spread among cluster members, as mentioned earlier in this manuscript. Moreover, the homogeneity in dataset, reduction and analysis method will ensure internal consistency in the comparative results for the complete sample. This will enable detailed investigation of the average mass accretion rates, of their relationship with stellar mass and of the associated accretion rate dispersion as a function of age. This, in turn, will provide new insight onto the dynamics of disk accretion and its evolution over an age range corresponding to the planet-building era around young solar-type stars.

Bibliography

Abazajian, K., Adelman-McCarthy, J. K., Agüeros, M. A., et al. 2004, AJ, 128, 502

Abazajian, K. N., Adelman-McCarthy, J. K., Agüeros, M. A., et al. 2009, ApJS, 182, 543

Abramowitz, M. & Stegun, I. A. 1972, Handbook of Mathematical Functions

Adams, M. T., Strom, K. M., & Strom, S. E. 1983, ApJS, 53, 893

Affer, L., Micela, G., Favata, F., & Flaccomio, E. 2012, MNRAS, 424, 11

Affer, L., Micela, G., Favata, F., Flaccomio, E., & Bouvier, J. 2013, MNRAS, 430, 1433

Alcalá, J. M., Natta, A., Manara, C. F., et al. 2014, A&A, 561, A2

Alencar, S. H. P., Teixeira, P. S., Guimarães, M. M., et al. 2010, A&A, 519, A88

Alexander, R. D. & Armitage, P. J. 2006, ApJ, 639, L83

Allard, F., Homeier, D., & Freytag, B. 2012, Royal Society of London Philosophical Transactions Series A, 370, 2765

Ambartsumian, V. A. 1947, Stellar Evolution and Astrophysics, Acad. Sci. Armenian S.S.R., Yerevan

Ambartsumian, V. A. 1949, Astron. Zh., 26, 3

Appenzeller, I. & Mundt, R. 1989, A&A Rev., 1, 291

Artemenko, S. A., Grankin, K. N., & Petrov, P. P. 2012, Astronomy Letters, 38, 783

Astier, P., Guy, J., Regnault, N., et al. 2006, A&A, 447, 31

Baglin, A., Auvergne, M., Barge, P., et al. 2009, in IAU Symposium, Vol. 253, IAU Symposium, ed. F. Pont, D. Sasselov, & M. J. Holman, 71–81

Banerjee, R. & Pudritz, R. E. 2006, ApJ, 641, 949

Baraffe, I., Chabrier, G., Allard, F., & Hauschildt, P. H. 1998, A&A, 337, 403

Baraffe, I., Chabrier, G., & Gallardo, J. 2009, ApJ, 702, L27

Barentsen, G., Vink, J. S., Drew, J. E., et al. 2011, MNRAS, 415, 103

Bate, M. R. 2009, MNRAS, 397, 232

Bate, M. R., Bonnell, I. A., & Bromm, V. 2003, MNRAS, 339, 577

Baxter, E. J., Covey, K. R., Muench, A. A., et al. 2009, AJ, 138, 963

Beckwith, S. V. W., Sargent, A. I., Chini, R. S., & Guesten, R. 1990, AJ, 99, 924

Bell, C. P. M., Naylor, T., Mayne, N. J., Jeffries, R. D., & Littlefair, S. P. 2013, MNRAS, 434, 806

Bergemann, M., Ruchti, G. R., Serenelli, A., et al. 2014, A&A, 565, A89

Bertin, E. 2011, in Astronomical Society of the Pacific Conference Series, Vol. 442, Astronomical Data Analysis Software and Systems XX, ed. I. N. Evans, A. Accomazzi, D. J. Mink, & A. H. Rots, 435

Bertin, E. & Arnouts, S. 1996, A&AS, 117, 393

Bertout, C. 1989, ARA&A, 27, 351

Bertout, C., Basri, G., & Bouvier, J. 1988, ApJ, 330, 350

Bessell, M. S., Castelli, F., & Plez, B. 1998, A&A, 333, 231

Biazzo, K., Alcalá, J. M., Covino, E., et al. 2012, A&A, 547, A104

Bilir, S., Karaali, S., & Tunçel, S. 2005, Astronomische Nachrichten, 326, 321

Blaauw, A. 1958, Ricerche Astronomiche, 5, 105

Boulade, O., Charlot, X., Abbon, P., et al. 2003, in Society of Photo-Optical Instrumentation Engineers (SPIE) Conference Series, Vol. 4841, Instrument Design and Performance for Optical/Infrared Ground-based Telescopes, ed. M. Iye & A. F. M. Moorwood, 72–81

Bouvier, J., Alencar, S. H. P., Boutelier, T., et al. 2007a, A&A, 463, 1017

Bouvier, J., Alencar, S. H. P., Harries, T. J., Johns-Krull, C. M., & Romanova, M. M. 2007b, Protostars and Planets V, 479

Bouvier, J., Cabrit, S., Fernandez, M., Martin, E. L., & Matthews, J. M. 1993, A&A, 272, 176

Bouvier, J., Chelli, A., Allain, S., et al. 1999, A&A, 349, 619

Bouvier, J., Covino, E., Kovo, O., et al. 1995, A&A, 299, 89

Bouvier, J., Grankin, K., Ellerbroek, L. E., Bouy, H., & Barrado, D. 2013, A&A, 557, A77

Bouvier, J., Grankin, K. N., Alencar, S. H. P., et al. 2003, A&A, 409, 169

Bouvier, J., Matt, S. P., Mohanty, S., et al. 2014, Protostars and Planets VI, 433

Calvet, N. & D'Alessio, P. 2011, Protoplanetary Disk Structure and Evolution, ed. P. J. V. Garcia, 14–54

Calvet, N. & Gullbring, E. 1998, ApJ, 509, 802

Calvet, N., Muzerolle, J., Briceño, C., et al. 2004, AJ, 128, 1294

Camenzind, M. 1990, in Reviews in Modern Astronomy, Vol. 3, Reviews in Modern Astronomy, ed. G. Klare, 234–265

Castelli, F. & Kurucz, R. L. 2004, ArXiv Astrophysics e-prints

Cauley, P. W., Johns-Krull, C. M., Hamilton, C. M., & Lockhart, K. 2012, ApJ, 756, 68

Cieza, L. & Baliber, N. 2007, ApJ, 671, 605

Claret, A. & Bloemen, S. 2011, A&A, 529, A75

Clarke, C. J. & Pringle, J. E. 2006, MNRAS, 370, L10

Cody, A. M. & Hillenbrand, L. A. 2010, ApJS, 191, 389

Cody, A. M., Stauffer, J., Baglin, A., et al. 2014, AJ, 147, 82

Cohen, M. 1973, MNRAS, 161, 85

Cohen, M. & Kuhi, L. V. 1979, ApJS, 41, 743

Costigan, G., Vink, J. S., Scholz, A., Ray, T., & Testi, L. 2014, MNRAS, 440, 3444

Covey, K. R., Ivezić, Ž., Schlegel, D., et al. 2007, AJ, 134, 2398

Covey, K. R., Lada, C. J., Román-Zúñiga, C., et al. 2010, ApJ, 722, 971

Dahm, S. E. 2008, Handbook of Star Forming Regions, Volume I, 966

Dahm, S. E. & Simon, T. 2005, AJ, 129, 829

Donati, J.-F. & Landstreet, J. D. 2009, ARA&A, 47, 333

Donati, J.-F., Skelly, M. B., Bouvier, J., et al. 2010, MNRAS, 402, 1426

Dreyer, J. L. E. 1888, MmRAS, 49, 1

Duchêne, G., Ménard, F., Stapelfeldt, K., & Duvert, G. 2003, A&A, 400, 559

Dullemond, C. P., Natta, A., & Testi, L. 2006, ApJ, 645, L69

Dutrey, A., Guilloteau, S., & Ho, P. 2007, Protostars and Planets V, 495

Dworetsky, M. M. 1983, MNRAS, 203, 917

Eaton, N. L., Herbst, W., & Hillenbrand, L. A. 1995, AJ, 110, 1735

Edwards, S., Hartigan, P., Ghandour, L., & Andrulis, C. 1994, AJ, 108, 1056

Elias, J. H., Frogel, J. A., Matthews, K., & Neugebauer, G. 1982, AJ, 87, 1029

Ercolano, B., Mayr, D., Owen, J. E., Rosotti, G., & Manara, C. F. 2014, MNRAS, 439, 256

Fallscheer, C. & Herbst, W. 2006, ApJ, 647, L155

Fang, M., Kim, J. S., van Boekel, R., et al. 2013, ApJS, 207, 5

Fazio, G. G., Hora, J. L., Allen, L. E., et al. 2004, ApJS, 154, 10

Feigelson, E. D. & Babu, G. J. 2012, Modern Statistical Methods for Astronomy, Cambridge University Press

Ferreira, J. 1997, A&A, 319, 340

Fűrész, G., Hartmann, L. W., Szentgyorgyi, A. H., et al. 2006, ApJ, 648, 1090

Finlator, K., Ivezić, Ž., Fan, X., et al. 2000, AJ, 120, 2615

Fiorucci, M. & Munari, U. 2003, A&A, 401, 781

Flaccomio, E., Micela, G., Favata, F., & Alencar, S. P. H. 2010, A&A, 516, L8

Flaccomio, E., Micela, G., & Sciortino, S. 2006, A&A, 455, 903

Flaccomio, E., Micela, G., Sciortino, S., et al. 2005, ApJS, 160, 450

Fonseca, N. N. J., Alencar, S. H. P., Bouvier, J., Favata, F., & Flaccomio, E. 2014, A&A, 567, A39

Frank, A., Ray, T. P., Cabrit, S., et al. 2014, Protostars and Planets VI, 451

Frank, J., King, A., & Raine, D. J. 2002, Accretion Power in Astrophysics: Third Edition

Fruth, T., Kabath, P., Cabrera, J., et al. 2012, AJ, 143, 140

Fukugita, M., Ichikawa, T., Gunn, J. E., et al. 1996, AJ, 111, 1748

Gahm, G. F., Loden, K., Gullbring, E., & Hartstein, D. 1995, A&A, 301, 89

Gammie, C. F. 1996, ApJ, 457, 355

Garcia, P. J. V., Natta, A., & Walmsley, M. 2011, Circumstellar Disks around Young Stars, ed. P. J. V. Garcia, 1–13

Ghosh, P. & Lamb, F. K. 1979, ApJ, 232, 259

Gillen, E., Aigrain, S., McQuillan, A., et al. 2014, A&A, 562, A50

Goodman, A. A., Crutcher, R. M., Heiles, C., Myers, P. C., & Troland, T. H. 1989, ApJ, 338, L61

Grankin, K. N., Bouvier, J., Herbst, W., & Melnikov, S. Y. 2008, A&A, 479, 827

Grankin, K. N., Melnikov, S. Y., Bouvier, J., Herbst, W., & Shevchenko, V. S. 2007, A&A, 461, 183

Gregory, S. G., Donati, J.-F., Morin, J., et al. 2012, ApJ, 755, 97

Gullbring, E., Hartmann, L., Briceño, C., & Calvet, N. 1998, ApJ, 492, 323

Gutermuth, R. A., Megeath, S. T., Myers, P. C., et al. 2009, ApJS, 184, 18

Haro, G. & Herbig, G. H. 1955, Boletin de los Observatorios Tonantzintla y Tacubaya, 2, 33

Hartmann, L. 1998, Accretion Processes in Star Formation, Cambridge Astrophysics Series, 32

Hartmann, L. 2009, Accretion Processes in Star Formation: Second Edition (Cambridge University Press)

Hartmann, L., Calvet, N., Gullbring, E., & D'Alessio, P. 1998, ApJ, 495, 385

Hartmann, L., D'Alessio, P., Calvet, N., & Muzerolle, J. 2006, ApJ, 648, 484

Hartmann, L. & Stauffer, J. R. 1989, AJ, 97, 873

Helsel, D. R. 2012, Statistics for Censored Environmental Data, Wiley

Henderson, C. B. & Stassun, K. G. 2012, ApJ, 747, 51

Henyey, L. G., Lelevier, R., & Levée, R. D. 1955, PASP, 67, 154

Herbig, G. H. 1953, Leaflet of the Astronomical Society of the Pacific, 6, 338

Herbig, G. H. 1954, ApJ, 119, 483

Herbig, G. H. 1957, in IAU Symposium, Vol. 3, Non-stable stars, ed. G. H. Herbig, 3

Herbig, G. H. 1962, Advances in Astronomy and Astrophysics, 1, 47

Herbig, G. H. 1977a, ApJ, 217, 693

Herbig, G. H. 1977b, ApJ, 214, 747

Herbig, G. H. & Bell, K. R. 1988, Lick Observatory Bulletin No. 1111

Herbig, G. H. & Kameswara Rao, N. 1972, ApJ, 174, 401

Herbst, W., Bailer-Jones, C. A. L., Mundt, R., Meisenheimer, K., & Wackermann, R. 2002, A&A, 396, 513

Herbst, W., Eislöffel, J., Mundt, R., & Scholz, A. 2007, Protostars and Planets V, 297

Herbst, W., Herbst, D. K., Grossman, E. J., & Weinstein, D. 1994, AJ, 108, 1906

Herczeg, G. J. & Hillenbrand, L. A. 2008, ApJ, 681, 594

Herschel, W. 1786, Royal Society of London Philosophical Transactions Series I, 76, 457

Herschel, W. 1789, Royal Society of London Philosophical Transactions Series I, 79, 212

Horne, J. H. & Baliunas, S. L. 1986, ApJ, 302, 757

Ivezić, Ž., Sesar, B., Jurić, M., et al. 2008, ApJ, 684, 287

Johns-Krull, C. M. 2007, ApJ, 664, 975

Johnson, H. L. 1965, ApJ, 141, 170

Johnson, H. L. 1966, ARA&A, 4, 193

Joy, A. H. 1942, PASP, 54, 15

Joy, A. H. 1945, ApJ, 102, 168

Kant, I. 1755, Allgemeine Naturgeschichte und Theorie des Himmels

Keene, J. & Masson, C. R. 1990, ApJ, 355, 635

Kenyon, S. J. & Hartmann, L. 1987, ApJ, 323, 714

Kenyon, S. J. & Hartmann, L. 1995, ApJS, 101, 117

Kenyon, S. J. & Hartmann, L. W. 1990, ApJ, 349, 197

Königl, A. 1991, ApJ, 370, L39

Kraus, A. L. & Hillenbrand, L. A. 2007, AJ, 134, 2340

Ku, W. H.-M. & Chanan, G. A. 1979, ApJ, 234, L59

Kulkarni, A. K. & Romanova, M. M. 2008, MNRAS, 386, 673

Kurosawa, R. & Romanova, M. M. 2013, MNRAS, 431, 2673

Kurosawa, R., Romanova, M. M., & Harries, T. J. 2008, MNRAS, 385, 1931

Lada, C. J. 2005, Progress of Theoretical Physics Supplement, 158, 1

Lada, C. J. & Lada, E. A. 2003, ARA&A, 41, 57

Lada, C. J., Muench, A. A., Luhman, K. L., et al. 2006, AJ, 131, 1574

Lada, C. J., Young, E. T., & Greene, T. P. 1993, ApJ, 408, 471

Lamm, M. H., Bailer-Jones, C. A. L., Mundt, R., Herbst, W., & Scholz, A. 2004, A&A, 417, 557

Lamm, M. H., Mundt, R., Bailer-Jones, C. A. L., & Herbst, W. 2005, A&A, 430, 1005

Laplace, P.-S. 1798, Exposition du système du monde

Larson, R. B. 1969, MNRAS, 145, 271

Lenz, D. D., Newberg, J., Rosner, R., Richards, G. T., & Stoughton, C. 1998, ApJS, 119, 121

Littlefair, S. P., Naylor, T., Harries, T. J., Retter, A., & O'Toole, S. 2004, MNRAS, 347, 937

Littlefair, S. P., Naylor, T., Mayne, N. J., Saunders, E. S., & Jeffries, R. D. 2010, MNRAS, 403, 545

Luhman, K. L. 1999, ApJ, 525, 466

Luhman, K. L., Stauffer, J. R., Muench, A. A., et al. 2003, ApJ, 593, 1093

Lynden-Bell, D. & Pringle, J. E. 1974, MNRAS, 168, 603

Magnier, E. A. & Cuillandre, J.-C. 2004, PASP, 116, 449

Makidon, R. B., Rebull, L. M., Strom, S. E., Adams, M. T., & Patten, B. M. 2004, AJ, 127, 2228

Manara, C. F., Robberto, M., Da Rio, N., et al. 2012, ApJ, 755, 154

Manara, C. F., Testi, L., Natta, A., & Alcalá, J. M. 2015, A&A, 579, A66

Margulis, M., Lada, C. J., & Snell, R. L. 1988, ApJ, 333, 316

Mathieu, R. D. 1986, Highlights of Astronomy, 7, 481

Matt, S. & Pudritz, R. E. 2005a, ApJ, 632, L135

Matt, S. & Pudritz, R. E. 2005b, MNRAS, 356, 167

Mayne, N. J. & Naylor, T. 2008, MNRAS, 386, 261

McGinnis, P. T., Alencar, S. H. P., Guimarães, M. M., et al. 2015, A&A, 577, A11

McQuillan, A., Aigrain, S., & Mazeh, T. 2013, MNRAS, 432, 1203

Ménard, F. & Bertout, C. 1999, in NATO Advanced Science Institutes (ASI) Series C, Vol. 540, NATO Advanced Science Institutes (ASI) Series C, ed. C. J. Lada & N. D. Kylafis, 341

Mendoza V., E. E. 1966, ApJ, 143, 1010

Mendoza V., E. E. 1968, ApJ, 151, 977

Mendoza V., E. E. & Gomez, T. 1980, MNRAS, 190, 623

Meyer, M. R., Calvet, N., & Hillenbrand, L. A. 1997, AJ, 114, 288

Mohanty, S., Jayawardhana, R., & Basri, G. 2005, ApJ, 626, 498

Morgan, W. W., Hiltner, W. A., Neff, J. S., Garrison, R., & Osterbrock, D. E. 1965, ApJ, 142, 974

Muzerolle, J., Calvet, N., Hartmann, L., & D'Alessio, P. 2003a, ApJ, 597, L149

Muzerolle, J., Hillenbrand, L., Calvet, N., Briceño, C., & Hartmann, L. 2003b, ApJ, 592, 266

Muzerolle, J., Luhman, K. L., Briceño, C., Hartmann, L., & Calvet, N. 2005, ApJ, 625, 906

Natta, A., Testi, L., & Randich, S. 2006, A&A, 452, 245

Naylor, T. 2009, MNRAS, 399, 432

Nguyen, D. C., Scholz, A., van Kerkwijk, M. H., Jayawardhana, R., & Brandeker, A. 2009, ApJ, 694, L153

Padoan, P., Kritsuk, A., Norman, M. L., & Nordlund, Å. 2005, ApJ, 622, L61

Park, B.-G., Sung, H., Bessell, M. S., & Kang, Y. H. 2000, AJ, 120, 894

Pecaut, M. J. & Mamajek, E. E. 2013, ApJS, 208, 9

Piche, F. 1993, PASP, 105, 324

Pickles, A. J. 1998, PASP, 110, 863

Press, W. H., Teukolsky, S. A., Vetterling, W. T., & Flannery, B. P. 1992, Numerical recipes in C. The art of scientific computing

Prim, R. C. 1957, Bell Syst. Tech. J., 36, 1389

Pringle, J. E. 1981, ARA&A, 19, 137

Ramírez, S. V., Rebull, L., Stauffer, J., et al. 2004, AJ, 127, 2659

Rebull, L. M. 2001, AJ, 121, 1676

Rebull, L. M., Cody, A. M., Covey, K. R., et al. 2014, AJ, 148, 92

Rebull, L. M., Makidon, R. B., Strom, S. E., et al. 2002, AJ, 123, 1528

Rebull, L. M., Stauffer, J. R., Ramirez, S. V., et al. 2006, AJ, 131, 2934

Rebull, L. M., Wolff, S. C., & Strom, S. E. 2004, AJ, 127, 1029

Regnault, N., Conley, A., Guy, J., et al. 2009, A&A, 506, 999

Reipurth, B., Yu, K. C., Moriarty-Schieven, G., et al. 2004, AJ, 127, 1069

Rigliaco, E., Natta, A., Randich, S., Testi, L., & Biazzo, K. 2011, A&A, 525, A47

Rigliaco, E., Natta, A., Testi, L., et al. 2012, A&A, 548, A56

Romanova, M. M., Ustyugova, G. V., Koldoba, A. V., & Lovelace, R. V. E. 2002, ApJ, 578, 420

Romanova, M. M., Ustyugova, G. V., Koldoba, A. V., & Lovelace, R. V. E. 2004, ApJ, 610, 920

Romanova, M. M., Ustyugova, G. V., Koldoba, A. V., & Lovelace, R. V. E. 2012, MNRAS, 421, 63

Rucinski, S. M. 1985, AJ, 90, 2321

Rydgren, A. E. & Vrba, F. J. 1981, AJ, 86, 1069

Samadi, R., Fialho, F., Costa, J. E. S., et al. 2007, ArXiv Astrophysics e-prints

Scargle, J. D. 1982, ApJ, 263, 835

Schmidt-Kaler, T. 1982, in Landolt-Börnstein, ed. K. Schaifers, & H. Voigt, Vol. 2 (Berlin: Springer), 449

Shakura, N. I. & Sunyaev, R. A. 1973, A&A, 24, 337

Shu, F., Najita, J., Ostriker, E., et al. 1994, ApJ, 429, 781

Shu, F. H. & Adams, F. C. 1987, in IAU Symposium, Vol. 122, Circumstellar Matter, ed. I. Appenzeller & C. Jordan, 7–22

Sicilia-Aguilar, A., Henning, T., & Hartmann, L. W. 2010, ApJ, 710, 597

Siess, L., Dufour, E., & Forestini, M. 2000, A&A, 358, 593

Skrutskie, M. F., Cutri, R. M., Stiening, R., et al. 2006, AJ, 131, 1163

Smith, M. A., Bianchi, L., & Shiao, B. 2014, AJ, 147, 159

Sousa, A., Alencar, S., Bouvier, J., et al. 2015, ArXiv e-prints

Stahler, S. W. & Palla, F. 2005, The Formation of Stars (Wiley-VCH)

Stassun, K. G., Mathieu, R. D., Mazeh, T., & Vrba, F. J. 1999, AJ, 117, 2941

Stauffer, J., Cody, A. M., Baglin, A., et al. 2014, AJ, 147, 83

Stauffer, J., Cody, A. M., McGinnis, P., et al. 2015, AJ, 149, 130

Stetson, P. B. 1996, PASP, 108, 851

Stone, J. M. & Balbus, S. A. 1996, ApJ, 464, 364

Strom, S. E. 1972, PASP, 84, 745

Sung, H., Bessell, M. S., & Chun, M.-Y. 2004, AJ, 128, 1684

Sung, H., Bessell, M. S., Chun, M.-Y., Karimov, R., & Ibrahimov, M. 2008, AJ, 135, 441

Sung, H., Bessell, M. S., & Lee, S.-W. 1997, AJ, 114, 2644

Sung, H., Stauffer, J. R., & Bessell, M. S. 2009, AJ, 138, 1116

Taylor, J. 1997, Introduction to Error Analysis, the Study of Uncertainties in Physical Measurements, 2nd Edition (University Science Books)

Taylor, M. B. 2005, in Astronomical Society of the Pacific Conference Series, Vol. 347, Astronomical Data Analysis Software and Systems XIV, ed. P. Shopbell, M. Britton, & R. Ebert, 29

Teixeira, P. S., Lada, C. J., Marengo, M., & Lada, E. A. 2012, A&A, 540, A83

Teixeira, P. S., Lada, C. J., Young, E. T., et al. 2006, ApJ, 636, L45

Terebey, S., Chandler, C. J., & Andre, P. 1993, ApJ, 414, 759

Tody, D. 1993, in Astronomical Society of the Pacific Conference Series, Vol. 52, Astronomical Data Analysis Software and Systems II, ed. R. J. Hanisch, R. J. V. Brissenden, & J. Barnes, 173

Torres, C. A. O. & Ferraz Mello, S. 1973, A&A, 27, 231

Vasconcelos, M. J. & Bouvier, J. 2015, A&A, 578, A89

Venuti, L., Bouvier, J., Flaccomio, E., et al. 2014, A&A, 570, A82

Venuti, L., Bouvier, J., Irwin, J., et al. 2015, A&A, 581, A66

Vogt, S. S. 1981, ApJ, 250, 327

Vrba, F. J., Chugainov, P. F., Weaver, W. B., & Stauffer, J. S. 1993, AJ, 106, 1608

Walker, M. F. 1956, ApJS, 2, 365

Walker, M. F. 1972, ApJ, 175, 89

Walkowicz, L. M., Basri, G., & Valenti, J. A. 2013, ApJS, 205, 17

Walter, F. M. 1986, ApJ, 306, 573

Walter, F. M., Brown, A., Mathieu, R. D., Myers, P. C., & Vrba, F. J. 1988, AJ, 96, 297

Walter, F. M. & Kuhi, L. V. 1981, ApJ, 250, 254

Walter, F. M. & Kuhi, L. V. 1984, ApJ, 284, 194

Werner, M. W., Roellig, T. L., Low, F. J., et al. 2004, ApJS, 154, 1

White, R. J. & Basri, G. 2003, ApJ, 582, 1109

Wolf, C. 1884a, Bulletin Astronomique, Serie I, 1, 431

Wolf, C. 1884b, Bulletin Astronomique, Serie I, 1, 313

Wolf, M. 1924, Astronomische Nachrichten, 221, 379

Wolf-Chase, G., Moriarty-Schieven, G., Fich, M., & Barsony, M. 2003, MNRAS, 344, 809

Worden, S. P., Schneeberger, T. J., Kuhn, J. R., & Africano, J. L. 1981, ApJ, 244, 520

Young, E. T., Teixeira, P. S., Lada, C. J., et al. 2006, ApJ, 642, 972

Zanni, C. & Ferreira, J. 2013, A&A, 550, A99

Appendices

Appendix A

List of referred publications

Sousa, A., Alencar, S., Bouvier, J., Stauffer, J., **Venuti, L.**, Hillenbrand, L., Cody, A. M., Teixeira, P., Guimarães, M., McGinnis, P., Rebull, L., Flaccomio, E., Fürész, G., Micela, G., & Gameiro, J., *CSI 2264: Accretion process in classical T Tauri stars in the young cluster NGC 2264*, Astronomy & Astrophysics (2015, in press)

Venuti, L., Bouvier, J., Irwin, J., Stauffer, J. R., Hillenbrand, L. A., Rebull, L. M., Cody, A. M., Alencar, S. H. P., Micela, G., Flaccomio, E., & Peres, G., *UV variability and accretion dynamics in the young open cluster NGC 2264*, Astronomy & Astrophysics, Volume 581, id.A66 (2015)

McGinnis, P. T., Alencar, S. H. P., Guimarães, M. M., Sousa, A. P., Stauffer, J., Bouvier, J., Rebull, L., Fonseca, N. N. J., **Venuti, L.**, Hillenbrand, L., Cody, A. M., Teixeira, P. S., Aigrain, S., Favata, F., Fürész, G., Vrba, F. J., Flaccomio, E., Turner, N. J., Gameiro, J. F., Dougados, C., Herbst, W., Morales-Calderón, M., & Micela, G., *CSI 2264: Probing the inner disks of AA Tauri-like systems in NGC 2264*, Astronomy & Astrophysics, Volume 577, id.A11 (2015)

Stauffer, J., Cody, A. M., McGinnis, P., Rebull, L., Hillenbrand, L. A., Turner, N. J., Carpenter, J., Plavchan, P., Carey, S., Terebey, S., Morales-Calderón, M., Alencar, S. H. P., Bouvier, J., **Venuti, L.**, Hartmann, L., Calvet, N., Micela, G., Flaccomio, E., Song, I., Gutermuth, R., Barrado, D., Vrba, F. J., Covey, K., Padgett, D., Herbst, W., Gillen, E., Lyra, W., Guimarães, M. M., Bouy, H., & Favata, F., *CSI 2264: Characterizing Young Stars in NGC 2264 With Short-Duration Periodic Flux Dips in Their Light Curves*, Astronomical Journal, Volume 149, Issue 4, article id. 130 (2015)

Venuti, L., Bouvier, J., Flaccomio, E., Alencar, S. H. P., Irwin, J., Stauffer, J. R., Cody, A. M., Teixeira, P. S., Sousa, A. P., Micela, G., Cuillandre, J.-C., & Peres, G., *Mapping accretion and its variability in the young open cluster NGC 2264: a study based on u-band photometry*, Astronomy & Astrophysics, Volume 570, id.A82 (2014)

Stauffer, J., Cody, A. M., Baglin, A., Alencar, S., Rebull, L., Hillenbrand, L. A., **Venuti, L.**, Turner, N. J., Carpenter, J., Plavchan, P., Findeisen, K., Carey, S., Terebey, S., Morales-Calderón, M., Bouvier, J., Micela, G., Flaccomio, E., Song, I., Gutermuth, R., Hartmann, L., Calvet, N., Whitney, B., Barrado, D., Vrba, F. J., Covey, K., Herbst, W., Furesz, G., Aigrain, S., & Favata, F., *CSI 2264: Characterizing Accretion-burst Dominated Light Curves for Young Stars in NGC 2264*, Astronomical Journal, Volume 147, Issue 4, article id. 83 (2014)

Appendix B

Mapping accretion and its variability in the young open cluster NGC 2264: a study based on u-band photometry

L. Venuti[1,2,3], J. Bouvier[1,2], E. Flaccomio[4], S. H. P. Alencar[5], J. Irwin[6], J. R. Stauffer[7], A. M. Cody[7], P. S. Teixeira[8], A. P. Sousa[5], G. Micela[4], J.-C. Cuillandre[9], and G. Peres[3]

[1] Univ. Grenoble Alpes, IPAG, F-38000 Grenoble, France
[2] CNRS, IPAG, F-38000 Grenoble, France
[3] Dipartimento di Fisica e Chimica, Università degli Studi di Palermo, Piazza del Parlamento 1, 90134 Palermo, Italy
[4] Istituto Nazionale di Astrofisica, Osservatorio Astronomico di Palermo G.S. Vaiana, Piazza del Parlamento 1, 90134 Palermo, Italy
[5] Departamento de Física - ICEx - UFMG, Av. Antônio Carlos, 6627, 30270-901 Belo Horizonte, MG, Brazil
[6] Harvard-Smithsonian Center for Astrophysics, 60 Garden Street, Cambridge, MA 02138, USA
[7] Spitzer Science Center, California Institute of Technology, 1200 E California Blvd., Pasadena, CA 91125, USA
[8] Universität Wien, Institut für Astrophysik, Türkenschanzstrasse 17, 1180, Vienna, Austria
[9] Canada - France - Hawaii Telescope Corporation, 65-1238 Mamalahoa Highway, Kamuela, HI, 96743, USA

Published in *Astronomy & Astrophysics*, Volume 570, A82 (2014)

A&A 570, A82 (2014)
DOI: 10.1051/0004-6361/201423776

Astronomy & Astrophysics

Mapping accretion and its variability in the young open cluster NGC 2264: a study based on *u*-band photometry⋆,⋆⋆

L. Venuti[1,2,3], J. Bouvier[1,2], E. Flaccomio[4], S. H. P. Alencar[5], J. Irwin[6], J. R. Stauffer[7], A. M. Cody[7], P. S. Teixeira[8], A. P. Sousa[5], G. Micela[4], J.-C. Cuillandre[9], and G. Peres[3]

[1] Univ. Grenoble Alpes, IPAG, 38000 Grenoble, France
e-mail: Laura.Venuti@obs.ujf-grenoble.fr
[2] CNRS, IPAG, 38000 Grenoble, France
[3] Dipartimento di Fisica e Chimica, Università degli Studi di Palermo, Piazza del Parlamento 1, 90134 Palermo, Italy
[4] Istituto Nazionale di Astrofisica, Osservatorio Astronomico di Palermo G.S. Vaiana, Piazza del Parlamento 1, 90134 Palermo, Italy
[5] Departamento de Física – ICEx – UFMG, Av. Antônio Carlos, 6627, 30270-901 Belo Horizonte, MG, Brazil
[6] Harvard-Smithsonian Center for Astrophysics, 60 Garden Street, Cambridge, MA 02138, USA
[7] Spitzer Science Center, California Institute of Technology, 1200 E California Blvd., Pasadena, CA 91125, USA
[8] Universität Wien, Institut für Astrophysik, Türkenschanzstrasse 17, 1180 Vienna, Austria
[9] Canada–France–Hawaii Telescope Corporation, 65-1238 Mamalahoa Highway, Kamuela, HI 96743, USA

Received 7 March 2014 / Accepted 29 July 2014

ABSTRACT

Context. The accretion process has a central role in the formation of stars and planets.
Aims. We aim at characterizing the accretion properties of several hundred members of the star-forming cluster NGC 2264 (3 Myr).
Methods. We performed a deep *ugri* mapping as well as a simultaneous *u*-band+*r*-band monitoring of the star-forming region with CFHT/MegaCam in order to directly probe the accretion process onto the star from UV excess measurements. Photometric properties and stellar parameters are determined homogeneously for about 750 monitored young objects, spanning the mass range ∼0.1–2 $M_{\odot}$. About 40% of the sample are classical (accreting) T Tauri stars, based on various diagnostics (H_{α}, UV and IR excesses). The remaining non-accreting members define the (photospheric + chromospheric) reference UV emission level over which flux excess is detected and measured.
Results. We revise the membership status of cluster members based on UV accretion signatures, and report a new population of 50 classical T Tauri star (CTTS) candidates. A large range of UV excess is measured for the CTTS population, varying from a few times 0.1 to ∼3 mag. We convert these values to accretion luminosities and accretion rates, via a phenomenological description of the accretion shock emission. We thus obtain mass accretion rates ranging from a few 10^{-10} to $\sim 10^{-7}$ $M_{\odot}$/yr. Taking into account a mass-dependent detection threshold for weakly accreting objects, we find a >6σ correlation between mass accretion rate and stellar mass. A power-law fit, properly accounting for censored data (upper limits), yields $\dot{M}_{\rm acc} \propto M_{*}^{1.4\pm0.3}$. At any given stellar mass, we find a large spread of accretion rates, extending over about 2 orders of magnitude. The monitoring of the UV excess on a timescale of a couple of weeks indicates that its variability typically amounts to 0.5 dex, i.e., much smaller than the observed spread in accretion rates. We suggest that a non-negligible age spread across the star-forming region may effectively contribute to the observed spread in accretion rates at a given mass. In addition, different accretion mechanisms (like, e.g., short-lived accretion bursts vs. more stable funnel-flow accretion) may be associated to different $\dot{M}_{\rm acc}$ regimes.
Conclusions. A huge variety of accretion properties is observed for young stellar objects in the NGC 2264 cluster. While a definite correlation seems to hold between mass accretion rate and stellar mass over the mass range probed here, the origin of the large intrinsic spread observed in mass accretion rates at any given mass remains to be explored.

Key words. accretion, accretion disks – stars: formation – stars: low-mass – stars: pre-main sequence – ultraviolet: stars – open clusters and associations: individual: NGC 2264

1. Introduction

The disk accretion phase assumes a pivotal role in the scenarios of early stellar evolution and planetary formation. Circumstellar disks are the ubiquitous result of the earliest stages of star formation, surrounding the vast majority of solar-type protostars at an age of ∼1 Myr. Mass accretion from the inner disk to the central star regulates the star-disk interaction over the few subsequent million years; this process has a direct, long-lasting impact on the basic properties of the system, by providing at the same time mass and angular momentum. Angular momentum transport and mass infall have a most important part in dictating the dynamical evolution of protoplanetary disks, hence setting the environmental conditions which eventually lead to the formation of planetary systems (Armitage 2011).

The widely accepted paradigm for mass accretion in young stellar objects (YSOs) is that of magnetospheric accretion (Camenzind 1990; Königl 1991). A cavity of a few stellar radii extends from the stellar surface to the inner disk rim, as an effect of the inner disk truncation by the stellar magnetosphere ($B \sim 2$ kG). Accretion columns, channeled along the magnetic

⋆ Based on observations obtained with MegaPrime/MegaCam, a joint project of CFHT and CEA/DAPNIA, at the Canada-France-Hawaii Telescope (CFHT) which is operated by the National Research Council (NRC) of Canada, the Institut National des Sciences de l'Univers of the Centre National de la Recherche Scientifique (CNRS) of France, and the University of Hawaii.
⋆⋆ Full Tables 2–4 are only available at the CDS via anonymous ftp to cdsarc.u-strasbg.fr (130.79.128.5) or via http://cdsarc.u-strasbg.fr/viz-bin/qcat?J/A+A/570/A82

field lines, regulate the transport of material from the disk inner edge to the central star; as the accreting material impacts onto the stellar surface at near free-fall velocity, accretion shocks are produced near the magnetic poles. This picture is strongly supported by its predictive capability of the main observational features of accreting young solar-type stars (classical T Tauri stars, or CTTS): UV, optical and IR excess compared to the photospheric flux; spectral "veiling"; broad emission lines; inverse P Cygni profiles; pronounced spectroscopic and photometric variability (e.g. Bouvier et al. 2007b).

Several studies (e.g. Muzerolle et al. 2003; Rigliaco et al. 2011) have shown that the rates ($\dot{M}_{\rm acc}$) at which mass accretion occurs tend to scale with the mass of the central object (M_*). Notwithstanding this general trend, a large spread in the $\dot{M}_{\rm acc}$ values at a given M_* appears to be a constant feature (e.g. Hartmann et al. 2006); this is indicative of a complex and dynamic picture, shaped by a variety of parameters and concurrent processes. Similarly, observations suggest a progressive decrease of $\dot{M}_{\rm acc}$ over the age of the systems (Hartmann et al. 1998; Sicilia-Aguilar et al. 2010), following the time evolution and dispersal of circumstellar disks (Haisch et al. 2001; Hillenbrand 2005). The large spread associated with the effective relationship attests that a multiplicity of elements concur to the disk dissipation; moreover, the initial conditions in which stars are formed (e.g. Dullemond et al. 2006) and local environmental properties (e.g. Guarcello et al. 2007) are likely to significantly affect the evolutionary pattern of individual star-disk systems.

Statistical surveys of the accretion properties of young stars provide essential insight into the dynamics of accretion. Large, homogeneously characterized samples of objects, spanning several ranges of parameters, are crucial to achieve a proper understanding of the physics governing the disk accretion history of forming stars and to explore different facets of the accretion mechanisms. To this respect, extensive mapping surveys of well-populated star-forming regions at UV wavelengths (e.g. Rigliaco et al. 2011; Manara et al. 2012) provide a most interesting standpoint, as they allow to directly probe accretion for large samples of stars from the excess emission produced in the shocked impact layer at the base of the accretion column.

Such single epoch surveys efficiently trace the instantaneous spread of accretion properties in a given star-forming region; however, they are unable to probe the nature of such a spread, i.e. to determine whether this is due to variability of individual objects or to an intrinsic spread amongst objects. And yet, a key aspect of the accretion dynamics is the intrinsic variability profile of the process (i.e., the amplitude and characteristic timescales of the variability in $\dot{M}_{\rm acc}$). The enhanced variability typical of young stars, cornerstone of the very definition of the T Tauri class (Joy 1945), is manifest over a broad range of wavelengths (X-rays, UV, optical, IR) and of time baselines (hours, days, years); a variety of processes concur to shape the variability pattern of individual objects, with a significant contribution coming from the geometry of the system. Understanding to which extent and on which timescales the accretion process is intrinsically variable, and characterizing its variability on a statistical basis compared to individual cases, is of utmost importance in order to accurately interpret the information provided by large accretion surveys and thus infer a detailed picture of the accretion process.

Multi-epoch surveys hence provide a more accurate description of the accretion process, as they allow to probe the time evolution of single snapshots of the accretion properties and, thus, to investigate how accretion occurs. This has been addressed in a few recent studies (e.g. Nguyen et al. 2009; Fang et al. 2013), which explored the variability of spectral accretion diagnostics for tens of objects with a few observing epochs over several months. Such efforts provided very valuable constraints on the average accretion variability shown by typical classical T Tauri stars (CTTS). However, a much tighter time sampling is needed in order to recover an estimate of the effective intrinsic accretion variability, isolated from geometric contributions which are simply due to a varying visible portion of the accretion spots during stellar rotation.

We have recently conducted an extensive observational program specifically aimed at addressing the issue of YSOs variability over the full spectrum. The coordinated synoptic investigation of NGC 2264 (CSI 2264; Cody et al. 2013) project was devised as a coordinated multi-wavelength exploration of the hours-to-weeks variability of the pre-main sequence (PMS) population of the star-forming region NGC 2264. The space telescopes CoRoT and *Spitzer* provided the backbone of the optical and IR investigations, with simultaneous continuous monitoring over 40 and 30 days respectively; the Flames multi-object spectrograph at the Very Large Telescope (VLT) provided a full set of spectra covering 20 different epochs for ~100 young stars, while multi-band optical+UV photometric monitoring obtained at the Canada-France-Hawaii Telescope (CFHT) provided contemporaneous, synoptic measures of the accretion rates and their variability from the direct diagnostics of the UV excess, with an overall time coverage of 14 consecutive days and several measurements per night. The targeted region, NGC 2264, has long been a benchmark for star formation studies, thanks to its youth (~3 Myr), its richness (~1500 known members, both CTTS and non-accreting, weak-lined T Tauri stars, or WTTS), its relative proximity ($d \sim 800$ pc), the low extinction on the line of sight and the association with a molecular cloud complex that significantly reduces the contamination from background stars (see Dahm 2008 for a recent review on the region).

As part of the CSI 2264 campaign, this paper specifically focuses on the issue of accretion properties and accretion variability in the PMS population of NGC 2264. Section 2 describes the photometric dataset obtained at CFHT, on which the study reported here is based. Section 3 reports on the characterization of photometric accretion signatures, which allowed us to perform a new, accretion-driven census of NGC 2264 members; an extensive, homogeneous investigation of individual stellar properties is also reported. In Sect. 4, we describe the procedure adopted to convert the UV excess measurement to a $\dot{M}_{\rm acc}$ estimate; we analyze the $\dot{M}_{\rm acc}$ over M_* distribution thus inferred and compare this picture with the amount of variability registered over a baseline of two weeks; we further probe the origin of this variability and infer a specific estimate of the intrinsic accretion variability as opposed to rotational modulation detected during the monitoring. Results are discussed in Sect. 5; our conclusions are synthetized in Sect. 6. This provides a complete picture of a whole star-forming region and its several hundred members at short wavelengths, from a specifically accretion-oriented perspective. A more detailed characterization of the variability properties monitored at CFHT and their relation to the underlying physics will be addressed in a forthcoming paper (Venuti et al., in prep.).

2. Observations and data reduction

2.1. CFHT MegaCam surveys of NGC 2264: data reduction and photometric calibration

We surveyed NGC 2264 in two multiwavelength observing campaigns at the CFHT, using the wide-field optical camera

MegaCam; the camera has a field of view (FOV) of ∼1 deg^2 (Boulade et al. 2003), thus fitting the whole region in a single telescope pointing. Five broad-band filters (u^*, g', r', i', z') are adopted at the camera; their design, close to the Sloan Digital Sky Survey (SDSS) photometric system (Fukugita et al. 1996), ensures high efficiency for faint object detection and deep sky mapping.

2.1.1. Mapping survey

The first MegaCam survey of NGC 2264, held on Dec. 12, 2010, consisted of a deep $u^*g'r'$ mapping of the region. In the r'-band, five short exposures (10 s) were obtained, using a dithering pattern in order to compensate for the presence of bad pixels and small gaps on the CCD mosaic. In the u^*-band and g'-band, the same 5-step dithering procedure was repeated in two different exposure modes, short (10 s) and long (60 s), in order to obtain a good signal/noise (S/N) for the whole sample of objects without saturating the brightest sources. All images were obtained over a continuous temporal sequence within the night. On Feb. 28, 2012, concurrently with the monitoring survey reported in Sect. 2.1.2, we additionally obtained a deep i'-band mapping, in order to reconstruct a full 4-band picture of NGC 2264 together with the $u^*g'r'$ survey of Dec. 2010. Similarly to previous observations, a dithering pattern was used, along with two different exposure times: 180 s, to detect all sources in the FOV, and 5 s, to recover the bright sources saturated in the long exposure.

Raw data have been preliminarily processed at the CFHT, in order to correct for instrumental signatures across the whole CCD mosaic (i.e., bad pixel clusters or columns, dark current, bias, non-uniformity in the response), and a first astrometric and photometric calibration has been performed. The subsequent photometric processing of the images obtained during the survey has been handled as described below.

For each spectral band and each exposure time, single dithered images have been combined, in order to discard spurious signal detections (e.g., cosmic rays) and correct for small CCD gaps. The photometric images thus assembled (one in the r'-band and two for each other filter, corresponding to the two different exposure times) have then been processed using the SExtractor (Bertin & Arnouts 1996) and PSFEx (Bertin 2011) tools, in order to identify true sources in the FOV and extract the relevant photometry. At first, we run a preliminary aperture photometry procedure with a detection threshold of $10\,\sigma$ above the local background, in order to extract only brighter sources; this selection of objects has been used as input to run a pre-PSF fitting routine, aimed at testing the optimal parameters for the PSF function to be used for analyzing the images. A final, complete single-band catalog has eventually been produced from each image processed with SExtractor by performing a new PSF-fitting run with a lower detection threshold of 3σ, thus recovering the fainter component of the population.

A first filtering of each catalog population, based on the properties of the extracted sources and on the relevant extraction flags, allowed us to discard the stellar component potentially affected by saturation or other detection problems. Long and short exposure catalogs corresponding to the same spectral band, when present, have then been merged, in order to obtain a unique photometric catalog for each spectral band and avoid duplicates. The sample of objects common to both the long-exposure and short-exposure catalogs has been used to evaluate the photometric accuracy, to correct the short-exposure photometry for small magnitude offsets with photometry obtained from the long exposures and to define a confidence magnitude threshold below which photometry could begin to be affected by saturation. Objects have been preferentially taken from the long-exposure catalog; sources brighter than the long-exposure threshold have been retrieved from the short-exposure catalog, when available; sources brighter than the short-exposure threshold have been discarded.

A complete calibration of the CFHT instrumental magnitudes to the SDSS photometric system, including a correction for both offset and color effect, has then been performed. The calibration procedure has not been anchored to a sample of standard stars in the FOV; instead, we used an ensemble of around 3000 stars, present in the CFHT FOV, for which SDSS photometry was available from the seventh SDSS Data Release (Abazajian et al. 2009), to statistically calibrate the CFHT magnitudes to the SDSS system. The matching of sources between the SDSS and the CFHT catalogs has been performed using the TOPCAT (Taylor 2005) tool, fixing a matching radius of 1 arcsec and retaining only closest matches. The statistical ensemble of stars used for the calibration has been selected among the objects with complete CFHT $u^*g'r'i'$ photometry and that matched the magnitude limits for 95% detection repeatability for point sources defined for the SDSS photometric survey (Abazajian et al. 2004). The calibration procedure adopted is based on the results of the photometric calibration study of the CFHT/MegaCam photometry to the SDSS system performed by Regnault et al. (2009). We compared the distribution of SDSS colors over the ensemble of stars with the SDSS dwarf color loci tabulated in literature (Covey et al. 2007; Lenz et al. 1998) and retained, for calibration purposes, only objects whose colors matched the tabulated ranges. After checking their consistency with the observed trends, Regnault's linear calibration relations have then been used to fit the $(m_\lambda^{\rm CFHT} - m_\lambda^{\rm SDSS})$ vs. $(m_\lambda^{\rm SDSS} - m_{\lambda+1}^{\rm SDSS})$ distributions in u^*, g' and r', by keeping the angular coefficient fixed and adapting the intercept value. In the i'-band, for which the filter in use at MegaPrime has been changed, due to accidental breakage, after the epoch of acquisition of data used in Regnault et al. (2009)'s study, no evident color dependence of the offset between the two photometric systems has been observed; the i'-band photometry has therefore been uniquely corrected for a constant offset. The system of 4 calibration equations thus obtained (one for each spectral band; Eqs. (1)–(4)) has then been solved to obtain the final conversion from CFHT instrumental magnitudes to SDSS photometry.

$$u_{\rm CFHT} - u_{\rm SDSS} = -0.211\ (u_{\rm SDSS} - g_{\rm SDSS}) - 0.63 \quad (1)$$

$$g_{\rm CFHT} - g_{\rm SDSS} = -0.155\ (g_{\rm SDSS} - r_{\rm SDSS}) - 0.51 \quad (2)$$

$$r_{\rm CFHT} - r_{\rm SDSS} = -0.03\ (r_{\rm SDSS} - i_{\rm SDSS}) \quad (3)$$

$$i_{\rm CFHT} - i_{\rm SDSS} = -0.02. \quad (4)$$

A complete $u^*g'r'i'$ catalog of NGC 2264, containing ∼9000 sources in the FOV, has been built by cross-correlating the single-band catalogs on TOPCAT. A matching radius of 1 arcsec has been fixed for identifying common sources detected in the u^*, g', r' concurrent observations, while a larger matching radius of 2 arcsecs has been introduced to match $u^*g'r'$ sources with their i'-band counterpart, to account for a lower astrometric accuracy (lower angular resolution) characterizing the i'-band field, due to poorer seeing conditions at the time of acquisition of the i'-band images. Sources have been identified by retaining only best matches; we address potential problems in the derived colors associated with misidentifications and multiple matches in Sect. 2.2. Final SDSS $u'g'r'i'$ (hereafter *ugri*) photometry has

then been associated to each source in the catalog using the derived calibration relations.

2.1.2. Monitoring survey

The second MegaCam survey of NGC 2264, performed in Feb. 2012, consisted in monitoring the u^*-band and r'-band variability of the entire stellar population of the region over a mid-term timescale (Feb.14-28, i.e., 2 weeks), as a part of the CSI 2264 project. On each observing night during the run, the region was imaged repeatedly, with a temporal cadence varying from 20 min to 1.5 h. Each u^*r' observing block was performed using a 5-step dithering pattern, with single exposures of 3 s in the r'-band and 60 s in the u^*-band.

The procedure adopted for the photometric processing of the images obtained during the u^*r' monitoring survey is similar to that applied to the mapping survey images, but each exposure has been individually processed in order to retrieve the luminosity variations over different timescales. The i-band image (Sect. 2.1.1) has been used as the astrometric reference exposure, as the nebulosity component was the least conspicuous in this image compared to the other filters; for each source, an aperture has been placed down on each u^* and r' image at the position predicted from the i-band source detection and the amount of flux within this aperture has been extracted to build the light curve.

A preliminary quality check on the CFHT light curves consisted in closely examining a sample of NGC 2264 members with known periodicities, in order to attempt to recover their periods from the phase-folded CFHT light curves. This allowed us to ascertain the global accuracy of the u^*r' time series photometry, albeit occasionally affected by isolated discrepant points and non-negligible scatter due to poorer observing conditions. In order to locate the potentially problematic observing sequences, we examined the time series photometry for the whole sample of field stars in the CFHT FOV and derived, for each observing sequence, the distribution of median zero-point offsets referred to the master frame. The zero-point offset, for a given object, is defined as the mag difference between the frame of interest and the master frame; in case of large deviation from zero, the zero-point offset distribution associated to an observing sequence thus signals that the observation has been carried out through clouds. This translates to significantly lower than average S/N for a given source, which implies that, even for the brightest stars, no accurate measurements can be inferred from that specific observation; hence, epochs matching this description have not been used for any subsequent analysis.

As done earlier for the *ugri* snapshot survey, the instrumental light curve photometry has been calibrated to the SDSS system, referring the procedure to the calibrated photometry from the first CFHT survey. No offsets and color effects have been noticed in the r'-band (hereafter r-band) photometry, while a correction for both contributions has been applied to the u^*-band photometry from the $(u^*_{\rm CFHT\_lc} - u)$ vs. $(u - r)$ plane:

$$u^*_{\rm CFHT\_lc} - u = -0.1343\ (u - r) - 0.1009. \quad (5)$$

2.2. The CFHT catalog of NGC 2264

Figure 1 shows a MegaCam color picture of the field imaged at CFHT during the NGC 2264 campaign. The star-forming region extends over the central part of the field, with the most active sites of star formation located at the center of the image, northward of the Cone Nebula (cf. Dahm 2008).

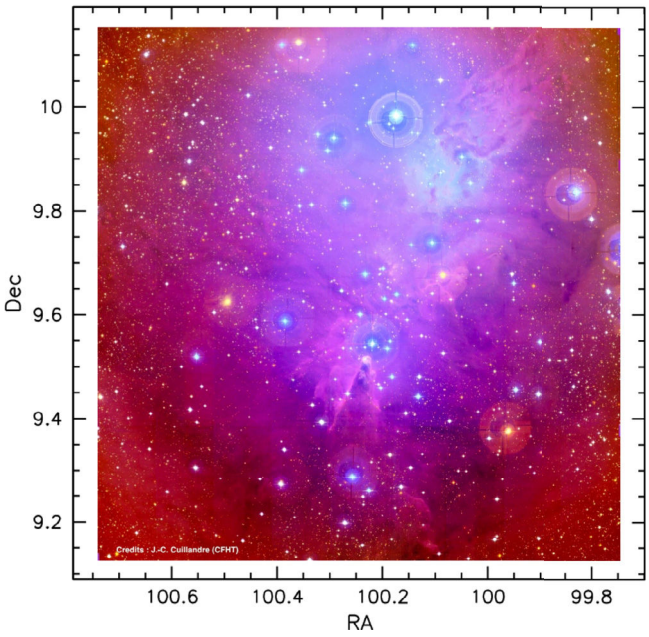

Fig. 1. CFHT/MegaCam *ugr* color image of NGC 2264.

Table 1. Detection limits and completeness in the CFHT *ugri* survey of NGC 2264.

(mag)	u	g	r	i
mag range*	15–23.5	14–21.5	13.5–20.5	13–19.5
Saturation start	<12.5	<13	<13.5	12.5
Detection limit	23.5	21.5	20.5	19.5
Completeness	21.5	19.5	18.5	17.5

Notes. Values reported are conservative estimates. (*) Values referred to the main body of the magnitude distribution of the catalog population.

We obtained a complete *ugri* dataset and photometric monitoring for ~9000 sources in the field, exploring the area projected onto the star-forming region as well as the periphery of the cluster and background/foreground sky. Table 1 provides some details on the photometric properties of the population of the CFHT catalog. The survey is complete down to $u \sim 21.5$ and $r \sim 18.5$ and the monitored objects span a range of ~7 mag. The photometry is globally accurate up to a few $\times 10^{-2}$ mag and the relative accuracy rises up to order of 10^{-3} mag for brighter objects.

In order to evaluate the probability of misidentifications as a result of the procedure adopted for matching sources in different catalogs, and thus evaluate the potential impact on the photometric properties inferred for individual sources, we reconsidered all multiple identifications within the allowed matching radii and closely examined their spatial distribution. The sources with potentially multiple identifications amount to ~2.9% of the population of the catalog. The difference in offset distance between the best match and the next best match is less than 0.5 arcsec for only 23% of these cases. Less than 20% of the multiply matched sources are located within the region occupied by most NGC 2264 members. For the statistical purposes of this study, this component is assumed to be negligible.

3. The PMS population of NGC 2264

A global picture of the photometric properties of the stellar population can be achieved from the analysis of color–color

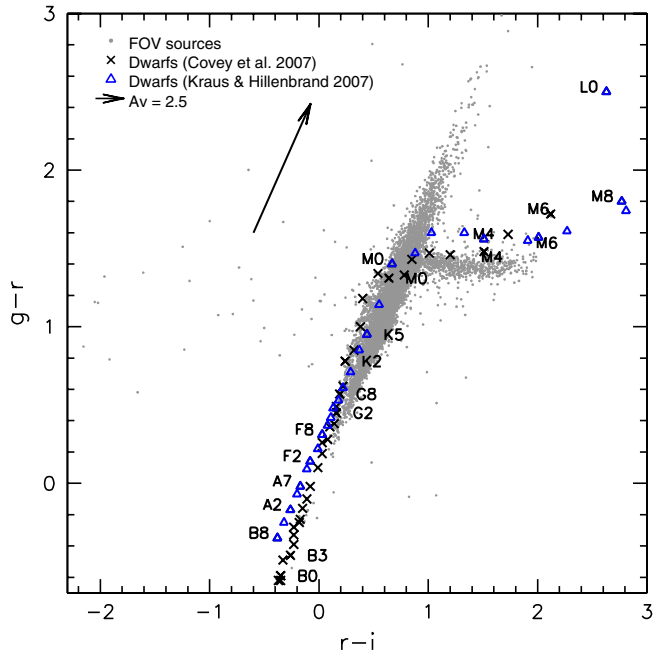

Fig. 2. $(r-i, g-r)$ color–color diagram for objects monitored at CFHT. Empirical dwarf color sequences from Covey et al. (2007) and Kraus & Hillenbrand (2007) are shown as black crosses and blue triangles, respectively. The reddening vector is traced based on the reddening parameters in the SDSS system provided by the Asiago Database on Photometric Systems (ADPS; Fiorucci & Munari 2003).

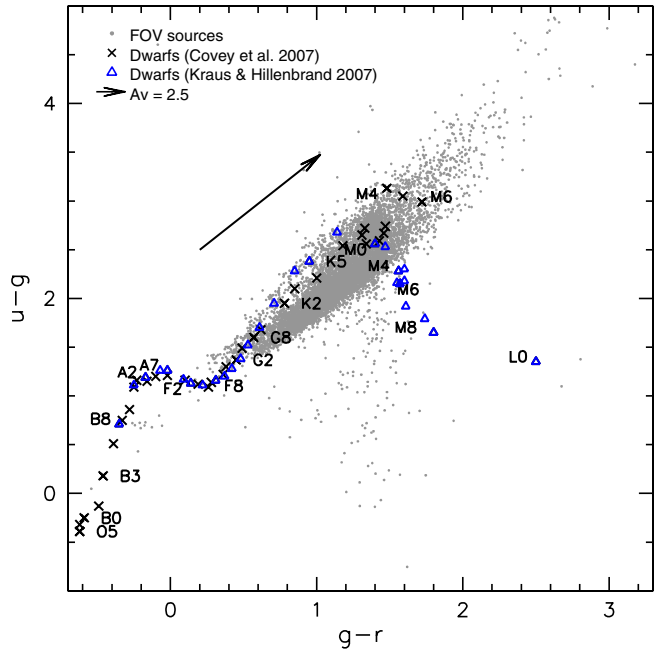

Fig. 3. $(g-r, u-g)$ color–color diagram for objects monitored at CFHT. Empirical dwarf color sequences from Covey et al. (2007) and Kraus & Hillenbrand (2007) are shown as black crosses and blue triangles, respectively. The reddening vector is traced based on the reddening parameters in the SDSS system provided by the ADPS (Fiorucci & Munari 2003).

diagrams, as shown in Figs. 2–3. Empirical dwarf SDSS color sequences (Covey et al. 2007; Kraus & Hillenbrand 2007) have been overplotted to the diagrams in order to follow the observed color distribution and investigate the relationship between color loci and stellar properties.

In Fig. 2, earlier-type field stars are located along the diagonal ellipse, with foreground or slightly reddened objects on the lowermost part of the distribution and background stars at the uppermost end; M-type stars are predominantly located on the horizontal branch, whose $g-r$ position is in good agreement with the value of ∼1.4 mentioned in previous studies (Covey et al. 2007; Finlator et al. 2000; Fukugita et al. 1996; Annis et al. 2011). A number of objects can be located to the left (i.e., blueward) of the standard locus in $r-i$; only for a part of them this displacement may be ascribed to photometric inaccuracies. The most likely explanation for these objects is that they are highly variable, and the inferred $r-i$ color is spurious due to the large epoch difference between the r-band and i-band photometry (the over one year time lapse between the ugr and the i-band mappings of the region, as discussed in Sect. 2).

Similarly, a progression of increasing spectral types and reddening effects can be observed from left to right along the ellipse in Fig. 3; an interesting locus is defined by the point dispersion at $0.5 \leq g-r \leq 2.0$, below the main body of the color distribution, as it shows $u-g$ color excesses presumably linked with the YSO accretion activity, manifest at UV wavelengths with a flux excess compared to the photospheric emission. An offset of a few tenths of a mag is observed between the mean locus of field stars in our survey and the sequences of Covey et al. (2007) and Kraus & Hillenbrand (2007). This offset cannot be explained with imprecisions in our calibration. A possible explanation may lie in a lower than solar standards metallicity of the field population probed here; at any rate, this disagreement has no impact on our analysis, as we uniquely used our internal reference sequence to probe the photometric accretion signatures of members, as illustrated in the following sections.

We further pursued the color signatures of different YSO types in the SDSS filters by analyzing the color properties of known members of the region with respect to the loci traced on the diagrams by the large population of field stars. Known members were identified amidst the population of the region based on a wide collection of photometric/spectroscopic data available in the literature from various surveys of the cluster; membership and further information on the WTTS (no disk evidence) vs. CTTS (disk-accreting) nature of selected members have been inferred based on one or more of the following criteria: i) H_α emitter from narrow-band photometry and variability from the data of Lamm et al. (2004) and following their criteria; ii) X-ray detection (Ramírez et al. 2004; Flaccomio et al. 2006) and location on the cluster sequence in the $(I, R-I)$ diagram when R,I photometry is available; iii) H_α emitter from spectroscopy (H_α EW > 10 Å, H_α width at 10% intensity >270 km s^{-1}); iv) radial velocity member according to Fűrész et al. (2006); v) member according to Sung et al. (2008; cf. criteria enumerated earlier) and Sung et al. (2009; *Spitzer* Class I/Class II). It is worth remarking that this preliminary analysis of membership and TTS classification is not based on direct accretion criteria.

Around 700 known members have been matched in the CFHT catalog within a matching radius of 1 arcsec; among these, ∼60% are classified as weak-lined T Tauri stars (WTTS). Figures 4 and 5 show the color properties of these groups of objects respectively in the $(r-i, g-r)$ and $(g-r, u-g)$ diagrams.

In redder filters, as shown in Fig. 4, both CTTS and WTTS define a single color sequence following the one traced by field stars. A few CTTS appear well blueward of this sequence, reflecting multi-year variability that is evidently more common in the CTTS than the WTTS. Conversely, accreting and non-accreting stars define two clear distinct distributions on the $(g-r, u-g)$ diagram in Fig. 5, with the latter displaying colors

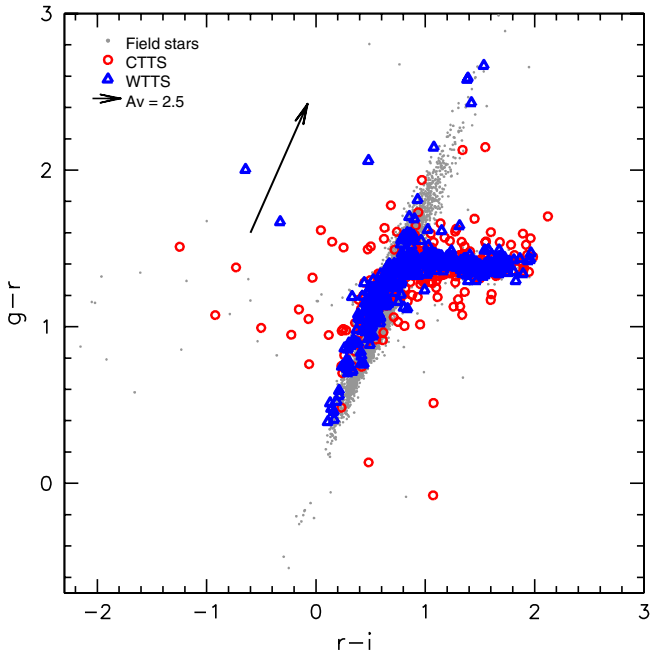

Fig. 4. $(r-i, g-r)$ color–color diagram for NGC 2264 members monitored at CFHT. Field stars, non-accreting cluster members (WTTS) and accreting cluster members (CTTS) are depicted as gray dots, blue triangles and red circles, respectively. The reddening vector is traced based on the reddening parameters reported in the ADPS (Fiorucci & Munari 2003).

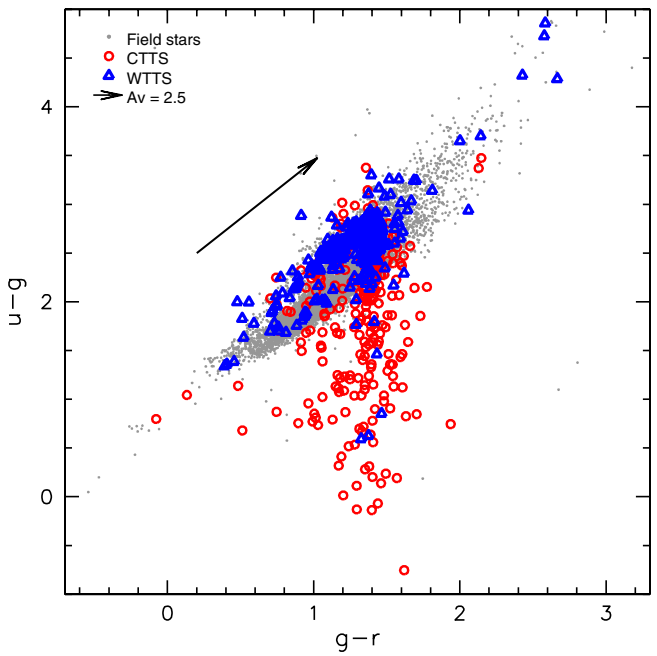

Fig. 5. $(g-r, u-g)$ color–color diagram for NGC 2264 members monitored at CFHT. Field stars, WTTS and CTTS are depicted as gray dots, blue triangles and red circles, respectively. The reddening vector is traced based on the reddening parameters reported in the ADPS (Fiorucci & Munari 2003).

consistent with the photometric properties of field stars and the former located at smaller (i.e., bluer) $u-g$ values compared to the main color locus defined by dwarfs.

These distinctive features are well observed in Fig. 6, which shows how members distribute on the $(u-r, r)$ color–magnitude

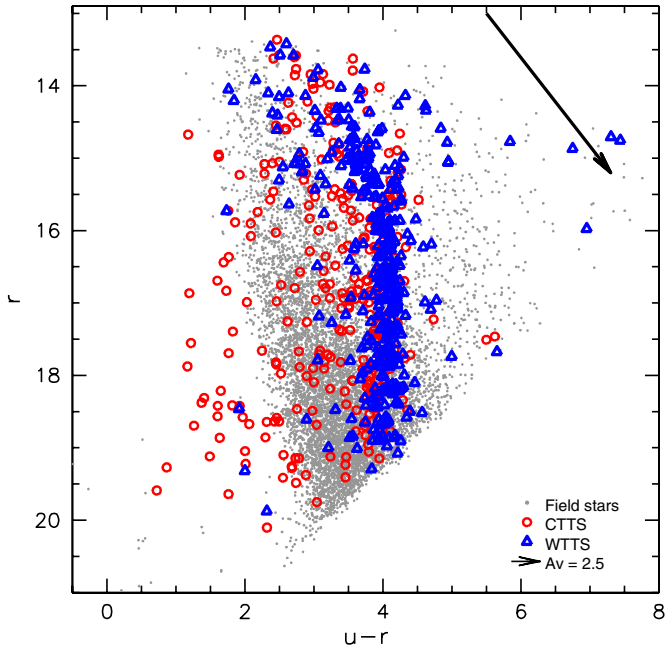

Fig. 6. $(u-r, r)$ color–magnitude diagram for NGC 2264 members monitored at CFHT. Field stars, WTTS and CTTS are depicted as gray dots, blue triangles and red circles, respectively. The reddening vector is traced based on the reddening parameters reported in the ADPS (Fiorucci & Munari 2003).

diagram. There, the cluster sequence is clearly traced by WTTS, while CTTS appear broadly scattered to the left as a result of their u-band excess, indicative of active accretion activity, compared to WTTS. A number of presumed non-accreting members show a non-negligible displacement blueward/redward of the main locus; these two groups of objects are discussed further in Sect. 3.2.2.

Two main inferences can be drawn from these diagrams:

1. CTTS and WTTS members do differentiate in the SDSS colors on the basis of photometric accretion signatures at short wavelengths (UV flux excess);
2. the UV excess linked with accretion, detected in the u-band, does not affect significantly the observations in filters at longer wavelengths, as emphasized by the substantial agreement of the CTTS and WTTS color sequences in Fig. 4 and the color saturation at $g-r \sim 1.4$, a behavior common to field stars.

These photometric properties, observed for different ensembles of stars, enable us to perform a new membership and population study on an individual basis, from an accretion-driven perspective. This analysis has the twofold purposes of investigating the presence, in the CFHT FOV, of additional objects that are new candidate members, and of re-examining the classification of known members, looking in both cases for classification outliers in the diagram loci dominated by accretion.

3.1. UV excess vs. different accretion diagnostics

In order to ascertain the coherence of the classification based on the UV excess detection on these diagrams and define some confidence limits for a reliable identification of accreting members, we compared the u-band excess information drawn from CFHT photometry with different diagnostics commonly used

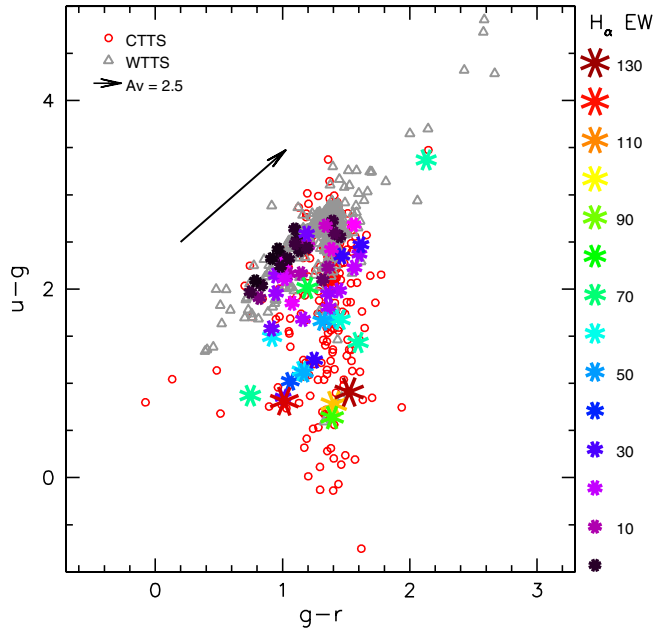

Fig. 7. $u-g$ vs. $g-r$ colors for NGC 2264 members are compared to the H_α EW. Asterisks mark members for which H_α EW is available from the CSI 2264 campaign (see text). Asterisk colors and sizes are scaled according to the value of H_α EW.

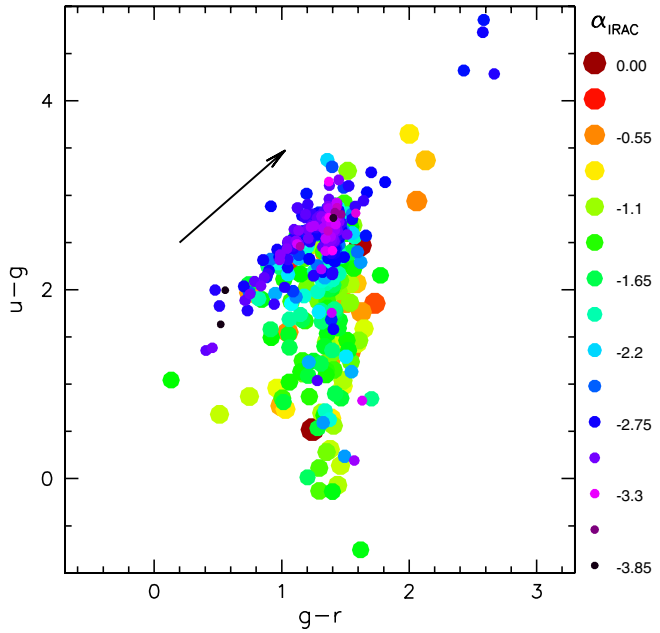

Fig. 8. $u-g$ vs. $g-r$ colors for NGC 2264 members are compared to the α_{IRAC} diagnostics, which probes the inner disk properties (see text). Colors and sizes of symbols are scaled according to the value of α_{IRAC} from the data of Teixeira et al. (2012).

to investigate accretion, such as the equivalent width (EW) and the width at 10% intensity in the Hα emission line, probing the accretion funnel, or the mid-infrared emission, that signals the presence of material in the inner disk when a flux excess compared to the photospheric level is detected.

Figure 7 shows the same color–color diagram as in Fig. 5 with additional information on the Hα EW values measured for the subsample of objects having VLT/Flames spectra from the CSI 2264 campaign (A. Sousa, UFMG). A threshold value commonly adopted to identify accreting YSOs from Hα emission is Hα $EW \geq 10$ Å (Herbig & Bell 1988), while a more robust scheme relating the threshold value to the stellar spectral type has been introduced by White & Basri (2003). As can be observed in Fig. 7, the UV excess and the Hα EW diagnostics are fully consistent, with the objects having the least Hα EWs located on the color locus traced by WTTS and field stars, while a region of the diagram dominated by accretion can clearly be delimited below the field stars distribution and identified from the detection of a UV excess.

A useful tool for characterizing presence and properties of a circumstellar disk is the examination of the infrared spectral energy distribution (SED) of the system. A particularly interesting indicator of the SED morphology is the measure of its slope in the spectral range of interest (i.e., the spectral index α first introduced by Lada 1987): smaller amounts of material in the inner disk result in smaller contributions, i.e. smaller flux excesses, at mid-IR wavelengths and hence more negative values of the α-index, which approaches the slope of a reddened blackbody, while positive values of the mid-IR SED slope are specific to deeply embedded, Class I sources. In Lada et al. (2006), the α-index diagnostics for disks is applied to the mid-IR emission sampling between 3.6 and 8 μm performed with the *Spitzer* instrument IRAC for the young cluster IC 348; the same tool has been adopted by Teixeira et al. (2012) to characterize the evolutionary state of NGC 2264 members based on the inner disk properties. We compare their results to the colors of NGC 2264 YSOs in the $(g-r, u-g)$ diagram in Fig. 8. Following the classification proposed in Table 2 of Teixeira et al. (2012), values of $\alpha_{IRAC} \lesssim -2$ are indicative of objects with anaemic disks or naked photospheres, while objects with thick disks (hence likely to be actively accreting) are characterized by $\alpha_{IRAC} > -2$. Indeed, as can be observed in Fig. 8, objects in the first α_{IRAC} group are mainly located on the WTTS/dwarf locus in $u-g$ vs. $g-r$, while objects showing a UV excess (and thus actively accreting stars) have the largest values of α_{IRAC}, as globally expected.

3.2. UV census of the NGC 2264 population

3.2.1. New CTTS candidates in NGC 2264

A most interesting locus to identify accreting members is the data points dispersion below the main body of the distribution in Fig. 5. In fact, this allows easy detection and measurement of the u-band excess with respect to WTTS. The inferred color excess estimate is independent of distance and has no significant dependence on visual extinction A_V, as WTTS define a color sequence nearly parallel to the reddening vector down to ∼M0 spectral type. For later-type stars, the color sequence traced by WTTS turns down, saturating at $g-r \sim 1.4$ (cf. Fig. 4); the implications of this for the UV excess measurement are discussed in Sect. 4. In order to minimize the contamination, we traced a straight line, parallel to the reddening vector, bordering the accretion-dominated area below the lower envelope of the dwarf color locus (Fig. 9); we then selected as new CTTS candidates all the objects lying in this region and marked as field stars. For all these objects, a preliminary check of the photometry on the CFHT field images has been performed, in order to discard the sources whose flux measurements could be affected by detection issues (e.g., too faint source, presence of two close sources, partial projection of the source on CCD gaps or bad pixel rows).

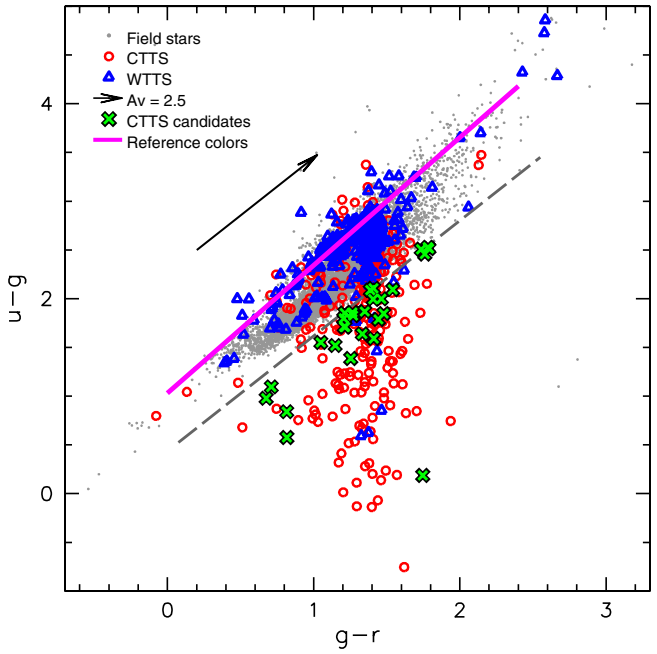

Fig. 9. Selection of new CTTS candidates from the $(g-r, u-g)$ diagram. The gray dashed line traces a conservative boundary separating the accretion-dominated region of the diagram from the color locus of non-accreting stars (see text). Field stars, WTTS and known CTTS are depicted as gray dots, blue triangles and red circles, respectively; the new CTTS candidates selected from this diagram are marked as green crosses. The purple line fitting the upper envelope of the WTTS distribution traces the reference sequence of photospheric colors that has been adopted for measuring the UV excess of accreting stars (see Sect. 4).

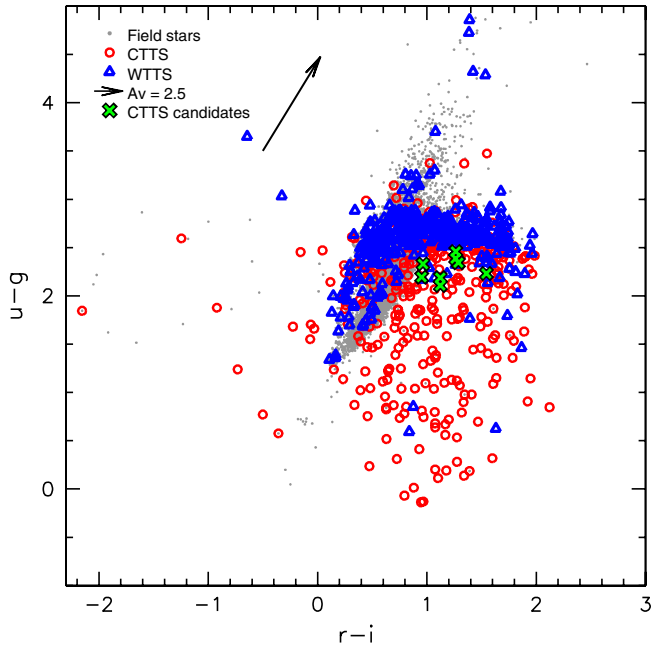

Fig. 10. $(r-i, u-g)$ diagram for cluster members and field stars in the NGC 2264 field. Field stars, WTTS and known CTTS are depicted as gray dots, blue triangles and red circles, respectively. Gray dots encircled in red correspond to new CTTS candidates selected on different diagrams (Fig. 9 or Fig. 4.) Green crosses mark the additional CTTS candidates selected on this diagram.

A second group of new CTTS candidates has been extracted from the color distribution in Fig. 4, namely among the color outliers located to the left and, to a smaller extent, below the main color distribution. Similarly to the procedure adopted for the selection of objects on the diagram in Fig. 5, a check on the photometry quality for all the objects of interest has preceded the identification of new candidates.

A third color–color diagram of interest for the analysis of membership is the one depicting $u-g$ vs. $r-i$ (Fig. 10); as a "transitional" diagram between $u-g$ vs. $g-r$ (Fig. 5; direct UV excess detection) and $g-r$ vs. $r-i$ (Fig. 4; nearly horizontal photospheric color sequence for late-type stars, with no color saturation on $r-i$), this diagram provides a greater sensitivity to the UV excess for spectral types ≥M0. Additional, later-type CTTS candidates have then been identified on this diagram, and their photometric properties inspected similarly to what done for the candidate members extracted earlier.

A second aspect of our selection of new candidate, actively accreting YSOs concerns the group of already known members which had previously been considered WTTS (that is, YSOs without evidence of significant, ongoing accretion at the time of the previous surveys). We examined the locations of these putative WTTS in our several diagrams (Figs. 4 through 9) and identified a significant number whose colors fell generally within the UV-bright regions – for example, the small group of blue points located below the normal dwarf locus in Fig. 5. This procedure allowed us to re-classify 19 WTTS members as CTTS, which add to the 50 newly accretion-identified candidates; this varied status does not necessarily reflect an erroneous previous classification, but may as well be the result of a long-term (∼years) variability in the accretion activity of the objects.

The results of our UV-based membership investigation are provided in Table A.1 (new CTTS candidates) and Table A.2 (re-classified CTTS). This revised census of accreting members we infer for NGC 2264 likely encompasses all objects showing a strong UV excess, hence a significant amount of accretion. However, our sample might not be exhaustive regarding the weakly-accreting CTTS component. Indeed, a non-negligible overlap between the CTTS and WTTS populations can be seen in Figs. 5, 6, which cannot be efficiently probed with our diagnostics. Hence, we do identify some new CTTS, but we might be missing a number of lower accretors, showing a smaller UV excess that cannot be easily separated from the color properties of WTTS/field stars.

The wide FOV of CFHT/MegaCam allowed us to probe a quite extended region around the cluster, encompassing most of the FOVs adopted in previous surveys. It is thus of interest to examine the spatial distribution of the new CTTS candidates, selected as described in Sect. 3.2.1, compared to the distribution of known NGC 2264 members on the CFHT FOV. This comparison is shown in Fig. 11. A fraction of the object positions are projected onto the main cluster region, while a significant part are located on the periphery or beyond. This provides evidence for a wider spatial spread of the PMS population associated with NGC 2264, and attests to the presence of actively accreting members far from the original sites of star formation, currently known to be located towards the north and the center of the field imaged at CFHT (Dahm 2008).

3.2.2. Field stars contamination in the NGC 2264 sample

Based on the discussion in Sect. 3.2.1, another potentially interesting location for our accreting members census is the data point dispersion to the left of the cluster sequence

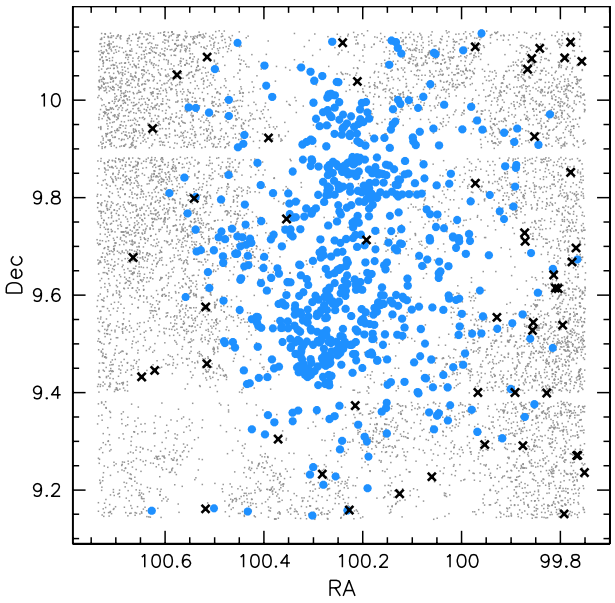

Fig. 11. Spatial distribution of the new CTTS candidates from the CFHT u-band survey. Field stars, known cluster members and new CTTS candidates are depicted as small gray dots, blue dots and black crosses, respectively.

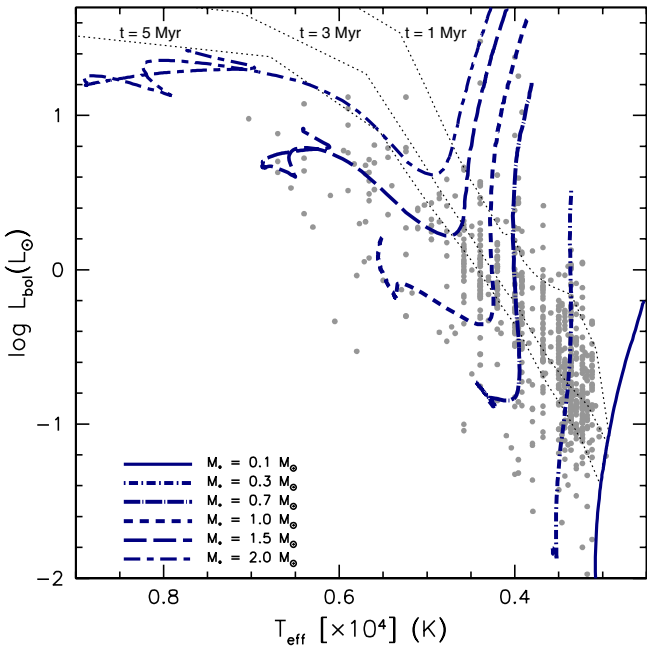

Fig. 12. HR diagram for NGC 2264 members. Mass tracks and isochrones from Siess et al. (2000)'s models are plotted over the point distribution.

(WTTS distribution) in Fig. 6. A direct search for candidate members in this color–magnitude locus would hardly be straightforward, due to the distance-dependence and to the vast preponderance of field stars; on the other hand, this diagram provides an additional test bench for investigating the nature of individual groups of objects.

Similarly to Fig. 5, we can identify on Fig. 6 a group of putative non-accreting members with inferred $u - r$ colors bluer than expected. This feature, suggestive of ongoing accretion activity for a young cluster member, is consistently observed on different color-magnitude diagrams (g vs. $u - g$, i vs. $u - i$) for several of these objects; interestingly, these objects populate the thin lower branch of the WTTS distribution, below the main WTTS locus, on the lower part of the dwarf locus in Fig. 5 ($u-g$ vs. $g - r$ diagram). Little spectroscopic information is available for this group of stars; contrary to what is expected for objects clearly showing accretion activity, the level of variability exhibited by many of these objects during our monitoring is not significant over the noise level defined, as a function of magnitude, by field stars in our survey (see Venuti et al., in prep.). Additionally, several of these putative members would be located close to or onto the MS-turnoff (or below) in the HR diagram of the region (Fig. 12). We therefore suspect at least a part of these objects to possibly be misclassified dwarfs instead. A list of objects with questioned membership, of the relevant CFHT photometry and of the original selection criteria is provided in Table A.3.

Another interesting group of objects in Fig. 6 is the sample of WTTS displaced redward of the main cluster sequence. Most of these objects consistently appear significantly reddened through all CFHT photometric diagrams; in several cases, they display little variability. While contamination by field stars might be partly reflected in the observed properties, most of the objects in this stellar group would actually look like very young, or equivalently overluminous, objects on the HR diagram of the region (i.e., they are located on the upper right envelope of the data point distribution in Fig. 12). This would rather suggest binarity and/or earlier (i.e., more embedded) evolutionary status as possible explications of the distinctive properties of these objects.

3.3. NGC 2264 members in the CFHT survey: individual extinction and stellar parameters

The sample of PMS stars retrieved or newly identified in the CFHT survey amounts to about 750 objects. Based on the multiband photometry obtained during our campaign, as well as on the collection of previous literature data in different spectral bands, we performed an extensive investigation of individual stellar parameters (like extinction, mass and radius); this is aimed at characterizing the properties of members in a uniform and self-consistent manner.

Extinction towards NGC 2264 is known to be low (cf. Dahm 2008, for a review of literature results), with a typical value of $\lesssim$0.4 mag for the visual extinction A_V. Indeed, the good agreement of the cluster sequence with the color locus traced by foreground stars on Fig. 4 and the color saturation at $\sim$1.4 in $g-r$ (cf. discussion at the beginning of Sect. 3) is consistent with a low value of the average A_V. We use the photometric properties displayed in this diagram to derive an estimate of the individual A_V for late-type stars, i.e. the group of members located on the horizontal branch in the color locus. For this group of objects, A_V is determined by displacing each point along the reddening direction until the lowermost envelope of the branch distribution defined by field stars is reached and computing the corresponding amount of reddening. This procedure has the advantage of relying solely on observed quantities, without involving the comparison with an external reference sequence that would intrinsically introduce an additional source of uncertainty on the result.

For earlier-type stars ($\lesssim$M0), the cluster sequence is nearly parallel to the reddening direction in Fig. 4, thus preventing a direct A_V determination from the object location on the diagram. For this group of objects, we derive a first estimate of the individual A_V from the analysis of the infrared photometry in the JHK_S filters, as measured in the 2MASS survey (Skrutskie et al. 2006). This consists in comparing their infrared colors with the JHK_S color sequence for dwarfs (Covey et al. 2007) and with the CTTS infrared locus defined in Meyer et al. (1997) and

Table 2. Photometry for NGC 2264 members monitored at CFHT.

Mon-ID[1]	RA	Dec	u	g	r	i
Mon-000007	100.47109	9.96755	15.850	14.807	14.674	14.192
Mon-000008	100.45248	9.90322	19.656	17.083	15.839	19.887
Mon-000009	100.53812	9.80134	18.208	16.043	15.011	14.532
Mon-000011	100.32187	9.90900	18.548	16.808	15.531	14.535
Mon-000014	100.52772	9.69214	18.895	15.879	14.280	13.445
Mon-000015	100.53796	9.98410	19.427	16.172	14.589	13.786
Mon-000017	100.38330	10.00680	18.402	15.972	14.930	14.496
Mon-000018	100.30520	9.91909	19.311	16.526	15.366	14.613
Mon-000020	100.53849	9.73427	19.964	17.213	15.891	15.267
Mon-000021	100.24772	9.99594	18.174	15.835	14.810	14.452

Notes. Uncertainties on the photometric measurements are estimated to range from ~0.15 to ~0.004 from the faintest to the brightest objects in u and g, from ~0.015 to ~0.0015 in r and 5–10 times smaller in i. [(1)] Object identifiers adopted within the CSI 2264 project (see Cody et al. 2014). A full version of the Table is available at the CDS. A portion is shown here for guidance regarding its form and content.

converted to the 2MASS photometric system as in Covey et al. (2010) (K. Covey, private communication). Additional A_V estimates for a part of these sources are available from previous, similar studies (e.g., Rebull et al. 2002, where A_V is investigated from the color excess on $R-I$, or Cauley et al. 2012, where A_V is computed by fitting stellar spectra with spectral templates) and/or derived from our optical photometry collection (from the measurement of the color excess on $R-I$, $V-I$ or $B-V$ in order of preference). In the absence of a direct A_V estimate from CFHT photometry, all available A_V derivations have been examined and their consistency checked on the color properties displayed in the CFHT diagrams, in order to discard discrepant estimates; an average value has then been adopted as a final estimate.

To evaluate the uncertainty on our individual A_V estimates, we collected all available A_V determinations for any object in our sample, and measured the amount of scatter observed among values inferred from different authors/methods. This comparison allowed us to conclude that different A_V estimates are typically consistent within a radius of a few 0.1 mag, which then provides an order-of-magnitude uncertainty on the A_V values adopted in this study.

Of the sample of CFHT members, spectral type is known for around 50% and has been retrieved, in order of preference, from the studies of Dahm & Simon (2005), Rebull et al. (2002) or Walker (1956). For the remaining objects, the spectral type has been derived from the comparison of the dereddened colors with the empirical optical color sequence of Covey et al. (2007). We used the dereddened photometry of members with known spectral type, earlier than M1, to recalibrate the empirical spectral type–color sequence onto CFHT photometry. Spectral types were converted to effective temperatures $T_{\rm eff}$ following the scale of Cohen & Kuhi (1979), checked for consistency against the scale of Luhman et al. (2003).

Bolometric luminosities have been derived from the dereddened J-band photometry retrieved from the 2MASS catalog, adopting $T_{\rm eff}$–dependent J-band bolometric corrections (BC_J) obtained as a fit to the $T_{\rm eff}$–BC_J scales of Pecaut & Mamajek (2013) and Bessell et al. (1998). A cluster distance value of 760 pc (Sung et al. 1997) has been adopted for the conversion to absolute magnitudes; this commonly adopted estimate of distance has been recently strengthened by the results of Gillen et al. (2014), who performed a detailed characterization of a newly identified, well sampled low-mass PMS eclipsing binary in NGC 2264, with strong evidence of membership and an inferred distance of 756±96 pc. For a few tens of objects, for which J-band photometry from the 2MASS survey was not available, $L_{\rm bol}$ has been derived using an empirical calibration relationship between the dereddened r-band photometry and $L_{\rm bol}$, which has been inferred from the distribution of dereddened r-band magnitudes vs. $L_{\rm bol}$ values derived from the J-band photometry over the whole sample.

Stellar masses have been determined by placing each object on the Hertzsprung-Russell diagram and comparing their position with the mass tracks of the PMS model grid of Siess et al. (2000; Fig. 12). A track-fitting tool provided by L. Siess on his webpage has been used to interpolate the mass value between two mass tracks. CFHT members span a wide range of masses, varying from 0.1 to 2 $M_\odot$. Stellar radii have been determined from the estimates of $L_{\rm bol}$ and $T_{\rm eff}$ as

$$R_* = \sqrt{\frac{L_{\rm bol}}{4\pi\sigma T_{\rm eff}^4}}$$

where σ is the Stefan-Boltzmann constant.

Photometric data and stellar parameters for the whole population of NGC 2264 members monitored at CFHT are reported in Tables 2 and 3, respectively.

4. UV excess and accretion in NGC 2264

The investigation of YSOs at short wavelengths offers a unique window on the accretion mechanisms: it provides one of the most direct probes to the hot emission from the impact layer where the accreting material hits the stellar surface at near free-fall velocities, producing a shocked area up to several $\times 10^3$ K hotter than the stellar photosphere. This enhanced luminosity at UV wavelengths is reflected in the characteristic color properties of accretion-dominated objects compared to non-accreting young stars (cf. Figs. 5 and 6) and hence provides a direct proxy to the accretion luminosity, which in turn enables the investigation of the rates of mass accretion in individual systems.

The u-band flux excess is trivially given by

$$F_u^{\rm exc} = F_u^{\rm obs} - F_u^{\rm phot}, \quad (6)$$

Table 3. Spectral type, extinction and stellar parameters for NGC 2264 members monitored at CFHT.

Mon-ID	Status[1]	SpT	SpT_ref.[2]	A_V	$L_{\rm bol}$ ($L_\odot$)	M_* ($M_\odot$)	R_* ($R_\odot$)	log t (yr)
Mon-000007	c	K7	s		1.28	0.69	2.36	6.09
Mon-000008	w	K5	s	0.3	0.241	0.80	0.85	
Mon-000009	w	F5	p	2.3	2.31	1.3	1.24	
Mon-000011	c	K7	s	0.3	0.79	0.70	1.86	6.34
Mon-000014	w	K7:M0	p	1.2	3.9	0.66	4.22	5.68
Mon-000015	w	K7:M0	p	1.0	2.70	0.65	3.50	
Mon-000017	c	K5	s	0.2	0.71	1.13	1.45	
Mon-000018	w	K3:K4.5	p	0.6	1.70	1.47	2.03	6.60
Mon-000020	w	K7	s	0.4	0.44	0.71	1.39	6.70
Mon-000021	c	K5	s	0.4	0.96	1.20	1.69	6.69

Notes. [(1)] "c" = CTTS; "w" = WTTS; "cc" = CTTS candidate. [(2)] "s" = spectroscopic SpT estimate (retrieved from literature); "p" = photometric SpT estimate (from CFHT optical colors). A full version of the Table is available at the CDS. A portion is shown here for guidance regarding its form and content.

where $F_u^{\rm obs}$ is the measured flux in the u-band and $F_u^{\rm phot}$ is the amount of flux that would be expected from a purely photospheric emission. It is important to remark that, in order to isolate the component of additional flux produced in the accretion shock and thus probe accretion onto the star, the flux excess (compared to dwarfs) due to the enhanced chromospheric activity of T Tauri stars has to be included in the photospheric emission. This issue is addressed by taking the photometric properties observed for the WTTS population as the reference for the definition of the UV excess. The color excess will thus correspond to the difference between the observed stellar colors and the expected photospheric colors based on the properties of the non-accreting counterparts of the objects of interest:

$$E(u-m) = (u-m)_{\rm obs} - (u-m)_{\rm phot+chrom}. \quad (7)$$

As discussed in Sect. 3, no significant impact of the accretion luminosity is observed on the stellar flux detected at filters redder than the u-band; hence, the color excess of Eq. (7) basically corresponds to the u-band excess revealing the presence of accretion, $E(u) \simeq E(u-m)$.

We measured the UV color excess of accreting stars in two different ways, from the properties displayed on the $u-g$ vs. $g-r$ and r vs. $u-r$ diagrams (Figs. 5 and 6, respectively), as detailed below.

– In the first case (Fig. 5), we referred the color excess measurement to a straight line nearly parallel to the reddening vector and following the upper part of the WTTS distribution, as shown in Fig. 9. $E(u)$ is thus measured as

$$E(u) = (u-g)_{\rm obs} - (u-g)_{\rm ref}, \quad (8)$$

where $(u-g)_{\rm ref}$ is the reference (i.e., expected) color at the observed $g-r$ level, $(u-g)_{\rm ref} = 1.312\,(g-r)_{\rm obs} + 1.03$. The WTTS color sequence is in good agreement with the reference line until spectral type ~M0, and hence the adoption of this reference sequence allows us to derive a UV excess estimate essentially unaffected by reddening. For later-type stars, however, the real WTTS color sequence turns down on the diagram; this implies that the extrapolation of the WTTS trend at spectral types earlier than M0 to the whole sample yields an excess overestimation (i.e., more negative values of $E(u)$) for M-type stars. As the bulk of M-type WTTS lies about 0.2 mag below the reference line, we corrected for this bias by adding a constant offset of 0.2 mag to the $E(u)$ estimates derived for this group of objects.

– In the second case, as can be observed on Fig. 6, WTTS nicely trace the cluster sequence over the whole range of magnitude. We thus dereddened the u, r photometry and defined the sequence of reference colors as the least-squares fit polynomial to the resulting WTTS distribution. The UV excess is thus provided by

$$E(u) = (u-r)_{\rm obs} - (u-r)_{\rm ref}, \quad (9)$$

where $(u-r)_{\rm ref}$ is the reference color at brightness $r_{\rm obs}$. Due to the small number of points and the large scatter affecting the definition of the sequence at the brighter end, we decided to restrict our UV excess analysis to objects fainter than 14.5 in r.

This second method, compared to the first, has the disadvantage of being intrinsically more uncertain, as it is subject to errors in A_V determination (while the first method is essentially A_V-independent); on the other hand, the application of this method to u- and r-band observations taken during the monitoring survey allows us to derive both a global picture of accretion in NGC 2264 from the average photometry, and a variability range for the UV excess on a timescale of a few weeks (cf. Sect. 4.2).

An average rms error of ~0.16 mag has been associated to the UV excess determinations, in order to account for the scatter of the WTTS distribution around the reference sequence.

From Eq. (6) and

$$E(u) = u_{\rm obs} - u_{\rm phot} \quad (10)$$

we obtain

$$F_u^{\rm exc} = F_u^{\rm obs}\left(1 - 10^{+0.4\,E(u)}\right) = F_u^0\,10^{-0.4\,u}\left(1 - 10^{+0.4\,E(u)}\right), \quad (11)$$

where u is the (dereddened) apparent u-band magnitude of the object, $E(u)$ is the UV excess computed as in Eqs. (8)–(9) and F_u^0 is the SDSS u-band zero-point flux ($F_u^0 = 3767.2$ Jy).

We used Eq. (11) (cf. also Rigliaco et al. 2011) to measure the u-band flux excess over the whole sample and then converted $F_u^{\rm exc}$ to $L_u^{\rm exc}$ using a distance of 760 pc.

The results of a similar, single epoch photometric survey to detect and measure mass accretion in NGC 2264 from the UV excess diagnostics have been reported in Rebull et al. (2002). The authors measured the UV excess displayed by accreting stars from U-band and V-band photometry, by comparing the

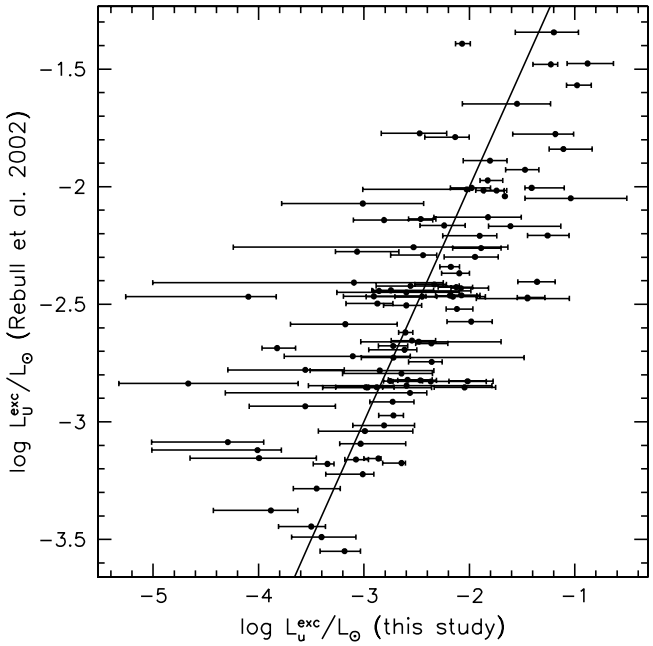

Fig. 13. UV excess luminosity measurements obtained in this study are compared to Rebull et al. (2002)'s for objects in common to both samples (Rebull, priv. comm.). On the *x*-axis, dots correspond to the median L_u^{exc} detected during the 2 week-long CFHT monitoring, while variability bars depict the actual range in L_u^{exc} values measured at different observing epochs during the survey. The equality line is traced as a solid line to guide the eye.

observed colors with colors expected based on the spectral type of individual objects. In Fig. 13, we compare their measured UV excess luminosities (L. Rebull, priv. comm.) with both the median L_u^{exc} values and the relevant variability ranges we detect here, on a timescale of a couple of weeks, for CTTS targeted in both surveys (about 100). As can be observed, data points result to be well distributed around the equality line; the rms scatter measured about the line, amounting to 0.5 dex, is quite consistent with the average amount of variability on L_u^{exc} (about 0.6 dex) detected across the sample from CFHT monitoring.

4.1. Accretion luminosity and mass accretion rates

The *u*-band excess luminosity represents a single component of the total excess emission over the whole spectral range. In order to characterize the properties of the accretion process, it is therefore necessary to also take the flux excess at unobserved wavelengths into account, i.e., to apply a bolometric correction.

Gullbring et al. (1998) showed that a direct correlation exists between the total accretion luminosity L_{acc} and the excess luminosity observed in the *U*-band. This is indeed expected, since the excess emission likely dominates the observed flux at wavelengths <4500 Å (i.e., below the *g*-band filter). In order to achieve this result, they measured the excess emission from spectra covering the range 3200–5400 Å, for a sample of 26 CTTS. They modeled the excess spectrum from the accretion spot assuming a region of constant temperature and density (slab model) and used this model fit to estimate the amount of excess emission at unobserved wavelengths. The authors eventually resolved to adopt a uniform correction factor, across the whole sample, for the ratio of total-to-observed excess flux, corresponding to a $T \sim 10\,000$ K. For each object, they subsequently synthetized a *U*-band magnitude from the observed spectrum and computed the corresponding flux excess. The comparison of the two quantities (L_{acc} and L_U^{exc}) enabled the authors to yield a well-determined calibration equation, $\log(L_{acc}/L_\odot) = 1.09^{+0.04}_{-0.18} \log(L_U^{exc}/L_\odot) + 0.98^{+0.02}_{-0.07}$, that was ultimately consistent with the model predictions of Calvet & Gullbring (1998), who introduced a detailed description of the accretion shock region.

Here we adopt a simple phenomenological approach to derive a direct relationship between the *u*-band excess luminosity and the total accretion luminosity L_{acc}. In a first approximation, we describe the stellar emission as a blackbody emission at the photospheric temperature T_{phot}. Similarly, the emission from the accretion spot is approximated by a blackbody at $T = T_{spot}$. The excess emission linked with accretion is thus given by the difference between the flux emitted by the distribution of accretion spots and the flux emitted by a corresponding area, of the same extension, on the stellar photosphere. In terms of blackbodies, this becomes the difference between a blackbody flux density at $T = T_{spot}$ and a blackbody flux density at $T = T_{phot}$, both integrated over the same area. In this picture, the ratio r of total-to-observed flux excess in the *u*-band, i.e. the corrective factor to be introduced to derive the total L_{acc} from L_u^{exc}, can be estimated as

$$r = \frac{\sigma T_{spot}^4 - \sigma T_{phot}^4}{\pi \int_u (B_{T_{spot}}(\lambda) - B_{T_{phot}}(\lambda))\, d\lambda}, \quad (12)$$

where the integration is performed over the *u*-band window. No assumptions on the filling factor are needed in this description.

In order to investigate the relationship between L_u^{exc} and L_{acc}, we selected a subsample of 44 CTTS, covering the spectral type range M3.5:K2 (or equivalently the mass range ~0.2–1.8 $M_\odot$) and whose variability, monitored in the *u*-band ($\lambda_{eff} = 3557$ Å) and *r*-band ($\lambda_{eff} = 6261$ Å) at CFHT, is likely accretion-dominated. An extensive spot modeling (cf. Bouvier et al. 1993) of the simultaneous $u + r$ variability amplitudes has been performed in order to assess the dominating features of the variability displayed by individual objects; accretion-dominated sources have been identified as well-represented variables in terms of a surface spot distribution ~10^3 to several $\times 10^3$ K hotter than the stellar photosphere. A full description of the variability analysis for the CFHT NGC 2264 members will be provided in a forthcoming paper (Venuti et al., in prep.).

For each of the selected objects, we adopted the individual T_{spot} estimate inferred from spot models, that corresponds, for a given object, to the color temperature of the spot distribution that best reproduces the simultaneous flux variations observed at different wavelengths; T_{phot} is derived from the spectral type as described in Sect. 3.3. We then derived, for each object, the ratio r of Eq. (12), through a numerical integration of $B(\lambda)$ in the spectral range 3257–3857 Å (cf. Fukugita et al. 1996); an uncertainty on the value of r has been inferred correspondingly to the uncertainty on the spot temperature T_{spot}. Based on these estimates, the percentage of the total excess flux detectable in the *u*-band is on average ~10%. The accretion luminosity L_{acc} is then computed as $L_{acc} = r\, L_u^{exc}$.

A least-squares fit to the $\log(L_u^{exc}/L_\odot)$ vs. $\log(L_{acc}/L_\odot)$ distribution inferred as previously described provided us with the following calibration relationship:

$$\log\left(\frac{L_{acc}}{L_\odot}\right) = (0.97 \pm 0.03) \log\left(\frac{L_u^{exc}}{L_\odot}\right) + (1.09 \pm 0.07). \quad (13)$$

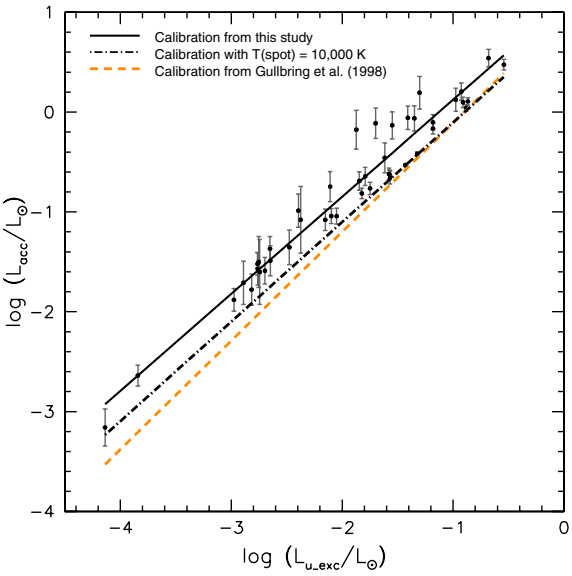

Fig. 14. $L_{\rm acc}$–$L_u^{\rm exc}$ calibration relationship. The black solid line traces the relationship derived in this study, while the orange dashed line represents the relationship by Gullbring et al. (1998). The data points represent the u-band excess luminosity and the accretion luminosity estimates inferred on an individual basis for a sample of 44 CTTS in our survey (see text). The error bars reflect the uncertainty on the individual $T_{\rm spot}$ estimates. The black dashed-dotted line shows the calibration line that would be inferred, with the procedure followed in this study, in the assumption $T_{\rm spot}$ = 10 000 K.

Figure 14 compares our result with the calibration inferred from the study of Gullbring et al. (1998); the parameters of the two calibrations are fairly consistent within the error bars. The locus traced by our point distribution is globally consistent with the prediction of Gullbring et al.'s study, albeit showing a systematic shift above their calibration line. Our estimates result to be larger by a factor of $\lesssim$2 to 4, corresponding to a difference from ∼0.2 dex at the highest $\dot{M}_{\rm acc}$ regimes (∼10^{-7} $M_\odot$/yr) to ∼0.6 dex at the lowest $\dot{M}_{\rm acc}$ regimes (∼10^{-10} $M_\odot$/yr).

This difference between the two conversions is significantly reduced if we adopt, in our approach, a constant spot temperature of 10 000 K, an assumption closer to the uniform correction, at $T \sim$ 10 000 K, that was introduced in Gullbring et al.'s method. Indeed, individual $T_{\rm spot}$ estimates adopted in our study cover a wide range of values, with a mean around ∼6500 K, a spread of ∼2000–3000 K at a given stellar temperature and nominal $T_{\rm spot}$ that can reach up to ∼9000–11 000 K and down to ∼5000 K. As described earlier, spot temperatures, in our approach, are inferred case by case by fitting simultaneous optical (r-band) and UV (u-band) variability amplitudes with spot models. Hence, these correspond to the color temperatures that best reproduce the observed, λ-dependent contrast of the spot distribution with the stellar reference emission level (which is the effect we aim at accounting for when introducing a bolometric correction). As the peak of the emission of a blackbody in the u-band occurs around 10 000 K, lower $T_{\rm spot}$ estimates naturally imply that a larger correction factor is needed in order to recover the total flux emitted by the spot. While, for a typical photosphere ($T \sim$ 4000 K), 12% of the excess emission of a 10 000 K spot is observed in the u-band, this percentage reduces to ∼10% for a 7000 K spot and to less than 8% for a 6000 K spot. In order to evaluate how much of the discrepancy could actually be due to this effect, we repeated our procedure assuming a constant $T_{\rm spot}$ = 10 000 K over the whole subsample of objects; as shown in Fig. 14, this indeed would allow us to mostly cancel the offset between the two calibrations.

We are aware of the simplified nature of the blackbody approximation for stellar and spot fluxes; at the same time, we stress that the results inferred from this description are not inconsistent with those obtained from more sophisticated pictures. The discrepancy, albeit systematic, between $L_{\rm acc}$ estimates from Eq. (13) and those from Gullbring et al. (1998)'s calibration is smaller than, or comparable to, the usual estimates of the uncertainty affecting the accretion rate measurements (∼0.5 dex), and a non-negligible contribution to this offset may actually derive from the different assumption on the correction factors adopted across the samples of objects considered in each study. Figure 10 of the theoretical study performed by Calvet & Gullbring (1998), though it provides full endorsement of Gullbring et al.'s relationship, yet depicts the complexity of achieving a detailed physical representation of the accretion shock. The range of predictions from model configurations they explored would lie, on Fig. 14 of our work, across the region delimited by our (Eq. (13)) and Gullbring et al. (1998)'s relationship.

Considering this, and the fact that each model has its own limitations, we believe it beneficial to explore whether, and to which extent, information deduced from data might actually be sensitive to different model assumptions. We therefore adopt the calibration in Eq. (13) to estimate the total $L_{\rm acc}$ from the measured u-band luminosity excess, and will refer at the same time to Gullbring et al.'s, where relevant, for comparison purposes.

If we assume that the accretion energy is reprocessed entirely into the accretion continuum (cf. Herczeg & Hillenbrand 2008), the mass accretion rate $\dot{M}_{\rm acc}$ can be derived from $L_{\rm acc}$ as

$$\dot{M}_{\rm acc} = \left(1 - \frac{R_*}{R_{\rm in}}\right)^{-1} \frac{L_{\rm acc} R_*}{G M_*} \sim 1.25 \, \frac{L_{\rm acc} R_*}{G M_*}, \qquad (14)$$

where M_* and R_* are the parameters of the central star, $R_{\rm in}$ is the inner disk radius and we are assuming that the accretion funnel originates at the truncation radius of the disk, at $R_{\rm in} \sim 5\,R_*$ (Gullbring et al. 1998).

Figure 15 compares the $\dot{M}_{\rm acc}$ distributions inferred from each of the two UV derivations described at the beginning of Sect. 4. The diagram reports the $\dot{M}_{\rm acc}$ determinations for every accreting object, in the sample, that displays a UV excess according to the identification procedure previously described. The two distributions are on average consistent, within a small mass-dependent offset likely reflecting a residual overestimation of the $(u-g)$ color excess from Fig. 9 (see discussion around Eq. (8)). Variability is likely to affect, at least partly, the scatter observed within ±0.25 dex around the fitting line (see Sect. 4.2).

Figure 16 shows the mass accretion rate distribution inferred for a population of 236 high-confidence NGC 2264 members, as a function of stellar mass, whose range extends down to ∼0.1 $M_\odot$ and up to ∼1.5 $M_\odot$. These objects have been classified as CTTS, i.e., accreting objects, as opposed to WTTS among the PMS population analyzed so far, based on spectroscopic criteria (H_α EW, H_α width at 10% intensity) and/or photometric criteria (significant UV excess from the CFHT sample, $\alpha_{\rm IRAC}$ value consistent with Class II sources from the data of Teixeira et al. 2012, large variability from the CFHT photometry; see Venuti et al., in prep., for this last point). The accretion parameters for these objects are reported in Table 4. The nominal values of the accretion rates are computed from the photometry corresponding to the median UV excess detected during the CFHT/MegaCam 2-week long monitoring and are estimated to be accurate within a factor of ∼3 typically.

Table 4. UV excess, u-band excess luminosity, $\dot{M}_{\rm acc}$ and $\dot{M}_{\rm acc}$ variability estimates for NGC 2264 accreting members.

Mon-ID	$(u-g)$ exc.	$(u-r)$ exc.[1]	$\log L_u^{\rm exc}/L_\odot$[1]	$\log \dot{M}_{\rm acc}^{(u-g)}$	$\log \dot{M}_{\rm acc}^{(u-r)}$[1]	$\log \dot{M}_{\rm max}/\dot{M}_{\rm med}$[2]	$\log \dot{M}_{\rm med}/\dot{M}_{\rm min}$[3]
Mon-000007	–0.16	–0.65	–1.50	–7.17	–7.22	0.32	
Mon-000011	–0.97	–1.95	–0.88	–7.53	–6.73	0.24	0.19
Mon-000017	0.03	–0.27	–2.14		–8.24*	0.02	
Mon-000028	–1.79	–1.40	–3.38	–8.90	–9.13	0.40	0.59
Mon-000040	–0.46	–0.34	–3.89	–9.24	–9.37	0.20	0.55
Mon-000042	–0.17	–0.01	–5.08	–9.34	–9.48*		
Mon-000053	–0.35	–0.11	–4.31	–9.06	–9.46	0.33	
Mon-000056	0.04	0.01			–8.24*		
Mon-000059	–1.91	–1.11	–3.32	–8.36	–8.91	0.26	0.57
Mon-000063	–0.53	–1.03	–2.56	–8.62	–8.21	0.15	

Notes. [(1)] Value measured at the median luminosity state of the system. [(2,3)] Variability range detected around the median $\dot{M}_{\rm acc}$ level during the 2 week-long *ur* monitoring. If no accretion activity is detected above the detection limit for the object at the minimum/median luminosity level, but some significant accretion is detected at the brightest state, only the upper variability bar is reported (i.e., $\log \dot{M}_{\rm max}/\dot{M}_{\rm med(upper)}$); if the object is a non-detection in accretion, no variability measurement is reported. [(*)] Upper limit. A full version of the Table is available at the CDS. A portion is shown here for guidance regarding its form and content.

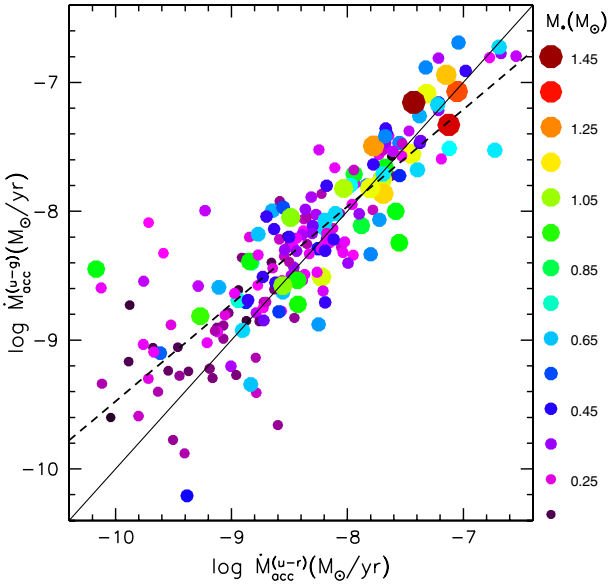

Fig. 15. $\dot{M}_{\rm acc}$ values obtained with the two methods described in the text. $\dot{M}_{\rm acc}$ values on the y-axis are inferred from *ugr* snapshot photometry, while $\dot{M}_{\rm acc}$ values on the x-axis correspond to the median UV excess detected during the *ur* monitoring. Colors and sizes of symbols are scaled according to stellar mass M_*. The solid line marks the equality line; the linear regression to the point distribution is traced as a dashed line.

A confidence detection threshold for $\dot{M}_{\rm acc}$ has been computed by evaluating the average scatter of the WTTS around the reference color sequence and testing the corresponding level of "noise" on the UV excess – and consequently accretion rate – determination. Namely, the magnitude-dependent rms scatter of WTTS around the reference sequence has been measured to compute a (magnitude-dependent) minimum UV excess level to be detected in order to be confident that accretion is indeed the dominant source of excess. This allowed us to trace a conservative boundary separating the objects with an unambiguous $\dot{M}_{\rm acc}$ detection from the objects for which it is not possible, a priori, to evaluate the relevance of spurious contributions (i.e., chromospheric activity) to the apparent UV excess. For the accreting objects for which the actually measured UV excess is less than the corresponding boundary value, only an upper limit at the detection threshold has been reported for $\dot{M}_{\rm acc}$.

Little extensive investigation of mass accretion rates in NGC 2264 has been reported in the literature prior to the survey we are currently performing. Here we refer again to the study of Rebull et al. (2002). Those authors reported $\dot{M}_{\rm acc}$ estimates for about 75 CTTS in the region; their accretion rates are derived from the measured UV excess luminosities by adopting Gullbring et al. (1998)'s relationship to obtain the total $L_{\rm acc}$ values. Results of the comparison of our $\dot{M}_{\rm acc}$ estimates with theirs, for the few tens of sources in common (that cover nonetheless about 2 orders of magnitude in $\dot{M}_{\rm acc}$), are quite consistent with what deduced from the comparison of the measured $L_{\rm UV}^{\rm exc}$ (Fig. 13). When using the same $L_u^{\rm exc}$–$L_{\rm acc}$ calibration, $\dot{M}_{\rm acc}$ estimates from the two studies distribute around the equality line, with an rms scatter of about 0.5 dex, pretty consistent with the average amount of $\dot{M}_{\rm acc}$ variability we detect on week timescales during our monitoring (see Sect. 4.2).

Some important features can be observed on Fig. 16. The $\dot{M}_{\rm acc}$ distribution globally traces a mass-dependent trend, showing an average increase of the mass accretion rates with stellar mass. The existence of such a trend has been investigated from observations over the last decade, albeit with a large uncertainty on the quantitative estimate of the actual relationship, which is likely to be dependent, among other factors, upon the probed stellar mass range and the mean age and age spread across the cluster (cf., e.g., Hartmann et al. 2006 and references therein, Rigliaco et al. 2011, Manara et al. 2012). Scattering of objects at a given stellar mass (see discussion later in the Section) also contributes to increasing the uncertainty on the actual relationship. Another important point to this respect is to understand the actual role played by detection biases in the observed mass-$\dot{M}_{\rm acc}$ trend. As previously discussed, the statistical sample of accretion rates is limited at the lower $\dot{M}_{\rm acc}$ end (Fig. 16), due to the impossibility of an accurate detection below a certain threshold; for this group of objects, only an upper limit to the actual $\dot{M}_{\rm acc}$ value can be inferred. Contrast effects favor the detection of smaller accretion rates on cooler, i.e. lower-mass stars over higher-mass stars (as can be seen in Fig. 16), thus unavoidably introducing a mass dependence. It is thus of interest to assess

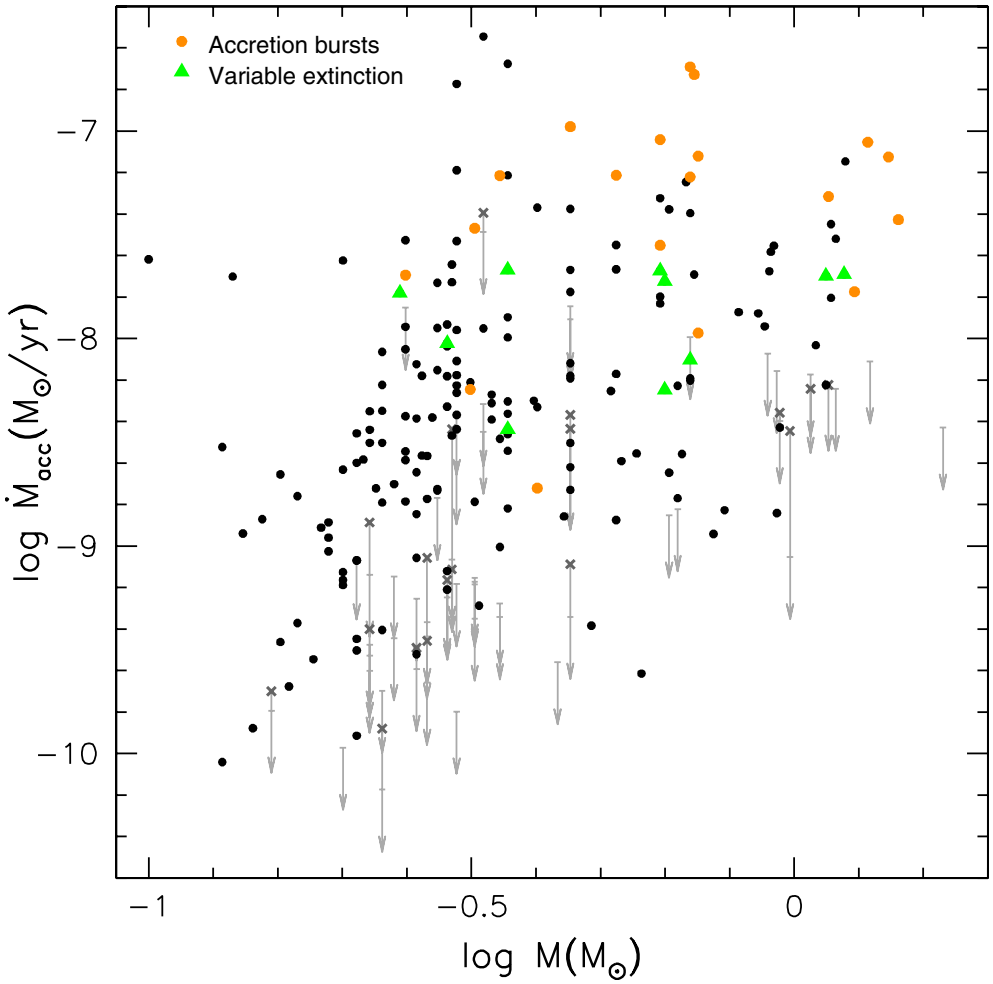

Fig. 16. $\dot{M}_{acc}$ distribution as a function of stellar mass for the population of NGC 2264 accreting members observed at CFHT. Upper limits are shown for those objects that fall below the estimated confidence threshold for accretion detection (see text). For some objects, no significant $\dot{M}_{acc}$ has been detected at the median state of the system, but they do show a significant accretion activity (i.e., above the detection level) at the brightest state; in these cases, an upper limit is placed at the detection threshold, while a cross marks the maximum $\dot{M}_{acc}$ actually detected. Orange dots and green triangles mark two subgroups of objects dominated respectively by stochastic accretion bursts and variable extinction from a rotating inner disk warp (Stauffer et al. 2014).

the degree of disentanglement between the observed mass-$\dot{M}_{acc}$ dependence and the effects of censoring in the data.

A statistical approach that allows us to infer a robust measure of correlation in a given sample, in presence of multiple censoring (both ties, here points at the same x-value but with different y-values, and non-detections, i.e. upper limits), is a generalization of Kendall's τ test for correlation (see Feigelson & Babu 2012; Helsel 2012). The test consists in pairing the data points (measurements and upper limits) in all possible configurations and, for each pair, measuring the slope (positive or negative) of the line connecting the two points. A pair of data points having the same x-value will be counted as an indeterminate relationship, likewise a pair of upper limits; upper limits will uniquely contribute a definite relationship when paired with actual detections at higher y-value. The number of times positive slopes occur is then compared to the number of negative slopes, and their difference weighted against the total number of available pairs. This defines the statistical correlation coefficient, τ. In this picture, upper limits have the effect of lowering the likelihood of a correlation, if this is present in the data, as they introduce a number of indeterminate relationships among the tested pairs. Conversely, no correlation will be found in a pure sample of upper limits, even though these trace a well-defined trend, since the number of pairs with definite relationship will be zero. In the null hypothesis of no correlation, τ is expected to follow a normal distribution centered around zero; by measuring the deviation from zero of the actually found value, in terms of σ, it is thus possible to assess a confidence level for the presence of correlation in a given sample.

The application of this statistical tool to our data allowed us to establish the presence of a correlation ($\tau \sim 0.28$) that appears to hold across the whole mass range studied here with a confidence of more than 6σ. The robustness of this result was tested against a similar search for correlation in randomly generated distributions of $\dot{M}_{acc}$ in the log range $[-10.5, -6.5]$ for the same stellar population with the same individual detection thresholds. The τ distribution inferred from 100 iterations is peaked around $\tau = 0.00$ (no correlation) with a σ of 0.04; this suggests that indeed an intrinsic correlation is observed in our data to a significance of $>6\sigma$. We then inferred a statistical estimate for the slope following the approach of Akritas-Theil-Sen nonparametric regression (see Feigelson & Babu 2012):

1. we derived a first guess for the slope from a least-squares fit to the data distribution and explored a range of ±0.5 around this first estimate with a step of 0.005;

2. for each value x, we subtracted the xM_* trend from the initial $\dot{M}_{\rm acc}$ distribution and repeated the Kendall's τ computation procedure on the distribution of residues thus inferred.

The best fitting trend is the one that, subtracted to the point distribution, produces $\tau = 0$, while an error bar can be inferred corresponding to the interval of values that produce $\tau < |\sigma|$. We applied this procedure to both the mass-$\dot{M}_{\rm acc}$ distribution inferred from the $u-r$ excess distribution (see discussion around Eq. (9)) and the one inferred from the $u-g$ excess distribution (see discussion around Eq. (8)), obtaining respectively:

$$\dot{M}_{\rm acc} \propto M_*^{1.5\pm0.2} \quad (15)$$

$$\dot{M}_{\rm acc} \propto M_*^{1.3\pm0.2}. \quad (16)$$

The two trends are consistent within 1σ; the smaller exponent in Eq. (16) compared to Eq. (15) may reflect the small, mass-dependent offset between the $\dot{M}_{\rm acc}$ distributions inferred from the two methods (cf. Fig. 15). A slope of 1.7 ± 0.2, instead of the estimate in Eq. (15), would be inferred if we converted $u-r$ excesses to $L_{\rm acc}$ values following Gullbring et al. (1998). The two estimates are still consistent within 1σ; this comparison illustrates that a (small) range in values around the true slope may be induced by external factors such as the $L_u^{\rm exc}$–$L_{\rm acc}$ conversion.

The analysis of correlation described above refers to the homogeneous sample of Fig. 16 as a whole. While the relationship we infer seems to be robust across the whole sample, this likely provides a general, average information on the global trend of $\dot{M}_{\rm acc}$ with mass, not a punctual description of the trend. We notice, for instance, that little mass dependence is observed in the upper envelope of the $\dot{M}_{\rm acc}$ distribution above $M_* \sim 0.25\ M_\odot$. We attempted a more detailed investigation of the observed $\dot{M}_{\rm acc}$ vs. M_* relationship by probing separately two different, similarly populated mass bins, $M_* \leq 0.3\ M_\odot$ and $M_* > 0.3\ M_\odot$. In both subgroups, we found some evidence of correlation, albeit with different values and significance levels: a correlation with a slope of 3.3 ± 0.7 was inferred, to the 4σ level, in the lower-mass group, while a correlation with a slope of 0.9 ± 0.4 was obtained for the higher-mass group with a significance of 2.4σ. These results might suggest that the dependence of $\dot{M}_{\rm acc}$ on M_* is not uniform across the whole M_*–$\dot{M}_{\rm acc}$ range, but shallower at higher masses and higher accretion rates; on the other hand, a closer investigation of the M_*–$\dot{M}_{\rm acc}$ relationship from separate, small subsamples is necessarily more uncertain than the assessment of a general correlation trend observed across the whole sample.

Another remarkable feature on Fig. 16 is the large dispersion in the $\dot{M}_{\rm acc}$ values observed at each stellar mass, covering a range of ~2 to 3 dex. Similar results have been inferred from previous statistical surveys of accretion in a given cluster (see, e.g., the recent studies of Rigliaco et al. 2011 on σ Ori and of Manara et al. 2012 on the ONC). This implies that only the average behavior of the actual trend of $\dot{M}_{\rm acc}$ with M_* can be deduced, and suggests that different accretion regimes may co-exist within the same young stellar population. To this respect, we highlight in Fig. 16 the accretion properties of two, morphologically well-distinct, classes of YSOs in NGC 2264, both actively accreting. The first corresponds to the newly identified (Stauffer et al. 2014) class of objects whose light curves are dominated by accretion bursts. The second class includes objects whose light curves show periodic or quasi-periodic flux dips likely resulting from a rotating inner disk warp partly occulting the stellar emission (Bouvier et al. 2007a; Alencar et al. 2010). As can be seen in Fig. 16, both classes of objects show a level of accretion on average larger than the mean level of accretion activity detected across the population of NGC 2264; however, the two classes are well distinguished, with the first showing a mean accretion rate about three times larger than the second.

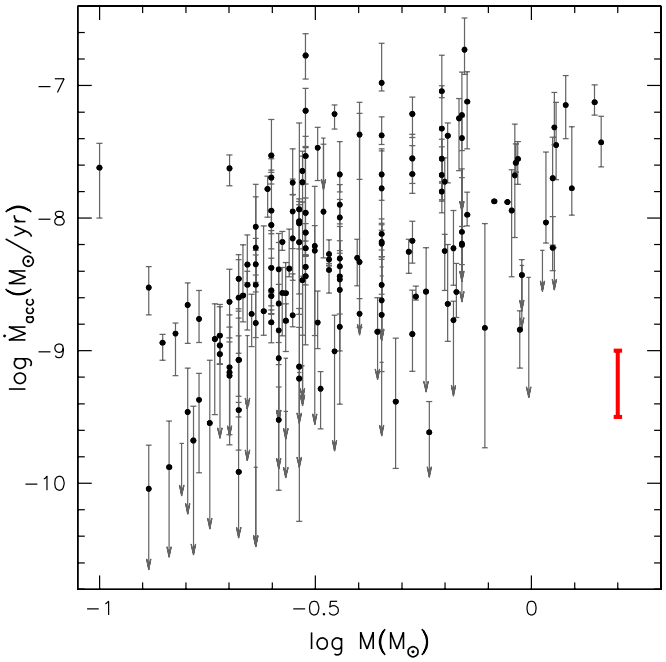

Fig. 17. Variability of the mass accretion rates observed for NGC 2264 members over the 2-week long CFHT monitoring. Black dots correspond to the median $\dot{M}_{\rm acc}$ measured for each object (see Fig. 16). For each object, the relevant variability bar is displayed, corresponding to the difference between the maximum and the minimum $\dot{M}_{\rm acc}$ detected during the monitoring. A typical variability bar is shown in red.

4.2. Mid-term $\dot{M}_{acc}$ variability

The scatter in Fig. 16 could in principle partly arise from the huge photometric variability exhibited by T Tauri stars, both on short-term (hours) and mid-term (days) timescales (e.g., Ménard & Bertout 1999). Short-term variability can affect the $\dot{M}_{\rm acc}$ estimates inferred for single objects, but its contribution is likely negligible for our purposes (i.e., for a statistical mapping of accretion throughout the population of the cluster). On the other hand, mid-term variability, comprising the geometric effects linked with stellar rotation and the intrinsic accretion variability (timescales relevant for hot spots), might effectively blur the $\dot{M}_{\rm acc}$ distribution inferred from the mapping of the region, since each object is observed at an arbitrary phase.

In order to assess the contribution of mid-term variability to the $\dot{M}_{\rm acc}$ spread, we probed the variability of the detected $\dot{M}_{\rm acc}$, over timescales relevant to stellar rotation, by measuring the UV excess and correspondingly computing the mass accretion rate from each observing epoch during the CFHT u-band and r-band monitoring. On average, 16–17 points distributed over the 2-week long survey have been considered to probe variability. This procedure allowed us to robustly associate a range of variability to the individual average $\dot{M}_{\rm acc}$, inferred for each object as described in Sect. 4.1.

Figure 17 shows the results inferred from this analysis; each variability bar encompasses all values of $\dot{M}_{\rm acc}$ detected for the corresponding object during the monitoring (i.e., it traces the

Table 5. Average variability in $\dot{M}_{\rm acc}$ displayed, on week timescales, by different, mass-sorted, groups of accreting members of NGC 2264.

M_* **group** ($M_\odot$) :	**<0.4**	**0.4–1**	**>1**
$\langle M_* \rangle$ ($M_\odot$)	0.26	0.60	1.20
$\langle \log(\dot{M}_{\rm acc}^{\rm med}) \rangle$ ($M_\odot$/yr)	–8.36	–7.92	–7.58
$\langle \Delta\log \dot{M}_{\rm acc}{}^{1} \rangle$ (dex)	0.50	0.46	0.52
$\langle \log \frac{\rm bar_+}{\rm bar_-}{}^{2} \rangle$	–0.1 ± 0.3	0.0 ± 0.3	0.1 ± 0.2

Notes. Estimates only take into account objects for which a detection, and not an upper limit, is available for the lowest $\dot{M}_{\rm acc}$ phase. (1) $\log \dot{M}_{\rm acc}^{\rm max} - \log \dot{M}_{\rm acc}^{\rm min}$. (2) Index probing the symmetry of the variability bars around $\dot{M}_{\rm acc}^{\rm med}$: $\rm bar_+ = \log \dot{M}_{\rm acc}^{\rm max} - \log \dot{M}_{\rm acc}^{\rm med}$; $\rm bar_- = \log \dot{M}_{\rm acc}^{\rm med} - \log \dot{M}_{\rm acc}^{\rm min}$.

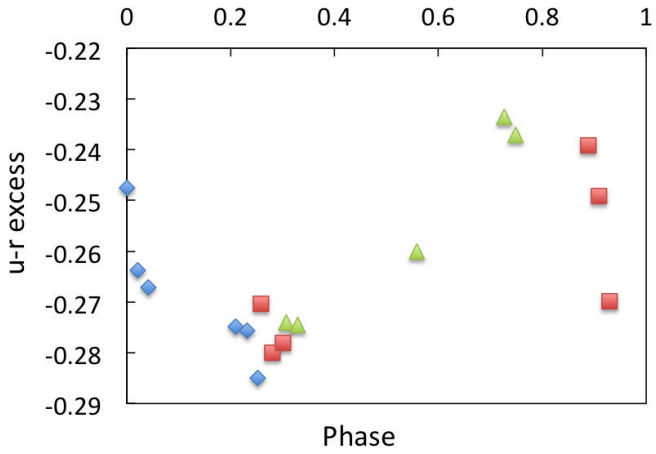

Fig. 18. Phased diagram of the variability of the UV excess monitored over a baseline varying from a few hours to a few rotational cycles for an NGC 2264 accreting member ($M_* = 1.13\ M_\odot$; $\dot{M}_{\rm acc} = 5.98 \times 10^{-9}\ M_\odot$/yr; $P_{\rm rot} = 4.767$ days, from Affer et al. 2013). The phase is computed starting from the epoch of the first measurement; the UV excess at each epoch is computed as described in Eq. (9). Different symbols correspond to different rotational cycles.

difference between the highest and the lowest detected $\dot{M}_{\rm acc}$). Objects for which only an upper limit to the average $\dot{M}_{\rm acc}$ had been derived have not been considered for this step of the analysis; for objects whose nominal $\dot{M}_{\rm acc}$ value fall below the detection threshold (Sect. 4.1) at certain epochs, an upper limit to the lowest apparent $\dot{M}_{\rm acc}$ has been drawn.

As can be observed in Fig. 17, variability properties are not uniform across the sample. No clear trends emerge with stellar mass or mass accretion rates; the geometry of individual systems might have a more important contribution in determining the apparent $\dot{M}_{\rm acc}$ variability on week timescales, as suggested by the very few points on the diagram, maybe observed in a pole-on configuration, that show a negligible variation in the measured mass accretion rate. The (a)symmetry of individual bars, albeit potentially affected by the specific temporal sampling, may reflect the way accretion proceeds onto the central object, as well as the dominant features of the system: a strongly asymmetric bar with the median $\dot{M}_{\rm acc}$ point close to the lower end can identify an object showing sudden, short-lived accretion bursts, while the opposite case well describes a system whose typical luminosity state is interspersed by short duration flux dips. These properties are indeed observed for some of the objects marked in Fig. 16.

The detected amplitudes of variability in $\dot{M}_{\rm acc}$ range from small fractions to ∼1 order of magnitude. In order to better visualize the average effects, we subdivided the sample of objects in Fig. 17 in three broad mass intervals ($M_* < 0.4\ M_\odot$; $0.4\ M_\odot \leq M_* \leq 1\ M_\odot$; $M_* > 1\ M_\odot$) and for each of them computed the mean $\dot{M}_{\rm acc}$ and amplitude of variability. These results are reported in Table 5, while a typical variability bar is represented in red in the lower right part of Fig. 17. On average, a variability of ∼0.5 dex in $\dot{M}_{\rm acc}$ is observed over a couple of weeks (which correspond to ∼2–3 rotational cycles for most of the objects; see Affer et al. 2013), against a typical $\dot{M}_{\rm acc}$ spread of ∼2 dex. This comparison clearly shows that the observed $\dot{M}_{\rm acc}$ spread at each mass is significantly larger than what can be accounted for by variability on week timescales, be it intrinsic (non-steady accretion) or geometric (rotational modulation).

4.3. Accretion variability: intrinsic vs. modulated

As discussed in Sect. 4.2 (see also Sect. 5.2), an average variability of ∼0.5 dex is derived when monitoring the observed $\dot{M}_{\rm acc}$ for individual objects over days-to-weeks timescales. This amount of variability is expected to incorporate both the intrinsic variability associated with the accretion process and the geometric effect of varying accretion shock projection along the line of sight as the star rotates.

An illustration of this is shown in Fig. 18. The underlying sinusoidal profile describes the geometric modulation of the accretion spot linked with stellar rotation, which is reflected in the measured UV excess and, consequently, in the value of $\dot{M}_{\rm acc}$ inferred at a given phase. Two additional effects contribute to the variability picture: the intrinsic variability of accretion on days timescales, reflected in the variation of the UV excess measured at the same phase in two different cycles, and the intrinsic variability of accretion on hours timescales, reflected in the rms variation of the UV excess measured within the same rotational cycle around a given phase (i.e., measurements obtained a few hours apart during the same night).

In order to probe the relative significance of these different contributions to the monitored $\dot{M}_{\rm acc}$ variability and characterize the intrinsic accretion variability over hours-to-days timescales, we selected a subsample of 35 accreting members of NGC 2264, subject to the following conditions:

1. being an actual detection in $\dot{M}_{\rm acc}$ (i.e., not an upper limit);
2. displaying a detectable periodicity, known from the study of Affer et al. (2013);
3. having rotational period small enough to be able to detect at least a partial superposition of different cycles in the phased diagram.

Affer et al. (2013)'s study of rotation in NGC 2264 is based on a 23 day-long optical monitoring of the star-forming region performed with the CoRoT satellite in March 2008. Accreting stars with detected rotational modulation amount to about 16% of the CTTS in our sample. These are distributed over the whole $\dot{M}_{\rm acc}$ range at all masses in Fig. 16, except at the lowest $\dot{M}_{\rm acc}$ regimes ($\lesssim 5\times10^{-10}\ M_\odot$/yr), typically populated by objects fainter than 17 in r and hence not attainable with CoRoT.

For each of these objects selected as described above, we phased the light curve of the UV excess and measured independently the average rms variation of detections obtained within the same observing night and the average rms variation of the

average UV excess measured in a given phase bin of 0.05 at different rotational cycles.

The average peak-to-peak variation in the color excess throughout the sample amounts to ~0.47 mag, which corresponds to a variation of ~0.52 dex in $\dot{M}_{\rm acc}$, consistent with what we found in Sect. 4.2. 50% of the objects show an average intrinsic rms variation of <0.1 mag at a given phase from cycle to cycle (80% at ≤0.15 mag and 90% at ≤0.25 mag). Hence, on average a ratio of ~0.25 between the intrinsic rms variation on day timescales and the peak-to-peak variation can be inferred. The average rms variation on hour timescales is smaller, amounting to ≤0.05 mag. On the assumption that the two contributions (accretion variability on hours vs. days timescales) are mutually independent, we conclude that these two sources of variability together contribute on average just ~28% of the observed peak-to-peak variation in the UV excess. For a typical $\Delta\dot{M}_{\rm acc}$ of 0.52 dex, intrinsic accretion variability is thus expected to contribute for about 0.15 dex, while a major contribution arises from the geometric modulation of the accretion shock.

Interestingly, in the picture of modulation-dominated variability and assuming a homogeneous phase sampling, we would expect to statistically observe symmetric variability bars around the average value of $\dot{M}_{\rm acc}$; this is indeed consistent with the results reported in Sect. 4.2 and synthetized in Table 5.

5. Discussion

Accretion is a key ingredient in early stellar evolution: it regulates the star-disk interaction over the first few million years, with a major impact on the dynamical evolution of both the central object and the protoplanetary disk. Inferring a complete picture of accretion within large, well-characterized samples of young stars allows us to explore the accretion properties over a variety of parameters (e.g., stellar mass, age, disk properties), and hence represents a crucial issue for understanding how accretion evolves on an individual vs. statistical basis.

5.1. The M_* – $\dot{M}_{acc}$ relationship

Understanding what relationship links disk accretion rates and the mass of central objects has been a major focus for studies of accretion in YSOs over the last years. A prime motivation for this lies in that the M_*–$\dot{M}_{\rm acc}$ relationship likely reflects the actual mechanisms governing the accretion process.

Hartmann et al. (2006) reviewed a number of different mechanisms which may be relevant to disk accretion and its variability and to the M_*–$\dot{M}_{\rm acc}$ relationship. As noted by those authors, several unrelated mechanisms may contribute to establishing this relationship, and those mechanisms may act differently in different mass regimes. A number of previous studies have attempted to better understand the mass dependence of the M_*–$\dot{M}_{\rm acc}$ relationship (Vorobyov & Basu 2008; Rigliaco et al. 2011; Fang et al. 2013); these analyses suggest a diminution of the steepness of the $\dot{M}_{\rm acc}$–M_* dependence as M_* increases from a few tenths or hundredths of solar mass to a few solar masses. This is consistent with what we observe here for NGC 2264; on the other hand, the overall trend observed in the subsolar-to-solar mass regimes appears to be significantly shallower than that observed in the intermediate (1–10 $M_\odot$) mass regime (Ercolano et al. 2014).

In this study, we examined the distribution of mass accretion rates over mass for a homogeneous population of 236 confirmed, accreting members in NGC 2264, covering the mass range ~0.1–1.5 $M_\odot$. We inferred the presence of a correlation between $\dot{M}_{\rm acc}$ and M_* and further showed that this result is not significantly affected by a mass-dependence in the $\dot{M}_{\rm acc}$ detection limits. The same fraction of accreting stars over the total young population (~40%) is roughly observed at lower (<0.4 $M_\odot$) and higher (>1 $M_\odot$) masses; unless the true fraction of accreting objects is considerably larger at higher masses than at lower masses, this attests that no significant selection biases towards lower-mass objects affect our accretion survey. Hence, we obtain $\dot{M}_{\rm acc} \propto M_*^{\alpha}$, with $\alpha \sim 1.4 \pm 0.3$ (Eqs. (15)–(16)). This exponent is smaller than the $\alpha = 2$ dependence inferred by Muzerolle et al. (2003) over the mass range 0.04–1 $M_\odot$; the trend they obtained, however, is strongly influenced by the substellar component of the PMS population, which is not probed in our study. Indeed, results similar to Muzerolle et al.'s findings have been subsequently inferred from studies probing a comparable mass range in the substellar down to planetary mass regimes (e.g., Mohanty et al. 2005 for a composite sample of members from different star-forming regions, Natta et al. 2006 in ρ Ohiuchi, Herczeg & Hillenbrand 2008 in Taurus, Alcalá et al. 2014 in Lupus). On the other hand, studies addressing more specifically the T Tauri mass regime have recently proposed somewhat lower estimates for the quantitative dependence of $\dot{M}_{\rm acc}$ on M_*. Rigliaco et al. (2011) probed a mass range, in σ Ori, similar to the one investigated in Muzerolle et al.'s study (0.06–1 $M_\odot$) and inferred a value of $\alpha = 1.6 \pm 0.4$. Barentsen et al. (2011) studied a population of 158 accreting stars, covering the mass range 0.2–2 $M_\odot$, in IC 1396, and inferred a M_*–$\dot{M}_{\rm acc}$ relationship with $\alpha = 1.1 \pm 0.2$. All these results are quite consistent with the estimate of slope here inferred. The range of α from these studies may in part reflect the inhomogeneous nature of the methodologies and stellar samples; however, taken at face value, the results suggest a possible dependence of α on mass, with the higher mass regime showing a shallower slope.

5.2. Accretion variability: what contribution to the $\dot{M}_{acc}$ spread at a given mass?

A ubiquitous result of the studies of $\dot{M}_{\rm acc}$ distributions for large samples of young stars is the significant spread observed in $\dot{M}_{\rm acc}$ at a given mass, enveloping the average trend over 2 to 3 orders of magnitude. CTTS are known to display a strong variability over different timescales; this takes contribution both from geometric effects linked with the rotational modulation of surface starspots and disk features (Herbst et al. 1994) and from the intrinsic variability of the accretion process. Variability could thus be partly responsible for the observed scatter.

In order to probe this effect, we monitored the UV excess and $\dot{M}_{\rm acc}$ variability for about 150 NGC 2264 accreting members over two full weeks, with typically 16–17 epochs for each object; this allowed us to show that variability on week timescales determines on average a variation of the detected $\dot{M}_{\rm acc}$ over ~0.5 dex, significantly smaller than the extent of the average $\dot{M}_{\rm acc}$ scatter.

This study complements the results inferred from recent studies that explored the variability in mass accretion rates on longer timescales. Nguyen et al. (2009) analyzed the $\dot{M}_{\rm acc}$ variability of a sample of 40 members in Taurus-Auriga and Chamaeleon I, from multi-epoch optical spectra distributed over ~10 months, with typically 4 epochs per object on a baseline varying from hours to months. They probed the accretion properties from Hα 10% width and Ca II flux and inferred a

median variability estimate amounting respectively to 0.65 dex and 0.35 dex. Fang et al. (2013) probed the $\dot{M}_{\rm acc}$ variability of several tens of members in L1641, monitored on timescales of 1, 10 and 22 months; measuring the amount of accretion from the full width of the H_α line at 10% intensity, the authors inferred a typical $\dot{M}_{\rm acc}$ variability of ~0.6 dex.

A recent spectroscopic survey of the $\dot{M}_{\rm acc}$ variability in T Tauri and Herbig Ae stars, addressing shorter ($\lesssim$hour to days) timescales, has been performed by Costigan et al. (2014). The authors probed accretion properties and their variability from H_α EW measurements for a sample of 14 objects; targets have been monitored over $\lesssim$1 h blocks, in some cases iterated within a single night, and repeated over a few nights. Combining the results of this short-term variability monitoring with multi-year information for a few objects, as well as with results from different surveys, the authors found that the dominant contribution to the observed variability in $\dot{M}_{\rm acc}$ arises from the days timescale, with a spread in accretion rates ranging from 0.04 to 0.4 dex.

All these results robustly show that variability on day-to-month timescales does not impact significantly on the large spread observed in $\dot{M}_{\rm acc}$ around the average $\dot{M}_{\rm acc}$–M_* trend; hence, the spread is real and possibly linked to the different evolutionary stages of individual objects (see Sect. 5.3). Additionally, a strong overlap in the age distributions for the populations of accreting (CTTS) and non-accreting (WTTS) members seems to hold; modulo the issue of an accurate age determination for young stars, this suggests that an intrinsically large range in $\dot{M}_{\rm acc}$ exists at a given mass and age, which may reflect various other parameters (like, e.g., the properties of the stellar magnetic field or the initial mass of the disk).

Remarkably, the order-of-magnitude estimates for the $\dot{M}_{\rm acc}$ variability inferred on day-to-week timescales (this study; Costigan et al. 2014) and on month-to-year timescales (Nguyen et al. 2009; Fang et al. 2013) are quite consistent; this suggests that the same mechanisms dominate variability over these baselines, with a major contribution arising from the mid-term variability component. This picture is supported by the results of the comparison, shown in Fig. 13, between the $L_{\rm UV}^{\rm exc}$ measurements obtained from ours and Rebull et al. (2002)'s survey of NGC 2264, respectively; what we observe in this case is that, indeed, UV excess luminosities measured at the two epochs are globally consistent, with an rms scatter, about the equality line, of the same order of magnitude as the average amount of variability detected during our 2 week-long CFHT monitoring.

5.3. What is the origin of the intra-cluster spread in $\dot{M}_{acc}$?

A star-to-star variety in the evolutionary stage and evolutionary scenario may provide an important contribution to the interpretation of the large range of accretion properties observed within the region. The cluster shows a hierarchical structure (see Dahm 2008 and references therein), with regions of active, current star formation embedded in a more widespread population of somewhat older stars (Sung et al. 2009). Several episodes of star formation may have occurred, as proposed by Adams et al. (1983). Despite the uncertainty on a quantitative estimate, there is a general consensus about an age spread of up to several Myr within the population of NGC 2264. It is thus of interest to attempt a characterization of the accretion properties relative to age indicators and disk evolutionary stages.

Looking at how points distribute on the HR diagram of the cluster (Fig. 12) and comparing this to model isochrones

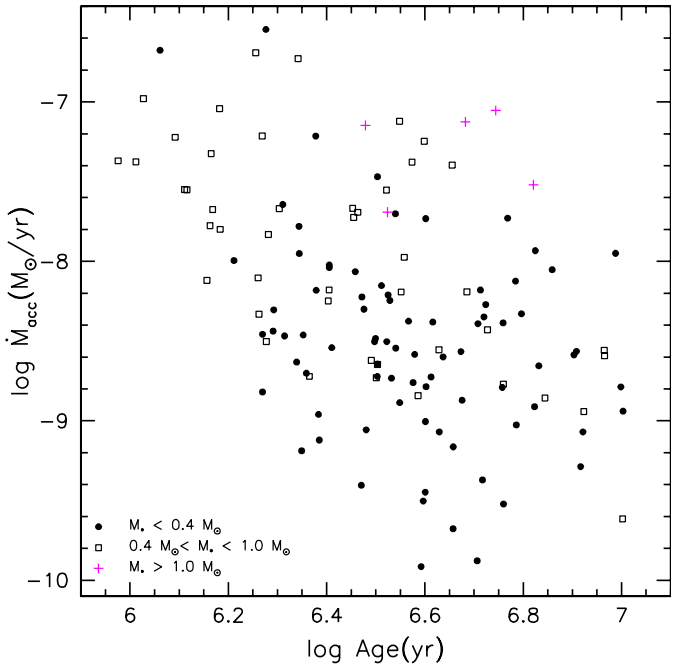

Fig. 19. Evolution of the accretion properties as a function of stellar age for NGC 2264 accreting members. Three different mass groups are compared: $M_* < 0.4\,M_\odot$ (filled circles); $0.4\,M_\odot \leq M_* \leq 1\,M_\odot$ (open squares); $M_* > 1\,M_\odot$ (crosses).

provides a debated indication on nominal ages. In order to probe the evolution of accretion properties with stellar age, we inferred an age estimate for each source from isochrone fitting, adopting the models of Siess et al. (2000). The results for accreting sources are displayed vs. the $\dot{M}_{\rm acc}$ estimates in Fig. 19. Only objects which are actual detections in $\dot{M}_{\rm acc}$ and whose age estimate from models is between ~10^6 yr and 10^7 yr have been retained for the comparison.

An overall decreasing trend of the average $\dot{M}_{\rm acc}$ with increasing stellar ages is traced in Fig. 19, consistently with previous results regarding the average evolution of accretion with stellar age (e.g. Hartmann et al. 1998; Sicilia-Aguilar et al. 2010; Manara et al. 2012). The anticorrelation trend is well described in the $M_* < 1\,M_\odot$ regime, reaching a significance of over 5σ according to a Spearman's rank order test (Press et al. 1992). A linear regression to this group of objects yields

$$\dot{M}_{\rm acc} \propto t^{-\eta},\ \eta \simeq 1.51, \tag{17}$$

quite consistent with the $\eta = 1.5$ estimate inferred by Hartmann et al. (1998). Little information can be achieved on the accretion properties of the higher-mass group ($M_* > 1\,M_\odot$) from our UV excess analysis.

The actual $\dot{M}_{\rm acc}$-age relationship may vary depending on the mass range probed, as suggested by the looser correlation that can be inferred from the least massive group of objects ($M_* < 0.4\,M_\odot$) compared to the 0.4–1 $M_\odot$ group. This might reflect truly different evolutionary timescales, but also be affected by uncertainties on the age estimates inferred from models. Indeed, a clear-cut decreasing trend is observed on the lower-left envelope of the data point distribution in Fig. 19, with the youngest group being among the most luminous sources in the sample. While limits on the detection of small accretion rates in luminous stars might somewhat affect the observed trend, a more significant bias here is likely introduced by the model age

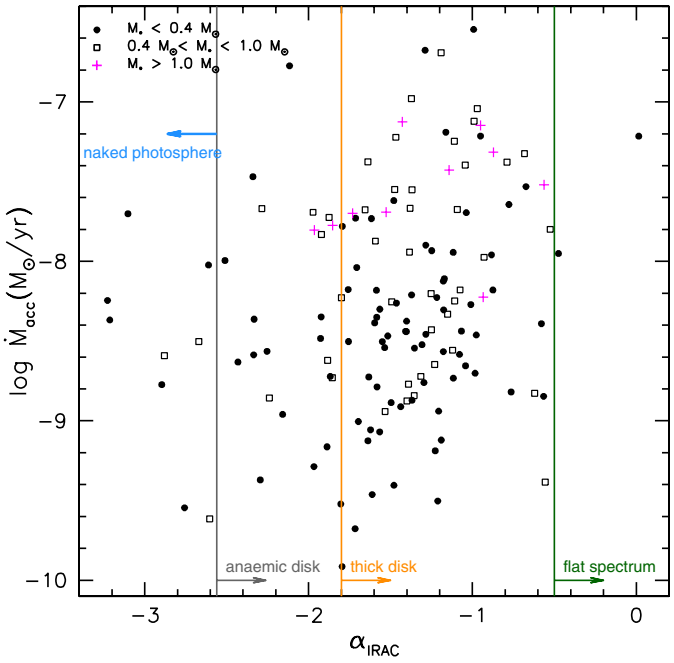

Fig. 20. $\dot{M}_{\rm acc}$–$\alpha_{\rm IRAC}$ relationship. The $\alpha_{\rm IRAC}$-based disk morphology classification follows Table 2 of Teixeira et al. (2012). Three different mass groups are compared: $M_* < 0.4\,M_\odot$ (filled circles); $0.4\,M_\odot \leq M_* \leq 1\,M_\odot$ (open squares); $M_* > 1\,M_\odot$ (crosses).

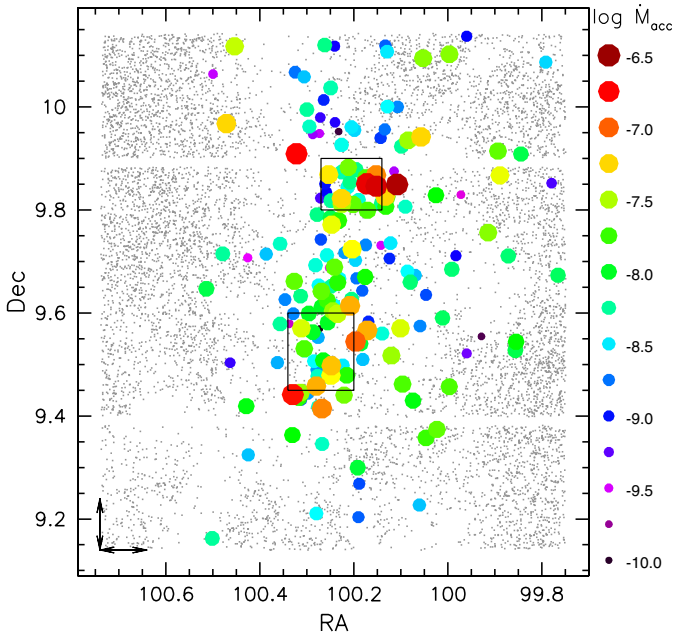

Fig. 21. Spatial mapping of accretion properties in NGC 2264. Small gray dots indicate the distribution of field stars, large dots indicate accreting cluster members. Only objects with an actual $\dot{M}_{\rm acc}$ detection are shown. Symbol colors and sizes are scaled according to the value of $\dot{M}_{\rm acc}$. The black boxes mark the regions of maximum stellar density in the cluster (from Lamm et al. 2004). Double arrows mark a physical distance of 1.5 parsecs.

estimates. We notice that lower-mass stars appear to be systematically older than higher-mass stars, based on model ages. If this is not a physical effect, but rather an artifact driven by systematics in the model, the actual anticorrelation trend that can be derived from Fig. 19 is, at best, doubtful.

The reliability of such time evolution analyses of accretion is subject to the assumption that the interpretation of the luminosity spread for a given PMS population on the HR diagram in terms of a true age spread is overall correct. However, this interpretation is subject to a severe controversy. Indeed, recent studies have questioned the accuracy of individual age estimates from the stellar luminosity. Baraffe et al. (2009) claimed that the luminosity spread observed on the HR diagram of a given star-forming region does not correspond to an actual age spread, but merely reflects the individual episodic accretion history, whose dynamics may mimic an age spread of up to a few Myr for coeval stars. While no consensus has obviously been achieved on this issue, an intrinsic age spread on the order of Myr, if present, is likely to be reflected in different properties of the region, such as the spatial distribution of members. This point is discussed in Sect. 5.4.

As mentioned in Sect. 3.1, information on the circumstellar disk morphology, hence on the evolutionary status, is conveyed by the mid-IR slope of the SED of the system. In Fig. 20, the accretion properties for three different mass groups of members are compared to the $\alpha_{\rm IRAC}$ classification from Teixeira et al. (2012). Smaller values of $\alpha_{\rm IRAC}$ correspond to more evolved disks; the average accretion rates decrease as disks become more evolved, albeit within a significant spread for each mass group.

These comparisons show that several parameters, beyond stellar mass, regulate the accretion evolution of individual systems and eventually contribute to shape the complex picture of a star-forming region such as we may infer from an extensive accretion survey.

5.4. A spatial mapping of accretion properties in NGC 2264

Characterizing the spatial distribution of accreting members according to their accretion properties is a useful tool to investigate the evolution dynamics of the region.

Figure 21 shows a spatial mapping of accretion in NGC 2264. Most accretors are projected onto the cluster; a part of the population of accreting or mildly accreting members are instead located on the peripheral regions. Some interesting features can be observed: the strongest accretors tend to be concentrated around the two known active sites of star formation within the cloud, a few parsecs apart, while the population of more moderate accretors tends to be more evenly distributed throughout the whole cluster. The halo of members is spread over a few parsecs around the star-forming sites.

This differential distribution of mass accretion rates may be the product of a sequential star formation process: the youngest stars, likely the most actively accreting, are indeed expected to be found close to their birth sites, while dynamical evolution over a few Myr (the average age of the cluster) can explain displacements up to a few parsecs relative to the original location where stars were formed. If this is the case, the distribution of $\dot{M}_{\rm acc}$ also reflects the presence of an intrinsic age spread within the region, hence corroborating the interpretation in terms of a time evolution over different ages.

We attempted to pursue further this scenario by investigating the spatial distributions of distinct, equal-sized groups of objects at the two age extremities in Fig. 19. If our interpretation is correct, we would expect the presumed younger member group to be spatially more compact than the older one. A statistical method to probe spatial compactness is the minimum spanning tree (MST) method (Prim 1957). This (see also Allison et al. 2009; Parker et al. 2011) consists in computing the minimum

path-length required to connect all points of a given sample in a network of direct point-to-point links with no closed loops. Shorter MST lengths will thus identify, to a certain degree of confidence, more compact populations. The significance of the result can be tested by randomly selecting two groups of objects of the same size and belonging to the same population as the two groups of objects under study, and computing the MST of the first random group, the MST of the second random group and the ratio between the two. The iteration of this procedure allows us to reconstruct the normal distribution of MST_1/MST_2 values when no significant difference exists between the spatial distributions of two given groups of objects selected among the population of interest.

For our population of accreting objects, sampled in random groups of 20 to 30 elements, we derived a normal distribution of MST ratios centered on 1.0 (homogeneous spatial distribution) with a σ of 0.2. Little evidence for an actual difference in the spatial distributions of "younger" vs. "older" members in Fig. 19 can be inferred when comparing the result of their MST test to this distribution. Somewhat smaller values than the mean of 1.0 are obtained from the $MST_{younger}/MST_{older}$ ratio, oscillating around a significance of 1.5σ that this difference is truly meaningful. This might suggest that the younger population is to some extent more compact than the older population; however, no conclusive evidence can be drawn from this analysis, and the small statistics at lower and higher ages in Fig. 19 yields some dependence of the specific result on the specific selection of objects for the two groups. On the other hand, the complexity of the cluster, with its clumpy structure, the presence of at least two separate poles of star formation, the association with several massive OB stars, intrinsically translates to a non-linearity in the cluster evolution and, consequently, to a certain degree of ambiguity in the information provided by the spatial distribution of more evolved members.

6. Conclusions

We have performed an extensive photometric investigation of accretion in the young open cluster NGC 2264. Our sample, homogeneous in the dataset and in the characterization of individual properties, includes ~750 members, spanning in mass the range ~0.1–2 $M_\odot$; of these, about 40% show ongoing accretion. Accretion activity has been traced from the detection and monitoring of the *u*-band excess emission relative to non-accreting young stars; we showed that this excess is a reliable indicator of accretion, matching the properties observed at different wavelengths (H_α emission, IR excess), with the advantage of providing alone a direct proxy to the accretion luminosity.

We re-examined the membership of the cluster from an accretion-related perspective, exploring a wider area around the spatial distribution of currently known members within the star-forming region. This allowed us to expand the census of accreting members, with the identification of 50 new candidates based on their accretion signatures at short wavelengths. We detected UV color excess ranging from a few tenths of a mag to ~3 mag, with a sensitivity of ~0.2 mag deriving from the definition of the reference color locus from the properties of non-accreting young stars. Following a new empirical prescription for the conversion of the UV excess into accretion luminosity, we inferred a complete picture of accretion in the cluster and monitored its variability over a few rotational cycles. A broad interval of $\dot{M}_{acc}$ values has been inferred within the region, ranging from $\sim 10^{-7}$ to a few $\times 10^{-10}$ $M_\odot$/yr; at any given stellar mass M_*, a large spread in $\dot{M}_{acc}$ values, typically extending over 2 orders of magnitude, is observed.

The average $\dot{M}_{acc}$ shows a statistically significant correlation with M_*; more uncertain is the functional form of this dependence, which in turn appears to be mass-dependent and likely time-evolving, as highlighted by the results inferred from previous studies for various young stellar populations. A statistical slope of 1.4 ± 0.3 for the $\log \dot{M}_{acc}$ over $\log M_*$ relationship is here derived for NGC 2264 in the mass sample probed; while the absence of the lower-mass (<0.1 $M_\odot$) stellar component may contribute to explain this less steep dependence than the value of ~2 proposed in several studies, the large spread of $\dot{M}_{acc}$ values observed at a given mass attests the mere indicative value of such a relationship, which weighs the contributions of several trends as well as of undetected regimes.

Little contribution to the spread in the $\dot{M}_{acc}$ vs. M_* distribution arises from $\dot{M}_{acc}$ variability, which is found to amount to ~0.5 dex on the average, at least on days to months timescales; hence, this spread is physically relevant and provides valuable insight on the complexity of the accretion and evolutionary picture for a given stellar population. A differential distribution of evolutionary stages among members, such as we may deduce from the HR diagram of the cluster and/or from disk evolution tracers (α_{IRAC}), would naturally impact the global accretion picture we may infer for the cluster as a whole. Indeed, $\dot{M}_{acc}$ is shown to anticorrelate with such intrinsic/evolutionary age indicators, although these trends are in turn not exempt from a large amount of scatter. The detected spread in $\dot{M}_{acc}$ may thus reflect the dynamics of cluster evolution and the presence of a non-negligible age spread among its members, be it the result of sequential star formation episodes and/or of a multiplicity of evolutionary patterns. Moreover, a diversity in the accretion regimes at play, from episodic, short-lived accretion bursts to steadier, funnel-flow accretion, may concur to shape the features of different stellar groups and result in a range of observed accretion rates, from the upper envelope of the $\dot{M}_{acc}$ vs. M_* distribution to lower accretion rate regimes.

An important contribution toward the achievement of a complete physical picture of the accretion process is provided by a detailed analysis of the variability properties. Geometric effects constitute an important filter to the effective variability profile for a given system, contributing up to 75%, on the average, of the detected $\dot{M}_{acc}$ variability; however, much information on the underlying physics is conveyed by the specific photometric signatures of this variability, and a comparative analysis over intrinsically different stellar groups may be of remarkable interest to discern different scenarios. This aspect will be fully addressed for the young stellar population of NGC 2264 in a forthcoming paper (Venuti et al., in prep.); this is intended to provide a complete characterization of the accretion process and its impact onto the dynamics of the cluster.

Acknowledgements. We would like to thank Christian Veillet, former director of CFHT, for granting discretionary time to perform the mapping survey in December 2010, and the Terapix center at Institut d'Astrophysique de Paris, and in particular Yannick Mellier, for the prompt processing of the MegaCam images obtained during this run. We also thank Nadine Manset and Jim Thomas at CFHT for efficient run scheduling and data retrieval procedures. We warmly thank Luisa Rebull for retrieving for us the L_{acc} values she derived for her 2002 paper on disk-bearing objects in NGC 2264. We thank Kevin Covey for discussions on SDSS dwarf sequences and Lynne Hillenbrand for discussions on bolometric corrections scales; we also acknowledge useful discussion on the $\dot{M}_{acc}$–M_* relationship with Beate Stelzer. This publication makes use of data products from the Sloan Digital Sky Survey and the Two Micron All Sky Survey. This project was in part supported by the grant ANR 2011 Blanc SIMI5-6 020 01. S.H.P.A. and A.P.S. acknowledge support from CNPq, CAPES and Fapemig.

Appendix A: Accretion-oriented revision of the census of NGC 2264 members: new CTTS candidate members and possible field contaminants

Table A.1. List of new candidate members from the accretion-based census of the population of NGC 2264.

Mon-ID	RA	Dec	Selection criteria	Additional information[1]
Mon-001428	100.19257	9.71302	UV, var I	likely CTTS based on IRAC light curve
Mon-005009	100.54131	9.79834	var II, lc	irregular IRAC/CoRoT light curves
Mon-005278	100.64755	9.43207	UV, var II	IR excess
Mon-005326	100.62129	9.44550	UV	
Mon-005385	100.35425	9.75632	UV, var I	flat IRAC light curve
Mon-005455	100.21510	9.37313	UV	flat IRAC light curve
Mon-005596	100.51573	9.45916	var I	flat IRAC light curve
Mon-005664	100.22703	9.15885	UV	spotted-like CoRoT light curve
Mon-005745	100.51810	9.16134	UV	
Mon-005807	100.28199	9.23241	UV, var I	
Mon-005836	100.37121	9.30430	UV	flat IRAC light curve
Mon-006037*	99.87232	9.72772	var II, lc	spotted-like CoRoT light curve
Mon-006079	99.87132	9.71070	UV, var I, var II	eclipsing binary/very short period binary
Mon-006144	99.92838	9.55441	UV	flat IRAC light curve
Mon-006183	99.97203	9.82939	UV, var II	flat IRAC light curve
Mon-006286	100.12552	9.19233	UV	
Mon-006324	99.95310	9.29308	UV	
Mon-006325	100.06032	9.22705	UV, var II	
Mon-006369	99.87573	9.29094	varI, var II	
Mon-006398	99.81027	9.61444	UV, var II	flat IRAC light curve
Mon-006409	99.81342	9.64136	UV	flat IRAC light curve
Mon-006429	99.79541	9.53839	UV, var I, var II	strong IR excess; IRAC light curve of YSO
Mon-006465	99.85484	9.54391	UV, var I, var II	eclipsing binary
Mon-006491	99.85625	9.52760	UV, var II, lc	IR excess; CoRoT light curve of CTTS
Mon-006498	99.82751	9.39888	UV	flat IRAC light curve
Mon-006515	99.77643	9.66813	UV	
Mon-006873	99.79239	9.15089	var I, var II	
Mon-006902	99.75107	9.23571	var I, var II	
Mon-006930	99.76703	9.27055	var II, lc	likely CTTS based on CoRoT light curve
Mon-006950	99.77920	9.85195	UV, var II	
Mon-006985	99.77939	10.11909	UV, var II	
Mon-006986	99.79149	10.08689	UV, var I, var II, lc	likely CTTS based on CoRoT light curve
Mon-006991	99.84169	10.10648	var II, lc	likely CTTS based on CoRoT light curve; IR excess
Mon-006999	99.86647	10.06352	var I	
Mon-007004	99.85813	10.08544	UV	
Mon-007018	99.97253	10.10931	var I, var II	
Mon-007402	100.62534	9.94183	var I	
Mon-007418	100.57599	10.05188	UV	
Mon-007461	100.24085	10.11788	UV, var II	probable MIPS 24 μm excess
Mon-007496	100.51515	10.08836	var I, var II	
Mon-007845	99.89187	9.40008	UV	
Mon-008139	99.75653	10.07972	UV	
Mon-008140	99.80434	9.61337	UV, var II	
Mon-008141	100.66490	9.67704	UV	
Mon-008142	99.76824	9.69662	UV, var I, var II	
Mon-014132	99.76480	9.27109	var II, lc	AA Tau-type CoRoT light curve; IR excess
Mon-020662	100.21076	10.03841	UV	
Mon-021771	100.51792	9.57561	var I, var II	flat IRAC light curve
Mon-025015	99.96704	9.40013	UV	
Mon-025101	99.85223	9.92528	UV, var II	
Mon-124054	100.39085	9.92262	UV, var I	

Notes. Selection criteria: UV = UV excess; var I = multi-year variability; var II = mid-term variability (i.e., on week timescales); lc = light curve morphology. [(1)] From *Spitzer* IRAC and/or CoRoT monitoring obtained during the CSI 2264 campaign (and/or additional IR photometry), when available. [(*)] WTTS candidate member.

Table A.2. List of NGC 2264 members, with no apparent accretion activity from previous surveys, reclassified as CTTS from this accretion-based census of the population of NGC 2264.

Mon-ID	RA	Dec	Selection criteria	Additional information[1]
Mon-000293	100.25166	9.68758	UV	
Mon-000316	100.23172	9.64025	UV	IR excess; likely CTTS based on IRAC light curve
Mon-000340	100.48304	9.67968	UV	flat IRAC light curve
Mon-000507	100.26089	9.85702	UV	flat IRAC light curve; possible 8 μm excess
Mon-000685	100.18949	9.81950	UV	flat IRAC light curve
Mon-000718	100.26733	9.34567	UV	flat IRAC light curve
Mon-000750	100.32659	9.52487	UV	flat IRAC light curve; possible 8 μm excess
Mon-000823	100.20891	9.95111	UV	
Mon-000914	100.21629	9.63220	UV	very strong IR excess
Mon-000957	100.19014	9.20354	UV	IR excess
Mon-000959	100.18845	9.26850	var	IR excess
Mon-001060	100.12844	10.00076	UV	IR excess; likely CTTS based on IRAC light curve
Mon-001211	99.95979	9.52143	UV	IR excess
Mon-001224	100.06953	9.67295	UV	
Mon-001241	100.14078	9.81216	UV	IR excess; likely CTTS based on IRAC light curve
Mon-001267	100.14299	9.42142	var	strong IR excess; IRAC light curve of YSO
Mon-001280	99.91768	9.30604	UV	strong IR excess
Mon-001576	100.13291	10.11898	UV	strong MIPS 24 μm excess
Mon-001582	100.49939	10.06379	UV	strong IR excess

Notes. Selection criteria: UV = UV excess; var = multi-year variability. [(1)] From *Spitzer*/IRAC monitoring obtained during the CSI 2264 campaign (and/or additional IR photometry), when available.

Table A.3. Objects with questioned membership from the CFHT UV-census.

Mon-ID	RA	Dec	u	g	r	i	Membership criteria
Mon-000003	100.43878	9.78583	20.460	18.204	16.924	16.206	P, X
Mon-000004	100.56094	9.84104	17.808	15.998	15.075	14.594	P, RV
Mon-000025	100.51118	9.97441	18.025	16.134	15.193	14.690	P, RV
Mon-000031	100.55471	9.76763	17.801	16.118	15.307	14.888	P, RV
Mon-000387	100.45535	9.68496	20.530	18.408	17.273	16.681	X
Mon-000414	100.55863	9.59579	18.446	16.440	15.431	14.944	P, RV
Mon-000593*	100.25704	9.35157	17.793	15.822	15.077	14.836	P, RV
Mon-000600*	100.20549	9.98095	22.567	19.684	18.106	17.212	X
Mon-000696*	100.33708	9.57170	20.309	19.512	19.589	18.516	h
Mon-000820	100.48089	9.50528	19.538	17.513	16.490	15.902	X
Mon-000944	100.45795	9.68479	20.258	18.274	17.185	16.629	X
Mon-000946*	100.20165	9.99424	21.252	18.810	17.472	16.715	II
Mon-000966	100.19639	9.30923	17.729	15.882	14.942	14.415	P, RV
Mon-000976	100.43282	9.15588	21.325	19.108	17.798	17.058	X
Mon-000983	100.24170	9.30085	16.047	14.663	14.206	14.042	RV
Mon-000988	100.08816	9.98401	20.823	18.249	16.758	15.930	P, RV
Mon-001043*	100.06439	9.71678	21.746	19.149	17.695	16.854	P, II/III
Mon-001046	99.98493	9.72542	15.811	14.455	14.048	13.881	RV
Mon-001086	99.88986	9.86127	18.279	16.524	15.639	15.144	P, RV
Mon-001192	100.16157	9.36066	17.954	15.866	15.079	14.799	RV
Mon-001207	99.98039	9.98644	21.113	18.345	16.911	16.009	h
Mon-001283*	99.86101	9.51055	21.364	18.750	17.590	17.012	RV
Mon-001289	99.85268	9.37588	16.778	15.082	14.379	14.084	P, RV
Mon-001293	99.89724	9.54233	18.331	16.315	15.239	14.681	P, RV
Mon-001311	99.81513	9.65357	18.014	16.134	15.181	14.684	P, RV
Mon-001393	100.55236	9.98531	17.072	15.373	14.609	14.195	P, RV
Mon-006019*	100.14231	9.42022	19.511	17.507	16.217	15.507	P
Mon-007454	100.12886	10.08013	17.799	16.099	15.494	15.140	P

Notes. Membership criteria, in the literature, for the listed objects: P = photometric member (i.e., located on a cluster sequence in the R vs. $R - I$ diagram); X = X-ray emitter, from Sung et al. (2009); RV = radial velocity member, from Fűrész et al. (2006); h = H_α emission candidate, from Sung et al. (2009); II = Class II object, from Sung et al. (2009); II/III = Class II/III object, from Sung et al. (2009). [(*)] More uncertain cases.

References

Abazajian, K., Adelman-McCarthy, J. K., Agüeros, M. A., et al. 2004, AJ, 128, 502
Abazajian, K. N., Adelman-McCarthy, J. K., Agüeros, M. A., et al. 2009, ApJS, 182, 543
Adams, M. T., Strom, K. M., & Strom, S. E. 1983, ApJS, 53, 893
Affer, L., Micela, G., Favata, F., Flaccomio, E., & Bouvier, J. 2013, MNRAS, 430, 1433
Alcalá, J. M., Natta, A., Manara, C. F., et al. 2014, A&A, 561, A2
Alencar, S. H. P., Teixeira, P. S., Guimarães, M. M., et al. 2010, A&A, 519, A88
Allison, R. J., Goodwin, S. P., Parker, R. J., et al. 2009, MNRAS, 395, 1449
Annis, J., Soares-Santos, M., Strauss, M. A., et al. 2011, ApJ, submitted [arXiv:1111.6619]
Armitage, P. J. 2011, ARA&A, 49, 195
Baraffe, I., Chabrier, G., & Gallardo, J. 2009, ApJ, 702, L27
Barentsen, G., Vink, J. S., Drew, J. E., et al. 2011, MNRAS, 415, 103
Bertin, E. 2011, in Astronomical Data Analysis Software and Systems XX, eds. I. N. Evans, A. Accomazzi, D. J. Mink, & A. H. Rots, ASP Conf. Ser., 442, 435
Bertin, E., & Arnouts, S. 1996, A&AS, 117, 393
Bessell, M. S., Castelli, F., & Plez, B. 1998, A&A, 333, 231
Boulade, O., Charlot, X., Abbon, P., et al. 2003, in SPIE Conf. Ser. 4841, eds. M. Iye, & A. F. M. Moorwood, 72
Bouvier, J., Cabrit, S., Fernandez, M., Martin, E. L., & Matthews, J. M. 1993, A&A, 272, 176
Bouvier, J., Alencar, S. H. P., Boutelier, T., et al. 2007a, A&A, 463, 1017
Bouvier, J., Alencar, S. H. P., Harries, T. J., Johns-Krull, C. M., & Romanova, M. M. 2007b, Protostars and Planets V (Tucson: University of Arizona Press), 479
Calvet, N., & Gullbring, E. 1998, ApJ, 509, 802
Camenzind, M. 1990, in Rev. Mod. Astron., ed. G. Klare, 3, 234
Cauley, P. W., Johns-Krull, C. M., Hamilton, C. M., & Lockhart, K. 2012, ApJ, 756, 68
Cody, A. M., Stauffer, J. R., Micela, G., Baglin, A., & CSI 2264 Team. 2013, Astron. Nachr., 334, 63
Cody, A. M., Stauffer, J., Baglin, A., et al. 2014, AJ, 147, 82
Cohen, M., & Kuhi, L. V. 1979, ApJS, 41, 743
Costigan, G., Vink, J. S., Scholz, A., Ray, T., & Testi, L. 2014, MNRAS, 440, 3444
Covey, K. R., Ivezić, Ž., Schlegel, D., et al. 2007, AJ, 134, 2398
Covey, K. R., Lada, C. J., Román-Zúñiga, C., et al. 2010, ApJ, 722, 971
Dahm, S. E. 2008, in Handbook of Star Forming Regions, Volume I: The Northern Sky USP Monograph Publications, ed. B. Reipurth, 4, 966
Dahm, S. E., & Simon, T. 2005, AJ, 129, 829
Dullemond, C. P., Natta, A., & Testi, L. 2006, ApJ, 645, L69
Ercolano, B., Mayr, D., Owen, J. E., Rosotti, G., & Manara, C. F. 2014, MNRAS
Fang, M., Kim, J. S., van Boekel, R., et al. 2013, ApJS, 207, 5
Feigelson, E. D., & Babu, G. J. 2012, Modern Statistical Methods for Astronomy (Cambridge University Press)
Fűrész, G., Hartmann, L. W., Szentgyorgyi, A. H., et al. 2006, ApJ, 648, 1090
Finlator, K., Ivezić, Ž., Fan, X., et al. 2000, AJ, 120, 2615
Fiorucci, M., & Munari, U. 2003, A&A, 401, 781
Flaccomio, E., Micela, G., & Sciortino, S. 2006, A&A, 455, 903
Fukugita, M., Ichikawa, T., Gunn, J. E., et al. 1996, AJ, 111, 1748
Gillen, E., Aigrain, S., McQuillan, A., et al. 2014, A&A, 562, A50
Guarcello, M. G., Prisinzano, L., Micela, G., et al. 2007, A&A, 462, 245
Gullbring, E., Hartmann, L., Briceno, C., & Calvet, N. 1998, ApJ, 492, 323
Haisch, Jr., K. E., Lada, E. A., & Lada, C. J. 2001, ApJ, 553, L153
Hartmann, L., Calvet, N., Gullbring, E., & D'Alessio, P. 1998, ApJ, 495, 385
Hartmann, L., D'Alessio, P., Calvet, N., & Muzerolle, J. 2006, ApJ, 648, 484
Helsel, D. R. 2012, Statistics for Censored Environmental Data (Wiley)
Herbig, G. H., & Bell, K. R. 1988, Third Catalog of Emission-Line Stars of the Orion Population, eds. G. H. Gerbig, & K. R. Bell, Santa Cruz: Lick Observatory
Herbst, W., Herbst, D. K., Grossman, E. J., & Weinstein, D. 1994, AJ, 108, 1906
Herczeg, G. J., & Hillenbrand, L. A. 2008, ApJ, 681, 594
Hillenbrand, L. A. 2005, STScI Symp. Ser. 19, ed. M. Livio [arXiv:astro-ph/0511083]
Joy, A. H. 1945, ApJ, 102, 168
Königl, A. 1991, ApJ, 370, L39
Kraus, A. L., & Hillenbrand, L. A. 2007, AJ, 134, 2340
Lada, C. J. 1987, in Star Forming Regions, eds. M. Peimbert, & J. Jugaku, IAU Symp., 115, 1
Lada, C. J., Muench, A. A., Luhman, K. L., et al. 2006, AJ, 131, 1574
Lamm, M. H., Bailer-Jones, C. A. L., Mundt, R., Herbst, W., & Scholz, A. 2004, A&A, 417, 557
Lenz, D. D., Newberg, J., Rosner, R., Richards, G. T., & Stoughton, C. 1998, ApJS, 119, 121
Luhman, K. L., Stauffer, J. R., Muench, A. A., et al. 2003, ApJ, 593, 1093
Manara, C. F., Robberto, M., Da Rio, N., et al. 2012, ApJ, 755, 154
Ménard, F., & Bertout, C. 1999, in NATO ASIC Proc. 540: The Origin of Stars and Planetary Systems, eds. C. J. Lada, & N. D. Kylafis, 341
Meyer, M. R., Calvet, N., & Hillenbrand, L. A. 1997, AJ, 114, 288
Mohanty, S., Jayawardhana, R., & Basri, G. 2005, ApJ, 626, 498
Muzerolle, J., Hillenbrand, L., Calvet, N., Briceño, C., & Hartmann, L. 2003, ApJ, 592, 266
Natta, A., Testi, L., & Randich, S. 2006, A&A, 452, 245
Nguyen, D. C., Scholz, A., van Kerkwijk, M. H., Jayawardhana, R., & Brandeker, A. 2009, ApJ, 694, L153
Parker, R. J., Bouvier, J., Goodwin, S. P., et al. 2011, MNRAS, 412, 2489
Pecaut, M. J., & Mamajek, E. E. 2013, ApJS, 208, 9
Press, W. H., Teukolsky, S. A., Vetterling, W. T., & Flannery, B. P. 1992, Numerical recipes in C, The art of scientific computing (Cambridge University Press)
Prim, R. C. 1957, Bell Syst. Tech. J., 36, 1389
Ramírez, S. V., Rebull, L., Stauffer, J., et al. 2004, AJ, 127, 2659
Rebull, L. M., Makidon, R. B., Strom, S. E., et al. 2002, AJ, 123, 1528
Regnault, N., Conley, A., Guy, J., et al. 2009, A&A, 506, 999
Rigliaco, E., Natta, A., Randich, S., Testi, L., & Biazzo, K. 2011, A&A, 525, A47
Sicilia-Aguilar, A., Henning, T., & Hartmann, L. W. 2010, ApJ, 710, 597
Siess, L., Dufour, E., & Forestini, M. 2000, A&A, 358, 593
Skrutskie, M. F., Cutri, R. M., Stiening, R., et al. 2006, AJ, 131, 1163
Stauffer, J., Cody, A. M., Baglin, A., et al. 2014, AJ, 147, 83
Sung, H., Bessell, M. S., & Lee, S.-W. 1997, AJ, 114, 2644
Sung, H., Bessell, M. S., Chun, M.-Y., Karimov, R., & Ibrahimov, M. 2008, AJ, 135, 441
Sung, H., Stauffer, J. R., & Bessell, M. S. 2009, AJ, 138, 1116
Taylor, M. B. 2005, in Astronomical Data Analysis Software and Systems XIV, eds. P. Shopbell, M. Britton, & R. Ebert, ASP Conf. Ser., 347, 29
Teixeira, P. S., Lada, C. J., Marengo, M., & Lada, E. A. 2012, A&A, 540, A83
Vorobyov, E. I., & Basu, S. 2008, ApJ, 676, L139
Walker, M. F. 1956, ApJS, 2, 365
White, R. J., & Basri, G. 2003, ApJ, 582, 1109

Appendix C

UV variability and accretion dynamics in the young open cluster NGC 2264

L. Venuti[1,2,3], J. Bouvier[1,2], J. Irwin[4], J. R. Stauffer[5], L. A. Hillenbrand[6], L. M. Rebull[5], A. M. Cody[5,7], S. H. P. Alencar[8], G. Micela[9], E. Flaccomio[9], and G. Peres[3]

[1] Univ. Grenoble Alpes, IPAG, F-38000 Grenoble, France
[2] CNRS, IPAG, F-38000 Grenoble, France
[3] Dipartimento di Fisica e Chimica, Università degli Studi di Palermo, Piazza del Parlamento 1, 90134 Palermo, Italy
[4] Harvard-Smithsonian Center for Astrophysics, 60 Garden Street, Cambridge, MA 02138, USA
[5] Spitzer Science Center, California Institute of Technology, 1200 E California Blvd., Pasadena, CA 91125, USA
[6] Astronomy Department, California Institute of Technology, Pasadena, CA 91125, USA
[7] NASA Ames Research Center, Kepler Science Office, Mountain View, CA 94035, USA
[8] Departamento de Física - ICEx - UFMG, Av. Antônio Carlos, 6627, 30270-901 Belo Horizonte, MG, Brazil
[9] Istituto Nazionale di Astrofisica, Osservatorio Astronomico di Palermo G.S. Vaiana, Piazza del Parlamento 1, 90134 Palermo, Italy

Published in *Astronomy & Astrophysics*, Volume 581, A66 (2015)

A&A 581, A66 (2015)
DOI: 10.1051/0004-6361/201526164

Astronomy & Astrophysics

UV variability and accretion dynamics in the young open cluster NGC 2264*,**

L. Venuti[1,2,3], J. Bouvier[1,2], J. Irwin[4], J. R. Stauffer[5], L. A. Hillenbrand[6], L. M. Rebull[5], A. M. Cody[5,7], S. H. P. Alencar[8], G. Micela[9], E. Flaccomio[9], and G. Peres[3]

[1] Univ. Grenoble Alpes, IPAG, 38000 Grenoble, France
e-mail: Laura.Venuti@obs.ujf-grenoble.fr
[2] CNRS, IPAG, 38000 Grenoble, France
[3] Dipartimento di Fisica e Chimica, Università degli Studi di Palermo, Piazza del Parlamento 1, 90134 Palermo, Italy
[4] Harvard-Smithsonian Center for Astrophysics, 60 Garden Street, Cambridge, MA 02138, USA
[5] Spitzer Science Center, California Institute of Technology, 1200 E California Blvd., Pasadena, CA 91125, USA
[6] Astronomy Department, California Institute of Technology, Pasadena, CA 91125, USA
[7] NASA Ames Research Center, Kepler Science Office, Mountain View, CA 94035, USA
[8] Departamento de Física – ICEx – UFMG, Av. Antônio Carlos 6627, 30270-901 Belo Horizonte, MG, Brazil
[9] Istituto Nazionale di Astrofisica, Osservatorio Astronomico di Palermo G.S. Vaiana, Piazza del Parlamento 1, 90134 Palermo, Italy

Received 23 March 2015 / Accepted 16 June 2015

ABSTRACT

Context. Photometric variability is a distinctive feature of young stellar objects; exploring variability signatures at different wavelengths provides insight into the physical processes at work in these sources.
Aims. We explore the variability signatures at ultraviolet (UV) and optical wavelengths for several hundred accreting and non-accreting members of the star-forming region NGC 2264 (∼3 Myr).
Methods. We performed simultaneous monitoring of *u*- and *r*-band variability for the cluster population with CFHT/MegaCam. The survey extended over two full weeks, with several flux measurements per observing night. A sample of about 750 young stars is probed in our study, homogeneously calibrated and reduced, with internally consistently derived stellar parameters. Objects span the mass range 0.1–2 $M_{\odot}$; about 40% of them show evidence for active accretion based on various diagnostics (H_{α}, UV, and IR excesses).
Results. Statistically distinct variability properties are observed for accreting and non-accreting cluster members. The accretors exhibit a significantly higher level of variability than the non-accretors, in the optical and especially in the UV. The amount of *u*-band variability is found to correlate statistically with the median amount of UV excess in disk-bearing objects, which suggests that mass accretion and star-disk interaction are the main sources of variability in the *u* band. Spot models are applied to account for the amplitudes of variability of accreting and non-accreting members, which yields different results for each group. Cool magnetic spots, several hundred degrees colder than the stellar photosphere and covering from 5 to 30% of the stellar surface, appear to be the leading factor of variability for the non-accreting stars. In contrast, accretion spots with a temperature a few thousand degrees higher than the photospheric temperature and that extend over a few percent of the stellar surface best reproduce the variability of accreting objects. The color behavior is also found to be different between accreting and non-accreting stars. While objects commonly become redder when fainter, typical amplitudes of variability for accreting members rapidly increase from the *r* to the *u* band, which indicates a much stronger contrast at short wavelengths; a lower color dependence in the photometric amplitudes is instead measured for diskless stars. Finally, we compare the *u*-band variability monitored here on two-week timescales with that measured on both shorter (hours) and longer (years) timescales. We find that variability on timescales of hours is typically ∼10% of the peak-to-peak variability on day timescales, while longer term variability on a timescale of years is consistent with amplitudes measured over weeks.
Conclusions. We conclude that for both accreting and non-accreting stars, the mid-term rotational modulation by hot and cold spots is the leading timescale for a variability of up to several years. In turn, this suggests that the accretion process is essentially stable over years, although it exhibits low-level shorter term variations in single accretion events.

Key words. accretion, accretion disks – stars: low-mass – stars: pre-main sequence – stars: variables: T Tauri, Herbig Ae/Be – open clusters and associations: individual: NGC 2264 – ultraviolet: stars

1. Introduction

The notion of photometric variability is at the very base of the T Tauri class definition (Joy 1945). Since the first pioneering work (see Herbig 1962), variability appears to be a ubiquitous property of these young stellar objects (YSOs), as universal a feature as bewildering in its intrinsic case-to-case diversity.

The variable nature of young stars manifests on a wide range of wavelengths and on different timescales (see Ménard & Bertout 1999 for a review). Intense X-ray emission and

* Based on observations obtained with MegaPrime/MegaCam, a joint project of CFHT and CEA/DAPNIA, at the Canada-France-Hawaii Telescope (CFHT) which is operated by the National Research Council (NRC) of Canada, the Institut National des Sciences de l'Univers of the Centre National de la Recherche Scientifique (CNRS) of France, and the University of Hawaii.

** Full Table 2 is only available at the CDS via anonymous ftp to cdsarc.u-strasbg.fr (130.79.128.5) or via http://cdsarc.u-strasbg.fr/viz-bin/qcat?J/A+A/581/A66

variability are exhibited by young cluster members both on short (∼hours) and mid-term (∼days) timescales, ensuing from magnetic flaring (Favata et al. 2005; also seen in the UV) and/or modulation effects linked with rotation (Flaccomio et al. 2010, 2012), respectively. YSOs are found to be variable in the optical on timescales ranging from fractions of days (e.g., Rucinski et al. 2008) to weeks, months, and years (e.g., Bouvier et al. 1993, 1995; Grankin et al. 2007, 2008); these variations reflect the geometry of the systems as well as the physics and intrinsic timescales pertaining to their dynamics. Variability on an assortment of timescales is also detected in the near- (e.g., Wolk et al. 2013) and mid-infrared (e.g., Günther et al. 2014), where a major contribution to the measured flux arises from thermal emission from the inner disk, when present.

An overall similarity in variability pattern appears to be shared by weak-lined T Tauri stars (WTTS), more evolved YSOs with no evidence of circumstellar disk; their light curves typically show a regular, periodic profile, with amplitudes ranging from $\lesssim$0.1 to ∼0.5 mag in the optical, and are stable over tens to hundreds of rotational cycles. A more complex and diverse picture is observed for classical T Tauri stars (CTTS), whose dynamics are dominated by the interaction with an active accretion disk. Optical light curves typically show large (up to a few mag) variability amplitudes and often irregular profiles, with semiperiodic components coexisting with rapid, stochastic flux variations and fading events. As a common rule, TTS variability amplitudes are found to decrease toward longer wavelengths, albeit with different rates for different types of sources.

A first thorough exploration of optical YSO variability and of its physical interpretation was provided by the study of Herbst et al. (1994). Based on *UBVRI* monitoring of 80 sources, covering tens of epochs over several years, the authors categorized three main types of mid-term TTS variability. Type I, responsible for the well-behaved, periodic light curves observed for WTTS, consists of a simple modulation effect produced by cool magnetic spots at the stellar surface during stellar rotation. Except for episodes of magnetic flaring, this is sufficient to explain the variability of disk-free YSOs. This also represents an underlying component in the variability of their similarly magnetically active, disk-bearing counterparts, where the physics of accretion and star-disk interaction plays a prominent role. Type II variability, specific to CTTS, originates in a changing mixture of cool magnetic spots and hot accretion spots at the surface of the star. Hot spots are the signatures of the impact of the accretion column from the inner disk onto the central object; the energetic emission produced in the shock produces a flux excess at short wavelengths (UV, soft X-rays), and hence these sources are bluer than photospheric colors would suggest. Periodic behavior can be observed in some cases, but irregular variation patterns are more common, which suggests shorter lifetimes for accretion spots than for magnetic spots. Type III variability is of a different nature, pertaining again only to disk-bearing sources. Objects in this category show light curves with typical brightness levels close to the maximum luminosity state, interspersed by dips of up to a few magnitudes, with little color dependence in the amplitude. Variable obscuration from circumstellar dust appears to be the dominant source of variability. A quasi-periodicity in the fading events may be observed (e.g., Bouvier et al. 2007); this is indicative of a concentration of material in the inner disk that rotates with the system and periodically occults part of the photosphere.

From this discussion, it is clear that large-scale, synoptic investigations of YSO variability signatures over the full wavelength range are critical for understanding the different nature of these systems. In addition, a time sampling on timescales short enough to trace the short-term variations and extending over timescales relevant to various processes is needed to achieve a detailed physical description of the processes at play at the stellar surface and in the star-disk interface. Remarkable progress in this respect was marked by the advent of space-based telescopes, with their exquisite cadence and photometric accuracy. The potential of such campaigns was illustrated by the *Spitzer* Space Telescope (Werner et al. 2004) InfraRed Array Camera (IRAC; Fazio et al. 2004) YSOVAR project (Morales-Calderón et al. 2011; Rebull et al. 2014) and by a first investigation of the star-forming region NGC 2264 (∼3 Myr) with the COnvection, ROtation and planetary Transits (CoRoT) optical space telescope (Alencar et al. 2010). In December 2011, the improved capability of space-based surveys in time-domain exploration and the advantages of a multiwavelength approach to YSOs variability were combined in the unprecedented "Coordinated Synoptic Investigation of NGC 2264" (CSI 2264) campaign (Cody et al. 2014). This consisted of a unique cooperative observing program aimed at mapping the photometric variability of the whole cluster (∼1500 known members) simultaneously in infrared, optical, UV, and X-ray wavelengths on timescales varying from hours to over a month. The primary components of the optical and infrared observations were performed with CoRoT and *Spitzer*/IRAC for a duration of 40 and 30 consecutive days, respectively. This dataset, described in detail in Cody et al. (2014), enabled a more accurate classification of the diverse nature of disk-bearing objects based on light-curve morphology, where defined classes included quasi-periodic, dippers, bursters, stochastic behavior, strictly periodic, and long-timescale variations. Complementary information gathered at similar and at different wavelengths with 13 additional space-borne and ground-based telescopes during the campaign allowed us to investigate the variable nature of these objects in more detail.

The UV wavelength domain offers a particularly interesting perspective on the star-disk interaction dynamics, as it provides one of the most direct diagnostics of disk accretion onto the central object. The association between UV excess displayed by TTS and infall of material onto the star from a surrounding region of moderate vertical extent was first suggested by Walker (1972), about twenty years before magnetospheric accretion models for disk accretion in CTTS were developed (e.g., Hartmann et al. 1994). In the current picture, accretion columns impact the stellar surface at near free-fall velocities, hence resulting in shock regions (hot spots) close to the magnetic poles. The energetic emission produced in these areas results in the distinctive UV flux excess detected for accreting stars compared to their non-accreting counterparts. Remarkably, very little systematic investigation of YSO variability in the UV exists in the literature to date, particularly studies encompassing large statistical populations of different nature with time coverage and sampling suitable to qualify different components. An interesting effort in this respect is provided by the study of Fallscheer & Herbst (2006), who monitored the *U*-band variability of about a hundred young stars in the NGC 2264 field to investigate disk-locking, using the UV excess as a proxy for accretion. Within the context of the CSI 2264 project, we performed a dedicated UV monitoring campaign of several hundred young members of NGC 2264 in February 2012, simultaneously with optical monitoring, at the Canada-France-Hawaii Telescope (CFHT). For the first time, this survey provides direct measurements of mass accretion rates ($\dot{M}_{\rm acc}$) and of their variability across a large statistical sample of coeval pre-main sequence (PMS) stars, all similarly characterized. The extent and homogeneity of the dataset

allows us to i) investigate the dependence of the mass accretion rate on stellar parameters such as mass and evolutionary age; ii) explore the nature of the wide spread in $\dot{M}_{\rm acc}$ values detected in any mass bin; iii) evaluate the typical amount of variability on $\dot{M}_{\rm acc}$ on timescales relevant to stellar rotation; iv) assess the contribution of geometric modulation effects to the detected amount of $\dot{M}_{\rm acc}$ variability. Results of this analysis were reported in Venuti et al. (2014, hereafter Paper I).

In a complementary effort, here we focus on exploring and characterizing the variability signatures at short wavelengths that pertain to different types of YSO variables. The paper is organized as follows. Section 2 provides a description of the monitoring survey and of the subsequent light-curve extraction and processing. Section 3.1 presents a comparison of the optical and UV variability level exhibited by accreting and non-accreting sources, which were probed using different variability indices. Variability and accretion indicators are combined in Sect. 3.2 to evaluate the impact of the accretion process on the substantial variability characteristic of CTTS. In Sect. 3.3, we explore the color signatures associated with different physical processes at the origin of YSO variability, that is, how steeply the variability amplitudes change from the optical to the UV. We show detailed color-magnitude-correlated variations for representative sources of different variability types and highlight how these diagrams reflect the underlying physics. In Sect. 3.4, we adopt a spot model description of the observed optical + UV variability amplitudes to derive a statistical depiction of the distinctive surface features of accreting vs. non-accreting objects. Our results are summarized and discussed in Sect. 4, while Sect. 5 presents our conclusions.

Table 1. Log of CFHT/MegaCam monitoring survey of NGC 2264 (Feb. 14−28, 2012).

Date	Flag$_{\rm phot}$ [1]	n° obs. seq. [2]	JD$_{\rm phot}$ [3]
Feb. 15	1	3	72.7 72.8 72.9
Feb. 16	1	3	73.7 73.8 73.9
Feb. 17	0	4	
Feb. 18	0	7	
Feb. 19	0	3	
Feb. 21	1	3	78.7 78.8 78.9
Feb. 24	1	3	81.7 81.8 81.9
Feb. 26	2	4	83.7 83.8
Feb. 27	2	4	84.8 84.9
Feb. 28	2	3	85.7 85.8
Feb. 29	0	1	

Notes. [(1)] Flag on observing conditions: 1 = night was photometric; 2 = parts of the night were photometric; 0 = night was non-photometric. [(2)] Number of observing sequences performed during the night (i.e., number of times the same observing block was repeated during the night). [(3)] Julian date (JD-2 455 900, truncated at the first decimal place) of observing sequences obtained in photometric conditions during the night.

2. Observations and data analysis

We extensively monitored the u- and r-band variability of NGC 2264 members from February 14 to 28, 2012, at the CFHT using the wide-field camera MegaCam ($0.96^\circ \times 0.94^\circ$ FOV). A full description of the monitoring survey and of the subsequent data processing and light-curve extraction has been provided in Paper I. Here, we summarize the main features of the observing campaign; we refer to Paper I for further details.

Targets were observed during 11 nights distributed along the 14-day-long run; among these, 7 nights were photometric. A single $u+r$ observing block, consisting of five dithered exposures in u and five dithered exposures in r, obtained consecutively, was performed repeatedly on each observing night during the run; each exposure was then individually processed to reconstruct the light variations of all sources on different timescales (hours to days).

The large population of field stars detected in the telescope aperture (∼8000 objects) was used to test the accuracy of the photometry of individual exposures by comparison with the master frame; photometric sequences obtained under poorer observing conditions (hence resulting in a large magnitude offset from the master frame) were rejected upstream. A log of the MegaCam monitoring survey of NGC 2264 is provided in Table 1.

A 5σ-clipping procedure was adopted to identify and reject occasional very discrepant points in the light curves; this occurred in less than 25% of the cases in the u-band and for just ∼5% of the r-band light curves.

The catalog of NGC 2264 members, assembled as described in Paper I, was used as the reference for the identification of members and field stars in the monitoring survey. Instrumental photometry was statistically calibrated to the Sloan Digital Sky Survey (SDSS) photometric system, using a population of ∼3000 stars in the CFHT FOV for which SDSS photometry is publicly available from the seventh SDSS Data Release (Abazajian et al. 2009). Our census of NGC 2264 members is complete down to $u \sim 21.5$ and $r \sim 18.5$ mag, with the brightest objects reaching apparent magnitudes of $u \sim 15$ and $r \sim 13.5$. A population of ∼750 members has been probed, spanning 0.1–2 $M_\odot$; of these, about 40% are actively accreting. Criteria adopted for member classification are detailed in Paper I and mainly include H_α emission, variability, and IR excess from both our and earlier surveys; for this part of the analysis, UV excess information from our data was used as a complement to refine the census of NGC 2264 members with the identification of previously unknown accreting sources in the cluster. Hereafter the objects with accretion disk signatures are referred to as CTTS, while those lacking any of them are called WTTS. A full list of stellar parameters for the targeted objects is provided in Table 3 of Paper I; CTTS/WTTS classification and spectral type estimates are reported in Table 2 of this paper[1].

Two main timescales contribute to the monitored variability: i) short-term (≲hours), dominated by short-lived events (like

[1] Objects Mon-904 and Mon-985, labeled as WTTS in Paper I, are here reclassified as CTTS. These objects are noted to be weak H_α emission stars in the literature; both display some UV excess in our data, though not sufficient per se to prove their accreting nature. *Spitzer* data show that these sources also possess some IR excess; in addition, they exhibit large variability amplitudes (0.7−0.8 mag in the optical). Considering all these elements, these objects appear to qualify as disk-bearing sources.

Table 2. Median photometry, variability amplitudes, light curve rms, J index, and color slopes for members discussed in this study.

CSIMon-#[1]	Var[2]	Class[3]	SpT[4]	med_u	med_r	amp_u	amp_r	rms_u	rms_r	J index	$\frac{\Delta r}{\Delta(u-r)}$	σ_{slope}[5]
000007	*	c	K7	17.22	14.49	1.104	0.207	0.34	0.05	32.97	0.174	0.004
000009		w	F5	18.21	14.99	0.019	0.010	0.005	0.003	0.11		
000011	*	c	K7	16.76	15.09	1.008	0.429	0.34	0.14	58.26	0.642	0.008
000014		w	K7:M0	18.88	14.25	0.023	0.007	0.006	0.003	0.20		
000015		w	K7:M0	19.39	14.55	0.028	0.008	0.008	0.003	0.60		
000017	*	c	K5	18.41	14.94	0.216	0.130	0.06	0.04	8.50	1.52	0.15
000018	*	w	K3:K4.5	19.05	14.99	0.192	0.073	0.03	0.02	2.05	0.70	0.08
000020	*	w	K7	20.02	15.94	0.153	0.109	0.04	0.03	1.65	1.2	0.3
000022		w	M4	21.80	17.72	0.238	0.044	0.06	0.016	0.20		
000023		w	M3	22.30	18.18	0.475	0.063	0.11	0.02	0.07		

Notes. A full version of the table is available in electronic form at the CDS. A portion is shown here for guidance regarding its form and content. [(1)] Object identifiers adopted within the CSI 2264 project (see Cody et al. 2014). [(2)] Variability flag; objects that exhibit a distinct level of variability stronger than that for field stars, based on the J-index indicator, are marked with an asterisk. [(3)] "c" = CTTS; "w" = WTTS (classification from Venuti et al. 2014). [(4)] Spectral type estimates from Venuti et al. (2014). [(5)] rms uncertainty on $\Delta r/\Delta(u-r)$ color slope.

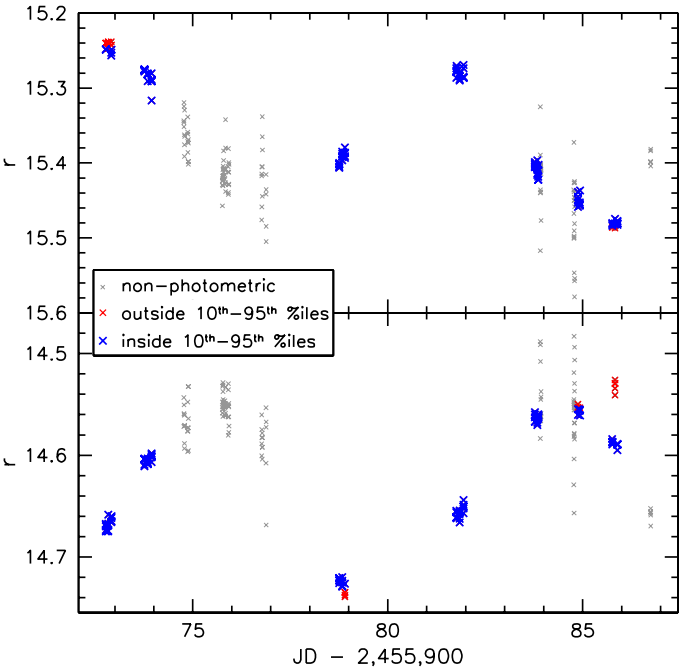

Fig. 1. Two examples of CFHT r-band light curves at the various steps of processing (detailed in Sect. 2): gray points indicate observations obtained in non-photometric nights or sequences, which were rejected for the present analysis; light-curve points excluded after 10th−95th percentile selection are marked in red; the final set of data points retained is shown in blue.

flares or bursts); and ii) mid-term (∼rotation period), dominated by geometric modulation effects. The latter is the component of interest for the present study. To smooth out short-term variability and the photometric noise components from single observing sequences, we computed the 10th and 95th percentile levels, in magnitudes, over the whole light curve and disregarded all points outside this range. These selective levels were set empirically upon examination of the full statistical sample of light curves; a more severe threshold was adopted at the brighter end to properly omit flares.

The various steps of light-curve processing are illustrated in Fig. 1 for two cases. Similar diagrams for individual objects were visually inspected at the end of the routine to verify accurate point selection. In the few tens of cases for which incorrect automatic selection resulted in biased amplitudes (e.g., when light-curve minima or maxima occurred close to non-photometric nights), this was corrected by hand.

3. Results

3.1. u-band variability of young stars in NGC 2264

Measuring the light-curve dispersion around the average photometric level provides a first snapshot of variability properties across the sample. Non-variable stars are expected to have weak stochastic fluctuations around their mean brightness due to the photometric noise that affects every measurement. On the other hand, light curves of intrinsically variable stars are expected to exhibit a significantly larger root-mean-square (rms) variation than that expected for photometric noise.

These populations of non-variable and variable stars can be observed in Fig. 2 for main-sequence dwarfs and young members in the NGC 2264 field. The light curve rms measured for field stars as a function of magnitude defines both in r and in u the photometric noise level at a given brightness. In each (m, rms_m) diagram, the young stars exhibit a distinct level of intrinsic variability over the photometric noise sequence; furthermore, accreting and non-accreting members tend to occupy statistically distinct but overlapping regions, with a median rms value 2.5 times higher for the first group than for the second, and increasing in both cases from the r to the u band. A two-sample Kolmogorov-Smirnov test, aimed at comparing the distribution in rms of accreting members to that of non-accreting objects both in u and in r, attests to the significantly different nature of the two populations, with a null-hypothesis probability of 10^{-24} in r and 10^{-37} in u. For fainter objects, the photometric noise affecting the light-curve measurements becomes more important, especially in the u band, which results in a certain degree of overlapping between the loci of variable and non-variable stars.

A more accurate variability tracer is provided by Stetson's (1996) J index. This probes the level of correlated variability between different wavelengths monitored at the same time, which significantly reduces the spurious contribution from stochastic noise to the detected variability level. Points in the u-band light curve are paired with the closest r-band epoch (at an average separation of 10 to 15 min). The J index is then defined as

$$J = \frac{\sum_{i=1}^{n} w_i \, \mathrm{sgn}(P_i) \sqrt{|P_i|}}{\sum_{i=1}^{n} w_i}, \quad (1)$$

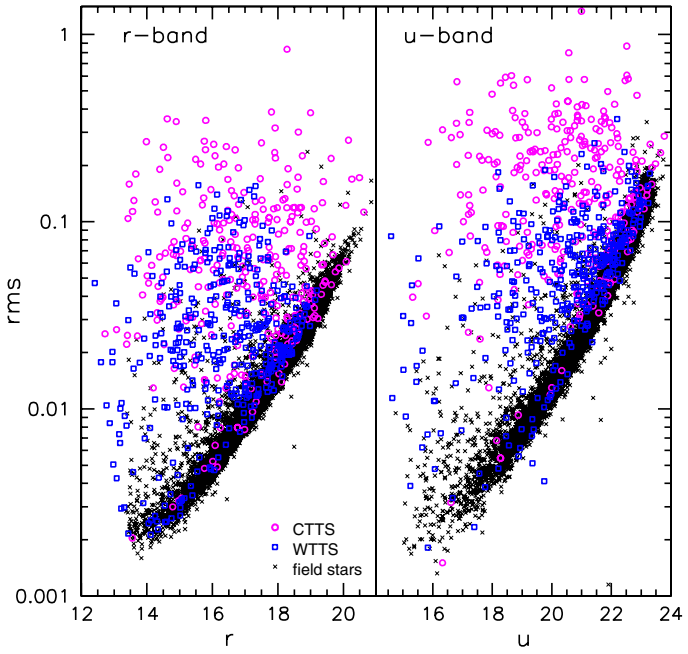

Fig. 2. *r*-band (*left panel*) and *u*-band (*right panel*) light-curve dispersion as a function of magnitude for different groups of monitored objects: field stars (black crosses), accreting NGC 2264 members (CTTS; magenta circles), and non-accreting members (WTTS; blue squares).

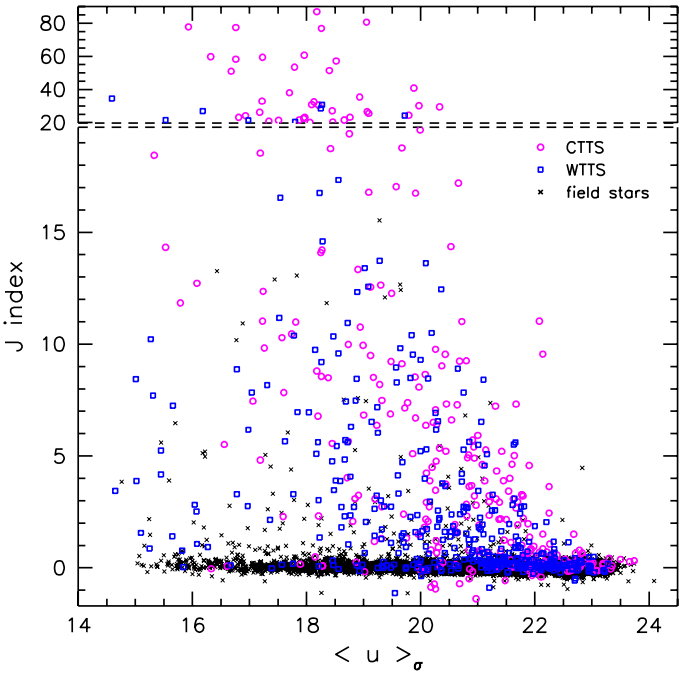

Fig. 3. Stetson's (1996) *J* index of correlated UV/optical variability as a function of *u*-band magnitude for different groups of monitored objects: field stars (black crosses), accreting NGC 2264 members (CTTS; magenta circles), and non-accreting members (WTTS; blue squares).

where i is the time index across the series, n is the total number of simultaneous u, r pairs (typically 98 over two weeks), "sgn" is the sign function, w_i is a weight, defined as in Fruth et al. (2012), to account for the actual time distance between paired u and r measurements, and P_i is the product of normalized residuals of paired observations:

$$P_i = \frac{n}{n-1}\left(\frac{u_i - \langle u\rangle_\sigma}{\sigma_i(u)}\right)\left(\frac{r_i - \langle r\rangle_\sigma}{\sigma_i(r)}\right). \quad (2)$$

(u_i and r_i being the magnitudes at time i, $\langle u\rangle_\sigma$ and $\langle r\rangle_\sigma$ the mean magnitudes and σ the photometric uncertainty).

A spurious, noise-driven "variability" component is expected to statistically average to zero throughout the whole time series. Conversely, a definite correlation is expected to exist between u- and r-band behavior for a truly variable star; this would result in values of J significantly different from zero.

Figure 3 shows the J distribution for cluster members and field stars in our survey. Field stars are predominantly located on a narrow, horizontal sequence centered on $J = 0$, independent of the object's brightness. A low percentage of field stars (∼3%) shows a significant amount of variability, attributable either to occasional spurious points or to an intrinsic variable nature (e.g., binaries, pulsators, active stars). Of the NGC 2264 members, about 63% show clear variability above the J sequence traced by field stars at the 3σ level (75% at 1σ level); this percentage rises to 72% (81%) when considering the accreting members alone. As for Fig. 2, CTTS display a significantly higher level of variability than WTTS, with the typical J value three to four times higher than that of non-accreting members.

A variability flag, median u- and r-band photometry, light-curve amplitudes, light curve rms, and J index values for individual members are reported in Table 2.

3.2. UV variability and accretion

As discussed in Sect. 3.1, CTTS are statistically found to exhibit significantly stronger variability than WTTS; this is especially observed at shorter wavelengths (u band). This suggests that accretion mechanisms, whose signatures can be most directly detected in the UV, are a primary cause of the enhanced variability of these young stars. We would then expect to observe a direct link between accretion diagnostics and variability indicators.

In Paper I, we reported on a full characterization of accretion properties for NGC 2264 members from the UV excess diagnostics; we showed that the UV color excess displayed by accreting stars relative to WTTS provides a direct proxy for the accretion luminosity.

In Fig. 4, we compare UV excess measurements to the level of u-band rms variability. The diagram is obtained as follows:

(a) We selected from Fig. 3 all CTTS (217) and WTTS (210) whose J index was at least 3σ higher than the typical location at the corresponding brightness on the field star sequence. For a given object, the measured light curve rms is the result of two independent contributions, intrinsic variability and photometric noise: $\sigma_{\rm meas} = \sqrt{\sigma^2_{\rm obj} + \sigma^2_{\rm noise}}$. To recover $\sigma_{\rm obj}$, we estimated the lowest magnitude-dependent noise component expected to affect the measurement as a fit to the lower envelope of the field star locus in Fig. 2 and quadratically subtracted this contribution from the measured rms values for young stars.

(b) UV excesses were measured as in Eq. (9) of Paper I for CTTS. The same procedure was applied here to compute a "UV excess" for WTTS, for comparison purposes. In WTTS, the UV excess definition has no direct meaning, but it provides a measure of the scatter of WTTS colors around the reference sequence. Enhanced chromospheric activity is expected to translate both into somewhat bluer

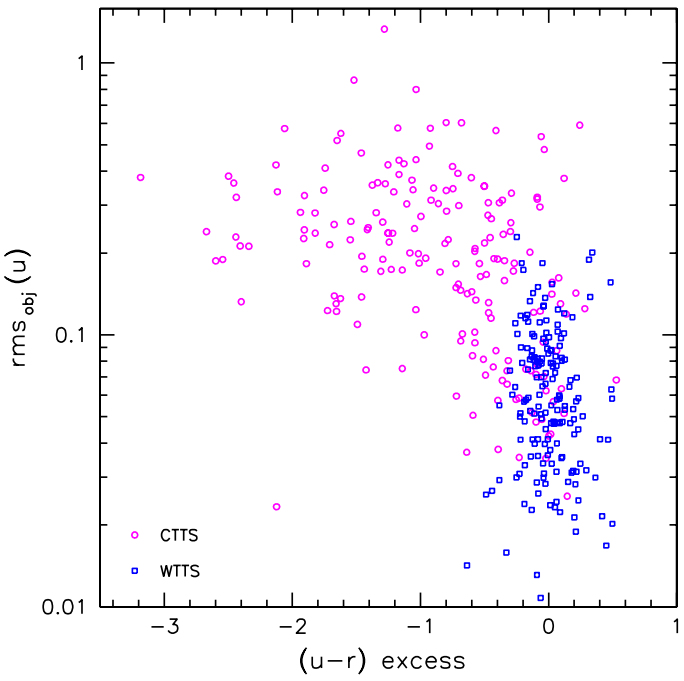

Fig. 4. UV excess measurements (see Paper I) are compared to the level of u-band rms variability detected for CTTS (magenta circles) and WTTS (blue squares) in NGC 2264. Objects displayed are all selected as significantly variable using the J-index indicator (see text). The UV excess increases from right to left on the diagram.

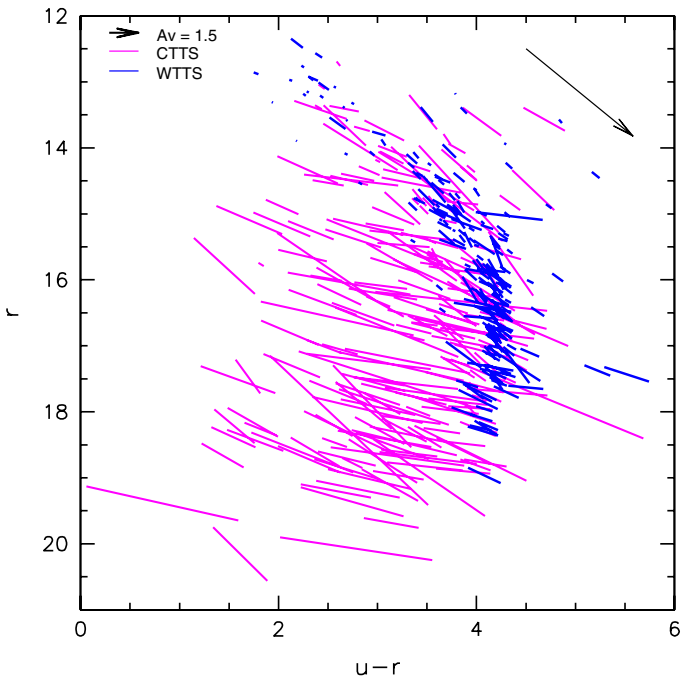

Fig. 5. Monitoring of color and magnitude variations on the $(u-r, r)$ diagram for CTTS (magenta lines) and WTTS (blue lines) in NGC 2264 on a timescale of weeks. Each bar represents a single object: the center of the bar is located at the color and r-band magnitude of the object at the median luminosity state, while the amplitudes along $u-r$ and r mark the total amount of variability detected during the CFHT monitoring (i.e., $(u-r)_{\rm max}-(u-r)_{\rm min}$ and $r_{\rm max}-r_{\rm min}$ over the 10th−95th percentiles range, respectively). The effects of reddening on the diagram are traced by the black arrow in the top right corner (Fiorucci & Munari 2003).

colors and stronger variability. Recent studies conducted on somewhat older PMS populations than NGC 2264 members (e.g., Kamai et al. 2014, on the Pleiades) have shown that more rapidly rotating objects might display bluer colors and stronger variability amplitudes in light curves. Hence, some correlation might be detected between color excess and amount of variability exhibited by WTTS. For the reasons discussed in Sect. 4 of Paper I, objects with $r < 14.5$ are not displayed in Fig. 4.

Spearman's non-parametric rank correlation test (Press et al. 1992) was adopted to probe the statistical significance of any relationship between UV color excess and u-band rms variability, both in the accreting and non-accreting groups in Fig. 4. A p-value of 0.07 is returned from the test for the latter. More importantly, direct evidence of a correlation between the accretion process and photometric variability at short wavelengths is provided by the distribution of accreting objects on this diagram. The bulk of the CTTS are located at a higher u-band rms level than the WTTS, as already observed in Fig. 2, and higher rms values correspond, on average, to higher (i.e., more negative) UV excesses. This correlation is estimated to be significant at the 6σ level.

3.3. UV variability and color signatures

Figure 4 shows the global accretion-variability connection across the cluster. This statistical information, however, is not all that is needed to achieve a detailed picture of how variability relates to the physics of individual objects, as illustrated by the wide spread of rms (u) values at any given UV excess.

More accurate information on the nature of YSO variability derives from investigating color variations. Indeed, while single-band amplitudes provide some indication on the contrast between stellar photosphere and the source of variability, color variations trace the wavelength dependence of this contrast and hence provide more direct clues to its physical origin.

In Fig. 5, UV colors and variability properties for NGC 2264 members in Fig. 4 are combined in a dynamic picture of the $(u-r, r)$ diagram of the cluster. A significant number of CTTS display markedly bluer colors than the corresponding location on the cluster sequence traced by WTTS, as a result of the distinctive UV excess linked with ongoing disk accretion. In addition, as illustrated in Fig. 4, high UV excesses are typically associated with strong variability, whereas a significantly lower level of variability, both in magnitude and in color, is observed on the same timescales for non-accreting objects.

The detailed picture of variability observed for individual objects may vary on a case-by-case basis, as shown in Fig. 5. This is reflected in the range of slopes associated with variability bars among both WTTS and, especially, CTTS. Different color signatures are expected to correspond to different physical scenarios. When variability is driven by spot modulation, systems are expected to be redder at fainter states, with variability amplitudes that decrease toward longer wavelengths; a steeper decrease with λ is expected for hot spots than for cold spots. When variability is due to opaque material that crosses the line of sight to the star, little color dependence is expected in the main occultation event.

This is well illustrated in the panels of Fig. 6, which compares brightness and color variation trends for four members of NGC 2264 that are dominated by different mechanisms. Panel a shows an example of a stochastic accretor (Stauffer et al. 2014) whose variability is dominated by short-lived, stochastic accretion bursts. The color light curve nearly retraces the features of

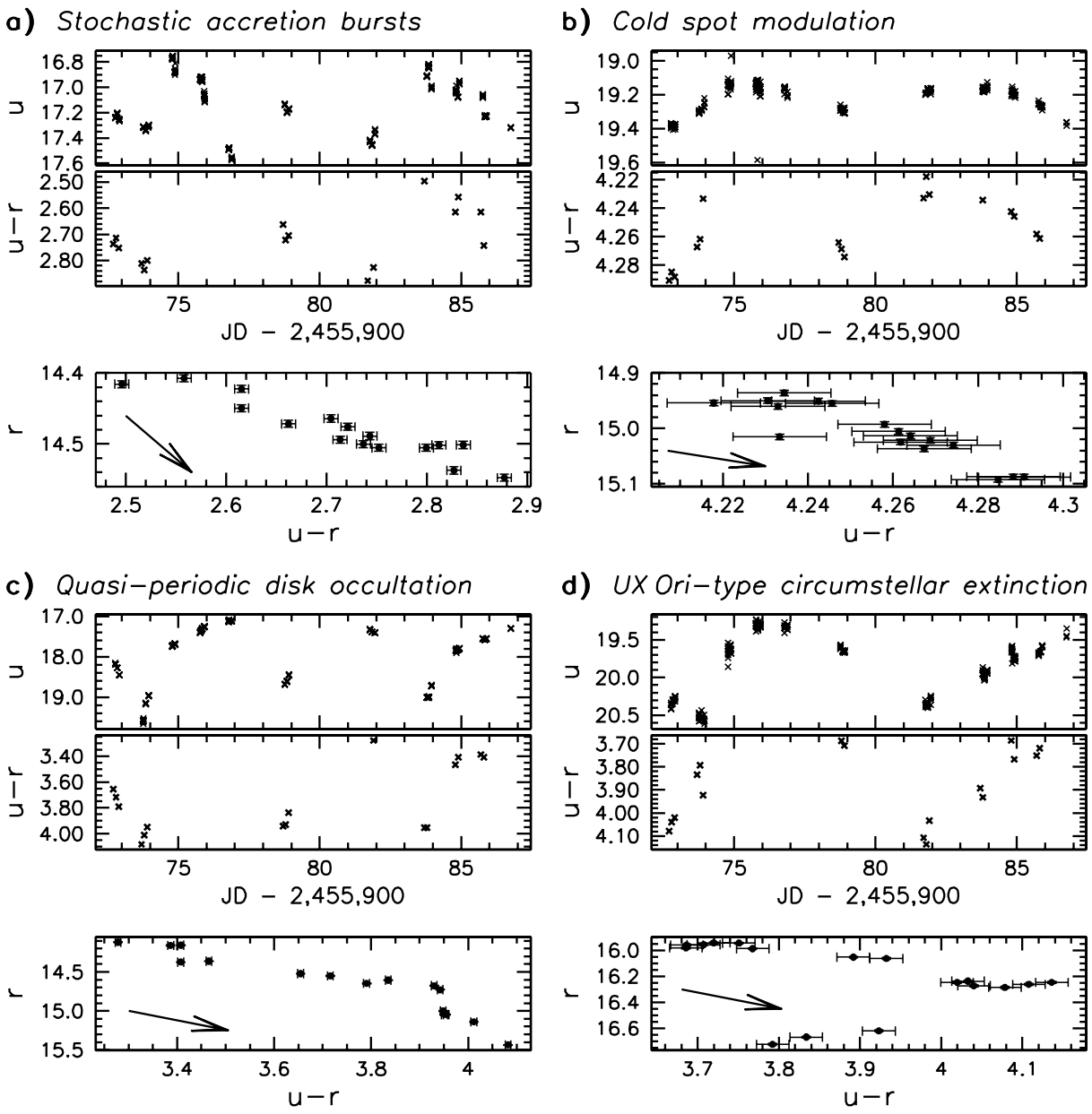

Fig. 6. *u*-band light curve, $u-r$ light curve, and r vs. $u-r$ variations for four different objects in NGC 2264: **a)** CSIMon-000877, a representative of the stochastic accretion bursters class; **b)** CSIMon-001247, a prototypical WTTS; **c)** CSIMon-000660, an AA Tau-like CTTS; **d)** CSIMon-000433, a UX Ori-like object. Light curves report all flux measurements obtained from the monitoring campaign for a better overview of the variability pattern, but only observing sequences obtained in photometric conditions (see Table 1) are retained for the color analysis. Each point in the r vs. $u-r$ diagram for a given object corresponds to the average $u-r$ color and r-band magnitude measured from a single observing sequence; error bars are associated with each point based on the lowest rms level detected for field stars at the corresponding brightness (see Fig. 2). The effects of interstellar reddening are traced as a vector in the bottom left quarter of each (r, $u-r$) diagram.

the magnitude light curve, as the system becomes consistently bluer for increasing brightness. The same global property is observed for case b, which depicts a WTTS member whose variability is produced by rotational modulation of cold magnetic spots. Cases b and a are distinguished by both i) the variation amplitudes, especially in color; and ii) the slope of the average r vs. $u-r$ trend (as can be deduced when comparing the direction traced by data points with the slope of the reddening vector, which is the same in each plot). A more complex trend is observed for case c, which illustrates an AA Tau-like CTTS (Alencar et al. 2010; McGinnis et al. 2015), that is, an object whose main variability features are driven by quasi-periodic occultations of part of the stellar surface from an inner disk warp. The r vs. $u-r$ diagram reveals two separate contributions of different nature to the overall variability profile: one with color signatures as expected for accretion spots (segment at linear increase of $u-r$ with r, with a slope consistent with that shown in panel a), and the other displaying gray brightness variations (segment flat in $u-r$), which is indicative of opaque material that crosses the line of sight to the source. These behavior changes occur within only two weeks and average to a global $\Delta r/\Delta(u-r)$ slope consistent with that traced by the reddening law. Another interesting behavior is shown in panel d. As in the previous case, the variability of this system is dominated by circumstellar extinction. The system generally becomes redder when fainter, with the exception of the first segment of the light

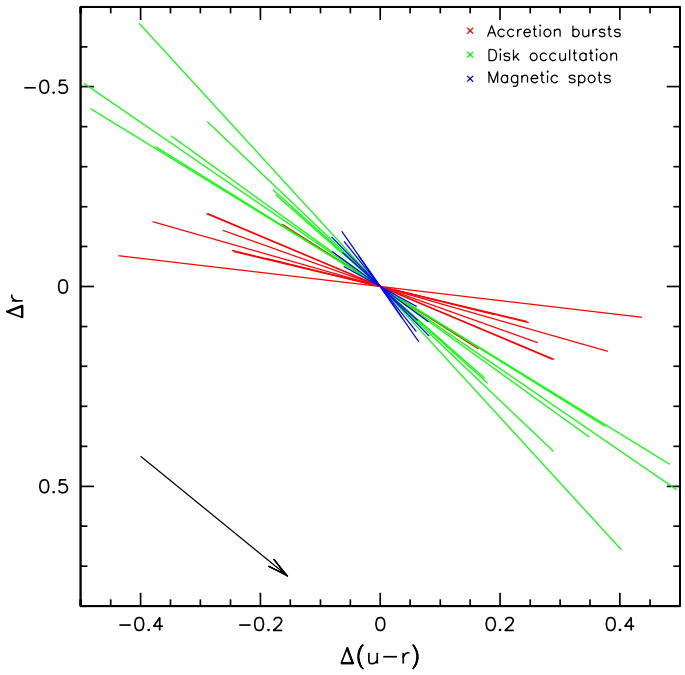

Fig. 7. Comparison of photometric amplitudes and $\Delta r/\Delta(u-r)$ slopes observed for representative objects of three different types of NGC 2264 members (stochastic accretors, WTTS, and AA Tau-like stars) whose variability is driven by accretion bursts (red lines), cold magnetic spots (blue lines), or disk occultation (green lines), respectively. Luminosity increases from the bottom up along the y-axis and objects become bluer from right to left along the x-axis.

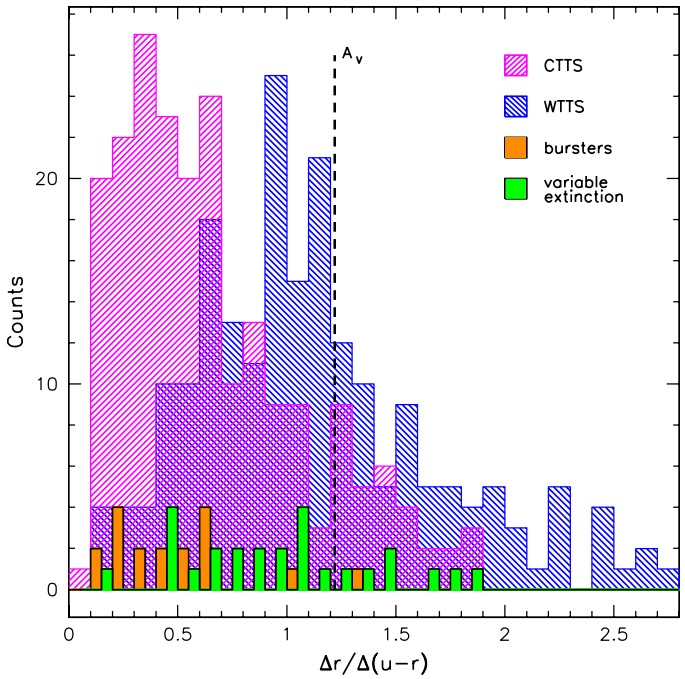

Fig. 8. Histograms of $\Delta r/\Delta(u-r)$ amplitude ratios are compared for WTTS (blue), all CTTS (magenta), accretion-burst-dominated CTTS (orange), and circumstellar extinction-dominated CTTS (green). Histogram bars for bursters and the variable extinction group are shifted by −0.025 and 0.025, respectively, relative to the bin center and are placed side by side for a better visual comparison of the overall distributions. The slope predicted by the interstellar extinction law is shown as a black dashed line.

curve, where a decrease in luminosity down to the minimum detected is accompanied by a marked decrease in $u-r$ (i.e., bluer colors). Again, two different components can be distinguished on the r vs. $u-r$ diagram. At first, the system becomes redder as it proceeds from maximum to a mean brightness state, with an overall trend consistent with what is expected for an accreting source; however, as the brightness drops below a certain level, the system is suddenly found to depart from the previous color trend and become bluer. This effect is reminiscent of the UX Ori phenomenon (Herbst et al. 1994).

Individual amplitudes and slopes may vary broadly among cases that share the same physical origin (as illustrated in Appendix A for a subsample of WTTS). Nevertheless, we would expect to observe noticeable differences between typical color−magnitude trends for distinct variable groups. Thus, we selected good representatives of the WTTS, burster (Stauffer et al. 2014), and AA Tau-like (McGinnis et al. 2015) classes. This selection favored objects in each group that showed the largest photometric amplitudes in CFHT bands, or equivalently were the least affected by noise and hence provided the clearest depiction of characteristic variability features. Amplitudes in color and in magnitude for these objects are compared in Fig. 7. WTTS show the smallest amplitudes and remarkably little color variations as the system moves from the brightest to the faintest state. Bursters show magnitude variations that are similar to those displayed by WTTS in the r band, but are associated with significantly larger color variations. The strongest variability amplitudes are observed for AA Tau objects, and the average $\Delta r/\Delta(u-r)$ slope detected on a timescale of weeks is found to be consistent with the slope expected for interstellar extinction.

These relative trends are confirmed when analyzing the color slopes for the whole sample of variable NGC 2264 members,

Table 3. Average color slopes for different typologies of light curves.

Object class	No.[1]	Median $\frac{\Delta r}{\Delta(u-r)}$	IQR[2]
WTTS	207	1.0	0.7
CTTS	212	0.6	0.5
↳ Bursters	18	0.5	0.4
↳ Circumstellar extinction	26	0.9	0.5

Notes. For comparison, the interstellar extinction slope is 1.22 (from data in Fiorucci & Munari 2003). [(1)] Number of objects in the corresponding class. [(2)] Interquartile range.

WTTS or CTTS, with a particular focus among the latter on objects showing either a stochastic burster or an AA Tau-like nature. Median slope and statistical dispersion measured in each of these four groups are listed in Table 3 (while individual values of $\Delta r/\Delta(u-r)$ are reported in Table 2 and corresponding distributions are illustrated in Fig. 8). CTTS show on average shallower slopes than WTTS; this difference is more marked when only considering accretion-dominated objects. AA Tau objects and WTTS display similar slope ranges, in turn consistent with the interstellar extinction slope.

3.4. Spot models

As discussed by several authors over the past few years (e.g., Paper I; Costigan et al. 2014; Grankin et al. 2007, 2008), baselines of days to weeks appear to be the leading timescales for YSO variability (at least up to several years). A major contribution to this variability arises, on average, from rotational modulation due to surface inhomogeneities, whose nature is linked

with the magnetic activity of the star and/or with ongoing disk accretion.

Interesting indications of the properties and dominating features of individual objects can thus be inferred by attempting to reproduce the observed multiwavelength variability signatures with spot models. In this picture, the variability is assumed to arise from a region (single spot or spot distribution) of different temperature at the stellar surface, whose emission modulates the observed luminosity of the star while it rotates.

Several studies, including extensive photometric monitoring and spectropolarimetric observations of individual objects (e.g., Donati et al. 2010), have shown that the surface of TTS is possibly covered by multiple spots or spot groups. While our capability of inferring a detailed description of surface spot distribution is limited by the poor geometric constraints, useful indications on effective temperature and area covered by spots can be deduced from the observed variability amplitudes at different wavelengths. As mentioned earlier, both cold (magnetic activity) and hot (accretion) spots at the stellar surface will produce the same qualitative effects: objects are expected to be redder at fainter states and variability amplitudes will be larger at shorter wavelengths. Spot parameters (notably temperature and fractional area coverage relative to stellar photosphere) are, then, uniquely determined by differential color variations, that is, by the rate at which the observed amplitudes decrease toward longer wavelengths (Vrba et al. 1993).

3.4.1. Model adopted in this study

To explore the nature of variability across the PMS population of NGC 2264, we followed the approach of Bouvier et al. (1993) and adopted a spot model that does not introduce any assumptions of the number and shape of spots at the stellar surface. The model assumes, however, i) a uniform temperature for all spots at the stellar surface; and ii) a blackbody distribution for stellar and spot emission.

As detailed in Bouvier et al. (1993), after Vogt (1981) and Torres & Ferraz Mello (1973), modulated variability amplitudes due to surface spots can be described as

$$\Delta m(\lambda) = -2.5 \log \left[1 - \frac{\mathcal{F}_{\rm eq}}{1 - \mu(\lambda)/3} \left(1 - \frac{S'(\lambda)}{S(\lambda)} \right) \right], \qquad (3)$$

where $S(\lambda)$ is the specific intensity of the immaculate photosphere at the stellar disk center, $S'(\lambda)$ is the same quantity for the spotted region, $S'(\lambda)/S(\lambda) = B_\lambda(T_{\rm spot})/B_\lambda(T_{\rm phot})$ in the blackbody approximation, $\mathcal{F}_{\rm eq}$ is a lower limit to the true fraction of stellar surface covered by spots, and $\mu(\lambda)$ is the linear limb-darkening coefficient.

Photospheric temperatures $T_{\rm phot}$ were inferred from the spectral types of the objects following the scale of Cohen & Kuhi (1979)[2], while linear limb-darkening coefficients were deduced from the compilation of Claret & Bloemen (2011), assuming solar metallicity and $\log g = 4$. Limb-darkening coefficients tabulated for spectral type M2 were uniformly extended to later spectral types that were not sampled in the reference compilation at the metallicity and gravity values adopted. Spot parameters $T_{\rm spot}$ and $\mathcal{F}_{\rm eq}$ are thus the only unknowns in Eq. (3) for a given object and were deduced from the model by fitting the expression for Δm to the observed u- and r-band variability amplitudes.

The limitations of this model and the implications of the assumptions are discussed extensively in Bouvier et al. (1993).

To find the ($T_{\rm spot}$, $\mathcal{F}_{\rm eq}$) pair that best describes the variability properties observed for a given object, we explored a two-dimensional grid, ranging from 1000 K to 10 000 K in $T_{\rm spot}$ and from 0.1% to 90% in $\mathcal{F}_{\rm eq}$, with a step of 5 K in $T_{\rm spot}$ and of 0.002% in $\mathcal{F}_{\rm eq}$. This parameter space range was enlarged when the best solution fell at the edge of the explored domain. For each point of the grid, the theoretical amplitudes Δm defined as in Eq. (3) were computed, and their agreement with the observed variability amplitudes was estimated through χ^2 statistics; the best solution is defined as the one that minimizes χ^2.

The significance of the result was evaluated by investigating how stable this "best" solution is relative to weak variations of the input "observed" amplitudes. Spot model predictions are typically affected by a degree of degeneracy between different spot parameters (see, e.g., Walkowicz et al. 2013); a given set of amplitudes could in principle be reproduced either in terms of more extended surface spots with a modest temperature difference relative to the stellar photosphere, or in terms of a smaller spot distribution with a larger temperature difference. To estimate the uncertainty on the spot model result for a given object, we did the following:

1. we took the u- and r-band amplitudes (amp_u, amp_r) and the associated error bars err_u, err_r (defined as $\mathrm{err}_m = \sqrt{2\sigma_m^2}$, where σ_m is the photometric noise at the relevant brightness location, traced as a fit to the lower envelope of the appropriate field stars distribution in Fig. 2);
2. we used the rejection method for generating random deviates within a normal distribution (Press et al. 1992) to produce 200 random ($\mathrm{amp}_u^{\rm test}$, $\mathrm{amp}_r^{\rm test}$) pairs, where $\mathrm{amp}_m^{\rm test}$ is extracted from a Gaussian distribution centered on amp_m with standard deviation err_m;
3. for each of the randomly generated (u, r) amplitude pairs, we ran the spot model in Eq. (3) and computed the spot parameters that best reproduced these test variability amplitudes;
4. the spot model results for each of the random amplitudes pairs were used to build a $T_{\rm spot}$ and a $\mathcal{F}_{\rm eq}$ distribution, whose mean and standard deviation were extracted as a best value and a corresponding uncertainty, respectively.

3.4.2. Global picture of TTS spot properties in NGC 2264

An overview of the different nature of modulated variability exhibited by accreting and non-accreting members of NGC 2264 is provided in Fig. 9 (see also Bouvier et al. 1995). This compares the u- and r-band amplitudes for different classes of members to cool (upper panel) and hot (lower panel) spot model predictions, computed assuming, for illustration purposes, a typical photospheric temperature of 4000 K and varying spot temperatures and filling factors.

A first interesting feature of these two diagrams is that u-band variability amplitudes are always larger than r-band amplitudes. This is consistent with expectations in the spot description of modulated variability. WTTS typically display lower variability amplitudes than CTTS, $\lesssim$0.4 mag in r and 0.5 mag in

[2] The scale of Cohen & Kuhi (1979) is similar to that of Kenyon & Hartmann (1995) for spectral types earlier than M1 and to that of Luhman et al. (2003) for later spectral types. It differs somewhat from the more recent determination of Pecaut & Mamajek (2013) for PMS stars, notably in the earlier (i.e., K) spectral type range. Our choice of favoring the scale of Cohen & Kuhi over that of Pecaut & Mamajek here is motivated by the fact that the color sequences on which the former is based provide a better match to the empirical cluster sequence in CFHT color−magnitude diagrams, especially for earlier type stars, than models relevant to the latter.

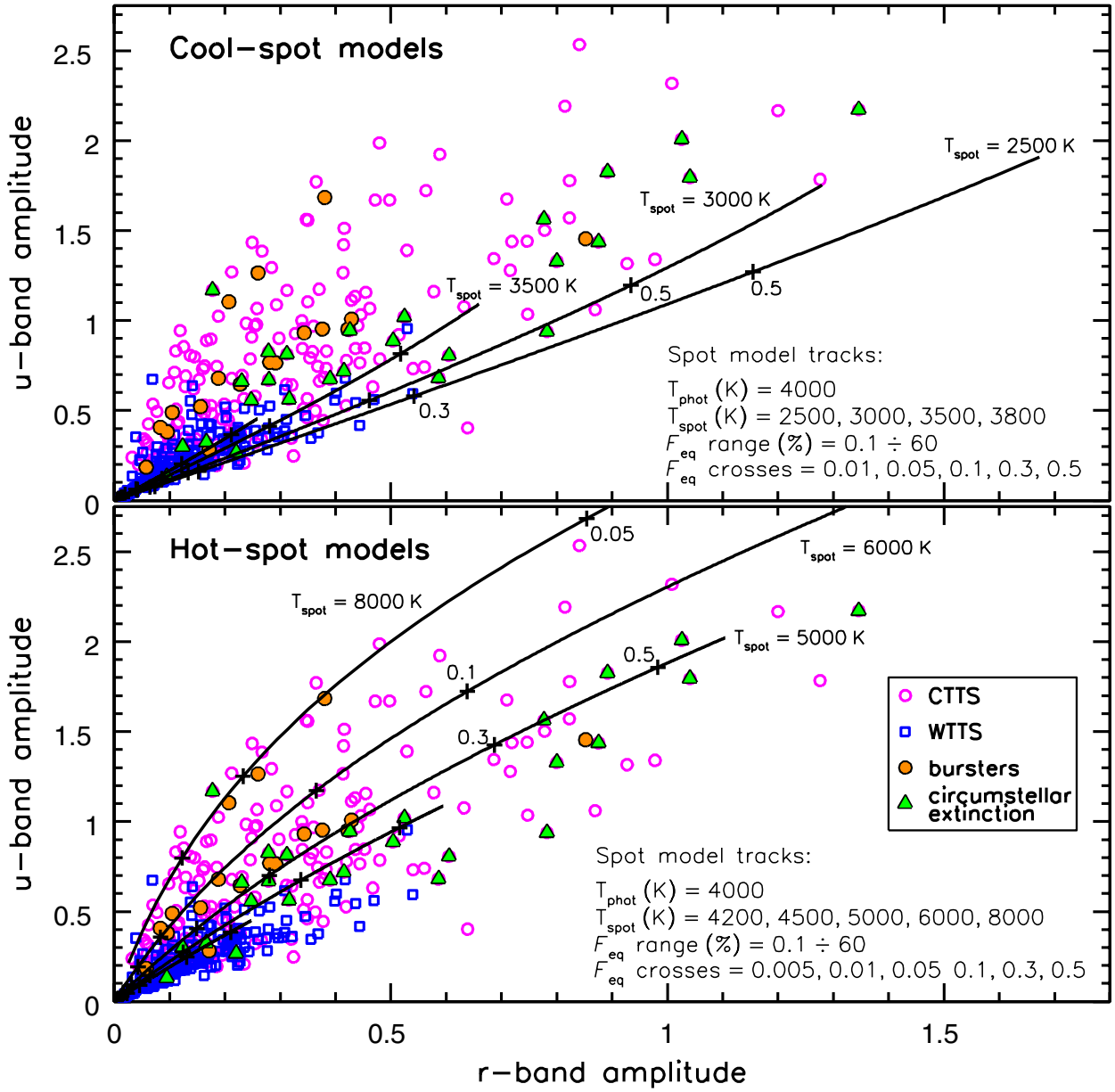

Fig. 9. *u*- and *r*-band variability amplitudes observed for WTTS (blue squares) and CTTS (magenta circles) are compared to cool (*upper panel*) and hot (*lower panel*) spot model predictions. Model tracks are traced assuming a fixed photospheric temperature $T_{\rm phot}$ of 4000 K (corresponding to a K7 star). Each model track corresponds to a different spot temperature $T_{\rm spot}$: in the *upper panel* (cool spots), four different $T_{\rm spot}$ values are considered, ranging from 200 K to 1500 K lower than $T_{\rm phot}$; in the *lower panel* (hot spots), five different $T_{\rm spot}$ values are explored, ranging from 200 K to 4000 K above the photospheric temperature. Along each track, $\mathcal{F}_{\rm eq}$ varies from 0.1% to 60%; reference values of the spot-to-star surface ratio are marked with crosses for clarity. For CTTS, two additional subclasses are highlighted: objects dominated by stochastic accretion bursts (Stauffer et al. 2014, orange dots) and objects dominated by circumstellar extinction (McGinnis et al. 2015, green triangles), either quasi-periodic (AA Tau objects) or aperiodic.

u. Cool spot model tracks, depicted in the upper panel of Fig. 9, span the WTTS locus over the entire amplitude range fairly well; this suggests that in most cases, WTTS variability can be convincingly reproduced in terms of cool magnetic spots, having a temperature of $\sim$500−1000 degrees lower than $T_{\rm phot}$ and covering up to $\sim$30% of the stellar surface. A smaller fraction of WTTS are located in the region of the diagram dominated by hot spots; enhanced chromospheric activity may explain the photometric properties observed for some of these objects, while others might actually be accreting stars at levels too low to be detected. A non-negligible overlap exists between the distributions in amplitudes of WTTS and CTTS; however, a more significant fraction of CTTS is observed to exhibit larger variability amplitudes than WTTS, and, at a given value of amp$_r$, the bulk of accreting members is located at larger *u*-band amplitudes than their non-accreting counterparts. Cool spot model predictions are not able to reproduce the color variability of objects located in this part of the CTTS distribution; a better fit to their photometric amplitudes is provided by hot-spot model tracks in the lower panel of Fig. 9. Temperature differences between hot spots and stellar photosphere range from $\lesssim$1000 K to several thousand K. Typical hot-spot distributions extend over $\sim$5–10% of the stellar surface for spots 2000 K-hotter than the photosphere and down to a few percent for the hottest spots.

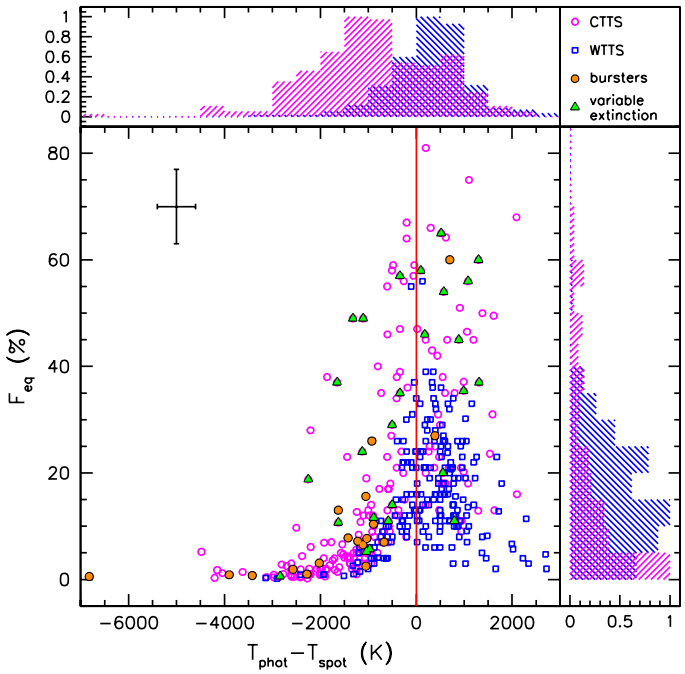

Fig. 10. Best spot model solutions for CTTS (magenta circles) and WTTS (blue squares) in NGC 2264 are statistically compared. A typical error bar is shown as a black cross in the upper left corner of the diagram. Error estimates result from the uncertainties on the photometric amplitudes, following the procedure described in Sect. 3.4.1, plus a lower order correction accounting for uncertainties on the photospheric temperature ($T_{\rm phot}$) and on the shape of the limb-darkening coefficients $\mu(\lambda)$. The red vertical line marks the zero-value temperature difference between stellar photosphere and spot distribution. For CTTS, objects dominated by stochastic accretion bursts are marked in orange, while green triangles correspond to AA Tau-like objects. Histograms shown in *side panels at the top and to the right* of the diagram compare the CTTS (magenta) vs. WTTS (blue) distribution in spot properties (temperature difference relative to the stellar photosphere and percentage of surface covered, respectively). The heights of histogram bars are normalized to the highest channel count in each distribution.

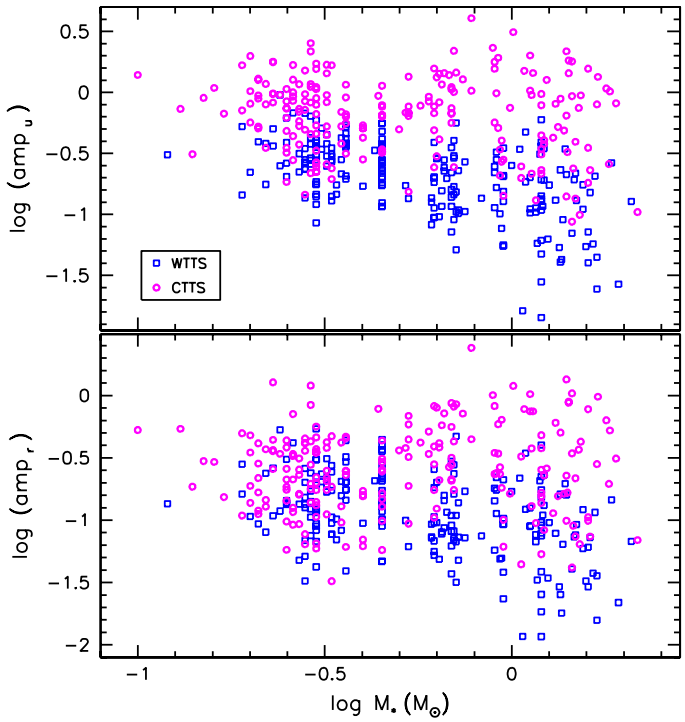

Fig. 11. Photometric amplitudes in the u band (*upper panel*) and in the r band (*lower panel*) as a function of stellar mass are compared for CTTS (magenta circles) and WTTS (blue squares). Mass estimates are derived as described in Paper I.

3.4.3. Spot model results

Figure 10 synthesizes the main features of the spot properties inferred, case by case, for the populations of CTTS and WTTS in NGC 2264, using the model described in Sect. 3.4.1.

Three distinct loci can be identified in this diagram. The first, located to the right of the red line (i.e., at positive values of $T_{\rm phot}$–$T_{\rm spot}$), below $\mathcal{F}_{\rm eq} = 40\%$, is the main locus populated by WTTS. In most cases, the best spot solution suggests a surface spot distribution ∼500 K colder than the stellar photosphere, extending over ∼10–30% of the stellar surface. A small number of CTTS are also located in this region of the diagram, with properties consistent with those deduced for WTTS, which suggests that cool spots of magnetic origin are still a primary cause of modulated variability in these cases.

The second locus is located to the left of the red line (i.e., at negative values of $T_{\rm phot}$–$T_{\rm spot}$) and is the locus primarily populated by CTTS. Spot distributions that best reproduce the observed photometric amplitudes in individual cases are typically ∼1000−2000 K hotter than the stellar photosphere, with a tail of objects for which temperature differences of over 3000−4000 K are predicted by spot model results. Although the $T_{\rm spot}$–$\mathcal{F}_{\rm eq}$ degeneracy in spot model results may play a non-negligible role in the anticorrelation between these two quantities, observed both to the left and right of the red line in Fig. 10, a significant difference between the distributions of CTTS and WTTS over $\mathcal{F}_{\rm eq}$ can be detected, with the former being largely located below 5–10%, while the latter are mainly comprised between 5–10% and 30%, as discussed earlier.

The third locus in the diagram is the point distribution around the $T_{\rm phot}$–$T_{\rm spot} = 0$ line, above $\mathcal{F}_{\rm eq} = 40\%$. This is mainly populated by CTTS. These objects stand out for the small temperature difference between photosphere and best spot model and for the corresponding high value of $\mathcal{F}_{\rm eq}$, significantly higher than the typical values for WTTS or CTTS. This suggests that for this subgroup of objects, spot models are ill-suited to describe the observed amplitudes and color properties, and hence other components may be dominating the observed variability. This conclusion is supported by several AA Tau-like objects in this group, whose variability is known to be dominated by quasi-periodic disk occultation.

4. Discussion

4.1. Photometric behavior of CTTS and WTTS at short wavelengths

From a statistical point of view, accreting YSOs (CTTS) exhibit significantly different variability properties from disk-free young stars (WTTS). Higher levels of variability are associated with the former group, both in the optical (r band) and, even more markedly, at UV wavelengths (u band); typical photometric amplitudes measured across the CTTS population amount to about three times those characteristic of the WTTS group.

A definite anticorrelation trend is observed between variability amplitudes and stellar mass for WTTS, both in the r and in the u band, as illustrated in Fig. 11. This would suggest that smaller and/or more uniformly distributed spots, translating into

more modest peak-to-peak luminosity variations, are found at the surface of more massive PMS stars than for lower mass objects. Conversely, no significant correlation properties are observed between mass and photometric amplitudes measured for CTTS.

Bluer CTTS (i.e., those displaying higher UV excess relative to photospheric colors) statistically tend to exhibit stronger UV variability. The UV excess is one of the most direct diagnostics of the accretion process; this statistical correlation, and the different variability behavior pertaining to the CTTS population compared to WTTS, suggest that the variability scenario observed for CTTS is dominated by an active circumstellar disk and not by magnetic activity common to non-accreting young stars (WTTS).

Variability amplitudes measured for WTTS are best interpreted in terms of geometric luminosity modulation from cool surface spots, a result of the magnetic activity of the star. Typical spot parameters found in this study for WTTS amount to an effective temperature ∼500 degrees colder than the photosphere, and area coverage from 5–10% to 30% of the stellar surface. Conversely, CTTS variability appears to be dominated by hot accretion spots, with typical effective temperatures up to 4000 K hotter than the stellar photosphere, and that extend over a few percent of the stellar surface.

It is important to point out that although CTTS and WTTS appear to be statistically distinct in many metrics, the two populations display a non-negligible overlap in photometric behavior. Some CTTS, classified as such based on "standard" indicators of accretion disk (H_α emission, near-IR or UV excess), are found to exhibit photometric properties consistent with objects that lack disk signatures, and vice versa. This would indicate that a continuum of possible behaviors instead of a clear-cut transition exists between the state of a "classical" T Tauri and that of a diskless, weak-lined T Tauri star. Figure 16 of Paper I clearly shows that a broad variety of accretion regimes coexists within the same young stellar population (from strong accretion rates $\dot{M}_{\rm acc} \sim 10^{-7}\ M_\odot$/yr down to marginal $\dot{M}_{\rm acc} \lesssim 10^{-10}\ M_\odot$/yr). On the other hand, some sources classified as WTTS by our criteria might actually be objects with low undetected accretion or in a "quiescent" state. Cases of WTTS-like young stars that episodically cross the CTTS-defining borders have indeed been reported in the literature (Murphy et al. 2011; Cieza et al. 2013).

4.2. Color trends

Independently of their specific nature, monitored members are typically found to become redder as they fade, and observed variability amplitudes are larger at shorter wavelengths. This property is well understood when considering a spot-dominated variability scenario (e.g., Bouvier et al. 1993; Vrba et al. 1993; Herbst et al. 1994).

While this qualitative trend is common to systems of different nature, the rate at which the amplitudes decrease with λ is more informative regarding the specific mechanisms at play. Different behaviors are indeed observed when comparing the typical $\Delta r/\Delta(u-r)$ slopes measured for the WTTS vs. CTTS classes. Accretion-dominated objects stand out for their significantly shallower slopes, which are indicative of a much stronger contrast at UV wavelengths than that measured at longer wavelengths. Ambiguous results are obtained for the WTTS class and the subgroup of disk-bearing objects (AA Tau objects), whose variability appears to be dominated by circumstellar extinction. Typical slopes measured in both cases are found to be consistent with each other and with the color slope predicted for interstellar extinction; a somewhat larger dispersion in values is detected across WTTS. A similarity in color behavior between what is observed for WTTS and what is expected in the case of circumstellar extinction (assuming interstellar extinction properties) was previously noted by Grankin et al. (2008) in the optical. We stress that while a linear trend appears to provide a detailed description of the color variation with magnitude for spotted stars (as also observed, on longer timescales, by Grankin et al. 2007, 2008), this merely provides average information on the actual color behavior observed for some AA Tau-like or circumstellar extinction-dominated systems (as illustrated in panels c and d of Fig. 6). Indeed, complex and phase-varying color behavior is well documented in AA Tau itself (Bouvier et al. 2003). The alternation of phases of colored and gray magnitude variations for these objects may indicate non-uniform extinction properties across the occulting screen (e.g., more opaque at the center and optically thin at the edges). Furthermore, increased veiling at the epochs of maximum accretion shock visibility (i.e., close to the occultation event, in the assumption that the inner disk warp is located at the base of the accretion column) may determine a sudden transition of the system between different color regimes.

Remarkably, Grankin et al. (2007) detected color slopes for CTTS that are quite similar to those measured for WTTS (Grankin et al. 2008) in optical bands (V, R). This result, compared with the present analysis, shows that hot and cold spots are primarily distinguished at short wavelengths.

4.3. Stability and leading timescales for u-band variability

The present study focuses primarily on the exploration of UV variability on timescales relevant to stellar rotation. However, comparing variability signatures on different timescales is instrumental in achieving a more complete picture of YSO dynamics.

The short timescales (hours) show little variability compared to the amount measured on days/weeks (more mid-term timescales). To estimate a typical amount of short-term variability, we computed the average rms scatter of photometric measurements obtained at different epochs within single nights (Sect. 2) across our sample. CTTS are typically found to display an rms variability of 0.06 mag on these time baselines, corresponding to barely 8−9% of the amplitudes measured during the full CFHT monitoring. Similar results are obtained for the WTTS group, with typical short-term rms variability of 0.025 mag, or about 10% with respect to the corresponding mid-term variability amplitudes.

This result was partly introduced in Sect. 4.3 of Paper I in the context of a more quantitative assessment of the contribution of modulated variability to the total amount of variability detected for accreting objects. We found that up to ∼75% of the UV variability measured for typical CTTS on week-long timescales (generally a few to several tenths of magnitude) is simply due to geometric effects of rotational modulation. Of the remaining fraction linked with intrinsic variability, a larger contribution can be attributed to cycle-to-cycle variations (possibly related to accretion spot evolution), while a smaller component is statistically contributed on hour-long timescales, which is more sensitive to unstable, stochastic behaviors in the accretion process.

To evaluate the effect of mid-term timescales on long-term (years) variations, we compared u-band photometry obtained during the CFHT/MegaCam monitoring survey of February 2012 with single-epoch photometry obtained with the

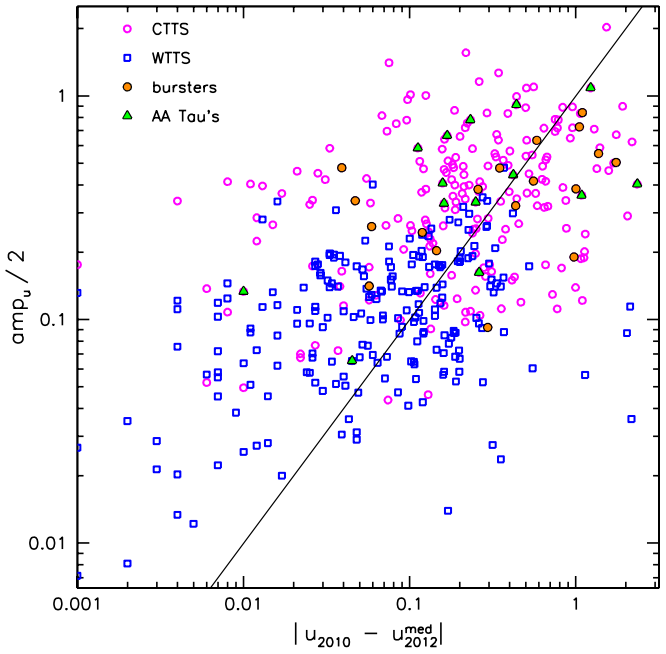

Fig. 12. u-magnitude differences between single-epoch photometry in December 2010 and median light curve photometry in February 2012 are compared to the semi-amplitudes of u-band light curves from February 2012 monitoring for WTTS (blue squares), CTTS (magenta circles), and CTTS accretion-dominated (orange dots) and extinction-dominated (green triangles) subgroups. The equality line is traced in black to guide the eye.

same instrument during a preliminary, single-epoch mapping survey performed in December 2010. Details on this first photometric run and on subsequent data reduction are provided in Paper I. If mid-term timescales dominate the variability pattern exhibited by TTS on longer baselines, we expect the photometric measure from the snapshot survey of December 2010 (u_{2010}) to correspond to a random epoch in the light curve of the object reconstructed from 2012 monitoring. Hence, when measuring the absolute difference between u_{2010} and the median light-curve magnitude from February 2012 (u^{med}_{2012}), we expect this difference to be smaller than (or similar to) half the variability amplitude amp$_u$ of the light curve. Conversely, if other variability mechanisms are predominant on year-long timescales, we expect to measure $|u_{2010} - u^{med}_{2012}|$ values on average higher than amp$_u$/2. This comparison is shown in Fig. 12 for all variable members considered in this study. A clear offset along the equality line is observed between the WTTS and the CTTS groups in the diagram, with the latter group located at significantly higher variability amplitude values. However, there are no significant differences between the two stellar groups in the indicator of interest here, that is, the $|u_{2010} - u^{med}_{2012}|/(\text{amp}_u/2)$ ratio. Both groups are distributed in clouds of similar properties about the equality line on the diagram, with a mean ratio of 0.8 (i.e., typical epoch-to-epoch difference that can be fully accounted for by mid-term variability) and comparable rms scatter. This suggests that similar timescales or mechanisms (notably rotational modulation) are responsible for the long-term variations observed in the two cases.

For the CTTS group, we additionally probed the stability of u-band variability on longer timescales (>10 years) by comparing the UV excess luminosity measured and monitored in our survey (see Paper I) with values measured in a similar single-epoch U-band survey of NGC 2264 performed by Rebull et al. (2002). Results of this comparison are shown in Fig. 13 of Paper I. Again, we observe that median UV excess luminosities from 2012 and single-epoch measurements from Rebull et al.'s study distribute around the equality line with an rms scatter consistent with the typical amount of variability detected on a timescale of weeks.

These results suggest that the mid-term timescale is the leading timescale for YSO variability, at least up to baselines of several years. The similarity of WTTS and CTTS in this respect also suggests that the typical dynamics of the accretion process on CTTS is intrinsically stable over timescales of years, although it may be variable in the shorter term. In other words, single accretion events may be shorter lived, and the dynamics of interaction between disk and stellar magnetosphere may lead to rapidly evolving surface spots (on timescales of a few rotational cycles or less) and irregular light curve morphology. However, the averaged spot properties, indicative of the intensity of mass accretion onto the star and of the mechanisms that regulate the process, can persist over timescales of years. Similar conclusions were presented by Grankin et al. (2007).

5. Conclusions

The work reported here provides a first extensive mapping of variability properties at short (UV) wavelengths for a whole star-forming region (the NGC 2264 cluster) and its several hundred members. The sample encompasses over 750 young stars in the region, of which about 40% show evidence of disk accretion. Variability was monitored simultaneously in the optical (r band) and in the UV (u band) over two full weeks, with multiple measurements per observing night. Our statistical analysis globally confirms and strengthens earlier results on the manifold nature of variability displayed by young stellar objects. Disk-bearing cluster members (CTTS) exhibit significantly higher levels of variability than non-accreting objects (WTTS) on timescales ranging from hours to weeks. A statistical correlation is observed between the amount of photometric variability and that of UV excess measured across the former group, which indicates that ongoing accretion and star-disk interaction are the main driving factors of the variable nature of CTTS. Amplitude ranges and color variations monitored for WTTS are best reproduced in terms of cool surface spots linked with magnetic activity, which modulate the luminosity of the star as it rotates. Hot-spot models are instead required to account for the stronger variability and steeper amplitude increase from the optical to the UV observed for typical CTTS. In both groups, similar amounts of variability are observed in the mid- (weeks) and long term (years); this indicates that rotational modulation is the main source of YSO variability over several hundred periods, independently of their accretion status. This in turn suggests that the underlying physical processes (namely magnetic activity in WTTS and disk accretion in CTTS) have a relatively stable nature in the longer term, although disk accretion can exhibit more erratic behavior in the shorter term.

Acknowledgements. We thank the anonymous referee for useful comments. This publication makes use of data products from the Sloan Digital Sky Survey. This project was in part supported by the grant ANR 2011 Blanc SIMI5-6 020 01. L.V. acknowledges partial funding for this work from program LLP Erasmus 2011/2012 at Università degli Studi di Palermo. S.H.P.A. acknowledges financial support from CNPq, CAPES and Fapemig.

Appendix A: Spotted stars and color slopes

Individual amplitudes and color slopes may vary broadly among cases that share the same physical origin for the observed

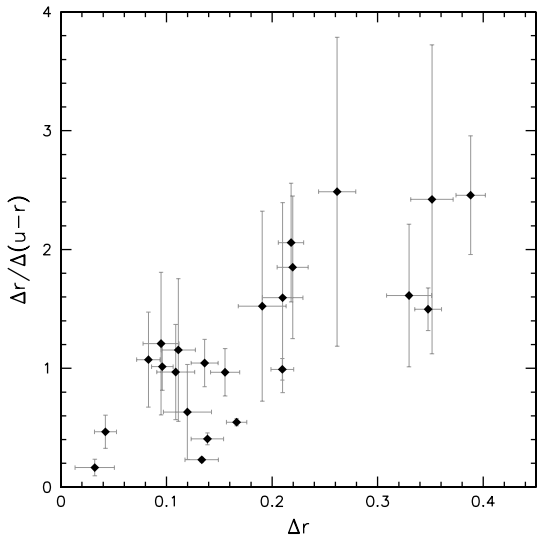

Fig. A.1. Measured r-band amplitudes (Δr) and corresponding slopes ($\Delta r/\Delta(u-r)$) are compared for WTTS members of spectral type M1 in our sample. Error bars on photometric amplitudes follow from the photometric noise estimate based on field stars sequence in Fig. 2; error bars on slope values are computed by simulating 1000 random ($\Delta r, \Delta(u-r)$) pairs uniformly distributed around the observed values within the uncertainties and measuring the corresponding scatter on computed slopes.

variability; this reflects intrinsic object-to-object differences in the relative surface extent and temperature contrast provided by the intervening layer. This point is illustrated in Fig. A.1 for a subset of WTTS members from our sample with uniform spectral type of M1 (hence homogeneous in photospheric temperature). For these diskless young stars, the observed variability is most straightforwardly interpreted in terms of surface magnetic spots, cooler than the stellar photosphere, that modulate the photospheric emission. Figure A.1 shows that larger r-band amplitudes of variability typically correspond to steeper $\Delta r\,/\,\Delta(u-r)$ slopes; this suggests that a less significant λ-dependence in the spot-to-star contrast is observed for objects with the largest variability amplitudes. This result can be understood if we consider that along the average trend, larger amplitudes reflect larger temperature differences between spot and stellar photosphere. Darker spots emit less flux, resulting in more marked luminosity differences between the phases of minimum and maximum spot visibility during stellar rotation. This luminosity difference, however, will be less colored, because the emission spectrum for darker spots peaks at longer wavelengths, and hence progressively contributes less in the observed λ-window; consequently, the net effect of darker spots in the spectral range of interest will be a more uniform flux decrease when the spot is in view. Similar trends to that shown in Fig. A.1 are found at different spectral types; the scatter in amplitudes around the average trend may reflect a variety in the effective percentage of stellar surface covered by spots (for a given temperature, spot distributions covering a larger area will produce larger variability amplitudes, but the color dependence of the contrast will remain unchanged). In addition, some marginal accretion activity might still be present in the more variable stars here classified as WTTS, hence contributing to the vertical scatter in values.

References

Abazajian, K. N., Adelman-McCarthy, J. K., Agüeros, M. A., et al. 2009, ApJS, 182, 543
Alencar, S. H. P., Teixeira, P. S., Guimarães, M. M., et al. 2010, A&A, 519, A88
Bouvier, J., Cabrit, S., Fernandez, M., Martin, E. L., & Matthews, J. M. 1993, A&A, 272, 176
Bouvier, J., Covino, E., Kovo, O., et al. 1995, A&A, 299, 89
Bouvier, J., Grankin, K. N., Alencar, S. H. P., et al. 2003, A&A, 409, 169
Bouvier, J., Alencar, S. H. P., Boutelier, T., et al. 2007, A&A, 463, 1017
Cieza, L. A., Olofsson, J., Harvey, P. M., et al. 2013, ApJ, 762, 100
Claret, A., & Bloemen, S. 2011, A&A, 529, A75
Cody, A. M., Stauffer, J., Baglin, A., et al. 2014, AJ, 147, 82
Cohen, M., & Kuhi, L. V. 1979, ApJS, 41, 743
Costigan, G., Vink, J. S., Scholz, A., Ray, T., & Testi, L. 2014, MNRAS, 440, 3444
Donati, J.-F., Skelly, M. B., Bouvier, J., et al. 2010, MNRAS, 402, 1426
Fallscheer, C., & Herbst, W. 2006, ApJ, 647, L155
Favata, F., Flaccomio, E., Reale, F., et al. 2005, ApJS, 160, 469
Fazio, G. G., Hora, J. L., Allen, L. E., et al. 2004, ApJS, 154, 10
Fiorucci, M., & Munari, U. 2003, A&A, 401, 781
Flaccomio, E., Micela, G., Favata, F., & Alencar, S. H. P. 2010, A&A, 516, L8
Flaccomio, E., Micela, G., & Sciortino, S. 2012, A&A, 548, A85
Fruth, T., Kabath, P., Cabrera, J., et al. 2012, AJ, 143, 140
Grankin, K. N., Melnikov, S. Y., Bouvier, J., Herbst, W., & Shevchenko, V. S. 2007, A&A, 461, 183
Grankin, K. N., Bouvier, J., Herbst, W., & Melnikov, S. Y. 2008, A&A, 479, 827
Günther, H. M., Cody, A. M., Covey, K. R., et al. 2014, AJ, 148, 122
Hartmann, L., Hewett, R., & Calvet, N. 1994, ApJ, 426, 669
Herbig, G. H. 1962, Adv. Astron. Astrophys., 1, 47
Herbst, W., Herbst, D. K., Grossman, E. J., & Weinstein, D. 1994, AJ, 108, 1906
Joy, A. H. 1945, ApJ, 102, 168
Kamai, B. L., Vrba, F. J., Stauffer, J. R., & Stassun, K. G. 2014, AJ, 148, 30
Kenyon, S. J., & Hartmann, L. 1995, ApJS, 101, 117
Luhman, K. L., Stauffer, J. R., Muench, A. A., et al. 2003, ApJ, 593, 1093
McGinnis, P. T., Alencar, S. H. P., Guimaraes, M. M., et al. 2015, A&A, 577, A11
Ménard, F., & Bertout, C. 1999, in The Origin of Stars and Planetary Systems, eds. C. J. Lada, & N. D. Kylafis, NATO ASIC Proc., 540, 341
Morales-Calderón, M., Stauffer, J. R., Hillenbrand, L. A., et al. 2011, ApJ, 733, 50
Murphy, S. J., Lawson, W. A., Bessell, M. S., & Bayliss, D. D. R. 2011, MNRAS, 411, L51
Pecaut, M. J., & Mamajek, E. E. 2013, ApJS, 208, 9
Press, W. H., Teukolsky, S. A., Vetterling, W. T., & Flannery, B. P. 1992, Numerical recipes in C. The art of scientific computing, 2nd edn. (New York: Cambridge University Press)
Rebull, L. M., Makidon, R. B., Strom, S. E., et al. 2002, AJ, 123, 1528
Rebull, L. M., Cody, A. M., Covey, K. R., et al. 2014, AJ, 148, 92
Rucinski, S. M., Matthews, J. M., Kuschnig, R., et al. 2008, MNRAS, 391, 1913
Stauffer, J., Cody, A. M., Baglin, A., et al. 2014, AJ, 147, 83
Stetson, P. B. 1996, PASP, 108, 851
Torres, C. A. O., & Ferraz Mello, S. 1973, A&A, 27, 231
Venuti, L., Bouvier, J., Flaccomio, E., et al. 2014, A&A, 570, A82
Vogt, S. S. 1981, ApJ, 250, 327
Vrba, F. J., Chugainov, P. F., Weaver, W. B., & Stauffer, J. S. 1993, AJ, 106, 1608
Walker, M. F. 1972, ApJ, 175, 89
Walkowicz, L. M., Basri, G., & Valenti, J. A. 2013, ApJS, 205, 17
Werner, M. W., Roellig, T. L., Low, F. J., et al. 2004, ApJS, 154, 1
Wolk, S. J., Rice, T. S., & Aspin, C. 2013, ApJ, 773, 145

Abstract

Disk accretion plays a most important role in the star formation scenario. It governs the interaction of young stars with their disks, with a long-lasting impact on stellar evolution, by providing both mass and angular momentum regulation. Accretion is also a central ingredient in the physics of star-disk systems at the epoch when planets start to form. In the picture of magnetospheric accretion, a cavity of a few stellar radii extends from the star surface to the inner disk rim. The star-disk interaction is then mediated by the stellar magnetic field, whose lines thread the inner disk and couple it to the central object. Material from the inner disk is channeled along the field lines in accretion columns that reach the star at near free-fall velocities. The impact produces localized hot shocks at the stellar surface, which determine the distinctive UV excess emission of accreting objects relative to non-accreting sources. Intrinsic time evolution, and varying visibility of surface features during stellar rotation, combine in the characteristic photometric variability of young stars, revealed by monitoring surveys.

In this thesis, I investigate the statistical properties of disk accretion and of its variability in the young open cluster NGC 2264 ($\sim$3 Myr). This comprises a population of over 700 objects, about similarly distributed between disk-bearing ($\sim$45%) and disk-free sources. I characterize accretion from the UV excess diagnostics; disk-free cluster members define the reference emission level over which the UV excess linked to accretion is detected and measured. The study is based on a homogeneous photometric dataset obtained at the Canada-France-Hawaii Telescope (CFHT), composed of a deep mapping of the region in four different bands (u, g, r, i) and of simultaneous optical (r-band) and UV (u-band) monitoring on timescales from hours to days for a period of 2 weeks. In the first part of the study, UV excesses are converted to accretion luminosities and mass accretion rates to derive a global picture of the accretion process across the cluster, and to investigate the dependence of the typical accretion properties on stellar parameters such as mass and age. A robust correlation is detected between the average accretion rate and stellar mass, but a significant dispersion in accretion rates is observed around this average trend at any given mass. I show that the extent of this spread cannot be accounted for by typical variability on week timescales; I discuss several aspects, including a diversity in accretion mechanisms and a non-negligible evolutionary spread among cluster members, which may contribute to the broad range of accretion regimes detected. In the second part of the study, I explore the variability signatures in the UV that pertain to different types of variable young stars. I show that accreting objects typically exhibit stronger variability than non-accreting objects, and that the color properties associated with the two groups are consistent with a statistically distinct origin of the variability features in the two cases. These are dominated, in the first case, by hot accretion spots, and in the second, by cold spots linked to magnetic activity. I compare the amounts of variability on timescales of hours, days and years, to assess the dominant components. The mid term (days) appears to be the leading timescale for variability in young stars up to years, with a major contribution from rotational modulation. In the third part of the study, I use a set of 38 day-long optical light curves obtained with the *CoRoT* satellite, close to the epoch of the CFHT survey, to investigate periodicity and rotation properties in NGC 2264. I derive the period distribution for the cluster and show that accreting and non-accreting objects exhibit statistically distinct properties: the second rotate on average faster than the first. I then illustrate the connection between accretion and rotation properties in the disk-locking scenario.

Key-words: young stars; disk accretion; UV excess; variability: T Tauri; rotation; open clusters: NGC 2264

Résumé

Le processus d'accrétion joue un rôle crucial dans le scénario de formation stellaire. Il régit l'interaction des étoiles jeunes avec leurs disques, en régulant l'échange de masse et de moment cinétique ; ainsi, il a un impact durable sur leur évolution. De plus, l'accrétion est un ingrédient essentiel de la physique des systèmes étoile-disque à l'époque de formation planétaire. Selon le modèle d'accrétion magnétosphérique, une cavité de quelques rayons stellaires s'étend de la surface de l'étoile au bord interne du disque. L'interaction se produit donc par le champ magnétique stellaire, qui pénètre le disque interne et l'attèle à l'objet central. Des colonnes d'accrétion se développent du disque interne suivant les lignes de champ, et atteignent l'étoile à des vitesses presque de chute libre. L'impact à la surface crée des chocs localisés, qui sont responsables de l'excès de luminosité UV distinctif des systèmes accrétants par rapport aux objets non-accrétants. L'évolution temporelle intrinsèque et l'effet d'alternance du côté visible des objets au cours de leur rotation se mélangent dans la variabilité photométrique typique des étoiles jeunes, révélée par les campagnes de suivi.

Durant ma thèse, j'ai mené une étude statistique du processus d'accrétion et de sa variabilité dans la région NGC 2264 ($\sim$3 Myr). Cet amas contient plus de 700 membres, repartis entre étoiles avec disque ($\sim$45%) et sans disque. J'ai qualifié l'accrétion par la diagnostique de l'excès UV ; les étoiles de l'amas privées de disque définissent le niveau d'émission de référence au-dessus duquel l'excès UV provenant du choc d'accrétion est décelé et mesuré. Mon étude se base sur un jeu de données photométriques obtenues au télescope Canada-France-Hawaii (CFHT), comprenant un relevé profond en 4 filtres (u, g, r, i) et un suivi simultané de variabilité optique (bande r) et UV (bande u) d'une durée de 2 semaines et avec échantillonnage de l'ordre des heures. Dans une première étape de cette étude, je convertis les excès UV en taux d'accrétion pour obtenir une image globale du processus à travers l'amas et examiner sa dépendance envers les paramètres stellaires. Le taux d'accrétion moyen corrèle avec la masse de l'étoile, bien qu'une dispersion significative autour de cette tendance moyenne soit observée à chaque masse. Je montre que cet étalement ne peut pas être justifié par la variabilité des objets ; une diversité de mécanismes d'accrétion et de stades évolutifs dans l'amas pourrait contribuer à la vaste gamme de régimes d'accrétion décelés. Ensuite, j'explore les signatures dans l'UV propres à des types distincts d'étoiles jeunes variables. Je montre que les étoiles accrétantes présentent en général une variabilité plus prononcée que les objets sans disque, et que les respectives variations de couleur sont cohérentes avec une origine différente de la variabilité associée aux deux groupes. Pour le premier groupe, ce sont les chocs d'accrétion à dominer, alors que le deuxième est dominé par des taches froides à la surface, dérivant de l'activité magnétique stellaire. Je compare les variations photométriques mesurées sur bases de quelques heures, quelques jours et quelques années, afin de déterminer quelles soient les composantes de variabilité les plus importantes. L'échelle de temps de quelques jours prévaut sur les autres délais investigués dans la variabilité enregistrée pour ces étoiles jeunes, avec une contribution majeure provenant de l'effet de modulation rotationnelle. Enfin, j'analyse les propriétés de rotation des étoiles de l'amas à partir d'un jeu de courbes de lumière optiques, d'une durée de 38 jours, obtenues avec le satellite CoRoT près de la campagne d'observation au CFHT. Je reconstruis la distribution de périodes de l'amas et montre que les objets sans disque tournent statistiquement plus vite que les objets accrétants. Cette connexion entre les propriétés d'accrétion et celles de rotation peut être interprétée dans le scénario de disk-locking.

Mots-clés : étoiles jeunes ; disques d'accrétion ; excès UV ; variabilité : T Tauri ; rotation ; amas ouverts : NGC 2264

Sommario

Il processo di accrescimento da disco svolge un ruolo cruciale nello scenario di formazione stellare. Esso governa l'interazione tra le stelle giovani e i dischi che le circondano, regolando lo scambio di materia e momento angolare, con impatto durevole sulla loro evoluzione. L'accrescimento è inoltre un ingrediente essenziale della fisica dei sistemi stella-disco all'epoca di formazione dei pianeti. Nel modello di accrescimento magnetosferico, una cavità di qualche raggio stellare si estende dalla superficie della stella al bordo interno del disco. L'interazione stella-disco è dunque mediata dal campo magnetico della stella, che permea il disco interno e lo aggancia all'oggetto centrale. Colonne di materia in accrescimento si formano dal disco interno lungo le linee di campo magnetico e raggiungono la superficie della stella a velocità prossime a quelle di caduta libera. L'impatto genera degli shocks circoscritti alla superficie, che producono l'eccesso di emissione UV tipico degli oggetti con accrescimento rispetto alle sorgenti che non accrescono. L'evoluzione temporale intrinseca e le mutevoli condizioni di visibilità dei sistemi durante la loro rotazione assiale si combinano nella variabilità fotometrica caratteristica delle stelle giovani, rivelata tramite le campagne di monitoraggio.

Nel corso di questa tesi, ho condotto uno studio statistico della variabilità di accrescimento nell'ammasso NGC 2264 ($\sim$3 Myr). La regione comprende più di 700 stelle giovani, di cui circa 45% con disco. Per caratterizzarne le proprietà di accrescimento, ho utilizzato la diagnostica dell'eccesso UV; le stelle senza disco dell'ammasso fungono da riferimento fotometrico per misurare l'eccesso UV prodotto negli shocks di accrescimento. Questo studio si fonda su un set di dati multi-banda, ottenuto al telescopio Canada-France-Hawaii (CFHT), costituito da una mappatura della regione in quattro filtri (u, g, r, i) e da un monitoraggio simultaneo della variabilità ottica (banda r) e UV (banda u) su tempi-scala dall'ora a un paio di settimane. Nella prima parte di questo studio, gli eccessi UV sono convertiti in tassi di accrescimento per ricavare un'immagine globale del processo in NGC 2264 e studiarne la dipendenza da parametri stellari quali massa ed età. Una tendenza di correlazione lega il tasso di accrescimento tipico e la massa delle stelle, benché una dispersione significativa di valori attorno a questa tendenza media sia osservata ad ogni massa. Tale dispersione non può essere spiegata tramite la variabilità degli oggetti; una diversità di meccanismi di accrescimento e di stadi evolutivi tra la popolazione dell'ammasso potrebbe contribuire alla vasta gamma di regimi di accrescimento rilevati. Nella seconda parte di questo elaborato, esamino i tratti caratteristici nell'UV di tipi distinti di variabilità tra le stelle giovani. I sistemi con accrescimento attivo sono in generale più variabili delle stelle senza disco, e le variazioni di colore osservate nei due gruppi suggeriscono una diversa origine della variabilità nei due casi. Negli oggetti con disco, questa è dominata dalle macchie calde prodotte nell'impatto delle colonne di accrescimento alla superficie della stella, mentre la variabilità delle sorgenti senza disco è dominata da macchie fredde legate alla loro attività magnetica. Un confronto della quantità di variabilità misurata su tempi-scala di ore, giorni e anni, volto a valutare quali siano i contributi più importanti, mostra che la variabilità su medio termine (giorni) domina sugli altri tempi-scala, specie tramite l'effetto di modulazione rotazionale. Nella terza parte di questo lavoro, analizzo le proprietà di rotazione delle stelle giovani dell'ammasso utilizzando un set di curve di luce ottiche di 38 giorni, ottenute dal satellite *CoRoT* in prossimità delle osservazioni CFHT. La distribuzione di periodi ricavata mostra che oggetti con disco e senza disco possiedono proprietà di rotazione statisticamente differenti: i primi ruotano in media più lentamente dei secondi. Queste caratteristiche possono essere interpretate nello scenario di disk-locking.

Parole-chiave: stelle giovani; accrescimento da disco; eccesso UV; variabilità: T Tauri; rotazione; ammassi aperti: NGC 2264